

Single Atom Alloys for Efficient and Selective Bond Activations: A Model Surface Chemistry Approach

A dissertation submitted by

Matthew D. Marcinkowski

In partial fulfillment of requirements for the degree of

Doctor of Philosophy in Chemistry

Tufts University

February 2017

Adviser: Professor E. Charles H. Sykes

Abstract

Heterogeneous catalysis is extensively utilized in the fabrication of chemicals and materials. Finding a catalyst that exhibits high selectivity and activity for a given process is often difficult as surfaces tend to be more active with strong binding of adsorbates, but more selective with weak binding. Typical heterogeneous catalysts utilize reactive metals such as Pd, Pt, Ir, and Ru. Not only are many of these metals expensive and rare, but they also frequently suffer from less than ideal catalytic selectivity. In addition, it is often difficult to determine the reaction mechanisms of heterogeneous catalysts, due the diversity of surface sites. New strategies are needed to efficiently use these expensive metals, and to improve catalytic selectivity.

This thesis uses a surface science approach to test the catalytic viability and map the reaction mechanism of single atom sites for a variety of industrially relevant reactions. We fabricate single atom alloys (SAAs), where Pd or Pt atoms exist as single isolated sites substituted into a Cu(111) lattice. The economically friendly SAA approach use allows for the activation of reactants using very small amounts of the expensive dopant metals, while still maintaining the high selectivity and low cost typical of Cu catalysts. The practicality of SAAs for a number of important reactions including H₂ activation, hydrogenations, dehydrogenations of O-H bonds, and C-H activation is examined. These reactions are relevant to a number of fields including the petrochemical, pharmaceutical, food, fine chemicals, and environmental industries. Using a combination of scanning tunneling microscopy and temperature programmed desorption/reaction,

the elementary steps of the reaction mechanisms can be mapped out at an atomic level. In general, it is found that SAAs are more active than pure Cu, with greater selectivity compared to Pd and Pt catalysts. The SAA approach allows for a catalyst where the best properties of the dopant metals and Cu are apparent, and can be widely applied to a number of catalytically relevant reactions.

Acknowledgements

“The true delight is in the finding out rather than in the knowing.”

-Isaac Asimov

My five years of graduate school would not have been nearly as enjoyable or successful without the teachers, co-workers, collaborators, friends and family I have had the pleasure of working and living with and I would like to take this opportunity to thank all of them. First, thanks to my advisor Charlie Sykes for all of his guidance throughout my Ph.D. I was lucky to have a P.I. who was very passionate about research, who always pushed for me to learn and understand more, but at the same time was a very reasonable, down to earth guy who I could have an engaging, conversation with in a social atmosphere. Thank you for your mentorship Charlie.

I also owe a great deal to my committee for providing critical insight into my work. Professor Arthur Utz has an extensive knowledge of surface science and it was always useful to be able to run ideas past him. Professor Samuel Thomas provided an organic chemists perspective to my work, which was very valuable given the number of organic adsorbates I worked with. Special thanks to Professor Yuriy Roman from MIT for agreeing to serve as my external committee member.

It was a pleasure working with all my collaborators including Angelos Michaelides, Manos Mavrikakis, Michail Stamatakis, and Maria Flytzani-Stephanopolous. I especially want to thank Professor Stephanopoulos who provided very helpful insight and constructive criticism to many of my papers and

presentations. I am also grateful to Professor Georgios Kyriakiou who taught me the ropes of surface science and temperature programmed desorption when I first joined the Sykes lab. Thanks to all the staff at Tufts for their hard work to keep the Chemistry Department running. Special thanks to Larry Aulenback for helping me to fix/set up countless pieces of equipment!

I have been lucky to work with many exceptional graduate students during my Ph.D. I owe a great deal to the former Sykes lab members senior to me who helped guide me including April Jewell, Emily Lewis, Colin Murphy, and Matt Boucher. Alex Pronschinske helped me extensively with making figures and statistics. Jilei Liu from the Stephanopoulos lab was key to the collaboration with Professor Stephanopolous's lab. Matthew Darby from the Stamatakis lab at UCL is currently working on DFT and KMC simulations to extend the C-H activation project. Thanks to all three Erics and Emily in the Utz Lab for letting us constantly steal your equipment and for being there to bounce ideas off of. I thank fellow Sykes group members past and present, Timothy Lawton, Allister McGuire, Mishan Blecher, Melissa Liriano, Brian Mernoff, Christopher Ivimey, Chloe Wong, Natalie Wasio, Benjamin Coughlin, Mostafa El-Soda, Rezwan Ali, Zhitao Wang, Dipna Patel, Alex Schilling, Matt Uhlman, and Amanda Larson for making the Sykes lab an enjoyable place to be. I would be remiss not to mention the exceptional efforts of the people I worked closest with during my Ph.D., Felicia Lucci and Andrew Therrien. It was a rewarding experience working with both of you and I appreciate all the help you both gave me throughout the years. Finally, thanks to former Sykes Lab member Michael Mattera and honorary Sykes

Lab member Joseph Chiarelli for providing insightful commentary on Olympic Curling.

I have been very lucky throughout my life to have made a number of long and lasting friendships. In the order I met you stretching from kindergarten to college and beyond, I thank Sean, Eric, Brian, Peter, John, Al, Anastasia, Dan, Andrew Staron, Doug, Alyssa, Caitlin, Leah, Kerry, Andrew Sokol, Amy, Sara, and Matt for being the best friends a guy could ask for.

I'm also eternally grateful for all the support my family has given me, not just throughout my Ph.D., but for my whole life. My in-laws Biff, Brenda have very warmly welcomed me into their family for almost 10 years and have been like a second set of parents to me. I've had a lot of great times with my brother-in-law Ben and his girlfriend Emily and it's been great living close to them in Medford/Someverville. I also want to thank my wife's grandparents and fellow Jumbos Ben and Judy, who have always been extremely generous and kind to me.

I became an uncle not once, but twice during my Ph.D. and niece Mia and my nephew Robert make me smile every time I see them. To their parents Ryan and Kate: thanks to both of you for exposing me to a lot of great music throughout the years and sharing your kids with me all the time! Despite being almost two years younger than me, my extremely intelligent sister Dana managed to become a Dr. before I did. Her great work ethic has been an inspiration to me and I thank her and her boyfriend Alex for being there for me. My parents, Andy and Susan, have always been there for me and provided me with encouragement, financial

support, and of course copious amounts of food. I wouldn't have been able to do this without the two of you and I am eternally appreciative for everything you've done and continue to do for me throughout my life. To my grandparents Tony, Gloria, Frank, and Barbara: thank you all your love and support and for helping me to become the person I am today.

Last, but certainly far from least, I want to thank my wife Taylor for all of her love, for being my best friend, and my rock to lean on for the past 10 years. I'm lucky to have found someone as special as you and we make a great team. We've had so many great memories throughout our years together, and here's to hoping for many more. Again thanks to all who helped me through these five challenging but rewarding years!

-Matthew D. Marcinkowski

Table of Contents

Abstract	ii
Acknowledgements	iv
Table of Contents	viii
List of Figures	xi
Chapter 1: Introduction	1
1.1 Heterogeneous Catalysis	1
1.2 Surface Science as a Tool in Heterogeneous Catalysis	2
1.3 Trends in the Reactivity of Surfaces	5
1.4 Alloy Catalysts	7
1.5 Single Atom Alloys	9
1.6 Spillover	11
1.7 Reactions of Interest	13
1.7.1 H ₂ Activation and Hydrogenation Reactions	14
1.7.2 Dehydrogenation of Formic Acid and O-H Activation	15
1.7.3 C-H Activation	16
1.8 Conclusion	16
1.9 References	17
Chapter 2: Experimental Methods	28
2.1 Temperature Programmed Desorption/Reaction Theory	28
2.2 Temperature Programmed Desorption/Reaction Experimental Methods ...	42
2.3 Scanning Tunneling Microscopy Theory	45
2.4 Scanning Tunneling Microscopy Experimental Methods	47
2.5 References	50
Chapter 3: Significant Quantum Effects in Hydrogen Activation	52
3.1 Introduction	52
3.2 Results and Discussion	55
3.3 Conclusion	71
3.4 Experimental Methods	72
3.4.1 TPD and STM Measurements	72

3.4.2 Theoretical	73
3.5 References	77
Chapter 4: Controlling a Spillover Pathway with the Molecular Cork Effect	82
4.1 Introduction	82
4.2 Results and Discussion	83
4.3 Conclusion	94
4.4 Experimental Methods	95
4.4.1 TPD and STM Measurements	95
4.4.2 Theoretical	96
4.5 References	97
Chapter 5: Initial Stages of Acetophenone Hydrogenation on a Pd/Cu Single Atom Alloy	100
5.1 Introduction	100
5.2 Results and Discussion	101
5.3 Conclusions	111
5.4 Experimental Methods	112
5.5 References	113
Chapter 6: A Microscopic View of the Active Sites for Selective Dehydrogenation of Formic Acid on Cu(111)	116
6.1 Introduction	116
6.2 Results and Discussion	119
6.3 Conclusion	134
6.4 Experimental Methods	135
6.5 References	136
Chapter 7: Selective Formic Acid Dehydrogenation on Pt/Cu Single Atom Alloys	141
7.1 Introduction	141
7.2 Results and Discussion	144
7.3 Conclusions	158
7.4 Experimental Methods	159
7.4.1 TPD and STM Measurements	159
7.4.2 Nanoparticle synthesis and catalytic activity measurements	160

7.5 References.....	161
Chapter 8: Evidence of Isotopic Scrambling between H ₂ O and D ₂ on Pd/Cu Alloys.....	166
8.1 Introduction.....	166
8.2 Results and Discussion	167
8.3 Conclusion	175
8.4 Experimental Methods	175
8.5 References.....	176
Chapter 9: A Route to More Efficient C-H Activation with Pt/Cu Single Atom Alloys.....	179
9.1 Introduction.....	179
9.2 Results and Discussion	181
9.3 Conclusion	187
9.4 Experimental Methods	188
9.5 References.....	189
Chapter 10: Future Directions and Conclusions	192
10.1 Alternative Molecular Corks.....	192
10.2 Hydrogenation of Benzaldehyde.....	196
10.3 C-H Activation Expanded: Density Functional Theory, Kinetic Monte Carlo and Catalysis Studies	198
10.4 Conclusion	201
10.5 References.....	202
Appendix.....	204
Appendix to Chapter 4.....	204
Appendix to Chapter 6.....	210
Appendix to Chapter 7	213
Appendix to Chapter 9	219
References.....	229

List of Figures

Figure 1.1 A collaborative effort between STM and TPD mapping the reaction mechanism of $A \rightarrow C + D$	4
Figure 1.2 Illustrations of the BEP and Sabatier Principles.....	6
Figure 1.3 Atomically resolved STM images of SAAs of Pd/Cu and Pt/Cu.....	11
Figure 1.4 Spillover of hydrogen and formate.....	13
Figure 2.1 Schematic of the experimental setup for TPD.....	29
Figure 2.2 Demonstration that the rate of desorption observed in a TPD experiment is a convolution of the remaining fractional coverage and the rate constant.....	32
Figure 2.3 Simulated TPD spectra for the three common desorption orders along with the Polanyi-Wigner expressions describing them.....	32
Figure 2.4 CO desorption from a 0.01 ML Pd/Cu(111) surface with the different peaks labeled.....	36
Figure 2.5 Pictures of the UHV chamber used for TPD experiments.....	43
Figure 2.6 Schematic of the experimental setup of STM.....	47
Figure 2.7 Picture of the LT-STM used in this thesis.....	49
Figure 3.1 Desorption of H_2 from Pd/Cu alloys.....	56
Figure 3.2 Plots of the uptake of H on Pd/Cu alloys as a function of Pd coverage after a 100 L H_2 dose.....	57
Figure 3.3 STM images of Pd/Cu alloys with a range of stoichiometries.....	58
Figure 3.4 The uptake of hydrogen and deuterium on 0.01 ML Pd/Cu(111).....	61
Figure 3.5 Quantum effects on the H_2 activation barrier.....	63
Figure 3.6 Top and side view snapshots taken from an 85 K <i>ab initio</i> path integral molecular dynamics simulation of a single H_2 at the classical saddle points for dissociative chemisorption on the Pd/Cu(111) surface.....	66
Figure 3.7 KMC simulations for H_2 uptake and D_2 uptake and their comparison with the experimentally measured values.....	68

Figure 3.8 Determination of the apparent activation barrier for KMC simulations of D_2 uptake.....	69
Figure 4.1 Preferred binding sites for hydrogen and CO.....	85
Figure 4.2 The molecular cork effect.....	88
Figure 4.3 Kinetic Monte Carlo simulations of the molecular cork effect.....	91
Figure 4.4 The molecular cork effect in a hydrogenation reaction.....	93
Figure 5.1 Uptake of acetophenone on clean Cu(111).....	103
Figure 5.2 Interaction of acetophenone with H on 0.01 ML Pd/Cu(111).....	103
Figure 5.3 The effect of hydrogen on acetophenone.....	107
Figure 5.4 STM images of acetophenone annealed up to 120 K on Cu(111) and Pd/Cu(111) surfaces.....	109
Figure 5.5 STM images probing for partially hydrogenated intermediates.....	110
Figure 6.1 Reaction of formic acid on Cu(111).....	119
Figure 6.2 Formic acid desorption from Cu(111).....	122
Figure 6.3 Formic acid chain structure on Cu(111).....	124
Figure 6.4 Formate and H atom intermediates on Cu(111).....	126
Figure 6.5 Structure sensitivity of formic acid dehydrogenation.....	129
Figure 6.6 Reactivity of formic acid on Cu(111).....	131
Figure 6.7 Reaction pathway for formic acid dehydrogenation on Cu(111).....	133
Figure 7.1 Decomposition of formic acid on metal surfaces.....	144
Figure 7.2 Comparison of dehydrogenation activity between Cu(111) and 0.01 ML Pt/Cu(111).....	148
Figure 7.3 Formate formation at 120 K.....	150
Figure 7.4 Product distribution for formic acid decomposition as a function of Pt/Cu alloy composition.....	153
Figure 7.5 HCOOH decomposition in a flow reactor.....	156
Figure 8.1 TPD spectra of the uptake of H_2O on Cu(111) at 85 K.....	167

Figure 8.2 Evidence of isotopic scrambling between D and H ₂ O on Pd/Cu alloys.....	169
Figure 8.3 Isotopic exchange on a range of Pd concentrations.....	173
Figure 9.1 Decomposition of methyl iodide on various metal surfaces.....	181
Figure 9.2 STM images revealing the various stages of the reaction of methyl iodide on Cu(111) and 0.01 ML Pt/Cu(111).....	184
Figure 9.3 High resolution STM images of mixed phase methyl and iodine after a 120 K anneal on Cu(111) and iodine on Cu(111) after a 450 K anneal.....	184
Figure 9.4 Schematics for the reaction of methyl groups with Cu(111), 0.01 ML Pt/Cu(111), and 1 ML Pt/Cu(111).....	187
Figure 10.1 DBS as a molecular cork.....	195
Figure 10.2 Co-adsorption of hydrogen and benzaldehyde on Pt/Cu alloys.....	197
Figure 10.3 KMC simulations of methyl decomposition on Cu(111), 0.01 ML Pt/Cu(111) and Pt(111).....	199
Figure 10.4 Potential energy diagram for the successive C-H scissions of C _x H _y	200
Figure 10.5 The H → D exchange reaction for butane on Cu, Pt and Pt ₁ Cu NPs.....	201
Appendix Figure 1 High resolution STM imaging and manipulation of individual CO molecules adsorbed at their preferred sites on the Pd/Cu alloy surface.....	205
Appendix Figure 2 CO TPD from clean Cu(111) after a saturation exposure of 10 L.....	206
Appendix Figure 3 CO TPD spectra from 0.01 ML of Pd in Cu(111) after a saturation exposure of 10 L and 0.1 L.....	207
Appendix Figure 4 TPD spectra for uncorked and corked hydrogen after a 190 K or 210 K anneal for 10 min.....	208
Appendix Figure 5 TPR spectra showing complete hydrogenation of styrene on a 0.01 ML of Pd in Cu(111) surface.....	209
Appendix Figure 6 Traces for m/z 44 and m/z 28 resulting from the decomposition of 1 L of formic acid exposed to Cu(111) at 85 K.....	210

Appendix Figure 7 STM image of multilayers of formic acid on Cu(111).....	211
Appendix Figure 8 CO TPD demonstrating how the crystal's step density can be calculated by integrating the different CO peaks.....	212
Appendix Figure 9 Formate on 0.01 ML Pt/Cu(111).....	213
Appendix Figure 10 STM image of 1.0 ML of Pt deposited on a Cu(111) surface at 380 K.....	214
Appendix Figure 11 TPR spectra for $^{13}\text{CO}_2$ resulting from depositing 1.5 L of H^{13}COOH onto surfaces with varied Pt coverage.....	215
Appendix Figure 12 DRIFTS spectra collected at different temperatures after exposing the Pt_1Cu -SAA catalyst to 5 μL formic acid carried by a 10 ml/min He flow.....	216
Appendix Figure 13 DRIFTS spectra collected at different temperatures after exposing the Cu-NP catalyst to 5 μL formic acid carried by a 10 ml/min He flow.....	216
Appendix Figure 14 DRIFTS spectra collected at different temperatures after exposing the PtCu-bimetallic catalyst to 5 μL formic acid carried by a 10 ml/min He flow.....	217
Appendix Figure 15 Methane desorption from various Langmuir exposures of methyl iodide on Cu(111) and 0.01 ML Pt/Cu(111).....	219
Appendix Figure 16 Desorption of CO from surfaces previously exposed to various amounts of methyl iodide.....	220
Appendix Figure 17 TPR traces for all desorption products observed following 4.5 and 15 L exposures of methyl iodide on both Cu(111) and 0.01 ML Pt/Cu(111).....	221
Appendix Figure 18 Methyl iodide and deuterium on Pt/Cu SAAs.....	223
Appendix Figure 19 Hydrogen desorption after adsorption of 4.5 L CH_3I on Cu(111), 0.01 ML Pt/Cu(111) and 1.0 ML Pt/Cu(111).....	225
Appendix Figure 20 TPR spectra of methane and ethene produced via reaction of 4.5 L of methyl iodide on various Pt/Cu(111) alloy surfaces.....	226
Appendix Figure 21 STM images of Cu(111) and 0.01 ML Pt/Cu(111) annealed to 1000 K.....	228

Chapter 1: Introduction

1.1 Heterogeneous Catalysis

The definition of a catalyst is a substance that increases the rate of a chemical reaction by lowering the activation barrier of the process. In the presence of a catalyst, less energy is required for a process, allowing it to proceed facily at lower temperatures and or pressures. A catalyst can also improve selectivity towards the desired product. Catalysis is pervasive throughout nature and the existence of life itself depends on enzymatic catalysis. In the past century, humanity has begun to extensively utilize catalysis for production of chemicals and materials.^{1,2} Catalysts see extensive use in the energy sector^{3,4}, pharmaceuticals⁵, the food industry⁶, and environmental chemistry^{7,8} among many other fields. In fact, it is estimated that approximately 90% of all chemicals and materials produces in modern industry make use of a catalyst at some point in their development.^{1,9}

Most of these processes (~85%), make use of a heterogeneous catalyst, where the reactants and the catalyst exist in different phases.¹⁰⁻¹³ Typically, the catalyst is in the solid phase while the reactants are in a gaseous phase. This makes the recovery of catalytic material much easier in these systems compared to homogeneous catalysis, where the reactants exist in the same phase as the catalyst. This advantage, along with the superior thermal stability of heterogeneous catalysts, accounts for their extensive use in industry.¹³ However, the chief disadvantage of heterogeneous catalysis is the limited number of

available active surface sites of the catalyst compared to a homogeneous catalyst.¹²⁻¹⁵ In a typical liquid phase homogeneous catalyst, each catalytic species acts as a single identical active site, whereas heterogeneous catalyst often consist of multifaceted oxide or metal particles with numerous sites, not all of which are active for the desired reaction.^{12,13} The heterogeneity of sites in a heterogeneous catalyst, although sometimes advantageous, causes two major problems: it often makes the mechanism of a chemical reaction difficult to determine due to the large number of potential active sites, and can be a detriment to selectivity as some sites may catalyze unwanted side reactions.^{12,13,16,17} In this thesis, we seek to alleviate both of these problems by using a surface science approach to elucidate elementary steps of a number of industrially important chemical reactions on model single atom alloy surfaces, which have been demonstrated to display high selectivity for a number of reactions.¹⁸⁻²¹

1.2 Surface Science as a Tool in Heterogeneous Catalysis

One of the key goals of surface science throughout its history has been to help solve reaction mechanisms in heterogeneous catalysis by building a fundamental understanding of the thermodynamics and kinetics behind the catalytic process by examining catalysts at the atomic level.^{1,2,15-17,22-29} Perhaps the most famous success story of this field is that of Gerhard Ertl, who won the Nobel Prize in Chemistry in 2007 in part for mapping out the mechanism of the Haber-Bosch process.^{30,31} Surface science studies are typically performed under ultra-high vacuum (UHV) conditions (10^{-9} to 10^{-12} torr) on single crystal surfaces. The use of UHV allows for the surface to be kept clean during experiments.^{2,29}

Studying single crystals allows for examination of surface properties at the atomic level, which can help elucidate reaction mechanisms, as it is often difficult to characterize multifaceted nanoparticle catalysts at the atomic scale.^{32–35} The work in this thesis makes use of two surface science techniques, scanning tunneling microscopy (STM) and temperature programmed desorption/reaction (TPD/R), both of which will be described in further detail in Chapter 2. Briefly, STM allows for the atomic scale imaging of a conductive surfaces using the quantum mechanical phenomenon of electron tunneling^{36–39} while TPD/R measures the desorption of species from a surface using a quadrupole mass spectrometer to give information about the kinetics and thermodynamics of fundamental surface reactions.^{40–44}

The combination of these two techniques can be a very powerful way of characterizing a chemical reaction occurring on a metal surface.^{19–21,45–49} STM allows for the direct visualization of molecular adsorbates and reaction intermediates, while TPD can measure the formation of reaction products and give information about reaction barriers. A schematic illustrating the collaborative interaction between the two techniques is shown in Figure 1.1 in terms of the potential energy diagram of the theoretical interaction $A \rightarrow C+D$ through a surface bound reaction intermediate B. After reactant A is adsorbed to the surface, supplying energy to the system will either desorb A or decompose it to an adsorbed intermediate B along with a gaseous product C. TPD can provide information about the barriers to desorb intact A and to the reaction $A_{(ads)} \rightarrow B_{(ads)}+C_{(g)}$, as well as identify the gaseous product C. If A simply

decomposed to B and C was not formed, no information could be obtained about this barrier from TPD, as it only provides information about species desorbing from the surface. STM can be used to provide atomic scale images of intact A as well as the intermediate B, probing their adsorption sites and surface structure. As more energy is provided to the surface B reacts to form the gaseous product D. TPD can be used to measure the barrier to produce D, and can also identify D. Under favorable circumstances, TPD and STM combined can map out large portions of a reactions mechanism and we use this combination of techniques extensively throughout this work.

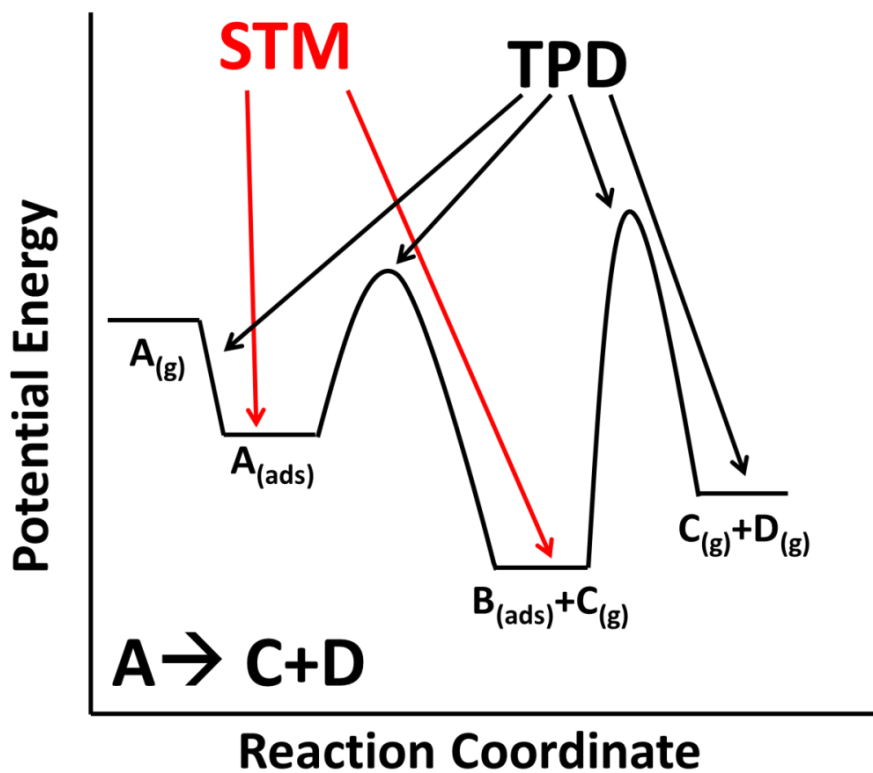


Figure 1.1 A collaborative effort between STM and TPD mapping the reaction mechanism of $A \rightarrow C + D$. STM provides information about the stages of the reaction marked with red arrows, while TPD does the same for the stages marked with black arrows.

1.3 Trends in the Reactivity of Surfaces

The selection of the most efficient catalyst for a given process is challenging due to the wide variety of materials available for use. Therefore, there has been significant work to predict ideal catalysts for important reactions.^{15,50-65} The adsorption strength of a molecule on a surface is one of the most important factors in determining its catalytic potential. The d-band model relates the binding strength of adsorbates to the position of the metal's d-band center relative to the Fermi level.^{15,51,52,55,56,64} Moving from right to left in the transition metal block in the periodic table, the d-band center tends to shift closer to the Fermi level.⁵¹ This leads to stronger bonding of adsorbates to metals on the left side of the transition metal block, since antibonding orbitals formed with these metals will be above the energy of the Fermi level, and therefore not filled. The opposite is true of metals on the right side of the periodic table; upon binding an adsorbate the antibonding orbitals will be below the Fermi level, and filled, leading to a weaker bond.^{15,51,52,55,56,64} Since the position of the d-band center, and thus binding strength, is based on a periodic trends, this allows for the construction of several predictive tools for the catalytic properties of metals.

There are two principles related to adsorption energy that are often invoked when characterizing catalysts. The first is the Brønsted-Evans-Polanyi Principle (BEP, also known as the Bell-Evans-Polanyi principle).⁶⁶⁻⁶⁸ The BEP relationship shows that there is a linear correlation between the activation energy and the adsorption energy within a family of similar reactions.⁶³ In other words, in general as a reaction becomes more exothermic (stronger binding, more negative

binding energy) the activation energy will be lowered, and as a reaction becomes more endothermic (weaker binding, more positive binding energy) the activation barrier will increase. This relationship is shown in the graph in Figure 1.2A using the dissociation of N_2 as an example. The second principle related to adsorption energy is more qualitative and is known as the Sabatier Principle.⁶⁹ The Sabatier Principle relates the adsorption energy to the catalytic activity of a surface.⁵² According to the principle, binding should be neither too strong nor too weak. Weak binding will allow for adsorbates to desorb without reacting, while strong bonding will not allow products to desorb. An intermediate binding strength is generally ideal, where the reactants bind strongly enough to react, but not strongly enough to keep the products from desorbing.⁵² This relationship led to the creation of so called “volcano” plots which predict the optimum catalyst for a reaction based on the Sabatier Principle.⁷⁰ An example of such a plot is shown in Figure 1.2B, using the decomposition of formic acid as an example.

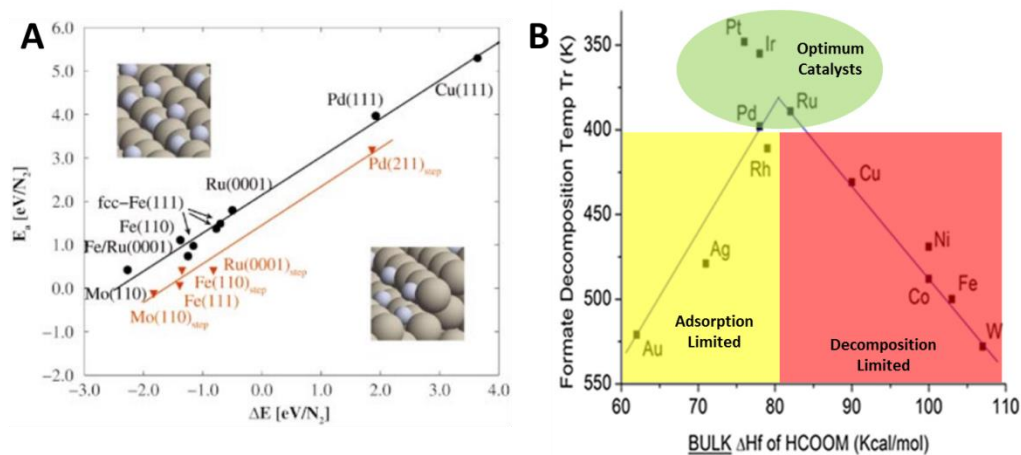


Figure 1.2 Illustrations of the BEP and Sabatier Principles. (A) Activation energies of N_2 dissociation vs. strength of $2N$ binding for a number of surfaces calculated via DFT.⁶⁵ (B) Plot of formate decomposition temperature vs formate binding energy. The decomposition temperature is for a fixed conversion, and is a measure of activity.⁶¹

The BEP and Sabatier principles make it challenging to fabricate catalysts that are both reactive and selective. In order for high activity to be obtained, reactants must be bound fairly strongly, as according to the BEP relationship this lowers the activation barrier of a reaction, which at a first glance seems ideal. However in this case, the activation barriers for unwanted side reactions are also lowered, meaning the selectivity of the catalyst will suffer. In this case, the Sabatier Principle also predicts that desorbing adsorbates is difficult, which may lead to catalyst deactivation.⁷¹⁻⁷³ On the other hand, catalysts that bind adsorbates weakly will exhibit high selectivity due to high activation barriers for undesirable reactions. Unfortunately, this also means that the activity for the desired reaction will remain low, as it will have a relatively high reaction barrier. It is difficult, if not impossible, to get off of the linear scaling relationships established by the BEP Principle using a catalyst composed of an individual metal. One strategy to get around this issue is the use of an alloy.

1.4 Alloy Catalysts

Alloy surfaces can display significantly different catalytic behavior from their constituents.^{60,74-79} The changes brought about by alloying are usually divided into two categories: ligand and ensemble effects.^{74,76-83} Ligand effects refer to electronic effects between metals in the alloy, while ensemble effects are geometric effects based on the arrangement of atoms in the alloy. Both of these effects can greatly alter the activity and selectivity of a catalyst. Ligand effects can be discussed in terms of the d-band model discussed in section 1.3.^{51,74,75,77,80} The introduction of a second metal shifts the d-band center due to orbital overlap

or strain from mixing atoms of two different sizes. For example, putting Pt into a Cu surface shifts the d-band center lower in energy relative to the Fermi level due to compressive strain from alloying the larger Pt atom into Cu. This causes the binding strength of adsorbates such as CO to be weaker on the Pt/Cu alloy relative to extended Pt surfaces.^{75,80,81,84} Alternatively, alloying a smaller Pd atom into a surface of larger Au atoms results in expansive that can increase the binding strengths of adsorbates as the d-band shifts up in energy and closer to the Fermi level.^{75,80,81} By selecting different metal combinations for alloys, the d-band center can therefore be tailored to allow for an ideal binding strength of adsorbates that allows for both high activity and selectivity, potentially escaping the linear scaling relationships of the BEP principle.

Ensemble effects refer to changes in the an alloys catalytic properties due to the positioning and arrangement of atoms in the alloy.^{74,76-83} By varying the ensemble size, the activity and selectivity of a catalyst can be tuned.^{18,49,76,85-88} If a reactive metal exists in larger ensembles it may give good activity, but selectivity may suffer.⁸⁵ Too small of an ensemble may result in reactive sites that prohibit some reactions from occurring, resulting in a loss of activity.⁸⁷ By tailoring ensembles of ideal size and configuration, it is possible to fabricate catalysts with ideal activity and selectivity. For example, Baddeley et al. examined the coupling of acetylene to benzene on Pd/Au alloys.⁸⁵ They found that Pd₆Au ensembles catalyzed the coupling reaction with high selectivity, while Pd₇ ensembles catalyze both coupling and decomposition. By adjusting the Au content in the surface, they were able to maximize the Pd₆Au ensembles in the

surface and obtain a highly active catalyst that was also selective to the desired reaction. Taking into consideration both ensemble and ligand effects alloys can be carefully modified to make ideal catalysts.

1.5 Single Atom Alloys

An extreme example of utilizing the ensemble effect, is to reduce the reactive site to a single atom. While this strategy can decrease activity, it usually provides the advantage of high selectivity and is economic as catalytic metals such as Pd and Pt are expensive and rare.⁸⁹⁻⁹⁶ Single atoms of Pt on N-doped carbon nanofibers have been shown to selectively catalyze the dehydrogenation of formic acid with high activity.⁹⁰ Pt and Au atoms on a variety of supports can catalyze the water-gas shift reaction⁹²⁻⁹⁶ and single Pt atoms on iron oxide supports can catalyze CO oxidation.⁹² This thesis will model industrially relevant reactions on single crystal alloy surfaces, containing isolated reactive metal sites, which we term single atom alloys (SAAs).

The Sykes group has extensively studied SAAs, both characterizing the alloy formation and examining the catalytic activity of the alloys.^{18-21,46-49,97-107} In SAAs, a small amount of a reactive metal such as Pt, Pd, or Ni are substituted into an unreactive metal such as Cu, Ag, or Au.^{18-21,46-49,97-107} The reactive metals exist as single isolated atoms in the host metal lattice. The idea behind this strategy is single reactive sites will allow for the activation of reactants, without the decrease in selectivity or susceptibility to deactivation that comes with larger ensembles of reactive metals. This thesis will focus on Pd/Cu(111) and

Pt/Cu(111) alloys.^{18,19,21,46,48,49,97,99,103,106} STM images of these surfaces are displayed in Figure 1.3. In general the BEP principle would predict that Cu is relatively unreactive, but can be highly selective, while Pd and Pt are typically very reactive but not very selective. Cu based SAAs have the added bonus of being economically friendly, as Pd and Pt are expensive and rare, while Cu is relatively abundant and cheap. Using very small amounts of Pd or Pt in a Cu host decreases the usage of these rare metals.

Both Pd and Pt have negative mixing enthalpies with Cu meaning Cu-Pd and Cu-Pt bonds are more favorable than Cu-Cu, Pd-Pd, or Pt-Pt bonds.¹⁰⁸ Pd is slightly more thermodynamically stable on the Cu surface, while Pt has a significantly higher surface free energy, meaning it prefers to be in the bulk.^{108,109} However, the large size of Pt and Pd compared to Cu limits the stability of a single atom in the bulk of a Cu crystal, and along with an activation barrier for diffusion into the bulk means higher temperatures are required for either metal to occupy bulk sites.^{97,103,110-112} Using a substrate temperature of 380 K when depositing either metal onto a Cu(111) surface allows for the creation of an alloy where most of the substituted atoms reside in the surface layer.^{97,103,110,111} In addition, this temperature allows for the formation of a relatively disperse alloy, compared to depositing at room temperature where Pd or Pt rich islands are formed.^{97,103,111} Pd alloys in at Cu surfaces by displacing an under-coordinated atom at the step edges.^{97,111,112} This leads to the formation of a Pd rich “brim” near the step edges. Pt can also alloy in via this mechanism, but also displaces Cu atoms directly from terrace sites, which causes the Pt/Cu alloy to be more disperse

than Pd/Cu.¹⁰³ It is known from the stable Cu₃Pt alloy that Pt can exist as single atoms in Cu^{84,113–116} and Pd atoms are also predicted to be stable in small ensembles in Cu.^{117–119} The Sykes group has shown that provided the amount of Pd or Pt deposited on the Cu crystal is small enough (<0.05 ML), the two reactive metals are known to exist as single isolated atoms in the Cu lattice, thus forming an SAA.^{97,103}

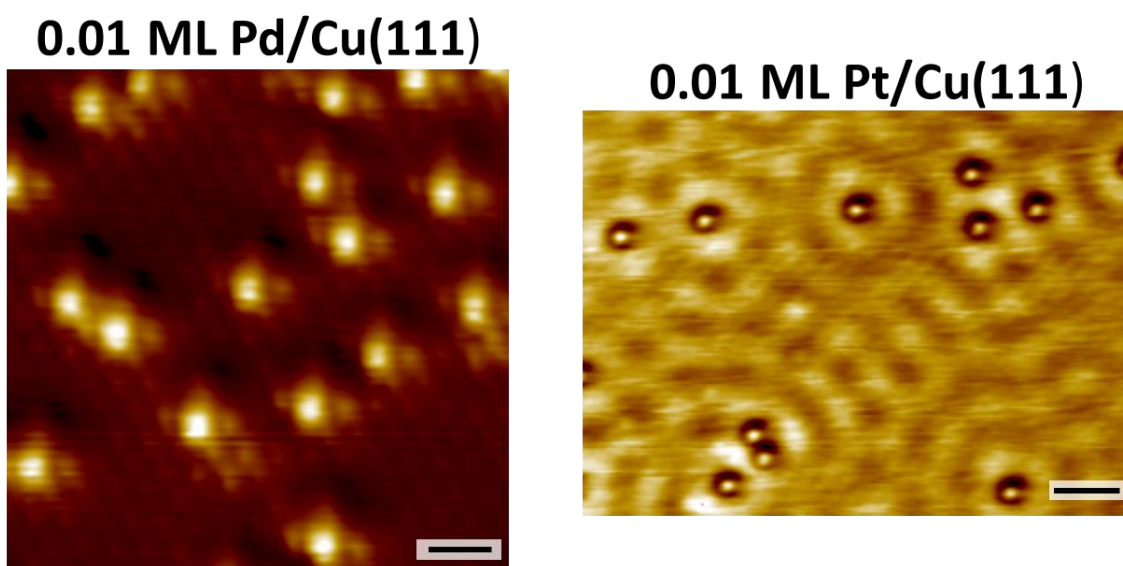


Figure 1.3 Atomically resolved STM images of SAAs of Pd/Cu and Pt/Cu. The bright protrusions in both images are the single atoms of Pd and Pt. The Pd/Cu image was obtained in a “brim” area close to a Cu step edge while the Pt/Cu image was taken from a Cu terrace. Scale bars for both images are 0.5 nm.

1.6 Spillover

Another advantage of using the SAAs is that reagents can often spillover from reactive metals to the inert host, which can improve reactivity and selectivity.^{18,19,46–48,89,99,104,105,120} Spillover is the movement of an activated species from the activation site to another site that would not normally activate this species under the same conditions.^{121–124} This allows for the activated species to

undergo reactions on the weaker binding surface which can improve selectivity. It also opens up the reactive sites to activate additional molecules potentially increasing activity. There are many examples of spillover in the literature especially involving the spillover of H_a or O_a atoms after activation of H₂ or O₂.¹²¹⁻¹²⁹ In nanoparticle studies spillover is usually invoked to describe the transport of the activated species from metal nanoparticles to the inert support.¹²¹⁻¹²⁹ However the Sykes group has demonstrated spillover can occur in SAA systems, particularly in the case of hydrogen.^{18,19,46-48,99,102,104,105} Both Pt and Pd single crystal surfaces easily activate hydrogen^{130,131}, but Cu single crystals are inactive for this process.¹³² However in a SAA system hydrogen can be activated at the Pt and Pd sites and then spillover onto the otherwise inactive Cu surface. STM experiments reveal the presence of hydrogen on Cu terraces away from Pt or Pd sites, and TPD experiments show that the hydrogen coverage is well above that of the dopant metals.^{20,48,99,102} Furthermore, it has been shown that due to this spillover, hydrogenation reactions are able to occur on the Cu surface, leading to improved selectivity.¹⁹ This thesis makes extensive use of hydrogen's ability to spillover from Pd or Pt to Cu, and also demonstrates the spillover of formate from Pt to Cu. STM images of these two processes are shown in Figure 1.4. Chapters 3, 4, 5, and 8 discuss the spillover of hydrogen on Pd/Cu alloys, while Chapter 7 discusses the spillover of formate.

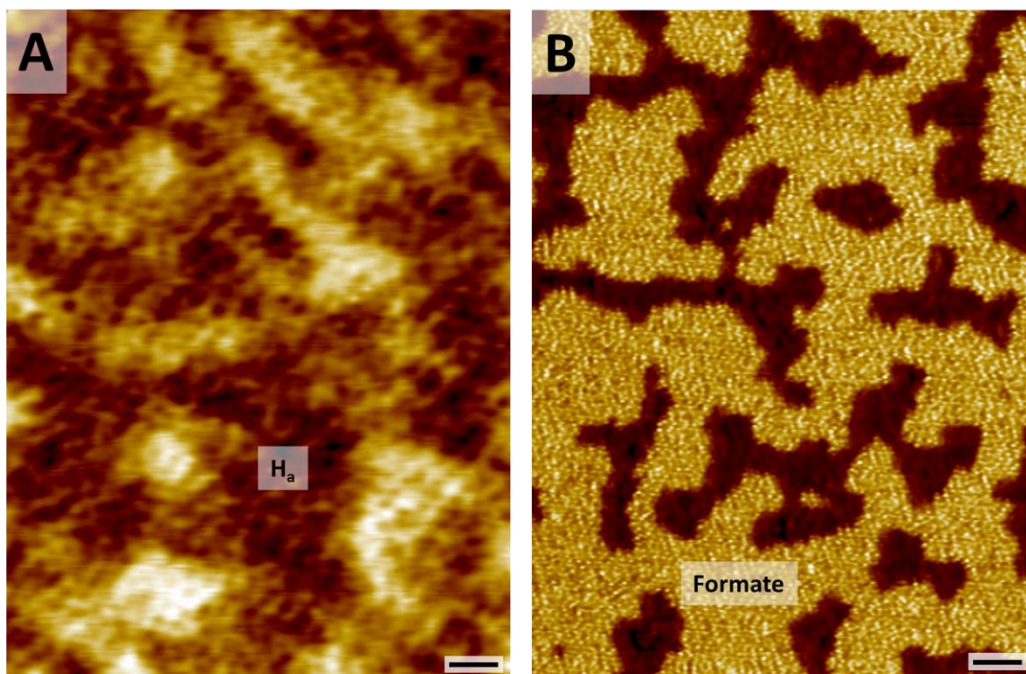


Figure 1.4 Spillover of hydrogen and formate. (A) Hydrogen atoms image as depressions on a 0.01 ML Pd/Cu(111) alloy. The image is taken on a Cu terrace away from the Pd rich brim. (B) Formate resulting from formic acid decomposition on a 0.01 ML Pt/Cu(111) alloy after annealing to 120 K. There are significantly more formate species than Pt atoms (>14:1) and Cu cannot active formic acid at this temperature.

1.7 Reactions of Interest

As discussed, this thesis will examine the catalytic behavior of Cu based SAAs, using model single crystal surfaces under UHV conditions in order to elucidate reaction mechanisms at the atomic scale. In general, it is expected that SAAs exhibit improved activity compared to Cu due to the introduction of reactive metals into the Cu lattice, while maintaining the high selectivity typically expected of Cu based catalysts. To examine this theory, we examine a number of industrially relevant probe reactions on the SAA surface, including H_2 activation, hydrogenations, and dehydrogenations including O-H and C-H activation. Our findings show that the SAAs offer selective chemistry for a variety of reactions.

1.7.1 H₂ Activation and Hydrogenation Reactions

Hydrogenation reactions are important to the petrochemical, pharmaceutical, fine chemicals, and food industries.¹³³⁻¹⁴⁰ H₂ activation is often the rate limiting step of these reactions and is also relevant for fuel cells, hydrogen storage devices, and sensing.^{4,121,122,125-127,141-145} For hydrogenation of both C=C and C=O double bonds metals such as Pt or Pd are frequently employed due to their facile activation of hydrogen, but often have issues with selectivity.^{137,140,146-149} Chapter 3 of this thesis takes an extensive look at hydrogen and deuterium activation on a Pd/Cu SAA surface using a combination of surface science and theory. We show that hydrogen can be facilely activated at the Pd atoms even at cryogenic temperature due to quantum tunneling effects and can then spillover to Cu where it can be used for selective hydrogenations. Chapter 4 furthers the work in Chapter 3 by examining how uptake and release of hydrogen can be controlled in the presence of CO for the purpose of hydrogen storage. It also applies the principles gleaned in Chapter 3 in order to selectively hydrogenate a C=C bond using the case of styrene to ethylbenzene. Chapter 5 also examines hydrogenation reactions on the Pd/Cu SAA, but for a C=O bond, using acetophenone as a probe molecule. Acetophenone is an important precursor for a number of pharmaceuticals and fine chemicals, hydrogenating it to the desired saturated alcohol is difficult as the thermodynamics and kinetics are unfavorable for C=O hydrogenation.^{138,148,150,151} We show that under UHV conditions the SAA is able to partially hydrogenate acetophenone molecules, stabilizing both hydrogen and acetophenone on the surface to elevated

temperatures. Overall, this thesis demonstrates that the Pd/Cu SAA is ideal for hydrogen activation and selective hydrogenation reactions.

1.7.2 Dehydrogenation of Formic Acid and O-H Activation

Formic acid is a potential hydrogen storage molecule that can dehydrogenate to form CO_2 and H_2 .¹⁵²⁻¹⁵⁷ The traditional Pt and Pd based catalysts used in formic acid fuel cells are highly active for formic acid dehydrogenation, but also catalyze an unwanted dehydration reaction that forms CO, which can poison the catalyst.^{58,154-161} Thus alternative catalysts for formic acid dehydrogenation are necessary. In Chapter 6, we examine the dehydrogenation of formic acid on Cu(111). Cu catalysts have too high of an activation barrier to be practical but formic acid decomposition has been extensively studied on low miller index Cu surfaces due to their high selectivity to dehydrogenation.¹⁶²⁻¹⁸⁶ Surprisingly, however, little work has been performed on Cu(111), leading us to characterize the reaction mechanism on this surface. We go a step further in Chapter 7 and examine the dehydrogenation of formic acid on Pt/Cu SAAs using both surface science and catalysis studies. Our surface science studies show a large increase in formic acid dehydrogenation on the SAA compared to Cu, but this does not translate over to the nanoparticle studies. This is because the SAA catalyzes the initial dehydrogenation step of formic acid to formate more efficiently than Cu, but does not catalyze the rate limiting step of the reaction which is the decomposition of formate to CO_2 and H_2 . While, the SAA is not particularly promising for formic acid dehydrogenation it is shown to activate O-H bonds efficiently. To examine this property further, we look at a

H→D exchange reaction for H₂O on Pd/Cu alloys in Chapter 8 which is of interest for both heterogeneous catalysis and electrochemical systems.¹⁸⁷⁻¹⁸⁹ We find that the alloy surface is able to perform this reaction by stabilizing (H₂O)_nD⁺ clusters on the surface while bare Cu is not.

1.7.3 C-H Activation

The increased production of shale gas has led to a large abundance of small alkanes such as ethane and propane.^{3,190} The ability to activate C-H bonds in alkanes would lead to a new way to produce alkenes, which are precursors to polymers.^{3,62} Pt based catalysts are often used for this process, but suffer from coking, as they can catalyze complete decomposition of the alkanes to carbon.¹⁹¹⁻¹⁹³ In Chapter 9, we approach this problem by looking at C-H activation on a Pt/Cu SAA using methyl groups produced by the decomposition of methyl iodide, which happens facilely on both Pt and Cu surfaces. We find that Cu can activate C-H bonds in methyls at 450 K while avoiding coking, while a 1 ML Pt/Cu(111) surface activates C-H bonds at 250 K, but suffers from coking. Using a Pt/Cu SAA we are able to activate C-H bonds at 350 K while avoiding the problem of coking that occurs on surfaces with larger Pt loadings.

1.8 Conclusion

This thesis will use a surface science approach to model industrially relevant reactions at the atomic level using a combination of TPD and STM on single crystal surfaces. Specifically, it examines reactions on Cu SAAs, where single atoms of a reactive, expensive metal are substituted in the lattice of an

inert, cheap host. By using an alloy surface we are able to escape the predictions made by the BEP and Sabatier principles allowing for a catalyst that is relatively highly active and very selective. The bimetallic nature of the alloy also makes spillover from the reactive sites to the inert Cu a possibility for a number of systems, which can further help to improve reactivity and selectivity. The combined use of STM and TPD allows us to examine barriers to reaction, visualize surface bound intermediates, and monitor desorption products in the SAA systems. Using these techniques we demonstrate that the SAA approach can be applied to a wide variety of chemical reactions including H₂ activation, hydrogenations of both C=C and C=O bonds, and dehydrogenations of O-H and C-H bonds.

1.9 References

- (1) Bowker, M. *The Basis and Applications of Heterogeneous Catalysis*; Oxford University Press, 1998.
- (2) Kolasinski, K. W. *Surface Science*, 3rd ed.; Wiley, 2012.
- (3) Sattler, J. J. H. B.; Ruiz-Martinez, J.; Santillan-Jimenez, E.; Weckhuysen, B. M. *Chem. Rev.* **2014**, *114*, 10613–10653.
- (4) Graetz, J. *Chem. Soc. Rev.* **2009**, *38*, 73–82.
- (5) Hoogenraad, M.; Van Der Linden, J. B.; Smith, A. A.; Hughes, B.; Derrick, A. M.; Harris, L. J.; Higginson, P. D.; Pettman, A. J. *Org. Process Res. Dev.* **2004**, *8*, 469–476.
- (6) King, J. W.; Holliday, R. L.; List, G. R.; Snyder, J. M. *J. Am. Oil Chem. Soc.* **2001**, *78*, 107–113.
- (7) Zeng, F.; Hohn, K. L. *Appl. Catal. B Environ.* **2016**, *182*, 570–579.
- (8) Yu, X.; Pickup, P. G. *J. Power Sources* **2008**, *182*, 124–132.
- (9) de Vries, J. G.; Jackson, S. D. *Catal. Sci. Technol.* **2012**, *2*, 2009.

- (10) Hapke, M. In *Lecture at the University of Rostock*; 2015.
- (11) Bell, A. T. *Science* **2003**, *299*, 1688–1691.
- (12) Copéret, C.; Chabanas, M.; Petroff Saint-Arroman, R.; Basset, J.-M. *Angew. Chem. Int. Ed.* **2003**, *42*, 156–181.
- (13) Farnetti, E.; Monte, R. Di; Kašpar, J. In *Inorganic and Bio-Inorganic Chemistry*; Bertini, I., Ed.; Eolss Publishers: Oxford, United Kingdom, 2009; Vol. II.
- (14) Taylor, H. S. *Proc. R. Soc. London. Ser. A* **1926**, *133*, 77–86.
- (15) Nørskov, J. K.; Bligaard, T.; Hvolbaek, B.; Abild-Pedersen, F.; Chorkendorff, I.; Christensen, C. H. *Chem. Soc. Rev.* **2008**, *37*, 2163–2171.
- (16) Somorjai, G. A. *Surf. Sci.* **1994**, *299–300*, 849–866.
- (17) Bonzel, H. P. *Surf. Sci.* **1977**, *68*, 236–258.
- (18) Kyriakou, G.; Boucher, M. B.; Jewell, A. D.; Lewis, E. A.; Lawton, T. J.; Baber, A. E.; Tierney, H. L.; Flytzani-Stephanopoulos, M.; Sykes, E. C. H. *Science* **2012**, *335*, 1209–1212.
- (19) Lucci, F. R.; Liu, J.; Marcinkowski, M. D.; Yang, M.; Allard, L. F.; Flytzani-Stephanopoulos, M.; Sykes, E. C. H. *Nat. Commun.* **2015**, *6*, 8550.
- (20) Boucher, M. B.; Zugic, B.; Cladaras, G.; Kammert, J.; Marcinkowski, M. D.; Lawton, T. J.; Sykes, E. C. H.; Flytzani-Stephanopoulos, M. *Phys. Chem. Chem. Phys.* **2013**, *15*, 12187–12196.
- (21) Boucher, M. B.; Marcinkowski, M. D.; Liriano, M. L.; Murphy, C. J.; Lewis, E. A.; Jewell, A. D.; Mattera, M. F. G.; Kyriakou, G.; Flytzani-stephanopoulos, M.; Sykes, E. C. H. *ACS Nano* **2013**, *7*, 6181–6187.
- (22) Tumuluri, U.; Rother, G.; Wu, Z. *Ind. Eng. Chem. Res.* **2016**, *55*, 3909–3919.
- (23) Somorjai, G. A. *J. Phys. Chem.* **1990**, *94*, 1013–1023.
- (24) Markovic, N. M.; Ross Jr., P. N. *Surf. Sci. Rep.* **2002**, *45*, 117–229.
- (25) Henderson, M. A. *Surf. Sci. Rep.* **2011**, *66*, 185–297.
- (26) Freund, H.-J. *J. Am. Chem. Soc.* **2016**, No. 111, 8985–8996.
- (27) Bonzel, H. P.; Krebs, H. J. *Surf. Sci.* **1982**, *117*, 639–658.
- (28) Besenbacher, F.; Chorkendorff, I.; Clausen, B. S.; Hammer, B.; Molenbroek, A. M.; Norskov, J. K.; Stensgaard, I. *Science (80-.)*. **1998**, *279*, 1913–1915.

- (29) Attard, G.; Barnes, C. *Surfaces*; Oxford University Press, 2004.
- (30) Ertl, G. *Angew. Chem. Int. Ed.* **2008**, *47*, 3524–3535.
- (31) Ertl, G. *Catal. Rev.* **1980**, *4940*, 201–223.
- (32) Cho, E. J.; Holback, H. *Mol. Pharm.* **2013**, *10*, 2093–2110.
- (33) McNeil, S. E. In *Characterization of Nanoparticles Intended for Drug Delivery*; Humana Press, 2011; pp 9–16.
- (34) Rioux, R. M.; Song, H.; Grass, M.; Habas, S.; Niesz, K.; Hoefelmeyer, J. D.; Yang, P.; Somorjai, G. A. *Top. Catal.* **2006**, *39*, 167–174.
- (35) Fischer-Wolfarth, J. H.; Farmer, J. A.; Flores-Camacho, J. M.; Genest, A.; Yudanov, I. V.; Rösch, N.; Campbell, C. T.; Schauermann, S.; Freund, H.-J. *Phys. Rev. B* **2010**, *81*, 241416.
- (36) Binnig, G.; Rohrer, H.; Gerber, C.; Weibel, E. *Phys. Rev. Lett.* **1982**, *49*, 57–61.
- (37) Binnig, G.; Rohrer, H.; Gerber, C.; Weibel, E. *Appl. Phys. Lett.* **1982**, *40*, 178–180.
- (38) Varga, P.; Schmid, M. *Appl. Surf. Sci.* **1999**, *141*, 287–293.
- (39) Schmid, M.; Stadler, H.; Varga, P. *Phys. Rev. Lett.* **1990**, *70*, 1441–1444.
- (40) King, D. A. *Surf. Sci.* **1975**, *47*, 384–402.
- (41) Redhead, P. A. *Vacuum* **1962**, 203–211.
- (42) Ranke, W. In *Lecture at the Fritz Haber Institut of the MPG*; Berlin, 2003.
- (43) Habenschaden, E.; Küppers, J. *Surf. Sci. Lett.* **1984**, *138*, L147–L150.
- (44) de Jong, A. M.; Niemantsverdriet, J. W. *Surf. Sci.* **1990**, *233*, 355–365.
- (45) Marcinkowski, M. D.; Murphy, C. J.; Liriano, M. L.; Wasio, N. A.; Lucci, F. R.; Sykes, E. C. H. *ACS Catal.* **2015**, *5*, 7371–7378.
- (46) Kyriakou, G.; Davidson, E. R. M.; Peng, G.; Roling, L. T.; Singh, S.; Boucher, M. B.; Marcinkowski, M. D.; Mavrikakis, M.; Michaelides, A.; Sykes, E. C. H. *ACS Nano* **2014**, *8*, 4827–4835.
- (47) Marcinkowski, M. D.; Jewell, A. D.; Stamatakis, M.; Boucher, M. B.; Lewis, E. A.; Murphy, C. J.; Kyriakou, G.; Sykes, E. C. H. *Nat. Mater.* **2013**, *12*, 523–528.
- (48) Lucci, F. R.; Marcinkowski, M. D.; Lawton, T. J.; Sykes, E. C. H. *J. Phys. Chem. C* **2015**, *119*, 24351–24357.

- (49) Liu, J.; Lucci, F. R.; Yang, M.; Lee, S.; Marcinkowski, M. D.; Therrien, A. J.; Williams, C. T.; Sykes, E. C. H.; Flytzani-Stephanopoulos, M. *J. Am. Chem. Soc.* **2016**, *138*, 6396–6399.
- (50) Bligaard, T.; Nørskov, J. K.; Dahl, S.; Matthiesen, J.; Christensen, C. H.; Sehested, J. *J. Catal.* **2004**, *224*, 206–217.
- (51) Hammer, B.; Nørskov, J. K. *Adv. Catal.* **2000**, *45*, 71–129.
- (52) Medford, A. J.; Vojvodic, A.; Hummelshøj, J. S.; Voss, J.; Abild-Pedersen, F.; Studt, F.; Bligaard, T.; Nilsson, A.; Nørskov, J. K. *J. Catal.* **2015**, *328*, 36–42.
- (53) Nørskov, J. K.; Bligaard, T.; Logadottir, A.; Bahn, S.; Hansen, L. B.; Bollinger, M.; Benggaard, H.; Hammer, B.; Sljivancanin, Z.; Mavrikakis, M.; Xu, Y.; Dahl, S.; Jacobsen, C. J. H. *J. Catal.* **2002**, *209*, 275–278.
- (54) Nørskov, J. K.; Rossmeisl, J.; Logadottir, A.; Kitchin, J. R.; Bligaard, T.; Jonsson, H. *J. Phys. Chem. B* **2004**, *108*, 17886–17892.
- (55) Nørskov, J. K.; Abild-Pedersen, F.; Studt, F.; Bligaard, T. *Proc. Natl. Acad. Sci.* **2011**, *108*, 937–943.
- (56) Hammer, B.; Nørskov, J. K. *Surf. Sci.* **1995**, *343*, 211–220.
- (57) Herron, J. A.; Scaranto, J.; Ferrin, P.; Li, S.; Mavrikakis, M. *ACS Catal.* **2014**, *4*, 4434–4445.
- (58) Yoo, J. S.; Abild-Pedersen, F.; Nørskov, J. K.; Studt, F. *ACS Catal.* **2014**, *4*, 1226–1233.
- (59) Greeley, J.; Nørskov, J. K. *Surf. Sci.* **2007**, *601*, 1590–1598.
- (60) Greeley, J.; Mavrikakis, M. *Nat. Mater.* **2004**, *3*, 810–815.
- (61) Tang, Y.; Roberts, C. A.; Perkins, R. T.; Wachs, I. E. *Surf. Sci.* **2016**, *650*, 103–110.
- (62) Zhao, Z.-J.; Chiu, C.; Gong, J. *Chem. Sci.* **2015**, *6*, 4403–4425.
- (63) Roy, S.; Goedecker, S.; Hellmann, V. *Phys. Rev. E* **2008**, *77*, 56707.
- (64) Hammer, B.; Nørskov, J. K. *Nature* **1995**, *376*, 238–240.
- (65) Logadottir, A.; Rod, T. H.; Nørskov, J. K.; Hammer, B.; Dahl, S.; Jacobsen, C. J. H. *J. Catal.* **2001**, *197*, 229–231.
- (66) Bell, R. P. *Proc. R. Soc. London, Ser. A* **1936**, *154*, 414.
- (67) Brønsted, J. N. *Chem. Rev.* **1927**, *5*, 231–338.
- (68) Evans, M. G.; Polanyi, M. *Faraday Trans.* **1935**, *32*, 875–894.

- (69) Sabatier, P. *Ber. Dtsch. Chem. Ges.* **1911**, *44*, 1984–2001.
- (70) Balandin, A. *Adv. Catal. Rel. Subj.* **1969**, *19*, 1–210.
- (71) Forzatti, P.; Lietti, L. *Catal. Today* **1999**, *52*, 165–181.
- (72) Dunleavy, J. K. *Platin. Met. Rev.* **2006**, *50*, 110–110.
- (73) Bartholomew, C. H. *Appl. Catal., A* **2001**, *212*, 17–60.
- (74) Rodriguez, J. A. *Surf. Sci. Rep.* **1996**, *24*, 223–287.
- (75) Liu, P.; Nørskov, J. K. *Phys. Chem. Chem. Phys.* **2001**, *3*, 3814–3818.
- (76) Maroun, F.; Ozanam, F.; Magnussen, O. M.; Behm, R. J. *Science (80-.)*. **2001**, *293*, 1811–1814.
- (77) Rodriguez, J. A. In *Handbook of Heterogeneous Catalysis*; Wiley, 2008; pp 1298–1309.
- (78) Boscoboinik, J. A.; Calaza, F. C.; Garvey, M. T.; Tysøe, W. T. *J. Phys. Chem. C* **2010**, *114*, 1875–1880.
- (79) Sinfelt, J. H. *Acc. Chem. Res.* **1977**, *10*, 15–20.
- (80) Bligaard, T.; Nørskov, J. K. *Electrochim. Acta* **2007**, *52*, 5512–5516.
- (81) Groß, A. *Top. Catal.* **2006**, *37*, 29–39.
- (82) Han, P.; Axnanda, S.; Lyubinetsky, I.; Goodman, D. W. *J. Am. Chem. Soc.* **2007**, *129*, 14355–14361.
- (83) Ponec, V. *Appl. Catal. A Gen.* **2001**, *222*, 31–45.
- (84) Castro, G.; Schneider, U.; Busse, H.; Janssens, T.; Wandelt, K. *Surf. Sci.* **1992**, *269*, 321–325.
- (85) Baddeley, C. J.; Tikhov, M.; Hardacre, C.; Lomas, J. R.; Lambert, R. M. *J. Phys. Chem.* **1996**, *100*, 2189–2194.
- (86) Chen, M.; Kumar, D.; Yi, C. *Science* **2005**, *310*, 291–293.
- (87) Gao, F.; Wang, Y.; Goodman, D. W. *J. Am. Chem. Soc.* **2009**, *131*, 5734–5735.
- (88) Chung, D. Y.; Kim, H.; Chung, Y.-H.; Lee, M. J.; Yoo, S. J.; Bokare, A. D.; Choi, W.; Sung, Y.-E. *Sci. Rep.* **2014**, *4*, 7450.
- (89) Fu, Q.; Luo, Y. *J. Phys. Chem. C* **2013**, *117*, 14618–14624.
- (90) Bulushev, D. A.; Zacharska, M.; Lisitsyn, A. S.; Podyacheva, O. Y.; Hage, F. S.; Ramasse, Q. M.; Bangert, U.; Bulusheva, L. G. *ACS Catal.* **2016**, *6*, 3442–

3451.

- (91) Thomas, J. M.; Saghi, Z.; Gai, P. L. *Top. Catal.* **2011**, *54*, 588–594.
- (92) Yang, X. F.; Wang, A.; Qiao, B.; Li, J.; Liu, J.; Zhang, T. *Acc. Chem. Res.* **2013**, *46*, 1740–1748.
- (93) Wang, C.; Yang, M.; Flytzani-Stephanopoulos, M. *AIChE* **2016**, *62*, 429–439.
- (94) Yang, M.; Wang, Y.; Herron, J. A.; Xu, Y.; Allard, L. F.; Lee, S.; Huang, J.; Mavrikakis, M.; Flytzani-Stephanopoulos, M. *Science* **2014**, *346*, 1498–1501.
- (95) Zhai, Y.; Pierre, D.; Si, R.; Deng, W.; Ferrin, P.; Nilekar, A. U.; Peng, G.; Herron, J. A.; Bell, D. C.; Saltsburg, H.; Mavrikakis, M.; Flytzani-Stephanopoulos, M. *Science (80-.)*. **2010**, *329*, 1633–1637.
- (96) Yang, M.; Liu, J.; Lee, S.; Zugic, B.; Huang, J.; Allard, L. F.; Flytzani-Stephanopoulos, M. *J. Am. Chem. Soc.* **2015**, *137*, 3470–3473.
- (97) Tierney, H. L.; Baber, A. E.; Sykes, E. C. H. *J. Phys. Chem. C* **2009**, *113*, 7246–7250.
- (98) Bellisario, D. O.; Han, J. W.; Tierney, H. L.; Baber, A. E.; Sholl, D. S.; Sykes, E. C. H. *J. Phys. Chem. C* **2009**, *113*, 12863–12869.
- (99) Tierney, H. L.; Baber, A. E.; Kitchin, J. R.; Sykes, E. C. H. *Phys. Rev. Lett.* **2009**, *103*, 246102.
- (100) Baber, A. E.; Tierney, H. L.; Lawton, T. J.; Sykes, E. C. H. *ChemCatChem* **2011**, *3*, 607–614.
- (101) Baber, A. E.; Tierney, H. L.; Sykes, E. C. H. *ACS Nano* **2010**, *4*, 1637–1645.
- (102) Jewell, A. D.; Peng, G.; Mattera, M. F. G.; Lewis, E. A.; Murphy, C. J.; Kyriakou, G.; Mavrikakis, M.; Sykes, E. C. H. *ACS Nano* **2012**, *6*, 10115–10121.
- (103) Lucci, F. R.; Lawton, T. J.; Pronschinske, A.; Sykes, E. C. H. *J. Phys. Chem C* **2014**, *118*, 3015–3022.
- (104) Therrien, A. J.; Pronschinske, A.; Murphy, C. J.; Lewis, E. A.; Liriano, M. L.; Marcinkowski, M. D.; Sykes, E. C. H. *Phys. Rev. B - Condens. Matter Mater. Phys.* **2015**, *92*, 1–5.
- (105) Lucci, F. R.; Darby, M. T.; Mattera, M. F. G.; Ivimey, C. J.; Therrien, A. J.; Michaelides, A.; Stamatakis, M.; Sykes, E. C. H. *J. Phys. Chem. Lett.* **2016**, *7*, 480–485.
- (106) Shan, J.; Lucci, F. R.; Liu, J.; El-Soda, M.; Marcinkowski, M. D.; Allard, L. F.; Sykes, E. C. H.; Flytzani-Stephanopoulos, M. *Surf. Sci.* **2016**, *650*, 121–

129.

- (107) Wang, Z.-T.; Darby, M. T.; Therrien, A. J.; El-Soda, M.; Michaelides, A.; Stamatakis, M.; Sykes, E. C. H. *J. Phys. Chem. C* **2016**, *120*, 13574–13580.
- (108) Christensen, A.; Ruban, A.; Stoltze, P.; Jacobsen, K.; Skriver, H.; Nørskov, J. K.; Besenbacher, F. *Phys. Rev. B* **1997**, *56*, 5822–5834.
- (109) Tyson, W. R.; Miller, W. A. *Surf. Sci.* **1977**, *62*, 267–276.
- (110) Dastoor, P. C.; O'Connor, D. J.; MacLaren, D. A.; Allison, W.; Noakes, T. C. Q.; Bailey, P. *Surf. Sci.* **2005**, *588*, 101–107.
- (111) Aaen, A. B.; Lægsgaard, E.; Ruban, A. V.; Stensgaard, I. *Surf. Sci.* **1998**, *408*, 43–56.
- (112) Canzian, A.; Mosca, H. O.; Bozzolo, G. *Surf. Sci.* **2004**, *551*, 9–22.
- (113) Schneider, U.; Castro, G. R.; Wandelt, K. *Surf. Sci.* **1993**, *287–288*, 146–150.
- (114) Zhang, C. J.; Baxter, R. J.; Hu, P.; Alavi, A.; Lee, M. H. *J. Chem. Phys.* **2001**, *115*, 5272–5277.
- (115) Shen, Y. G.; O'Connor, D. J.; Wandelt, K.; MacDonald, R. J. *Surf. Sci.* **1995**, *328*, 21–31.
- (116) Linke, R.; Schneider, U.; Busse, H.; Becker, C. *Surf. Sci.* **1994**, *307–309*, 407–411.
- (117) Illas, F.; Lopez, N.; Ricart, J. M.; Clotet, A.; Conesa, J. C.; Fernandez-Garcia, M. *J. Phys. Chem. B* **1998**, *102*, 8017–8023.
- (118) Fernández-García, M.; Conesa, J. C.; Clotet, A.; Ricart, J. M.; López, N.; Illas, F. *J. Phys. Chem. B* **1998**, *102*, 141–147.
- (119) Lopez, N.; Nørskov, J. K. *Surf. Sci.* **2001**, *477*, 59–75.
- (120) Fu, Q.; Luo, Y. *ACS Catal.* **2013**, No. 111, 1245–1252.
- (121) Conner, W. C.; Falconer, J. L. *Chem. Rev.* **1995**, *95*, 759–788.
- (122) Prins, R. *Chem. Rev.* **2012**, *112*, 2714–2738.
- (123) Inui, T. *Stud. Surf. Sci. Catal.* **1993**, *77*, 17–26.
- (124) Pajonk, G. M. *Appl. Catal. A Gen.* **2000**, *202*, 157–169.
- (125) Jung, K.-D.; Bell, A. T. *J. Catal.* **2000**, *193*, 207–223.
- (126) Wang, L.; Yang, R. T. *Catal. Rev. Sci. Eng.* **2010**, *52*, 411–461.

- (127) Cheng, H.; Chen, L.; Cooper, A. C.; Sha, X.; Pez, G. P. *Energy Environ. Sci.* **2008**, *1*, 338–354.
- (128) Li, Y.; Yang, R. T. *J. Am. Chem. Soc.* **2006**, *128*, 8136–81377.
- (129) Teichner, S. J. *Appl. Catal.* **1990**, *62*, 1–10.
- (130) Christmann, K.; Ertl, G.; Pignet, T. *Surf. Sci.* **1976**, *54*, 365–392.
- (131) Gdowski, G. E.; Felter, T. E.; Stulen, R. H. *Surf. Sci.* **1987**, *181*, L147–L155.
- (132) Anger, G.; Winkler, A.; Rendulic, K. D. *Surf. Sci.* **1989**, *220*, 1–17.
- (133) Haug, K. L.; Burgi, T.; Gostein, M.; Trautman, T. R.; Ceyer, S. T. *J. Phys. Chem. B* **2001**, *105*, 11480–11492.
- (134) Friedrich Bergius. *Nobel Lect.* **1932**, 244–276.
- (135) Chiu, M. E.; Kyriakou, G.; Williams, F. J.; Watson, D. J.; Tikhov, M. S.; Lambert, R. M. *Chem. Commun.* **2006**, 1283–1285.
- (136) Chiu, M. E.; Watson, D. J.; Kyriakou, G.; Tikhov, M. S.; Lambert, R. M. *Angew. Chem. Int. Ed.* **2006**, *45*, 7530–7534.
- (137) Hiyoshi, N.; Sato, O.; Yamaguchi, A.; Shirai, M. *Chem. Commun.* **2011**, *47*, 11546–11548.
- (138) Mohr, C.; Hofmeister, H.; Radnik, J.; Claus, P. *J. Am Chem. Soc.* **2003**, *125*, 1905–1911.
- (139) Pan, M.; Pozun, Z. D.; Brush, A. J.; Henkelman, G.; Mullins, C. B. *ChemCatChem* **2012**, *4*, 1241–1244.
- (140) Chen, B.; Dingerdissen, U.; Krauter, J. G. E.; Lansink Rotgerink, H. G. J.; Möbus, K.; Ostgard, D. J.; Panster, P.; Riermeier, T. H.; Seebald, S.; Tacke, T.; Trauthwein, H. *Appl. Catal. A Gen.* **2005**, *280*, 17–46.
- (141) Merte, L. R.; Peng, G.; Bechstein, R.; Rieboldt, F.; Farberow, C. A.; Grabow, L. C.; Kudernatsch, W.; Wendt, S.; Laegsgaard, E.; Mavrikakis, M.; Besenbacher, F. *Science (80-.)*. **2012**, *336*, 889–893.
- (142) Groß, A. *Surf. Sci.* **2012**, *606*, 690–691.
- (143) Wei, J.; Ji, H.; Guo, W.; Nevidomskyy, A. H.; Natelson, D. *Nat. Nanotechnol.* **2012**, No. June, 357–362.
- (144) Eliaz, N.; Eliezer, D.; Olson, D. L. *Mater. Sci. Eng. A* **2000**, *289*, 41–53.
- (145) Shegai, T.; Johansson, P.; Langhammer, C.; Käll, M. *Nano Lett.* **2012**, *12*, 2464–2469.

- (146) Vannice, M. A.; Sen, B. *J. Catal.* **1989**, *115*, 65–78.
- (147) Noller, H.; Lin, W. M. *J. Catal.* **1984**, *30*, 25–30.
- (148) Chen, C.-S.; Chen, H.-W.; Cheng, W.-H. *Appl. Catal. A* **2003**, *248*, 117–128.
- (149) Kluson, P.; Cervený, L. *Appl. Catal. A-General* **1995**, *128*, 13–31.
- (150) Gallezot, P.; Richard, D. *Catal. Rev.-Sci. Eng.* **1998**, *40*, 81–126.
- (151) Pan, M.; Brush, A. J.; Pozun, Z. D.; Ham, H. C.; Yu, W.-Y.; Henkelman, G.; Hwang, G. S.; Mullins, C. B. *Chem. Soc. Rev.* **2013**, *42*, 5002–5013.
- (152) Joó, F. *ChemSusChem* **2008**, *1*, 805–808.
- (153) Mellmann, D.; Barsch, E.; Bauer, M.; Grabow, K.; Boddien, A.; Kammer, A.; Sponholz, P.; Bentrup, U.; Jackstell, R.; Junge, H.; Laurenczy, G.; Ludwig, R.; Beller, M. *Chem. Eur. J.* **2014**, *20*, 13589–13602.
- (154) Johnson, T. C.; Morris, D. J.; Wills, M. *Chem. Soc. Rev.* **2010**, *39*, 81–88.
- (155) Rice, C.; Ha, S.; Masel, R. I.; Waszczuk, P.; Wieckowski, A.; Barnard, T. *J. Power Sources* **2002**, *111*, 83–89.
- (156) Rice, C.; Ha, S.; Masel, R. I.; Wieckowski, A. *J. Power Sources* **2003**, *115*, 229–235.
- (157) Jeong, K. J.; Miesse, C. M.; Choi, J. H.; Lee, J.; Han, J.; Yoon, S. P.; Nam, S. W.; Lim, T. H.; Lee, T. G. *J. Power Sources* **2007**, *168*, 119–125.
- (158) Li, Q.; He, R.; Gao, J.-A.; Jensen, J. O.; Bjerrum, N. J. *J. Electrochem. Soc.* **2003**, *150*, A1599–A1605.
- (159) Ha, S.; Larsen, R.; Masel, R. I. *J. Power Sources* **2005**, *144*, 28–34.
- (160) Yu, X.; Pickup, P. G. *Electrochem. Commun.* **2009**, *11*, 2012–2014.
- (161) Baschuk, J. J.; Li, X. *Int. J. Energy Res.* **2001**, *25*, 695–713.
- (162) Wachs, I. E.; Madix, R. J. *Surf. Sci.* **1979**, *84*, 375–386.
- (163) Ying, D. H. S.; Madix, R. J. *J. Catal.* **1980**, *61*, 48–56.
- (164) Bowker, M.; Madix, R. J. *Surf. Sci.* **1981**, *102*, 542–565.
- (165) Hayden, B. E.; Prince, K.; Woodruff, D. P.; Bradshaw, A. M. *Vacuum* **1983**, *33*, 876–877.
- (166) Hayden, B. E.; Prince, K.; Woodruff, D. P.; Bradshaw, A. M. *Surf. Sci.* **1983**, *133*, 589–604.

- (167) Crapper, M. D.; Riley, C. E.; Woodruff, D. P. *Surf. Sci.* **1986**, *171*, 1–12.
- (168) Henn, F. C.; Rodriguez, J. A.; Campbell, C. T. *Surf. Sci.* **1990**, *236*, 282–312.
- (169) Leibsle, F. M.; Haq, S.; Frederick, B. G.; Bowker, M.; Richardson, N. V. *Surf. Sci.* **1995**, *343*, L1175–L1181.
- (170) Bowker, M.; Rowbotham, E.; Leibsle, F. M.; Haq, S. *Surf. Sci.* **1996**, *349*, 97–110.
- (171) Bowker, M.; Haq, S.; Holroyd, R.; Parlett, P. M.; Poulston, S.; Richardson, N. *J. Chem. Soc., Faraday Trans.* **1996**, *92*, 4683–4686.
- (172) Haq, S.; Leibsle, F. M. *Surf. Sci.* **1997**, *375*, 81–90.
- (173) Poulston, S.; Bennett, R. A.; Jones, A. H.; Bowker, M. *Phys. Rev. B* **1997**, *55*, 888–891.
- (174) Bowker, M.; Poulston, S.; Bennett, R. A.; Stone, P.; Jones, A. H.; Haq, S.; Hollins, P. *J. Mol. Catal. A Chem.* **1998**, *131*, 185–197.
- (175) Stone, P.; Poulston, S.; Bennett, R. A.; Price, N. J.; Bowker, M. *Surf. Sci.* **1998**, *418*, 71–83.
- (176) Youngs, T. G. A.; Haq, S.; Bowker, M. *Surf. Sci.* **2008**, *602*, 1775–1782.
- (177) Crapper, M. D.; Riley, C. E.; Woodruff, D. P. *Surf. Sci.* **1987**, *184*, 121–136.
- (178) Woodruff, D. P.; McConville, C. F.; Kilcoyne, A. L. D. *Surf. Sci.* **1988**, *201*, 228–244.
- (179) Krastev, E. T.; Kuhl, D. E.; Tobin, R. G. *Surf. Sci.* **1997**, *387*, L1051–L1056.
- (180) Sambì, M.; Granozzi, G.; Casarin, M.; Rizzi, G. A.; Vittadini, A.; Caputi, L. S.; Chiarello, G. **1994**, *6028*, 309–322.
- (181) Nakamura, J.; Kushida, Y.; Choi, Y.; Uchijima, T.; Fujitani, T. *J. Vac. Sci. Technol. A* **1997**, *15*, 1568–1571.
- (182) Fujitani, T.; Choi, Y.; Sano, M.; Kushida, Y.; Nakamura, J. *J. Phys. Chem B* **2000**, *104*, 1235–1240.
- (183) Sotiropoulos, A.; Milligan, P. K.; Cowie, B. C. C.; Kadodwala, M. *Surf. Sci.* **2000**, *444*, 52–60.
- (184) Nakano, H.; Nakamura, I.; Fujitani, T.; Nakamura, J. *J. Phys. Chem. B* **2001**, *105*, 1355–1365.

- (185) Wühn, M.; Weckesser, J.; Wöll, C. *Langmuir* **2001**, *17*, 7605–7612.
- (186) Baber, A. E.; Mudiyansele, K.; Senanayake, S. D.; Beatriz-Vidal, A.; Luck, K. A.; Sykes, E. C. H.; Liu, P.; Rodriguez, J. A.; Stacchiola, D. J. *Phys. Chem* **2013**, *15*, 12291–12298.
- (187) Henderson, M. A.; London, A.; York, N.; Paris, O.; Tokyo, S. *Surf. Sci. Rep.* **2002**, *46*, 1–308.
- (188) Thiel, P. A.; Madey, T. E. *Surf. Sci. Rep.* **1987**, *7*, 211–385.
- (189) Hodgson, A.; Haq, S. *Surf. Sci. Rep.* **2009**, *64*, 381–451.
- (190) Bruijninx, P. C. A.; Weckhuysen, B. M. *Angew. Chem. Int. Ed.* **2013**, *52*, 11980–11987.
- (191) Jiang, F.; Zeng, L.; Li, S.; Liu, G.; Wang, S.; Gong, J. *ACS Catal.* **2015**, *5*, 438–447.
- (192) Larsson, M.; Hultén, M.; Blekkan, E. A.; Andersson, B. *J. Catal.* **1996**, *164*, 44–53.
- (193) Iglesias-Juez, A.; Beale, A. M.; Maaijen, K.; Weng, T. C.; Glatzel, P.; Weckhuysen, B. M. *J. Catal.* **2010**, *276*, 268–279.

Chapter 2: Experimental Methods

2.1 Temperature Programmed Desorption/Reaction Theory

Temperature programmed desorption (TPD) characterizes the fundamental process of a species' desorption from a surface. TPD can provide information about the rate, kinetic order, pre-exponential factor, and activation energy of desorption.¹⁻³ In addition, it can be used to probe packing structures, adsorption sites, and gives information about surface coverage. Finally, TPD can monitor chemical reactions, which is commonly called temperature programmed reaction (TPR). To perform a TPD experiment, a single crystal surface in ultra-high vacuum (UHV) is exposed to the gas of interest. Typically, the crystal is held at cryogenic temperatures to promote adsorption of the gas to the surface. The crystal is then moved into close proximity to the opening of a quadrupole mass spectrometer (QMS). The crystal is heated linearly with time, and as the surface temperature rises adsorbate-surface bonds are broken, causing adsorbates to desorb. The desorbing species are monitored with the QMS, creating a plot of mass spectrometer signal vs. time. The experimental setup of TPD is illustrated in Figure 2.1. TPD can provide information about the activation energy of desorption, which should be noted is not necessarily equal to the energy of adsorption. In system where there is no barrier to desorption the two energies are equal. However, in a system where there is a barrier to adsorption, due to microscopic reversibility a the species must overcome this barrier while desorbing, making the desorption barrier a sum of the adsorption energy and activation energy.³

The rate of desorption can be directly related to the mass spectrometer signal measured in a TPD experiment, which can be seen by equation 2.1

$$\frac{d\theta(T_s)}{dt} = \left(\frac{V}{ak_B T_g} \right) \left(\frac{dP}{dt} + \frac{SP}{V} \right) \quad (2.1)$$

where θ is the surface coverage, T_s is the sample temperature, t is time, V is the chamber volume, a is the adsorbent area, k_B is the Boltzmann constant, T_g is the gas phase temperature, P is the pressure increase over the background and S is the pumping speed of the chamber.⁴ The term $\frac{d\theta(T_s)}{dt}$ is an expression for the rate of desorption. The term $\left(\frac{V}{ak_B T_g} \right)$ is a constant for a given chamber. Therefore, as the pumping speed increases and $\frac{dP}{dt}$ becomes negligible the rate of desorption is directly related to the pressure increase over the background, which is detected using the QMS.

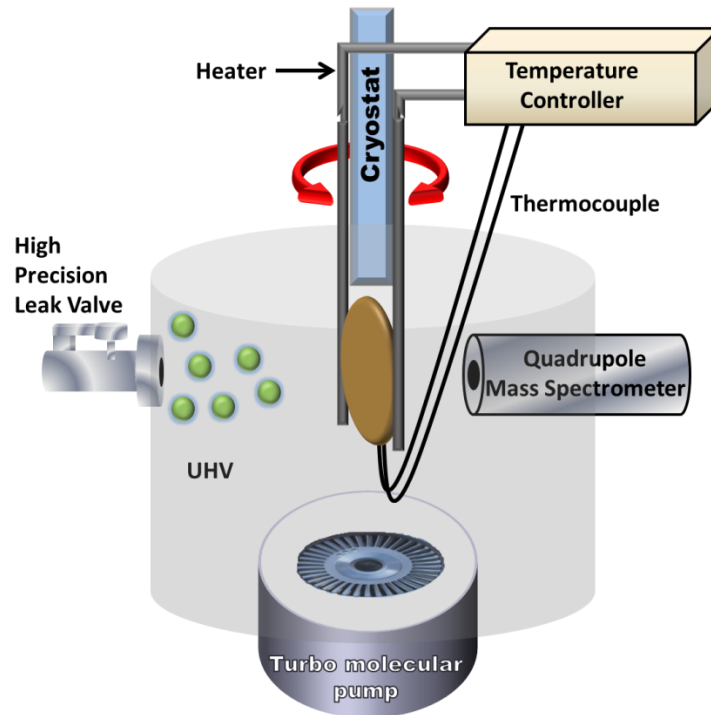


Figure 2.1 Schematic of the experimental setup for TPD.

Since TPD is directly measuring the rate of the reaction, a simple rate law can be written for a desorption process as shown in equation 2.2.

$$-\frac{d\theta}{dt} = k_d \theta^m \quad (2.2)$$

In this equation, k_d is the desorption rate constant and m is the desorption order.

As previously mentioned, TPD experiments are typically run using a linear heating rate which can be expressed by equation 2.3

$$T(t) = T_0 + \beta t \quad (2.3)$$

where T is temperature, T_0 is the initial temperature and β is the heating rate.

Taking the derivative of equation 2.3 in terms of time gives the relationship in equation 2.4.

$$\beta = \frac{dT}{dt} \quad (2.4)$$

Using this equation, the rate of desorption can be expressed in terms of temperature rather than time.

$$\frac{-d\theta}{dt} = \frac{-d\theta}{dT} \times \frac{dT}{dt} = \frac{-d\theta}{dT} \beta \quad (2.5)$$

Utilizing equation 2.5, equation 2.2 can be rewritten as equation 2.6.

$$\frac{-d\theta}{dT} = \frac{k_d}{\beta} \theta^m \quad (2.6)$$

Desorption is a process that obeys Arrhenius type kinetics, so k_d can be expressed as

$$k_d = Ae^{\left(\frac{-E_d}{RT}\right)} \quad (2.7)$$

where A is the pre-exponential factor, E_d is the activation energy of desorption and R is the ideal gas constant. The expression for k_d in equation 2.7 can be substituted into equation 2.6 to give equation 2.8.

$$\frac{-d\theta}{dT} = \frac{A}{\beta} \theta^m e^{\left(\frac{-E_d}{RT}\right)} \quad (2.8)$$

This expression is commonly known as the Polanyi-Wigner equation, after its original derivation by Michael Polanyi and Eugene Wigner, and it describes the behavior of desorbing species in a TPD experiment.⁵ Typically, it is expected that the rate of a process that follows Arrhenius behavior will increase exponentially with temperature as can be seen by the expression $e^{\left(\frac{-E_d}{RT}\right)}$. However, in TPD spectra there is a temperature at which the rate is at a maximum that is followed by a decrease in the rate. The reason for this is the Polanyi-Wigner equation also depends on the surface coverage, which is fixed at the beginning of the experiment. As the temperature increases, the surface coverage decreases, eventually reaching zero at which point the rate of desorption will also be zero. TPD peaks are therefore a convolution of the desorption rate constant and the surface coverage (Figure 2.2).¹

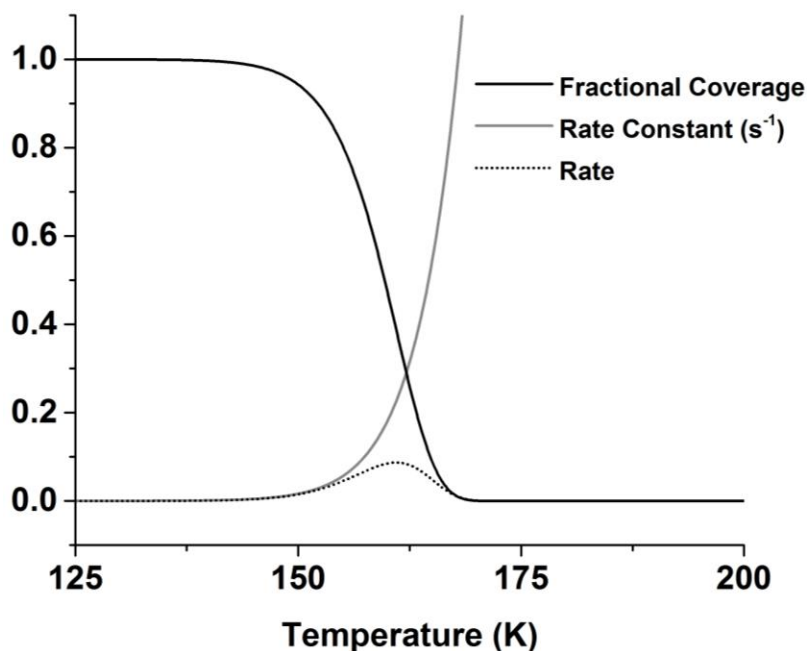


Figure 2.2 Demonstration that the rate of desorption observed in a TPD experiment (dotted line) is a convolution of the remaining fractional coverage (black line) and the rate constant (grey line).

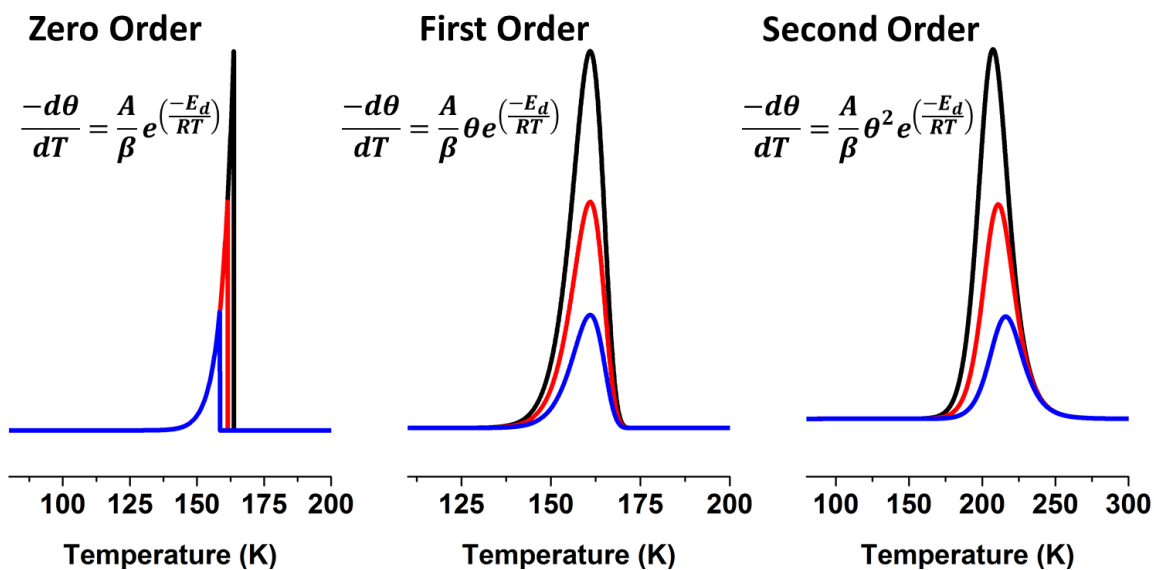


Figure 2.3 Simulated TPD spectra for the three common desorption orders along with the Polanyi-Wigner expressions describing them.

The effect surface coverage has on the rate of desorption is dependent on the order of desorption, and this parameter greatly affects the peak shape of a

TPD spectrum (Figure 2.3). As with most chemical processes, desorption is typically either zero, first or second in order. Species that desorb in a zero order process exhibit a series of peaks sharing a common leading edge that shift to higher temperatures with increasing coverage. In zero order desorption, the term for coverage drops from the Polanyi-Wigner equation and thus the rate is almost solely dependent on the rate constant. The rate reaches maximum at the point where adsorbed species still remain on the surface and the rate constant is at its highest, and then instantly drops to zero from this peak as the last species desorbs. Zero order desorption is most commonly observed in systems where species are held on the surface primarily through intermolecular interactions with themselves, rather than a strong interaction with the surface, such as desorption from multilayers.⁶ First order desorption is characterized by asymmetric peaks with an ascending leading edge. The maximum desorption rate remains at a constant temperature for all coverages in ideal first order desorption, although realistically in most experiments attractive or repulsive lateral interactions between molecules will cause the peak to shift slightly with coverage. First order desorption is typically seen by molecules that adsorb and desorb reversibly without undergoing any chemical reaction and in decomposition reactions.^{7,8} Second order desorption peaks are symmetric in nature and shift to lower temperature with increasing coverage. This behavior typically occurs when two surface species must recombine to desorb.⁹⁻¹¹ The peak shifts to lower temperature at higher coverage due to an increase in the probability of recombination.

Peak shape is only a qualitative indicator of desorption order. To quantitatively determine the order the following method can be applied.¹² The Polanyi-Wigner equation (Equation 2.8) is rearranged easily to the expression in Equation 2.9.

$$\ln\left(\frac{R_d}{\theta^m}\right) = \ln\left(\frac{A}{\beta}\right) - \frac{E_d}{RT} \quad (2.9)$$

R_d is an expression for the rate of desorption equivalent to $\frac{-d\theta}{dT}$. Using equation 2.9, plots can be made for $\ln\left(\frac{R_d}{\theta^m}\right)$ vs. $\frac{1}{T}$ while guessing the order. The plot with the correct order will yield a straight line, while incorrect guesses will not.¹²

It should be noted that the order of desorption will be determined by the rate limiting step of a process. For example, H atom recombination to form H_2 is expected to be second order in nature as two H atoms must recombine to form the gaseous product.⁹⁻¹¹ However, during the decomposition of formic acid it is common to observe H_2 peaks exhibiting first order kinetics.^{7,8} Formic acid decomposes to formate on many metal surfaces, and this formate then decomposes to CO_2 and H_2 . Formate decomposition on Cu surfaces occurs well above the temperature that H atoms would normally be able to recombine and desorb, and thus the rate limiting step to the production of H_2 in this case is the decomposition of formate, which is a first order process. Careful observations of desorption order can yield information about chemical reactions occurring on the surface.

TPD can also provide information about the number of unique packing structures and adsorption sites on a surface. As each adsorption site has a different adsorption energy, different temperatures will be required to desorb species from each different site. If the difference in temperature is great enough, distinct peaks for each site and or packing structure are observed in the TPD spectrum. As an example the desorption of CO from a 0.01 ML Pd/Cu(111) surface is shown in Figure 2.4 (black trace). CO on Cu terraces is known to exhibit three packing structures, a dense (7×7) unit cell, an intermediate (4×4) unit cell, and a least densely packed ($\sqrt{3} \times \sqrt{3}$) unit cell. These three phases desorb at 110 K, 130 K, and 170 K respectively.¹³⁻¹⁵ CO on under-coordinated Cu steps and defects is bound more strongly than on terraces and does not desorb until 220 K, giving rise to a fourth peak in the spectrum.¹⁶ Finally, CO binds more strongly to the single Pd sites than the Cu sites, and a fifth peak is observed at 270 K corresponding to these sites.¹⁷ It should be noted that although peaks for all these packing structures/sites are observed in TPD spectra, their identity is usually discovered with other techniques, as TPD gives no information about species on the surface, just what comes off.

The initial surface coverage of adsorbates can also be revealed by TPD. As discussed, the mass spectrometer signal is directly related to the rate of desorption. As desorption is a measure of molecules per second per unit area, an integral of the area under a TPD curve is proportional to the initial coverage. This coverage can be discovered by comparing the area to an area from a curve with a known coverage using the following expression

$$\theta_{unknown} = \frac{Area_{unknown}}{Area_{known}} \times \theta_{known} \quad (2.10)$$

where $\theta_{unknown}$ is the unknown coverage, $Area_{unknown}$ is the area under the TPD curve for the unknown coverage, $Area_{known}$ is the area under the TPD curve for the known coverage, and θ_{known} is the known coverage. Usually TPD requires assistance from another technique to find this known coverage. For example, in Figure 2.4 the black curve corresponds to a saturation dose of CO on the Pd/Cu(111) alloy. It is known from the literature that CO saturates a Cu(111) surface with a coverage of 0.52 ML.¹³⁻¹⁵ By taking the area under the black curve, which is known, the area under the red curve can be found using equation 2.10 providing the difference between the preferred binding sites for the Pd and Cu are taken into account (bridge and atop respectively).

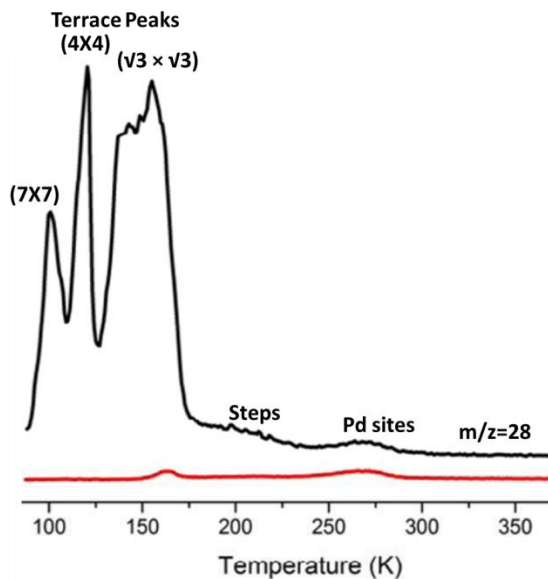


Figure 2.4 CO desorption from a 0.01 ML Pd/Cu(111) surface with the different peaks labeled. The black trace results from a saturation dose of CO, while the red trace results from an initial coverage of ~0.01 ML CO. Adapted from Ref. 17.

Mathematical analysis of a series of TPD spectra can yield information about the activation energy of desorption as well as the pre-exponential factor for the desorption process. There are multiple methods for yielding these parameters, although nearly all of them are based on manipulations of the Polanyi-Wigner equation.^{5,12} Complete analysis is one of the best methods for finding both parameters as it relies on very few assumptions.^{4,18} It uses the following natural log form of the Polanyi-Wigner equation.

$$\ln(R_d) = \ln\left(\frac{A\theta^m}{\beta}\right) - \frac{E_d}{RT} \quad (2.11)$$

By plotting $\ln(R_d)$ vs. $\frac{1}{T}$ a line can be obtained where $\frac{-E_d}{R}$ is equivalent to the slope and $\ln\left(\frac{A\theta^m}{\beta}\right)$ is equivalent to the intercept. As this expression is coverage dependent, it helps to fix the coverage. A coverage of interest, θ_r , is chosen and then a family of TPD curves with starting coverages greater or equal to θ_r are obtained. Each curve is integrated from right to left until the point where θ_r is reached. This point gives a value for both R_d and T , and a series of points from the family can be used to make a line. This process can be repeated for various values of θ_r to derive activation energies and pre-exponential factors for various starting coverages. For a figure demonstrating this process see the TPD lecture given by Ranke.³

Leading Edge Analysis, also known as Habenschaden-Küppers analysis, is another very accurate method for yielding the energy of desorption and pre-exponential factor from a TPD spectra.¹⁹ Equation 2.11 is also used for this

method, but the points for the line are taken from the leading edge of a single TPD spectrum. The assumption this method makes is that at the leading edge of a spectrum, the coverage changes very little and can be considered constant. This assumption holds true up to a 5% decrease in coverage. Leading Edge Analysis allows for the calculation of E_d at a fixed coverage from a single TPD spectrum and also for the calculation of A provided the coverage is known. In order for this method to be accurate, the signal to noise ratio at the leading edge must be excellent, as the signal in this region is usually very small.

Several methods of TPD analysis rely on a manipulation of the Polanyi-Wigner equation known as the Redhead equation.²⁰ Starting with the Polanyi-Wigner equation (2.8), it is known that T is at maximum (T_p) when the relationship in equation 2.12 is true.

$$\frac{-d\theta^2}{dT^2} = 0 \quad (2.12)$$

Hence, if equation 2.8 is differentiated and set to zero the following expression can be derived.

$$\frac{E_d}{RT_p^2} = \frac{A}{\beta} m \theta^{m-1} e^{\left(\frac{-E_d}{RT_p}\right)} \quad (2.13)$$

Redhead showed that for a first order desorption process there is a special case that be derived from this equation.²⁰ By setting $m=1$, followed rearranging, taking the natural log and solving for E_d the expression in equation 2.14 can be obtained.

$$E_d = RT_p \left(\ln \left(\frac{AT_p}{\beta} \right) - \ln \left(\frac{E_d}{RT_p} \right) \right) \quad (2.14)$$

The first natural log term is typically much larger than the second one. Furthermore, Redhead demonstrated that E_d is related linearly to T_p which allows for an estimate of the second natural log term to be made.²⁰ Using plots of E_d vs. T_p Redhead estimated that the value of the second natural log term was 3.46. With this estimate applied, equation 2.14 becomes the following expression.

$$E_d = RT_p \left(\ln \left(\frac{AT_p}{\beta} \right) - 3.46 \right) \quad (2.15)$$

Note that Redhead's original paper states a value of 3.64,²⁰ but the data presented in his graph is more consistent with a value of 3.46 which is quoted by most other sources.^{1-3,12} Equation 2.15 allows for an estimate of E_d to be calculated assuming a pre-exponential factor of 1×10^{13} based on the vibration frequency of an atom although recent studies show a value of 1×10^{15} may be more accurate.²¹ The greatest advantage of Redhead's analysis is that it can quickly give an estimate of E_d from a single TPD spectrum. However, the method is very inaccurate as it makes a number of assumptions including guessing the pre-exponential factor. The accuracy improves if the pre-exponential is known, but is still not as efficient as complete analysis or leading edge analysis.¹²

The Heating Rate Variation method also utilizes the form of the Redhead equation shown in Equation 2.13, and can be applied for first or second order desorption processes.²² For a first order process equation 2.13 becomes

$$\frac{E_d}{RT_p^2} = \frac{A}{\beta} e^{\left(\frac{-E_d}{RT_p} \right)} \quad (2.16)$$

Taking the natural log of this expression and rearranging gives

$$\ln\left(\frac{\beta}{T_p^2}\right) = \frac{-E_d}{RT_p} + \ln\left(\frac{AR}{E_d}\right) \quad (2.17)$$

To utilize equation 2.17, multiple TPD spectra are obtained using the same initial coverage, but different heating rates. For accurate results the heating rate should be varied by at least 3 orders of magnitude.^{12,22} A plot is then be made of $\ln\left(\frac{\beta}{T_p^2}\right)$ vs $\frac{1}{T}$ which yields a line with a slope equivalent to $\frac{-E_d}{R}$ and an intercept equivalent to $\ln\left(\frac{AR}{E_d}\right)$ allowing for a calculation of both E_d and A for the given coverage. A similar derivation can be made for a second order process. Equation 2.13 becomes

$$\frac{E_d}{RT_p^2} = \frac{2A\theta(T_p)}{\beta} e^{\left(\frac{-E_d}{RT_p}\right)} \quad (2.18)$$

for a second order process. However, as second order peaks are symmetrical the coverage at T_p is half the initial coverage and the expression can be simplified to equation 2.19.

$$\frac{E_d}{RT_p^2} = \frac{A\theta_0}{\beta} e^{\left(\frac{-E_d}{RT_p}\right)} \quad (2.19)$$

Similarly to the first order scenario taking the natural log and rearranging gives equation 2.20.

$$\ln\left(\frac{\beta}{T_p^2}\right) = \frac{-E_d}{RT_p} + \ln\left(\frac{AR\theta_0}{E_d}\right) \quad (2.20)$$

Plotting $\ln\left(\frac{\beta}{T_p^2}\right)$ vs. $\frac{1}{T}$ gives a plot with a slope equivalent to $\frac{-E_d}{R}$ and an intercept equivalent to $\ln\left(\frac{AR\theta_0}{E_d}\right)$ allowing for the calculation of both E_d and A for the given coverage.

While each analysis method discussed has its advantages and disadvantages, perhaps the most important consideration is how accurate the given method is. To test this, de Jong and Niemantsverdriet applied each method to simulated TPD spectra with known orders, coverage, pre-exponential factors and E_d .¹² The results show that complete analysis and leading edge analysis were consistently the most accurate. Heating rate variation gave fairly good accuracy, while Redhead analysis was very error prone. De Jong and Niemantsverdriet's paper is an excellent reference for descriptions of the various analysis method's and their pros and cons.¹²

While TPD can provide a lot of useful information about desorption kinetics, it is important to understand the limitations of the technique. TPD is a destructive technique, meaning the sample needs to be re-prepared prior to each experiment. TPD provides no information about what is on the surface, and only detects desorbing species. This means, any species remaining on the surface after the temperature ramp will not be detected. In this thesis, TPD is complimented with scanning tunneling microscopy, allowing for the detection of surface bound species. While TPD provides information about binding sites, packing structures, and coverage it cannot identify any of these solely on its own as previous discussed. In addition, if an overall process is desorption rate limited it can be

difficult to determine the temperature a reaction occurs at. Finally, care should be taken when analyzing TPD spectra as cross talk between masses can lead to false results.

2.2 Temperature Programmed Desorption/Reaction Experimental Methods

TPD experiments in this thesis were performed on a custom built UHV chamber purchased from MDC Vacuum Products, LLC (Figure 2.5A). A base pressure of $<1 \times 10^{-10}$ mbar is maintained through the use of a turbomolecular pump (Pfeiffer) backed by a RV5 rotary pump (Edwards). This pumping system is supplemented using titanium sublimation pumps (Moorfield) which are operated at a current of 42 A. The pressure in the chamber is monitored using a hot filament Th/Ir ion gauge (VG Scienta). All components obligatory for maintaining vacuum are powered through an uninterrupted power supply (Smart-UPS 3000) (APC) to protect vacuum in case of a loss of power to the building. Furthermore, the chamber incorporates a gate valve (VAT) situated between the main chamber and the turbomolecular pump that automatically shuts if power is lost to the chamber, which seals the chamber off in order to maintain a vacuum.

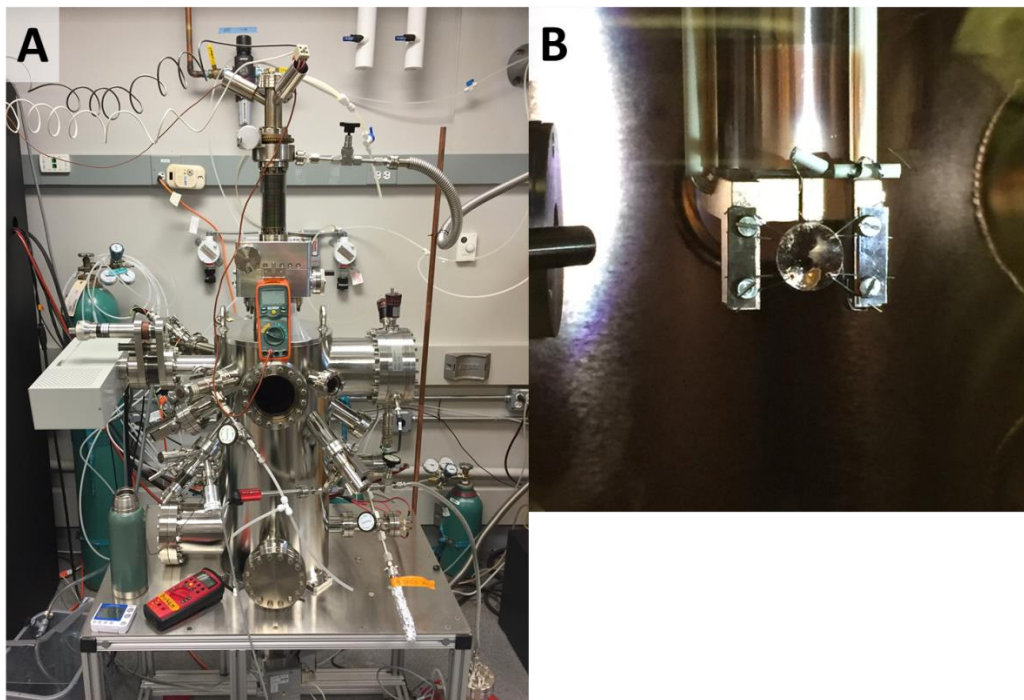


Figure 2.5 Pictures of the UHV chamber used for TPD experiments. (A) Outside view of the whole UHV chamber. (B) A look through the front view-port of the TPD chamber showing the mounted Cu(111) crystal.

All TPD experiments in this thesis were performed using a Cu(111) crystal (MaTeck), mounted in the TPD chamber (Figure 2.5B). The crystal has a diameter of 11 mm and is polished on the front side with a roughness of less than $0.03\mu\text{m}$ with an orientation accuracy of $<0.1^\circ$. A hole 1 mm deep and 0.2 mm in diameter is drilled into one of the sides of the crystal allowing for the insertion of a K-type thermocouple. The thermocouple is read by a Process Control Unit (Eurotherm), which also controls the heating rate. The crystal is mounted to the sample holder with Ta wires, which serves to resistively heat the crystal. Heating is achieved using a Genesys 750 W Programmable DC Power Supply (TDK Lambda), which in communication with the Process Control Unit can heat the crystal up to 800 K. During TPD experiments, unless otherwise stated, the heating

rate was 1 K/s. The crystal can be moved in both the x and y directions ± 10 mm from center, and ± 50 mm in the z direction. In addition it can be rotated 360. The crystal is coupled to a liquid nitrogen cryostat which allows it to be cooled to 85 K. The Cu(111) sample was cleaned before each day of experiments through cycles of Ar⁺ sputtering (1.50 kV/11 μ A) and annealing up to 750 K. Sputtering was performed using a cold cathode sputter gun (Omicron Nanotechnology).

To perform TPD experiments the chamber includes a quadrupole mass spectrometer (Hiden Hal/3F 301 RC system, Hiden Analytical) with an upper mass range of 300 amu. The ionization source is a yttria coated Ir filament run at an ionization energy of 70 eV. The QMS incorporates a dual Faraday Cup/Secondary Electron Multiplier (SEM) detector. The SEM can be safely operate up to pressures of 5×10^{-6} torr, while the Faraday Cup can be operated up to 1×10^{-4} torr. The QMS was offset by +0.3 amu, which was accounted for when performing TPD measurements. The QMS is mounted on a linear extender which allows for its translation up to 6 cm in the x direction.

Metal deposition in the UHV chamber was performed using a flux monitored EFM 3 electron beam evaporator (Omicron Nanotechnology, GmbH). The metal source is a 50 mm rod of either Pd or Pt, both with purities of 99.95% and purchased from Goodfellow. During metal deposition, the crystal was held at 380 K to promote single atom alloy formation. Metal coverages were calibrated using CO titrations assuming CO binds atop to Pd atoms^{23–25} and Pt^{26–28} atoms in Cu. Pd coverage was also calibrated using Auger Electron Spectroscopy (AES) which was performed using a LEED-AES system from OCI. The crystal was

exposed to gases by backfilling with the gas of interest using a high precision leak valve. Liquid samples were typically degassed through cycles of freeze-pump-thawing. Further experimental details on TPD procedures are given in relevant chapters.

2.3 Scanning Tunneling Microscopy Theory

Scanning tunneling microscopy (STM) is a powerful technique that allows for the visualization of the atomic structure of surfaces, making it a complimentary technique to TPD. A schematic of the experimental setup of the technique is shown in Figure 2.6 Developed by Binnig and Röhler in 1982, STM is based on a quantum phenomenon known as tunneling, where electrons are able to move from one conduction surface to another in close proximity through empty space, in which classically they should not be able to exist.^{29,30} Tunneling occurs due to an overlap in the wave functions of the two surfaces. In STM, an atomically sharp tip, typically made of W or Pt/Ir, is brought within nanometers of a conductive surface. Applying a voltage bias between the tip and the surface allows for electrons to tunnel between the two and serve as a probe. The direction of the tunneling electrons depends on how the bias is applied. Electrons will flow towards the object that is positively biased.^{1,2} The tunneling current is exponentially proportional to the distance between the tip and the surface as illustrated in Equation 2.21

$$I \propto e^{-2kd} \quad (2.21)$$

where I is the tunneling current, d is the distance between the two objects, and k is defined as

$$k = \sqrt{\frac{2m}{\hbar^2} (eU_B - E)} \quad (2.22)$$

where m is the mass of an electron, \hbar is Planck's constant divided by 2π , eU_B is the barrier height of the tunneling gap, and E is the energy of the state from which tunneling occurs.² Due to this relationship, the tunneling current is extremely sensitive to the distance between the tip and the surface enabling resolution of height changes less than 1 \AA , which in turn allows for resolution of individual atoms. STM actually images electronic states, but as these are correlated with the positions of atomic nuclei, STM images are correlated with the positions of atoms.² The STM tip is rastered across the surface using a piezoelectric material to precisely move the tip in the x , y and z directions. This allows for the creation of a topographical map of the surface.¹

There are two modes primarily used for scanning in STM. In constant height mode, the position of the tip is fixed. This means the tunneling current fluctuates as the tip samples various topographical heights across the surface. This mode is not frequently used, as the tip can easily crash if it encounters an area that is very topographically high. Typically constant current mode is used. In this mode the tunneling current is fixed, meaning the tip will adjust its height maintain a constant tunneling current, allowing it to react to changes in the topography of the surface. While STM can provide information about the local structure of a surface, and often differentiate between two distinct species on the surface^{31,32}, it

does not provide chemical identification.² For this reason STM is often performed under UHV, to keep the surface of interest clean and ensure only molecules of interest are observed.

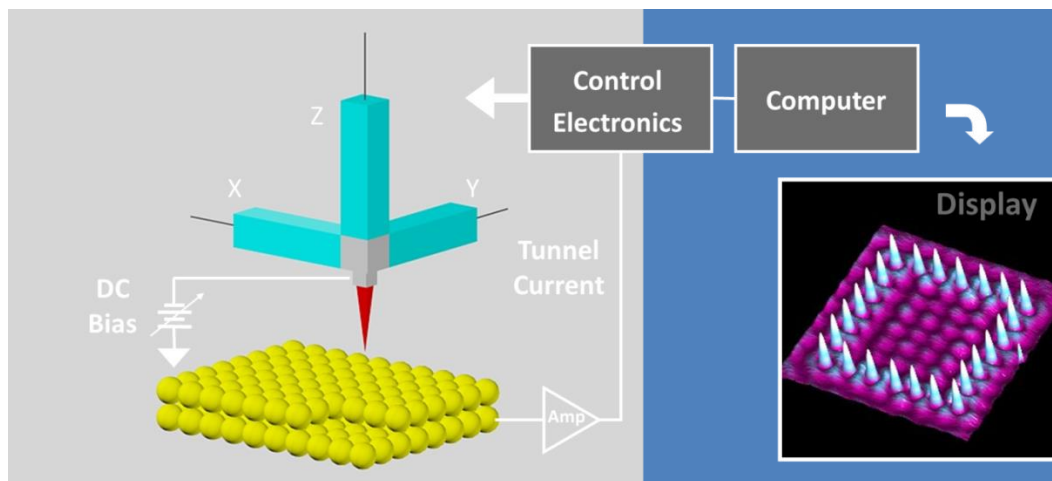


Figure 2.6 Schematic of the experimental setup of STM.

2.4 Scanning Tunneling Microscopy Experimental Methods

STM experiments in this thesis were performed using a commercially available Omicron Nanotechnology low temperature STM (LT-STM) (Figure 2.7). The entire instrument is housed in a quiet room and supported on air legs to suppress vibrations during measurements. The instrument consists of a chamber that contains the STM, which is connected to a separate preparation chamber via a gate valve. The pressure in the STM chamber is $<1 \times 10^{-11}$ mbar, while in the preparation chamber a pressure of $<5 \times 10^{-10}$ mbar is maintained. Both chambers are primarily pumped by ion getter pumps (Varian) supplemented by titanium sublimation pumps. The chambers can also be pumped via a turbomolecular pump

(Pfeiffer) which is typically used for any high pressure operations. Hot filament Th/Ir ion gauges (VG Scienta) read the pressure in each chamber.

The sample used in the STM experiments is a Cu(111) crystal (MaTeck) mounted on a Ta plate. The plate can be transferred between the STM stage for scanning, a carousel for storage, or a manipulator for annealing, sputtering, and metal deposition through the use of a wobble stick. In the STM stage the crystal can be cooled to either 5K or 80 K through a two-stage cryostat. For 5 K experiments, the inner dewar of the cryostat is filled with liquid helium while the outer cryostat is filled with liquid nitrogen. For operation at 80 K both dewars are filled with liquid nitrogen. Operation at cryogenic temperatures ensures that species on the surface remain stationary so they are easily imaged. The crystal can be annealed up to room temperature by removing it from the stage and placing it in the room temperature carousel for a set amount of time. However, the error in this process is great, ± 20 K. Anneals above room temperature can be performed in the manipulator which can safely heat the crystal to 1000 K. The crystal is exposed to adsorbates while in the STM stage, typically while the sample is at 5 K, using a high precision leak valve with a collimator directing the gas toward the stage.

Sample preparation including cleaning and metal deposition are performed in the preparation chamber with the sample held in the manipulator. The sample is cleaned via cycles of Ar^+ sputtering (1 kV/20 μA) using a cold cathode sputter gun (Omicron Nanotechnology) and annealing to 1000 K. After cleaning the sample is imaged in the STM chamber to ensure cleanliness. Metal deposition

was performed with flux monitored EFM 3 electron beam evaporators (Omicron Nanotechnology, GmbH) as was the case for TPD experiments. The crystal was held at 380 K during metal deposition. Before metal deposition occurred, the base pressure in the preparation chamber was lowered through flashing the titanium sublimation pumps so that very clean metal deposition could be achieved. Metal coverages were calibrated by counting.

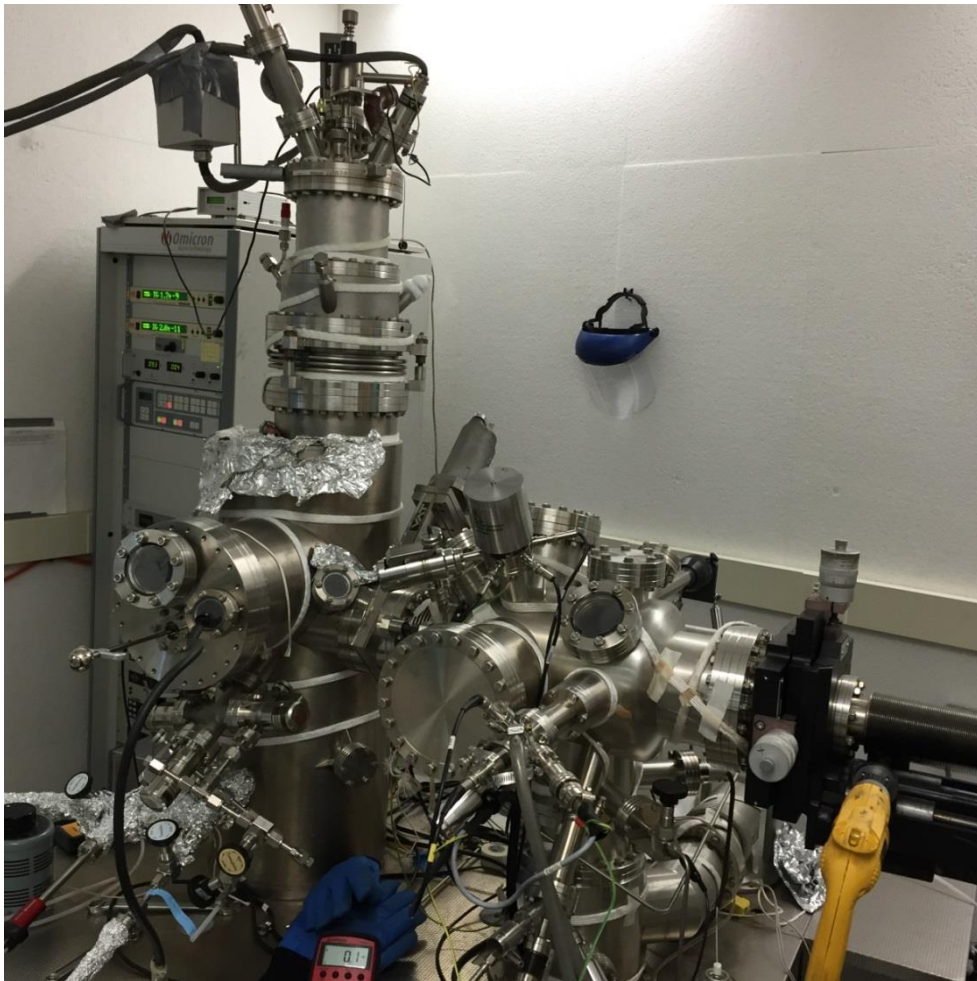


Figure 2.7 Picture of the LT-STM used in this thesis.

2.5 References

- (1) Attard, G.; Barnes, C. *Surfaces*; Oxford University Press, 2004.
- (2) Kolasinski, K. W. *Surface Science*, 3rd ed.; Wiley, 2012.
- (3) Ranke, W. In *Lecture at the Fritz Haber Institut of the MPG*; Berlin, 2003.
- (4) King, D. A. *Surf. Sci.* **1975**, *47*, 384–402.
- (5) Polanyi, M.; Wigner, E. *Z. Phys. Chem. Abt. A* **1928**, *139*, 439.
- (6) Hodgson, A.; Haq, S. *Surf. Sci. Rep.* **2009**, *64*, 381–451.
- (7) Wachs, I. E.; Madix, R. J. *Surf. Sci.* **1979**, *84*, 375–386.
- (8) Marcinkowski, M. D.; Murphy, C. J.; Liriano, M. L.; Wasio, N. A.; Lucci, F. R.; Sykes, E. C. H. *ACS Catal.* **2015**, *5*, 7371–7378.
- (9) Anger, G.; Winkler, A.; Rendulic, K. D. *Surf. Sci.* **1989**, *220*, 1–17.
- (10) Kyriakou, G.; Boucher, M. B.; Jewell, A. D.; Lewis, E. A.; Lawton, T. J.; Baber, A. E.; Tierney, H. L.; Flytzani-Stephanopoulos, M.; Sykes, E. C. H. *Science* **2012**, *335*, 1209–1212.
- (11) Christmann, K.; Ertl, G.; Pignet, T. *Surf. Sci.* **1976**, *54*, 365–392.
- (12) de Jong, A. M.; Niemantsverdriet, J. W. *Surf. Sci.* **1990**, *233*, 355–365.
- (13) Kirstein, W.; Krueger, B.; Thieme, F. *Surf. Sci.* **1986**, *176*, 505–529.
- (14) Kneitz, S.; Gemeinhardt, J.; Steinrück, H. *Surf. Sci.* **1999**, *440*, 307–320.
- (15) Raval, R.; Parker, S.; Pemble, M.; Hollins, P. *Surf. Sci.* **1988**, *203*, 353–377.
- (16) Bonicke, I.; Kirstein, W.; Spinzig, S.; Thieme, F. *Surf. Sci.* **1994**, *313*, 231–238.
- (17) Marcinkowski, M. D.; Jewell, A. D.; Stamatakis, M.; Boucher, M. B.; Lewis, E. A.; Murphy, C. J.; Kyriakou, G.; Sykes, E. C. H. *Nat. Mater.* **2013**, *12*, 523–528.
- (18) King, D. A.; Madey, T. E.; Yates, J. T. J. *J. Chem. Phys.* **1971**, *55*, 3236.
- (19) Habenschaden, E.; Küppers, J. *Surf. Sci. Lett.* **1984**, *138*, L147–L150.
- (20) Redhead, P. A. *Vacuum* **1962**, 203–211.
- (21) Campbell, C. T.; Sellers, J. R. V. *Chem. Rev.* **2013**, *113*, 4106–4135.
- (22) Falconer, J. L.; Madix, R. J. *Surf. Sci.* **1975**, *48*, 393–405.
- (23) Illas, F.; Lopez, N.; Ricart, J. M.; Clotet, A.; Conesa, J. C.; Fernandez-Garcia, M. *J. Phys. Chem. B* **1998**, *102*, 8017–8023.
- (24) Sakong, S.; Mosch, C.; Groß, A. *Phys. Chem. Chem. Phys.* **2007**, *9*, 2216–2225.
- (25) Lopez, N.; Nørskov, J. K. *Surf. Sci.* **2001**, *477*, 59–75.
- (26) Zhang, C. J.; Baxter, R. J.; Hu, P.; Alavi, A.; Lee, M. H. *J. Chem. Phys.*

2001, *115*, 5272–5277.

- (27) Schneider, U.; Castro, G. R.; Wandelt, K. *Surf. Sci.* **1993**, 287–288, 146–150.
- (28) Castro, G.; Schneider, U.; Busse, H.; Janssens, T.; Wandelt, K. *Surf. Sci.* **1992**, 269, 321–325.
- (29) Binnig, G.; Rohrer, H.; Gerber, C.; Weibel, E. *Phys. Rev. Lett.* **1982**, 49, 57–61.
- (30) Binnig, G.; Rohrer, H.; Gerber, C.; Weibel, E. *Appl. Phys. Lett.* **1982**, 40, 178–180.
- (31) Varga, P.; Schmid, M. *Appl. Surf. Sci.* **1999**, 141, 287–293.
- (32) Schmid, M.; Stadler, H.; Varga, P. *Phys. Rev. Lett.* **1990**, 70, 1441–1444.

Chapter 3: Significant Quantum Effects in Hydrogen Activation

This chapter was modified from an original paper published in 2014 by the same title by G. Kyriakou et al. from ACS Nano, volume 8, pages 4827-4835 and is supplemented by material from an original paper published in 2013 by the title “Single atom alloy surface analogs in Pd_{0.18}Cu₁₅ nanoparticles for selective hydrogenation reactions” by M. B. Boucher et al. from Phys. Chem. Chem. Phys., volume 15, pages 12187-12196.

STM images in Figure 3.3 were acquired by Timothy J. Lawton. DFT calculations were performed by Erlend R. M. Davidson and Angelos Michaelides in the Department of Chemistry at University College London. KMC simulations were performed by Guowen Peng, Luke T. Roling, Suyash Singh and Manos Mavrikakis in the Department of Chemical and Biological Engineering at University of Wisconsin.

3.1 Introduction

The making and breaking of bonds involving hydrogen atoms at the surfaces of materials plays a major role in nature. It is also relevant to heterogeneous catalysis, sensing, energy storage, and chemical reactions in the interstellar medium.¹⁻⁶ Therefore, understanding the adsorption and reaction dynamics of hydrogen on solid surfaces is of widespread importance and central to process improvement and materials engineering. The light mass of hydrogen makes it subject to quantum behavior, which can strongly affect its reactivity.⁷ It has been demonstrated both experimentally and theoretically that quantum

tunneling plays a role in a variety of reactions including conformational inversions, eliminations, and enzymatic reactions involving hydrogen.⁷⁻⁹ While it is known that quantum effects can have a significant effect on the rate of reactions involving hydrogen, our understanding of the regimes in which these quantum effects are important is currently not well developed.

Selective hydrogenations of both double and triple carbon bonds are important for a wide range of industrial processes.¹⁰ Given that molecular H₂ dissociation is often the rate-limiting step, olefin hydrogenations are typically performed over catalysts with a low barrier for H₂ dissociation. Heterogeneously catalyzed hydrogenation reactions often employ metals and alloys based on platinum, ruthenium, palladium, or nickel.¹⁰ These metals allow for the facile dissociation of molecular hydrogen due to a relatively low reaction barrier. In contrast, coinage metals like Cu and Au exhibit a higher barrier for the dissociation of molecular hydrogen and are less reactive towards hydrogen.¹¹⁻¹³ Many surface science studies have examined the quantum behavior of hydrogen.¹⁴⁻³¹ Experimental work has focused on the quantum tunneling-enabled diffusion of single hydrogen atoms on a variety of surfaces using field emission microscopy,¹⁶ helium spin-echo spectroscopy,¹⁷ optical diffraction,¹⁸⁻²⁰ and scanning tunneling microscopy (STM).²¹⁻²³ Recently, quantum tunneling was found to allow 2D self-assembly of hydrogen atoms at low temperature (5 K) on Cu(111).²⁴ The key observable difference between classical and tunneling reaction pathways is the temperature dependence of the reaction rate and

divergence from classical behavior is often detected through careful examination of kinetic isotope effects in chemical reactions.^{7,18,28,29,32}

We recently reported that addition of just 1% of a monolayer of Pd to the surface of Cu can promote the dissociation of hydrogen.^{33–35} These single atom Pd sites lower the energy barrier to hydrogen uptake, allowing it to dissociate and then spill over onto the bare Cu terraces.^{33–35} This Pd/Cu system is especially interesting due to the use of Pd/Cu alloy catalysts in a variety of hydrogenation reactions.^{36–40} Despite careful use of density functional theory (DFT) calculations, a number of recent studies could not explain these results.^{41–44} Here we use a well-defined model system and an array of sophisticated theoretical approaches that allow us to understand and quantify the precise role of quantum effects in hydrogen dissociation. We build upon our previous work, and examine the uptake of H₂ on Pd/Cu alloys with a range of Pd concentrations.³⁴ These results clearly demonstrate the ability of hydrogen to spillover onto Cu from low loadings of Pd. In addition, we studied the uptake of hydrogen and deuterium using temperature programmed desorption (TPD), DFT, path integral based DFT approaches to account for quantum nuclear effects, and kinetic Monte Carlo (KMC). The dissociative adsorption of molecular hydrogen and deuterium reveals vastly different rates and temperature dependence for the two species. The rate of hydrogen activation is higher at lower sample temperature, whereas deuterium activation slows down as the temperature is lowered. The dramatically different behavior observed in these experiments originates from the different extent of quantum tunneling for H₂ and D₂. In both cases our calculations indicate that

tunneling is relevant. KMC simulations indicate that in the case of H₂, the contribution from tunneling is so significant that the effective barrier is reduced to the point that H₂ uptake becomes dominated by thermodynamic effects. On the contrary, tunneling through the D₂ barrier is not as significant, and the D₂ uptake rate is dictated kinetically by the effective height of the barrier.

3.2 Results and Discussion

H₂ thermal desorption spectra were taken for a range of Pd concentrations deposited on the Cu(111) surface at 380 K as described in the experimental section (Figure 3.1). We have previously shown that the Cu(111) surface is inactive towards hydrogen dissociation and uptake, and that small amounts of Pd alloy into the surface layer of Cu(111) as individual, isolated atoms that can act as entry and exit sites for hydrogen dissociation and recombination, respectively.^{33,34,45} In the present work a range of Pd coverages (0.01 – 5 ML) alloyed into or on the surface layer of Cu(111) were studied. It was determined that in the single atom alloy regime (< 0.1 ML Pd) a single desorption peak is seen that shifts to progressively lower temperature as the Pd coverage increases, due to surface strain.³⁴ At Pd coverages > 0.3 ML H₂ desorption took place over a range of temperatures from 160 K up to 300 K, the upper limit of which is characteristic of desorption from bulk Pd(111).⁴⁶

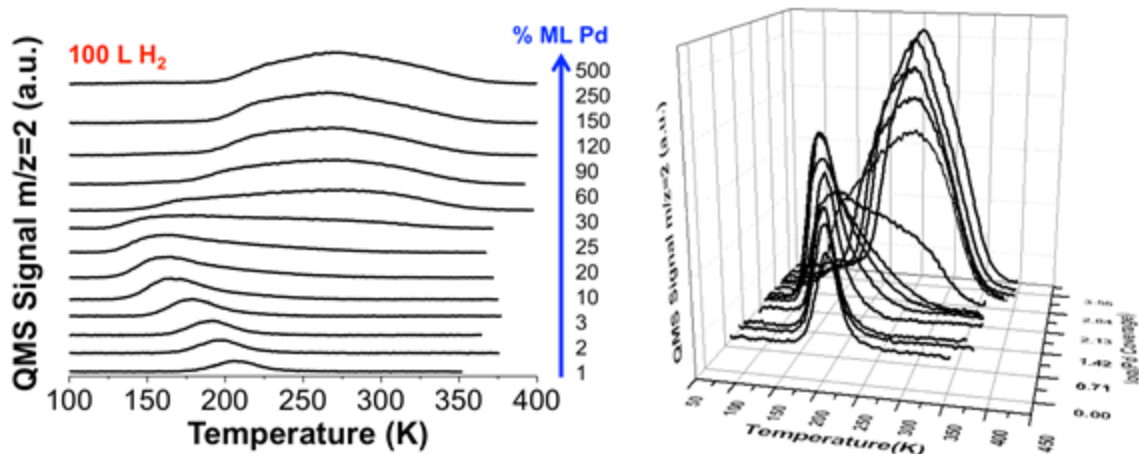


Figure 3.1 Desorption of H₂ from Pd/Cu Alloys. (Left) H₂ thermal desorption spectra from a range of Pd/Cu alloy surfaces acquired by depositing various amounts of Pd onto Cu(111) at 380 K and then dosing 100 L of H₂ at 85 K. (Right) 3D plot of the same data that emphasizes changes in the temperature and width of the hydrogen desorption peaks as a function of Pd coverage.

The H₂-TPD profiles clearly show that at Pd concentrations below 0.1 ML H₂ desorbs from a single site, which is indicated by a single desorption peak. These results are important when considering the use of Pd as a site for hydrogen uptake, dissociation, and spillover of H atoms onto an otherwise inert Cu surface. Ideally, exclusively isolated atoms of Pd must be present to avoid complete hydrogenation or decomposition of the reactants by larger Pd ensembles.³⁴ Figure 3.2 shows a plot of hydrogen uptake as a function of Pd coverage calculated from the H₂-TPD data presented in Figure 3.1.

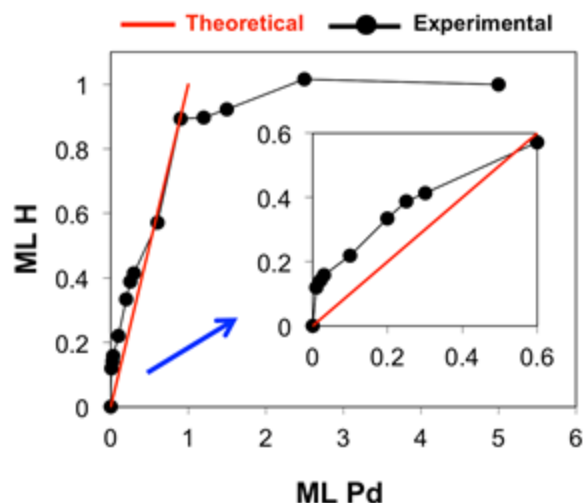


Figure 3.2 Plots of the uptake of H on Pd/Cu alloys as a function of Pd coverage after a 100 L H₂ dose.

The main plot in Figure 3.2 shows that H saturation is not reached until > 2 ML of Pd is deposited on Cu(111). This is due to second layer island formation before the first layer is complete as seen in the STM images in Figure 3.3. While at a glance H uptake appears to be linear with Pd coverage, at Pd coverages < 1 ML, inspection of the inset in Figure 3.2 indicates that the H uptake is higher than the amount of Pd in the surface. This provides strong evidence for H atom spillover onto the Cu(111) surface as under these conditions Cu(111) is completely inactive for H₂ activation. An increase in hydrogen uptake with increasing Pd concentration is due to an increased number of entry sites for hydrogen dissociation and spillover onto Cu(111). Figure 3.3 depicts STM images of a range of Pd coverages on Cu(111).

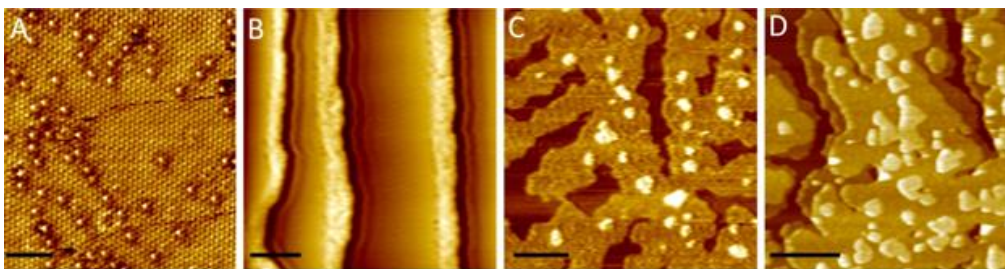


Figure 3.3 STM images of Pd/Cu alloys with a range of stoichiometries: (A) 0.01 ML Pd, (B) 0.1 ML Pd, (C) 1 ML Pd and (D) 2 ML Pd. Scale bars (A) 2 nm (B) 10 nm (C) 20 nm (D) 50 nm. Imaging conditions 0.05 – 0.15 V, 0.1-1.0 nA. Pd/Cu alloys were formed at 380 K.

At low Pd coverages, Pd is present in the form of individual, isolated atoms substituted into the Cu surface layer as can be seen in Figure 3.3A. The larger scale image in Figure 3.3B shows that the alloying site is the ascending step edges. Only at Pd coverages ~ 0.5 ML and greater are Pd islands observed on the surface as seen in Figures 3.3 C,D. It is obvious from these images that second and third layers grow before the first Pd ML is complete. These complex alloy surface structures, which consist of a mix of isolated Pd atoms, larger ensembles and continuous Pd islands lead to the broad H_2 desorption features observed in Figure 3.1.

Despite the TPD results, clearly showing that H_2 can be facily activated at 85 K by a 0.01 ML Pd/Cu(111) alloy, a number of theoretical and experimental studies have been unable to explain this occurrence.⁴¹⁻⁴⁴ Ramos et al. found a barrier of 0.25 eV for H_2 activation on the alloy surface using DFT and this was confirmed by a molecular beam study by Farías et al..^{41,44} These barriers are too high to allow for activation at 85 K as seen in our experiments. DFT Studies by Fu et al. confirmed the barrier of ~ 0.25 eV who hypothesized the discrepancy

between experimental results and theory was due to the presence of subsurface Pd atoms in contact with the surface Pd atom.^{42,43} However, STM studies show that under the conditions used to form the alloy Pd primarily exists in the surface layer,^{47,48} and furthermore other DFT predicts that Pd is more likely to exist as isolated species in a Cu lattice.^{33,49} To elucidate these discrepancies between our results and the expected barrier, we performed temperature dependent uptakes of both hydrogen and deuterium on the alloy surface.

The uptakes of hydrogen and deuterium on single atom alloy Pd/Cu surfaces as a function of temperature were obtained using TPD experiments, as shown in Figure 3.4A and B. The measurements were performed on the 0.01 ML Pd/Cu(111) alloy surface, which consists of 1% Pd in the form of individual, isolated Pd atoms substituted into the Cu(111) lattice.³³⁻³⁵ The surface was exposed to either hydrogen or deuterium at a selected sample temperature in the range of 75-193 K. The sample was subsequently warmed or cooled to 83 K, followed by the thermal desorption measurement. The 75 – 193 K temperature range reflects: (i) the minimum temperature to which our sample could be cooled; and (ii) the maximum temperature we could heat the sample to without desorption of gaseous hydrogen or deuterium. It is immediately clear that the uptakes of the two isotopes on the 0.01 ML Pd/Cu(111) surface are very different. Critically, the uptake of hydrogen *decreases* when the temperature is raised while deuterium's uptake *increases* at higher sample temperature. Isotope effects that lead to different rates of H *versus* D reactions are common, however, the completely opposite behavior observed here as a function of temperature is exceptional.

Figure 3.4C shows a natural log plot of the two uptake curves shown in Figures 3.4A and B as a function of inverse temperature. These plots were used to extract the apparent activation energy for the dissociative adsorption process. In the case of deuterium, the apparent activation energy was found to be 0.045 ± 0.005 eV and for hydrogen it was -0.023 ± 0.005 eV. The small negative apparent activation barrier of hydrogen on 0.01 ML Pd/Cu(111) suggests that the dissociation process involves more than a single step. Typically, negative apparent activation barriers in Arrhenius plots are indicative of the presence of a precursor state^{27,50,51}, however, we will show later in our analysis that it relates to the thermodynamics of H uptake.

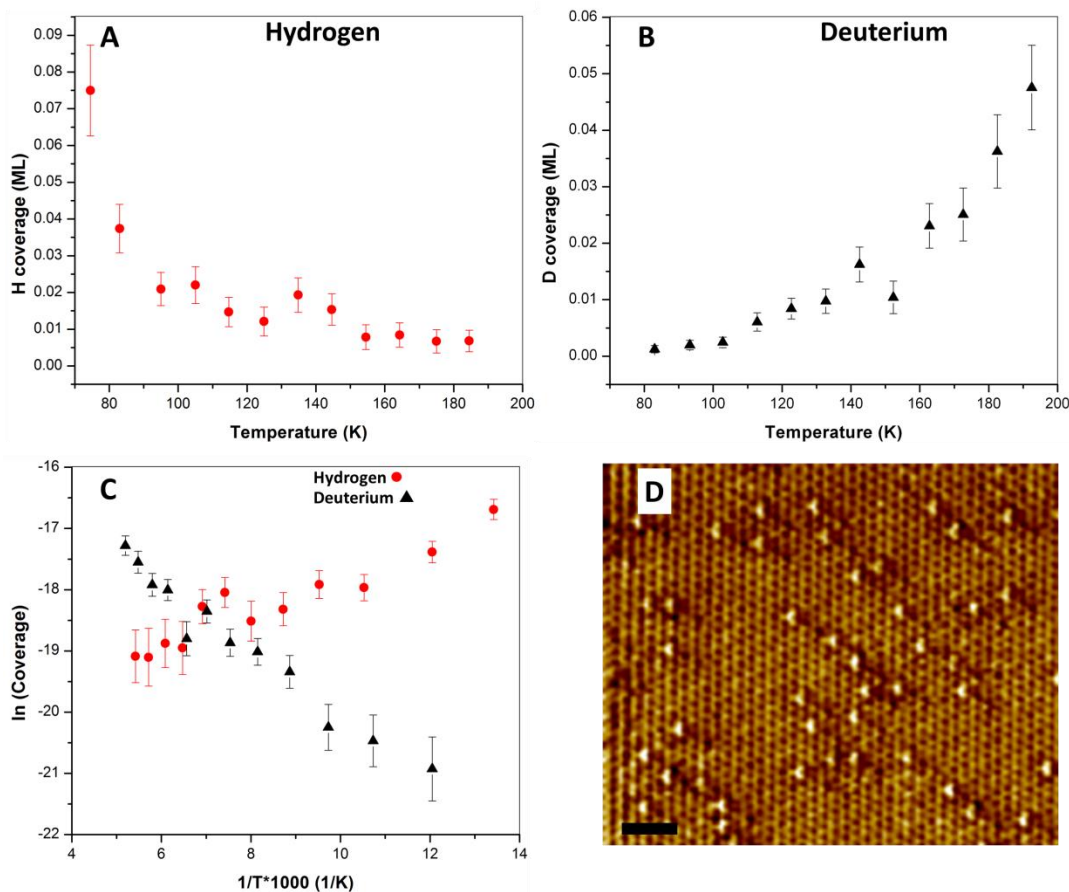


Figure 3.4 The uptake of hydrogen and deuterium on 0.01 ML Pd/Cu(111). (a) Uptake of hydrogen atoms on the alloy surface after an exposure of 5 L of molecular hydrogen at different temperatures. (b) Uptake of deuterium atoms on the alloy surface after an exposure of 200 L of molecular deuterium at different sample temperatures. The exposures of H₂/D₂ (5 L/200 L) were chosen to yield comparable surface coverages over the temperature range examined. (c) Arrhenius plots for the data shown in (a) and (b). Circles represent hydrogen data points and triangles are deuterium data points. (d) STM image of the 0.01 ML Pd/Cu(111) alloy, showing the single atom sites. Scanning conditions: I = 0.04 nA, V = 0.08 V, Scale Bar = 1 nm.

To elucidate the underlying mechanism and differences of the H₂/D₂ dissociation process on Pd/Cu(111) we performed DFT calculations for the process. The specific exchange-correlation functional used was the optB88-vdW functional⁵², which accounts for van der Waals (vdW) dispersion forces within the non-local vdW-DF scheme.⁵³ Full details of the computational setup are given in

the theoretical methods section. The classical DFT potential energy barrier for H₂ dissociation was calculated on a Cu(111)-(3x3) surface with a single Pd atom substitution (Figure 3.5A). Along the minimum energy pathway of H₂ dissociation, a weak physisorption well was identified, with H₂ found 1.9 Å above Pd. Starting from this physisorbed state (with a binding energy of about -0.1 eV relative to a H₂ molecule in the gas phase), the H—H bond dissociation occurs above the Pd atom with an energy barrier of 0.46 eV. The barrier obtained here with the optB88-vdW functional is slightly higher than that obtained in previous DFT calculations using a standard generalized gradient approximation functional and both barriers are much too high to account for the experimental observations.⁴¹

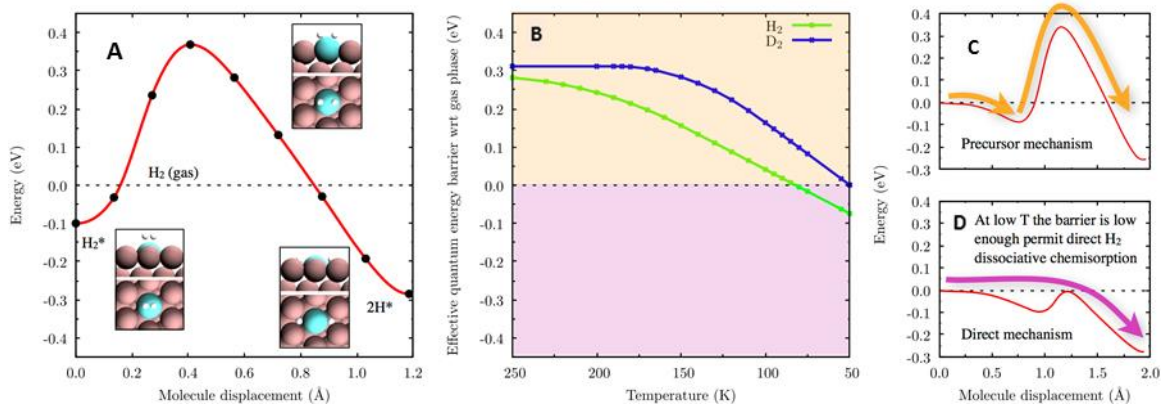


Figure 3.5 Quantum effects on the H₂ activation barrier. (a) Potential energy surface for H₂ dissociation from the physisorbed precursor state on the Pd/Cu(111) substrate. The total energy of the clean surface and the H₂ in the gas phase is used as the energy zero. Insets are top and side views of initial physisorbed precursor state (H₂*), transition state (TS), and final state (2H*). White, brown, and cyan spheres indicate H, Cu, and Pd atoms, respectively. (b) Temperature dependence of the effective quantum energy barrier (relative to the gas phase) obtained from harmonic quantum transition state theory calculations that take into account tunneling through the chemisorption barrier and zero point energies. It can be seen that below the quantum crossover temperature (260 K for H₂, 190 K for D₂) the effective energy barrier decreases as the temperature is lowered. The orange/pink regions of the graph correspond to two different mechanisms for chemisorption below 80 K for H₂ or 50 K for D₂. These two routes to chemisorption are the precursor-mediated process (c), or below 80 K for H₂ (50 K for D₂) a direct chemisorption for H₂ incident on a Pd site (d).

Bearing in mind that the computed DFT barrier is too high to account for the facile activation of H₂ below 100 K, as observed in experiments, we now consider how quantum nuclear effects may alter our physical picture of the dissociation process. The simplest and traditional first step is to consider how zero point energy (ZPE) will alter the energetics of the process. When we consider the effect of ZPE corrections, we do indeed find that they lower the energy barrier to dissociation. However, the reduction is small and the barriers remain too high at 0.37 eV for H₂ and 0.39 eV for D₂, as compared to the experimentally observed apparent barriers (-0.023 eV and 0.045 eV for H₂ and D₂, respectively). This

indicates that the experimental results cannot be explained through a simple consideration of the ZPE effect and that instead quantum mechanical tunneling is likely to play an important role in this process.

To account for quantum tunneling effects in this system, we have used two path integral based approaches. Specifically most calculations reported were obtained with harmonic quantum transition state theory (HQTST) (otherwise known as instanton theory)⁵⁴ although the more sophisticated ab initio path integral molecular dynamics (AIPIMD)^{55,56} approach was also used. The HQTST method is an efficient path-integral based approach that includes quantum tunneling by considering the spread of a “necklace” of beads over the top of the dissociation barrier. The beads are connected by mass and temperature-dependent springs, such that the classical limit (with all beads contracted to a single point) is recovered at high temperature and/or high mass. As the temperature is lowered, these springs weaken and the beads sample lower energy states on either side of the classical saddle point, resulting in a lowering of the quantum energy barrier due to tunneling through the classical potential. The HQTST calculations were performed on an analytical one-dimensional potential constructed to resemble our DFT energy profile for dissociative adsorption (Figure 3.5A). Figure 3.5B shows some of the key results of the HQTST calculations wherein the effective dissociation barriers for both H₂ and D₂ are plotted as a function of temperature. It can be seen that below the quantum-classical crossover temperature (which is the temperature below which classical and quantum mechanics diverge – in this system 260 K for H₂, 190 K for D₂), the effective quantum energy barrier

decreases as the temperature is lowered. A lower barrier will result in more facile chemisorption of H₂ from the physisorbed state following the precursor mechanism shown in Figure 3.5C. At 80 K (50 K) the effective quantum barrier for H₂ (D₂) to dissociatively chemisorb reaches zero (relative to H₂ or D₂ in the gas phase). This indicates that below these temperatures an incident molecule at a Pd site could undergo barrierless dissociation if, prior to doing so, it does not get trapped in the physisorbed state, as illustrated schematically in Figure 3.5D.

The HQTST calculations reveal that it is mainly tunneling that leads to the substantial reductions in the effective quantum dissociation barriers. To test this conclusion we performed a separate set of AIPIMD simulations in which the quantum delocalization of the breaking H₂ bond was examined at various points along the classical dissociation pathway. In AIPIMD the forces on the atoms are computed “on the fly” and it does not rely on a pre-determined potential energy surface. A snapshot from an 85 K AIPIMD simulation with the centre of mass of the H₂ fixed at the classical saddle point is shown in Figure 3.6. Clearly there is a large spread of the path integral beads associated with the two hydrogen atoms. Delocalization of the beads along the dissociation reaction coordinate is a signature for quantum tunneling through the potential barrier. The extent of the delocalization observed in the AIPIMD simulations is similar to the spreading observed in the HQTST calculations at the same temperature (See Supporting Information (SI) online for reference 57).

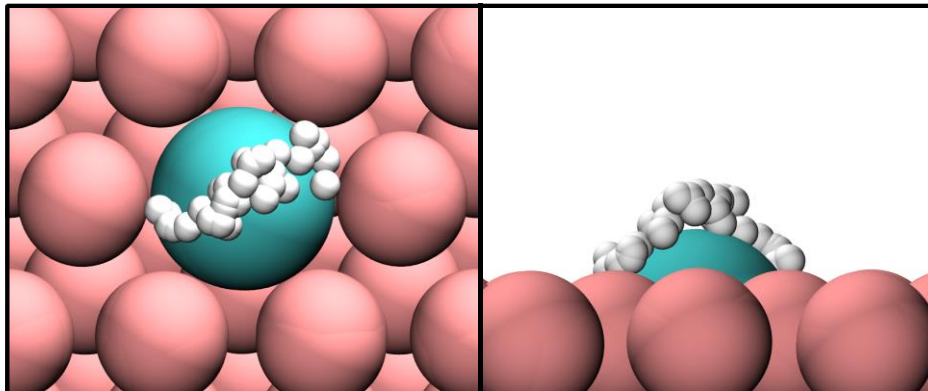


Figure 3.6 Top and side view snapshots taken from an 85 K ab initio path integral molecular dynamics simulation of a single H₂ at the classical saddle point for dissociative chemisorption on the Pd/Cu(111) surface. In this simulation each H atom is represented by 16 path integral replicas (“beads”). The large spread of the beads along the dissociation reaction coordinate indicates that at this temperature the H₂ molecule can tunnel through the dissociation barrier.

The path integral based DFT calculations reveal significant tunneling through the dissociation barrier at experimentally relevant temperatures, with a greater extent of tunneling for H₂ *versus* D₂ dissociation. To gain further insight into the experimentally observed differences in the H₂/D₂ uptake we performed a series of KMC simulations, making use of the data and insight gained from the various DFT calculations. With no adjustments to the DFT-derived parameters (energetics and reaction pre-factors), these simulations predict no quantifiable uptake of H (D) adatoms for the two cases that employ: (a) a DFT-derived (classical) activation energy barrier; and (b) a temperature-dependent quantum tunneling barrier obtained *via* the HQTST simulations. Therefore, to capture the experimentally-observed trends, systematic adjustments to the model parameters were performed until a reasonable agreement between the experimentally measured and model predicted surface coverages was reached. These adjustments were small (0.20 eV or less) and were within the typical error bars associated with

DFT calculations of processes at surfaces.⁵⁸ A more detailed account of these adjustments can be found in the supporting information to reference 57. In particular we found that the coverages predicted by our KMC simulations are very sensitive to the binding energy of H₂ (D₂) on the Pd sites. Perturbations as small as 0.005 eV (stabilization) of H₂ (D₂) can cause the surface coverages to increase by as much as 20% from their original values, thereby indicating that the binding strength of the precursor state plays a critical role in the overall reaction. Accordingly, the correct treatment of the weak interaction of H₂/D₂ with the metal surface is highly desirable for the detailed understanding of the phenomena studied here.^{59,60}

Figure 3.7 shows the results from the KMC simulations for H₂/D₂ uptake, plotted against the experimental observations. The surface coverage of H (D) adatoms is found to decrease (increase) monotonically with an increase in temperature, consistent with the experimental trends. Our KMC results suggest that these opposite trends for the surface coverages of H/D adatoms with increasing temperature are due to the fact that H₂ dissociation is *thermodynamically controlled*, while D₂ dissociation is *kinetically controlled* over the entire temperature regime.

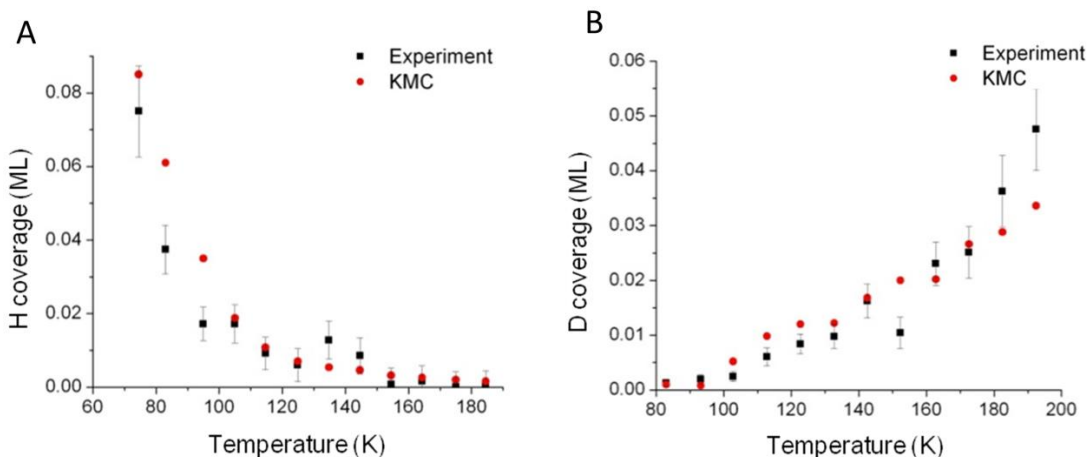


Figure 3.7 KMC simulations results for (a) H₂ uptake and (b) D₂ uptake, and their comparison with the experimentally measured values. For parameter values used to obtain these results, see the SI in reference 57.

In the case of H₂, our KMC simulations indicate that the decreasing trend of H adatom surface coverage with temperature is dictated by the thermodynamics, and not by the kinetics, of H₂ dissociation at surface Pd sites. In other words, the temperature-dependent activation energy barrier for this step is too small under all experimental conditions for it to be of great kinetic relevance, and the H surface coverage is governed by the thermodynamic driving force, *i.e.*, the reaction free energy of this step. Since this is an exothermic step, an increase in temperature is expected to disfavor H₂ dissociation. In particular, the reaction free energy of this elementary step increases with an increase in temperature, which results in a monotonically decreasing equilibrium constant. The decreasing H surface coverage, and hence the negative apparent activation energy barrier, is a direct consequence of this phenomenon.

Contrary to the H₂ case just described, the monotonically increasing trend in D adatom surface coverage is due to the fact that D₂ dissociation is kinetically

controlled. The temperature-dependent activation energy barrier for D_2 dissociation at surface Pd sites (SI reference 57) is large enough to ensure that it is the kinetically relevant rate controlling step over the entire temperature regime. Consequently, the D surface coverage is governed by the kinetics of this elementary step, thereby resulting in a monotonically increasing surface coverage with increasing temperature. In order to quantify this, we obtained the overall rate of D_2 dissociation from our model (total number of D_2 dissociation events, as obtained from our KMC model: ' E_{net} '). Plotting the natural log of E_{net} against $1/T$, (where T = temperature (K)), yields the apparent activation energy barrier of the overall reaction, as shown in Figure 3.8. This apparent activation energy barrier, as obtained from this analysis, is 0.032 eV, consistent with its experimental value (0.045 ± 0.005 eV).

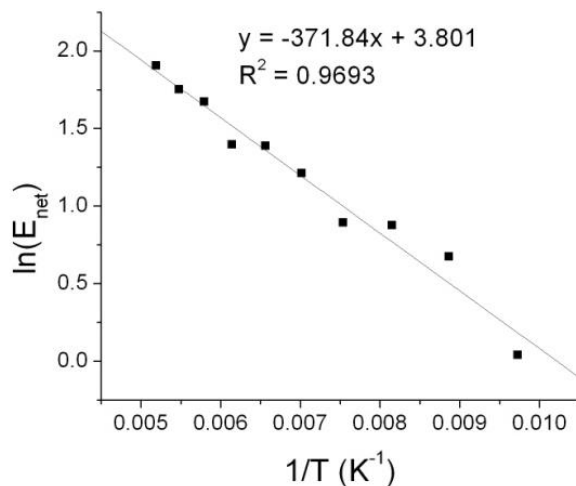


Figure 3.8 Determination of apparent activation energy barrier for KMC simulations of D_2 uptake. The logarithm of total number of D_2 dissociation events (E_{net}) is plotted against the inverse temperature. The apparent activation energy barrier, as calculated from the slope of the best-fit line, is 0.032 eV, consistent with the experimentally-determined value of 0.045 ± 0.005 eV.

The results of our KMC simulations suggest that both H₂ and D₂ dissociation proceed through the same reaction pathway. The dissociation of H₂ (D₂) to give surface H(D) adatoms occurs exclusively over Pd sites; for the temperature range employed in our experiments, no dissociation is observed over Cu sites because of the prohibitively high activation energy barrier. The KMC simulations suggest that H₂ (D₂) must land directly on or adjacent to surface Pd atoms, as the precursor states in the vicinity of Cu atoms are extremely short-lived and prefer to desorb at all temperatures rather than diffuse across the surface to a Pd site. This was verified by reducing the rate constants for H₂ (D₂) diffusion steps by several orders of magnitude from the calculated values and observing that the final results were essentially independent of the diffusion rates.

Finally, we note that our calculations indicate that dissociation can occur through two distinct processes, each due to the combination of van der Waals interactions and quantum tunneling. The first process involves the trapping of H₂ in the physisorbed state, which acts as a precursor to the dissociative chemisorption process (Figure. 3.5A and sketched in Figure. 3.5C). The second mechanism may become possible at very low temperatures when quantum effects are so pronounced that the effective chemisorption barrier drops below the gas phase H₂ energy zero (sketched in Figure 3.5D). Our HQTST calculations predict that this can happen at less than ~80 K for H₂ and less than ~50 K for D₂. This direct dissociation process occurs at lower temperatures than we have been able to probe in the current TPD experiments but it is an intriguing implication of the calculations that we hope to examine in future studies. More generally, the results

of this study suggest a novel approach for inducing selective reactions or isotope separations that utilize the vastly different rates of bond cleavage involving hydrogen and deuterium. For example, many important surface-catalyzed reactions involve C-H or O-H bond cleavage.⁶¹⁻⁶⁴ If the C or O atom remains at the same surface site before and after the bond breaks and most of the motion is of the light H atom, similar temperature-dependent activation barriers may occur and novel ways to control bond breaking developed.

3.3 Conclusion

We have shown experimentally that single atoms of Pd in a Cu(111) lattices are capable of facile activation of H₂ at 85 K, and allow for the spillover of H atoms to Cu. Furthermore we show that the dissociation of H₂ and D₂ molecules at single Pd atom surface sites in a Pd/Cu alloy occur at vastly different rates and with opposite trends as a function of sample temperature. Traditional DFT-based methods for modeling dissociation barriers are inadequate for explaining these results. Our experimental observations motivated us to take a theoretical approach using path integral based DFT simulations that account for the role of quantum nuclear effects in H₂/D₂ dissociation, coupled with KMC to model the dissociation rates over the relevant range of temperatures. Our theoretical data reveal that the dissociation barriers are strongly temperature-dependent and that H₂/D₂ dissociation is dictated by totally different thermodynamic/kinetic parameters. Within our theoretical framework, we see a positive slope in Arrhenius plots for H₂ uptake, which originates from temperature-dependent quantum tunneling aided by a precursor state, and a

negative slope for D₂ which can be explained by a scheme in which thermally assisted barrier crossing dominates tunneling and the effect of the precursor state. The breaking of chemical bonds involving H atoms is ubiquitous in nature, and our results provide a unique insight into the highly temperature-dependent quantum effects that dictate these rates. We also hope to apply this refined theoretical approach to other light-atom systems in order to search for regimes where important chemistry may become more controllable once quantum effects are fully understood and quantified.

3.4 Experimental Methods

3.4.1 TPD and STM Measurements

TPD measurements were performed using the instrument described in Chapter 2. The Cu(111) crystal could be resistively heated to 775 K and cooled to 73 K. Normally the crystal could only be cooled to 83 K with liquid nitrogen, but lower temperatures were reached by bubbling helium gas through the cryogenic dewar. The image in Figure 3.4D was acquired using the LT-STM described in Chapter 2. Pd coverages were calibrated using both AES and TPD of CO. Hydrogen 99.999% (AirGas) and Deuterium (99.999%) (AirGas) were used in this study. Hydrogen coverage calculations were based on a saturation coverage of unity when hydrogen was adsorbed on a 5 monolayer (ML) Pd film, assuming that the film terminates as Pd(111).

STM images in Figure 3.3 were acquired at 29 K with an Omicron NanoTechnology variable-temperature scanning tunneling microscope housed in

an ultrahigh vacuum chamber. A Cu(111) single crystal from Monocrystals Co. was prepared in a preparation chamber by Ar⁺ sputtering (1.5 keV, 25 μ A) and annealing (1000 K) cycles. Pd was deposited onto the surface by resistively heating a Pd wrapped W wire for different lengths of time while the surface was held at 380 K. Once the deposition was complete, the sample was transferred in vacuum to the microscope chamber where it was placed into the LHe-cooled STM stage in < 10 min. The microscope chamber operated at a base pressure of < 5 x 10⁻¹¹ mbar to ensure sample cleanliness. Scanning conditions for Pd on Cu(111) were voltages between -0.1 V and 0.1 V and currents < 2.1 nA. All biases refer to the sample voltage. Images were acquired with either Omicron or Bruker etched W tips.

3.4.2 Theoretical

Calculations of the classical barrier and pathway for H₂/D₂ dissociation were performed using the VASP code⁶⁵ with projector augmented wave (PAW) potentials.⁶⁶ Van der Waals dispersion forces were accounted for through the optB88-vdW functional,⁵² which accounts for dispersion forces within the non-local vdW-DF scheme⁵³ and has been implemented in VASP by Klimes *et al.*⁶⁷ The electronic states were expanded using plane waves with an energy cutoff of 600 eV. The Pd/Cu(111) surface was modeled by a five-layer slab with a (3 \times 3) surface unit cell with a Cu atom at the top layer substituted by a Pd atom. A vacuum layer equivalent of six atomic layers was used. The Brillouin zone was sampled using a (8 \times 8 \times 1) k-point mesh based on the Monkhorst-Pack scheme.⁶⁸ The two bottom-most Cu(111) layers were fixed during relaxation. All structures

were fully relaxed until the Hellmann-Feynman forces acting on the atoms were smaller than 0.01 eV/Å. The climbing image nudged elastic band (CI-NEB) method⁶⁹ was used to calculate the classical H₂/D₂ activation energy barrier. ZPE corrections to the classical barrier were obtained simply by taking the difference between the sum of real-valued harmonic vibrational frequencies at the transition state and at the physisorbed (initial) state.

Quantum tunneling effects were accounted for using two path integral based approaches. Most results reported have been obtained from the harmonic quantum transition state theory method (also known as instanton) on an analytic potential fitted to the underlying DFT potential energy surface. Specifically fitted to a DFT potential energy surface in which the atoms in the substrate were fixed at the positions they adopt prior to H₂ dissociation. Fixing the surface in this manner is an approximation but it also gives a sensible reaction coordinate as quantum effects frequently result in corner-cutting of the classical minimum energy path during reactions. Here the fixed surface results in a chemisorption barrier of 468 meV, only 6 meV higher than the barrier obtained when the surface is allowed to fully relax during the dissociation process. We used 200 beads in our instanton calculations, which were converged by comparing to 100 and 500 bead test calculations. AIPIMD simulations were also performed using 16 imaginary time-slices (known as beads) propagated by Langevin dynamics at 85 K and forces computed on-the-fly using DFT. For efficiency reasons we used a slightly less expensive computational set-up than the barrier height calculations above, in particular a three-layer slab was used with the bottom layer fixed, and the

Brillouin zone was sampled with a (4×4×1) k-point mesh. These reduced settings result in a classical chemisorption barrier of 465 meV, which is a very good representation of the fully converged system.

The kmos⁷⁰ framework was used for the implementation of Kinetic Monte Carlo (KMC) simulations. From a given state of the system, the KMC algorithm determines the probability of all possible transitions to other states according to the user-defined rates of all available elementary reaction steps. A reaction step is then chosen in accordance with this probability distribution, and the system assumes the new state determined by that reaction step. The simulation has no memory; that is, the probability of undergoing a particular transition is determined only by the current state of the system and not by any prior configuration. The simulation time step after each transition is selected randomly from a Poisson distribution with a mean that equals the sum of the rates of all available transitions from the original state. Simulations are allowed to proceed until the desired simulation time is reached (50 s for H₂, 200 s for D₂, same as the dosing times in the experiments).

The code input comprises the lattice structure, binding energies and minimum energy configurations of all the species involved in the reaction mechanism, activation energy barriers and pre-exponential factors for all elementary steps, simulation time, and the reaction temperature and pressure. All simulations were performed on a Pd/Cu catalytic surface represented as a lattice in which all types of atop (Pd, Cu) and three-fold hollow (Pd/Cu, Cu) sites were explicitly taken into account (see Figure S2 in SI in reference 57). In particular,

the lattice structure was represented by a 20x20 Cu(111) grid with periodic boundary conditions. 1% of the surface Cu atoms were randomly substituted by Pd atoms with the restriction that they could not be nearest neighbors. This is in agreement with studies that have shown that Pd atoms disperse in the surface layer of Cu(111)⁷¹ and that the most stable configurations for alloys with low Pd content (and coverages below $X_{\text{Pd}} = 0.4$) are those where the surface Pd atoms are surrounded by Cu atoms³³. This is also consistent with STM observations reported in past experimental studies.^{48,72} H_2 (D_2) molecular precursors were only allowed to adsorb atop surface atoms, while H (D) adatoms occupied only hollow sites, consistent with our DFT calculations indicating that adsorption of H adatoms is ~ 0.4 eV more stable on the hollow sites than the atop sites. Our DFT calculations show that adsorption of H (D) adatoms is thermodynamically favorable in up to three hollow sites around a single metal surface atom. Adsorption of a fourth, fifth, or sixth H (D) adatom around a metal surface atom is energetically unfavorable, with substantially weaker binding compared to that on other surface sites. The KMC simulations therefore allowed adsorption in up to three hollow sites around each metal surface atom. Simulations were performed at similar conditions as experiments: the surface coverage of H (D) was recorded after dosing with 10^{-10} atm H_2 for 50 s (10^{-9} atm D_2 for 200 s) at fixed temperatures in the range 75 K – 195 K. Each KMC simulation was performed a total of 25 times to obtain an average value of final surface coverage for each experimental condition being simulated.

All the model parameters, with the exception of sticking coefficients for H₂ (D₂), were rigorously derived from our DFT calculations. The sticking coefficients for the H₂(D₂) adsorption steps were assumed to be 1. The enthalpy estimates for the surface species and transition states were obtained by correcting the electronic energies, as obtained from our DFT calculations, for zero point energy (ZPE) contributions and temperature variations. The temperature-dependent activation energy barriers for the H₂/D₂ dissociation steps on Pd (Table 1, Step 3) were obtained from the HQTST calculations. For our modeling purposes, these quantum tunneling barriers were approximated to be linear functions of temperature until they reach their classical values, as shown in Figure S3 in the SI of reference 57. The classical activation energy barrier for the H₂ (D₂) dissociation step on Cu (Table S1, Step 4 SI ref 57) was obtained using the CI-NEB method⁶⁹; the barriers for all the surface diffusion steps (Table S1, Step 5-9 SI ref 57) were found to be insensitive parameters for the KMC simulations and were fixed at 0.12 eV, in agreement with our earlier studies.⁷³ The entropy values were directly calculated from the vibrational frequencies of the respective states, and the pre-exponential factors were calculated from entropy differences between the initial and transition states of the respective elementary steps. The rate constants for reactions involving bond-formation or bond-scission were calculated using transition state theory; collision theory was employed to calculate the rate constants for the adsorption-desorption steps.^{74,75}

3.5 References

- (1) Graetz, J. *Chem. Soc. Rev.* **2009**, 38, 73–82.

- (2) Armbrüster, M.; Kovnir, K.; Friedrich, M.; Teschner, D.; Wowsnick, G.; Hahne, M.; Gille, P.; Szentmiklósi, L.; Feuerbacher, M.; Heggen, M.; Girgsdies, F.; Rosenthal, D.; Schlögl, R.; Grin, Y. *Nat. Mater.* **2012**, *11*, 690–693.
- (3) Eliaz, N.; Eliezer, D.; Olson, D. L. *Mater. Sci. Eng. A* **2000**, *289*, 41–53.
- (4) Shegai, T.; Johansson, P.; Langhammer, C.; Käll, M. *Nano Lett.* **2012**, *12*, 2464–2469.
- (5) Sakintuna, B.; Lamari-Darkrim, F.; Hirscher, M. *Int. J. Hydrogen Energy* **2007**, *32*, 1121–1140.
- (6) Le Bourlot, J.; Le Petit, F.; Pinto, C.; Roueff, E.; Roy, F. *Astron. Astrophys.* **2012**, *541*, A76.
- (7) McMahon, R. J. *Science* **2003**, *299*, 833–834.
- (8) Masgrau, L.; Roujeinikova, A.; Johannissen, L. O.; Hothi, P.; Basran, J.; Ranaghan, K. E.; Mulholland, a J.; Sutcliffe, M. J.; Scrutton, N. S.; Leys, D. *Science* **2006**, *312*, 237–241.
- (9) Schreiner, P. R.; Reisenauer, H. P.; Ley, D.; Gerbig, D.; Wu, C.-H.; Allen, W. D. *Science* **2011**, *332*, 1300–1303.
- (10) Chen, B.; Dingerdissen, U.; Krauter, J. G. E.; Lansink Rotgerink, H. G. J.; Möbus, K.; Ostgard, D. J.; Panster, P.; Riermeier, T. H.; Seebald, S.; Tacke, T.; Trauthwein, H. *Appl. Catal. A Gen.* **2005**, *280*, 17–46.
- (11) Bettens, F. L.; Bettens, R. P. A.; Brown, R. D.; Godfrey, P. D. *J. Am. Chem. Soc.* **2000**, *122*, 5856–5860.
- (12) Pan, M.; Brush, A. J.; Pozun, Z. D.; Ham, H. C.; Yu, W.-Y.; Henkelman, G.; Hwang, G. S.; Mullins, C. B. *Chem. Soc. Rev.* **2013**, *42*, 5002–5013.
- (13) Hayden, B. E.; Hodgson, A. *J. Phys. Condens. Matter* **1999**, *11*, 8397–8415.
- (14) Mcintosh, E. M.; Wikfeldt, K. T.; Ellis, J.; Michaelides, A.; Allison, W. *J. Phys. Chem. Lett.* **2013**, *4*, 1565–1569.
- (15) Waluyo, I.; Ren, Y.; Trenary, M. *J. Phys. Chem. Lett.* **2013**, *4*, 3779–3786.
- (16) Dharmadhikari, C.; Gomer, R. *Surf. Sci.* **1984**, *143*, 223–242.
- (17) Jardine, A. P.; Lee, E. Y. M.; Ward, D. J.; Alexandrowicz, G.; Hedgeland, H.; Allison, W.; Ellis, J.; Pollak, E. *Phys. Rev. Lett.* **2010**, *105*, 136101.
- (18) Lee, A.; Zhu, X. D.; Deng, L.; Linke, U. *Phys. Rev. B* **1992**, *46*, 15472–15476.

- (19) Wong, A.; Lee, A.; Zhu, X. D. *Phys. Rev. B* **1995**, *51*, 4418–4425.
- (20) Wang, X.; Fei, Y. Y.; Zhu, X. D. *Chem. Phys. Lett.* **2009**, *481*, 58–61.
- (21) Lauhon, L. J.; Ho, W. *Phys. Rev. Lett.* **2000**, *85*, 4566–4569.
- (22) Kua, J.; Lauhon, L. J.; Ho, W.; Goddard, W. A. *J. Chem. Phys.* **2001**, *115*, 5620–5624.
- (23) Heinrich, A. J.; Lutz, C. P.; Gupta, J. A.; Eigler, D. M. *Science (80-.)*. **2002**, *298*, 1381–1387.
- (24) Jewell, A. D.; Peng, G.; Mattera, M. F. G.; Lewis, E. A.; Murphy, C. J.; Kyriakou, G.; Mavrikakis, M.; Sykes, E. C. H. *ACS Nano* **2012**, *6*, 10115–10121.
- (25) Okuyama, H.; Siga, W.; Takagi, N.; Nishijima, M.; Aruga, T. *Surf. Sci.* **1998**, *401*, 344–354.
- (26) Groß, A. *J. Chem. Phys.* **1999**, *110*, 8696–8702.
- (27) Hakanoglu, C.; Hawkins, J. M.; Asthagiri, A.; Weaver, J. F. *J. Phys. Chem. C* **2010**, *114*, 11485–11497.
- (28) Muto, H.; Matsuura, K.; Nunome, K. *J. Phys. Chem.* **1992**, *96*, 5211–5213.
- (29) Berger, H. F.; Leisch, M.; Winkler, A.; Rendulic, K. D. *Chem. Phys. Lett.* **1990**, *175*, 425–428.
- (30) Sundell, P. G.; Wahnström, G. *Surf. Sci.* **2005**, *593*, 102–109.
- (31) Sundell, P. G.; Wahnström, G. *Phys. Rev. B* **2004**, *70*, 81403.
- (32) Lee, A.; Zhu, X. D.; Wong, A.; Deng, L.; Linke, U. *Phys. Rev. B* **1993**, *48*, 11256–11259.
- (33) Tierney, H. L.; Baber, A. E.; Kitchin, J. R.; Sykes, E. C. H. *Phys. Rev. Lett.* **2009**, *103*, 246102.
- (34) Kyriakou, G.; Boucher, M. B.; Jewell, A. D.; Lewis, E. A.; Lawton, T. J.; Baber, A. E.; Tierney, H. L.; Flytzani-Stephanopoulos, M.; Sykes, E. C. H. *Science* **2012**, *335*, 1209–1212.
- (35) Marcinkowski, M. D.; Jewell, A. D.; Stamatakis, M.; Boucher, M. B.; Lewis, E. A.; Murphy, C. J.; Kyriakou, G.; Sykes, E. C. H. *Nat. Mater.* **2013**, *12*, 523–528.
- (36) Guzzi, L. *J. Catal.* **1999**, *182*, 456–462.
- (37) Aristizábal, A.; Contreras, S.; Barrabés, N.; Llorca, J.; Tichit, D.; Medina, F. *Appl. Catal. B Environ.* **2011**, *110*, 58–70.

- (38) Trawczyński, J.; Gheek, P.; Okal, J.; Zawadzki, M.; Gomez, M. J. I. *Appl. Catal. A Gen.* **2011**, *409–410*, 39–47.
- (39) Zheng, R.; Porosoff, M. D.; Weiner, J. L.; Lu, S.; Zhu, Y.; Chen, J. G. *Appl. Catal. A Gen.* **2012**, *419–420*, 126–132.
- (40) Coq, B.; Figueras, F. *J. Mol. Catal. A Chem.* **2001**, *173*, 117–134.
- (41) Ramos, M.; Martínez, a. E.; Busnengo, H. F. *Phys. Chem. Chem. Phys.* **2012**, *14*, 303.
- (42) Fu, Q.; Luo, Y. *J. Phys. Chem. C* **2013**, *117*, 14618–14624.
- (43) Fu, Q.; Luo, Y. *ACS Catal.* **2013**, No. 111, 1245–1252.
- (44) Farías, D.; Minniti, M.; Al Taleb, A.; Miranda, R. *Zeitschrift für Phys. Chemie* **2013**, *227*, 1491–1500.
- (45) Baber, A. E.; Tierney, H. L.; Lawton, T. J.; Sykes, E. C. H. *ChemCatChem* **2011**, *3*, 607–614.
- (46) Gdowski, G. E.; Felter, T. E.; Stulen, R. H. *Surf. Sci.* **1987**, *181*, L147–L155.
- (47) Tierney, H. L.; Baber, A. E.; Sykes, E. C. H. *J. Phys. Chem. C* **2009**, *113*, 7246–7250.
- (48) Aaen, A. B.; Lægsgaard, E.; Ruban, A. V.; Stensgaard, I. *Surf. Sci.* **1998**, *408*, 43–56.
- (49) Christensen, A.; Ruban, A.; Stoltze, P.; Jacobsen, K.; Skriver, H.; Nørskov, J. K.; Besenbacher, F. *Phys. Rev. B* **1997**, *56*, 5822–5834.
- (50) Ertl, G.; Lee, S. B.; Weiss, M. *Surf. Sci.* **1982**, *114*, 515–526.
- (51) Mortensen, J. J.; Hansen, L. B.; Hammer, B.; Nørskov, J. K. *J. Catal.* **1999**, *182*, 479–488.
- (52) Klimeš, J.; Bowler, D. R.; Michaelides, A. *J. Phys. Condens. Matter* **2010**, *22*, 22201.
- (53) Dion, M.; Rydberg, H.; Schröder, E.; Langreth, D. C.; Lundqvist, B. I. *Phys. Rev. Lett.* **2004**, *92*, 246401.
- (54) Andersson, S.; Nyman, G.; Arnaldsson, A.; Manthe, U. *J. Phys. Chem. A* **2009**, *113*, 4468–4478.
- (55) Marx, D.; Parrinello, M. *Z. Phys. B* **1994**, *95*, 143–144.
- (56) Marx, D.; Parrinello, M. *J. Chem. Phys.* **1996**, *104*, 4077.
- (57) Kyriakou, G.; Davidson, E. R. M.; Peng, G.; Roling, L. T.; Singh, S.;

- Boucher, M. B.; Marcinkowski, M. D.; Mavrikakis, M.; Michaelides, A.; Sykes, E. C. H. *ACS Nano* **2014**, *8*, 4827–4835.
- (58) Klimeš, J.; Michaelides, A. *J. Chem. Phys.* **2012**, *137*, 120901.
- (59) Groot, I. M. N.; Kleyn, A. W.; Juurlink, L. B. F. *Angew. Chemie - Int. Ed.* **2011**, *50*, 5174–5177.
- (60) Shan, J.; Kleyn, A. W.; Juurlink, L. B. F. *Chem. Phys. Lett.* **2009**, *474*, 107–111.
- (61) Michaelides, A.; Hu, P. *J. Chem. Phys.* **2001**, *114*, 5792–5795.
- (62) Michaelides, A.; Hu, P. *J. Am. Chem. Soc.* **2000**, *122*, 9866–9867.
- (63) Tiwari, A. K.; Nave, S.; Jackson, B. *Phys. Rev. Lett.* **2009**, *103*, 18–21.
- (64) Jiang, B.; Xie, D.; Guo, H. *Chem. Sci.* **2012**, 503–508.
- (65) Kresse, G.; Furthmüller, J. *Phys. Rev. B* **1996**, *54*, 11169–11186.
- (66) Kresse, G.; Joubert, D. *Phys. Rev. B* **1999**, *59*, 1758–1775.
- (67) Klimeš, J.; Bowler, D. R.; Michaelides, A. *Phys. Rev. B - Condens. Matter Mater. Phys.* **2011**, *83*, 195131.
- (68) Monkhorst, H. J.; Pack, J. D. *Phys. Rev. B* **1977**, *16*, 5188–5192.
- (69) Henkelman, G.; Uberuaga, B. P.; Jónsson, H. *J. Chem. Phys.* **2000**, *113*, 9901–9904.
- (70) Hoffmann, M. J.; Matera, S.; Reuter, K. *Comput. Phys. Commun.* **2014**, *185*, 2138–2150.
- (71) Ruban, A. V.; Skriver, H. L. *Comput. Mater. Sci.* **1999**, *15*, 119–143.
- (72) Bellisario, D. O.; Han, J. W.; Tierney, H. L.; Baber, A. E.; Sholl, D. S.; Sykes, E. C. H. *J. Phys. Chem. C* **2009**, *113*, 12863–12869.
- (73) Nilekar, A. U.; Greeley, J.; Mavrikakis, M. *Angew. Chemie - Int. Ed.* **2006**, *45*, 7046–7049.
- (74) Cortright, R. D.; Dumesi, J. A. *Adv. Catal.* **2001**, *46*, 161–264.
- (75) Dumesic, J. A.; Rudd, D. F.; Aparicio, L. M.; Rekoske, J. E.; Trevino, A. A. *The Microkinetics of Heterogeneous Catalysis (ACS Professional Reference Book)*; 1993.

Chapter 4: Controlling a Spillover Pathway with the Molecular Cork Effect

This chapter was modified from an original paper published in 2013 by the same title by M. D. Marcinkowski et al. from Nat. Mater., volume 12, pages 523-528.

KMC simulations were performed by Michail Stamatakis from the Department of Chemical Engineering at University College London.

4.1 Introduction

Hydrogen activation, uptake, and reaction are important phenomena in heterogeneous catalysis, fuel cells, hydrogen storage devices, materials processing and sensing.¹⁻¹¹ Much attention has been devoted to materials that exhibit facile activation and weak binding of hydrogen, as these properties lead to the best energy landscape for storage or chemical reactivity.¹²⁻¹⁴ Spillover is a common method by which a reagent can be activated at one location and then reacted at another, and it is commonly invoked to explain the synergistic relationship between metals in an alloy or metal/metal oxide mixtures.^{1,3-7,12,15} For example, in heterogeneous catalysis hydrogen spillover from metal particles to reducible oxide supports is implicated as an important step in a variety of reactions including hydrogenations, hydroisomerizations, and methanol synthesis.^{1,3,6} Hydrogen spillover has also been shown to significantly enhance the performance of hydrogen storage materials such as metal organic frameworks, zeolites and many carbon-based nanostructures.^{2,4-6} In these cases, the addition of small metal particles, typically Pt or Pd, promotes uptake by activating molecular H₂ and facilitating spillover of hydrogen atoms (H_a) onto the support. Despite these

advances, the mechanism of spillover in most systems remains poorly understood, and with the exception of hydrogen bridges¹⁶ in storage systems, methods for mediating the spillover pathway do not exist.

In this paper we describe how the hydrogen spillover pathway on the Pd/Cu alloy system can be controlled via the reversible adsorption of a spectator molecule (CO) at minority Pd atom sites. The use of a model system amenable to study by scanning tunnelling microscopy (STM) was critical in order to monitor the detailed distribution of Pd atoms, H_a and CO molecules, all of which are distributed heterogeneously at the atomic-scale. This information can then be related to temperature programmed desorption/reaction (TPD/R) data, and complex phenomena like spillover, competitive adsorption and storage can be understood.^{12,17–20}

4.2 Results and Discussion

It is well established that at low coverages (typically less than 0.1 monolayers (ML)), Pd atoms in the surface of Cu(111) exist predominantly as individual atoms that are isolated from one another.^{20–23} For this reason we term this particular type of alloy a *single atom alloy* (SAA).¹² Figure 4.1A shows the atomic-scale structure of such a SAA surface formed by depositing 0.01 ML of Pd on Cu(111) at a surface temperature of 380 K. This large scale image reveals that the Pd/Cu alloy is formed at the ascending step edges, leading to a rumpled appearance in the STM image termed a “brim”. As the distance from the step edge increases, the amount of Pd decreases to the point where little Pd is present on much of the Cu terrace. The high resolution inset shows atomic resolution of

the brim in which the Pd atoms appear ~ 20 pm higher than the surrounding Cu atoms and illustrates that they are spatially isolated from one another. We have previously demonstrated that such Pd/Cu SAA surfaces are active for H_2 dissociation.^{12,20} Figure 4.1B depicts H_a on a Cu terrace that originated from the dissociative adsorption of 2 L (L, 10^{-6} torr·s) of H_2 at Pd sites followed by spillover of H_a onto the Cu surface. Due to their lower density of states near the Fermi level, adsorbed hydrogen atoms appear as ~ 10 pm depressions in STM images¹². TPD measurements reveal that in the reverse process, H_2 is released from this surface in a single state centred at 210 K. A representative TPD spectrum is shown in Figure 4.2A that resulted from a 200 L dose of hydrogen on the 1% Pd/Cu alloy surface at 85 K, corresponding to a H_a coverage of 0.2 ML. The desorption mechanism is depicted in the schematic of Figure 4.2A. Individual Pd atoms bind H slightly more strongly, but offer a much lower barrier for dissociation and recombination as compared with Cu.²⁰ Therefore, as the system is heated the lowest energy pathway for hydrogen to escape the surface is via a Pd atom, as dictated by microscopic reversibility.²⁴ In this way the minority 1% Pd atoms act as a low energy entrance and exit routes for hydrogen to adsorb and desorb from the Cu surface. The overall behaviour also suggests that the availability and residence of H_a on the Cu surface may be finely tuned by adjusting the state of these Pd sites. For example, by utilizing a spectator molecule that preferentially occupies the Pd brim, the Pd sites can be selectively blocked.

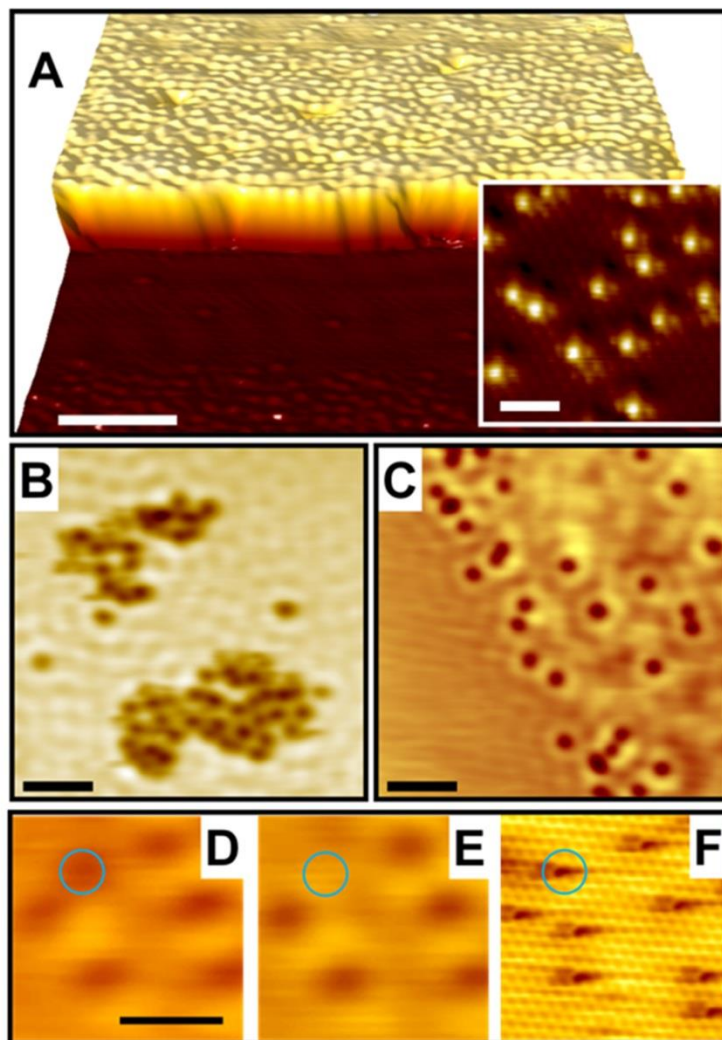


Figure 4.1 Preferred binding sites for hydrogen and CO. **(A)** STM image of a Pd/Cu alloy with 1% Pd atoms in the surface Cu layer. The Pd/Cu alloy forms preferentially at the ascending step edge as evidenced by the ruffled appearance of the brim, whereas the lower terrace is composed of pure Cu. Scale bar = 10 nm. Inset shows atomic resolution of isolated Pd atoms in the Cu(111) surface. Scale bar = 1 nm **(B)** Adsorbed hydrogen atoms appear as depressions and cluster into islands on the Cu terraces. Scale bar = 4 nm. **(C)** Small amounts of deposited CO molecules appear as individual depressions and bind preferentially to the Pd sites in the alloy brim, which covers the upper right hand side of the STM image. Scale bar = 7 nm. **(D, E)** Same area before and after a single CO molecule (depression highlighted with blue circle) was removed with a 4.8 V pulse from STM tip. **(F)** Atomic resolution image of the same region after all the CO molecules were removed showing that individual Pd atoms (appearing as depressions with this STM tip state) are the preferred adsorption sites. Scale bar = 2 nm.

In this regard, CO is an excellent candidate molecule as it adsorbs reversibly on both Cu and Pd surfaces and interacts much more strongly with low index Pd surfaces (500 K desorption) as compared to Cu (170 K desorption).²⁵⁻²⁷ The STM image shown in Figure 4.1C was obtained after exposing the 0.01 ML Pd/Cu SAA surface to a small amount (0.03 L = 0.003 ML) of CO at 5 K followed by annealing the sample to 60 K. Figure 4.1C reveals that the adsorbed CO molecules also appear in STM images as depressions with an apparent depth of ~15 pm. Depositing a very small amount of CO and subsequently annealing the sample below CO's desorption temperature resulted in the migration of the CO exclusively to the 1% atomic Pd sites in the brim (upper right side of image) indicating that at equilibrium Pd sites are preferred. To support this conclusion we performed molecular manipulation experiments in which, using voltage pulses (4.8 V) delivered by the STM tip, CO molecules were desorbed one-by-one. We then interrogated the nature of the surface sites beneath with atomic resolution. Figure 4.1D-F shows an example in which an individual CO molecule was removed from its preferred adsorption site prior to the area being completely cleared of CO and imaged with atomic resolution (see the Appendix Figure 1 for the complete experimental sequence). These experiments reveal an exact correlation between CO adsorption site and individual Pd atoms in the surface beneath and show that one CO molecule is adsorbed above each Pd atom in the surface. When the Cu/Pd SAA surface was exposed to 0.01 ML of CO at 150 K followed by 200 L of H₂ at 85 K, the only desorption product observed was CO, in a peak centred at 270 K (Figure 4.2B). CO desorption at 270 K is intermediate

between desorption from Cu(111) and Pd(111), consistent with CO adsorbed at atomic Pd sites.²⁵⁻²⁷ Note that the small exposure of CO ensures that the Pd brim is occupied by CO while the Cu terraces remain essentially CO free. Our quantitative TPD experiments allow us to titrate just enough CO to cover the 1% Pd sites but leave the Cu surface bare as shown in Appendix Figures 2 and 3. The absence of H₂ desorption indicates that, despite the availability of clean Cu sites for accommodating H_a, the Pd sites are blocked by CO molecules, which inhibit the dissociation of H₂ and the spillover of H_a. Similar active site blocking/poisoning effects for surface step edges have been reported in the literature.¹⁷⁻¹⁹ When the order of CO and H₂ exposures was reversed, such that 200 L of H₂ followed by 0.01 ML of CO were deposited, a more significant effect occurs. As shown in Figure 4.2C, the H₂ desorption peak is observed but is shifted 50 K higher in temperature to 260 K and is 20 K narrower than in the absence of CO.

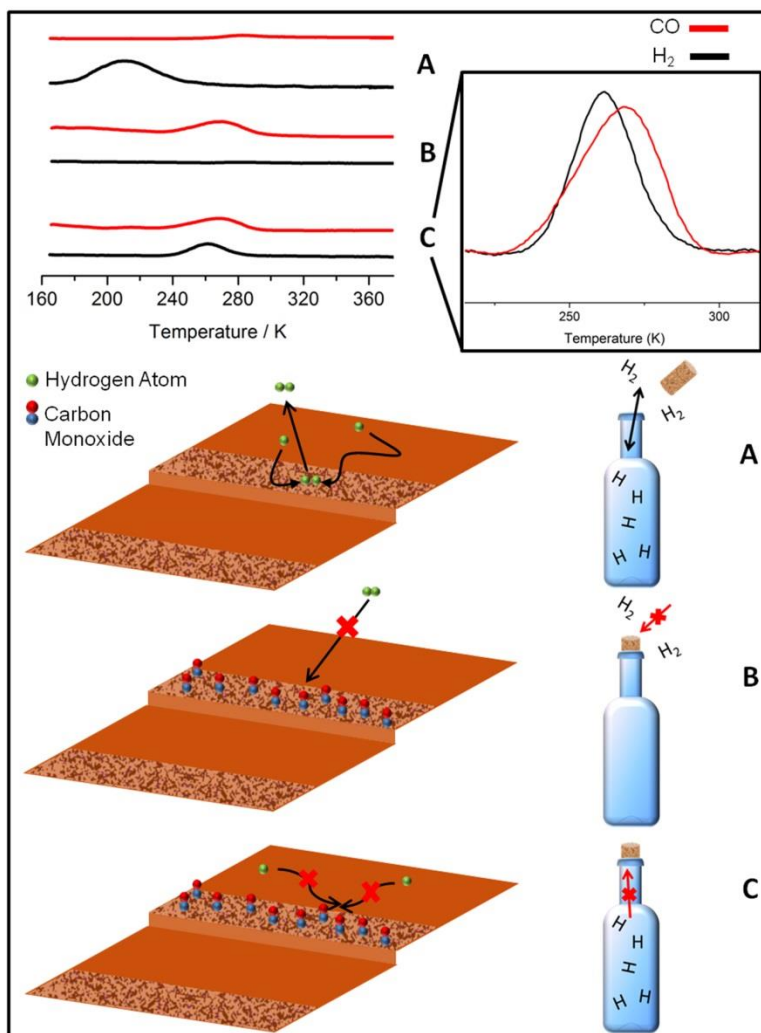


Figure 4.2 The molecular cork effect. Temperature programmed desorption spectra (A) In the absence of CO, hydrogen desorption occurs from the 1% Pd/Cu surface at 210 K. (B) Pre-dosing CO inhibits the uptake of hydrogen. (C) Deposition of CO after hydrogen uptake leads to higher temperature (260 K) hydrogen desorption. The inset shows that the low temperature tail of the CO desorption trace extends down to 230 K at which point H₂ begins desorbing. Schematics A-C illustrate CO's effect on either blocking hydrogen uptake or trapping adsorbed hydrogen on the surface above its regular desorption temperature.

This result indicates that CO adsorption at the minority 1% Pd sites blocks the re-association and desorption of H₂ at 210 K, the temperature at which H₂ would normally desorb. The inset of the spectrum in Figure 4.2C reveals that the desorption of H₂ begins as soon as the first CO desorbs. Moreover, the desorption

of H_2 also occurs over a smaller temperature range as H_a is trapped on the surface above its normal desorption temperature in a higher energy state. These points will be discussed in detail in terms of our simulations. The schematics in Figure 4.2 illustrate this new phenomenon that we term a “molecular cork” effect. H_a spills onto the Cu terraces filling the “bottle” via a Pd atom “bottleneck”. The bottle is then “corked” by adsorption of CO, preventing hydrogen from leaving until it is “uncorked” by CO desorption. If the cork is put in place prior to H_2 exposure, it is impossible for H_2 to get through the bottleneck, and no uptake is observed. In this way uptake on the whole surface can be turned on and off by the molecular cork at a minority (1%) site, and most importantly, hydrogen can be trapped on the surface above its normal desorption temperature. Corking and poisoning are not the same; poisoning is a stoichiometric effect in which the active sites of a catalyst are blocked one by one, whereas in the cork effect, blocking a minority site affects the reactant coverage of the whole surface. We show that the cork effect enables control of a catalytically important spillover pathway between two metals by selective molecular adsorption at atomic sites.^{17–}
¹⁹ CO adsorption enables hydrogen to be stored on the surface beyond its normal desorption temperature as shown in the isothermal experiments in Appendix Figure 4.

In terms of the interaction of CO with Pd/Cu alloy sites, both experimental and density functional theory (DFT) work indicate that CO interacts strongly with Pd atoms in the surface layer of bimetallic Pd/Cu systems.^{25–28} The trend in the adsorption states/energies as a function of Pd concentration predicts that CO binds

preferentially to higher coordinated Pd sites i.e. sites with more than one Pd atom. If the concentration of Pd is very small, as in our system, the CO is predicted to bind to sites atop the individual Pd atoms.²⁶⁻²⁸ This is consistent with one CO molecule being adsorbed at each Pd atom as confirmed by our STM molecular manipulation experiments. We hypothesize that the binding of CO to Pd in these SAAs electronically alters the Pd atoms, thus increasing the dissociation/recombination barrier and forcing H_a to adsorb/desorb only in the absence of CO.²⁶⁻²⁸

To support the experimental observations, we modelled the system using the kinetic Monte Carlo (KMC) method (see the Supplementary Information from reference 29). The simulations of the TPD spectra shown in Figure 4.3 are in excellent agreement with experiments, and are able to capture both the shift of the H₂ peak centre to higher temperatures as well as the narrower peak width in the corked system (Figure 4.3A and B). In an ensemble of 25 such KMC simulations, the average desorption temperature for the uncorked system was calculated to be ~211 K and a similar simulation scheme for the corked system yielded an average H₂ peak temperature of 246 K.

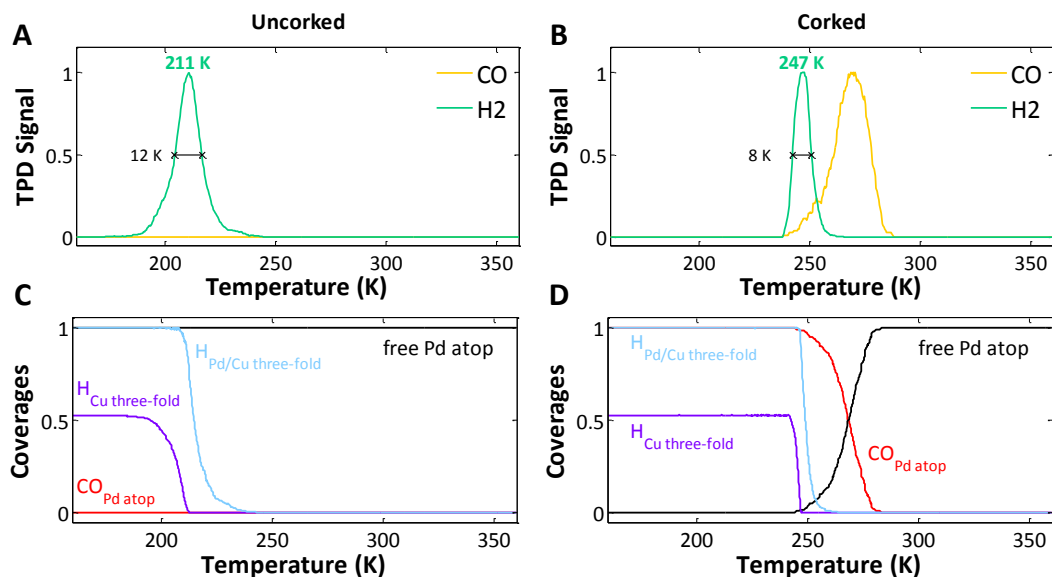


Figure 4.3 Kinetic Monte Carlo simulations of the molecular cork effect. Temperature programmed desorption spectra for the uncorked (A) and the corked (B) systems capture both the peak position and shape changes observed experimentally. The H_a and CO coverage profiles for the uncorked (C) and the corked (D) system reveal that hydrogen coverage on the entrance/exit Pd/Cu sites remains high even when the coverage on the Cu sites has dropped significantly.

This molecular cork effect is not limited to CO, as we also observe it during a surface-catalyzed chemical reaction in the absence of CO. We have recently shown that the Pd/Cu SAA is capable of hydrogenating styrene to ethylbenzene.¹² When 0.01 ML of Pd was added to a Cu(111) surface and exposed to 400 L of H_2 at 85 K in the absence of CO, H_2 desorbed in a single state centred at 205 K as shown in Figure 4.4. Exposing the same surface to 400 L of H_2 at 85 K followed by 0.06 ML of styrene (1) at 150 K yields the selective hydrogenation to ethylbenzene (2), during which the H_2 peak is shifted higher in temperature to 260 K. The inset of Figure 4.4 shows the desorption profiles of the hydrogenation product ethylbenzene and some un-reacted styrene. These results reveal that the presence of the reactants and products of a chemical reaction can themselves cork the atomic Pd sites in the same way as CO. Even a small amount

of styrene (0.01 ML) corks a 1% Pd/Cu alloy surface (Appendix Figure 5). Interestingly, as the cork effect produces trapped H_a , it may serve to increase the product yield in the hydrogenation reaction by keeping H_a on the surface at higher temperatures and allowing further hydrogenation to occur than if the reaction terminated at 205 K when the H_2 left the surface. A modest shift of ~ 50 K in the H_2 desorption temperature is predicted to have a large effect on conversion to products given that the rates of activated reactions increase rapidly with temperature. However, it is not possible to compare the reactivity of “uncorked” and “corked” H_a because the reactants themselves act as a cork.

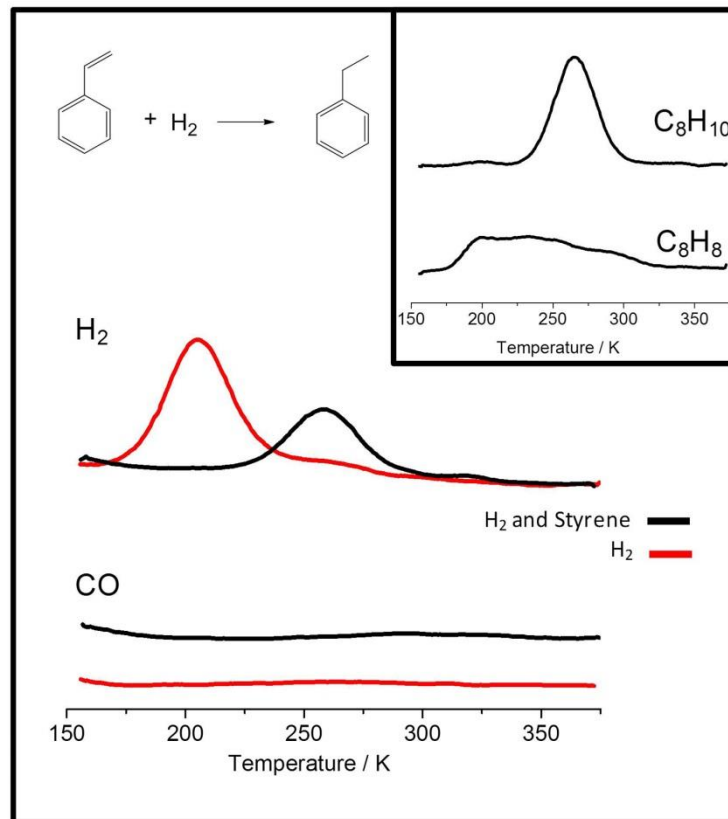


Figure 4.4 The molecular cork effect in a hydrogenation reaction. Temperature programmed reaction spectra reveal that during the hydrogenation of styrene to ethylbenzene, surface hydrogen remains on the surface 55 K hotter than when no styrene is present. Desorption traces indicate that this cork effect occurs in the absence of CO, and therefore the reactants/products themselves act as a molecular cork trapping adsorbed hydrogen atoms on the surface in a higher energy state.

While we have used a model system to illustrate the molecular cork effect in hydrogen dissociation and spillover between different regions of a Pd/Cu surface, we expect that this effect should be somewhat general for any heterogeneous system with a similar energetic landscape. Species other than CO should act as molecular corks and allow spillover between sites to be controlled. Many promising hydrogen storage materials require extremes of pressure or temperature to charge/discharge efficiently^{2,4-6,16}, and unwanted hydrogen release at ambient temperatures is often a problem.² We suggest that rather than altering

the storage material or the pressure of the container vessel, a chemical approach involving treatment with small amounts of a molecular cork molecule could be used to retard hydrogen desorption and enable long-term storage under ambient conditions. This is a reasonable proposal given that many systems that operate via spillover from small metal particles exhibit lower uptake/release barriers, reversible adsorption/desorption isotherms and even memory of sequential doses of H₂ and D₂ isotopes during discharge.^{5,16} In terms of catalysis, while weak binding is desirable for efficient, low temperature operation, processes with higher barriers to reaction cannot proceed as hydrogen is not stable on the surface at higher temperatures.¹³ The molecular cork effect serves to retain weakly bound, trapped H_a on the surface at higher temperature in a potentially more reactive form.³⁰ Given that the rates of chemical reactions increase rapidly with temperature, trapping H_a on the surface ~50 K beyond its desorption temperature should have a significant impact on conversion to products. This approach opens up interesting possibilities to activate reactions with higher barriers utilizing this new non-equilibrium state of surface-bound hydrogen.

4.3 Conclusion

In summary, we show that the spillover process, and hence the coverage of the entire surface, can be controlled via molecular adsorption at minority (1%) sites in a reversible manner. This is very different to the traditional picture of most interfacial processes, which involve uniform adsorption, reaction, and desorption of molecules. We show that CO adsorption can be used to block the hydrogen desorption channel, leading to a buildup of 2D pressure and the

eventual fast release of the hydrogen at higher temperatures: a phenomenon we term the “molecular cork” effect. This non-equilibrium process produces trapped, higher energy hydrogen atoms, which are potentially more reactive than regular surface bound hydrogen. We also suggest that the molecular cork effect could offer a new method for mediating the kinetics of hydrogen uptake and release from storage materials that rely on spillover from small metal particles.

4.4 Experimental Methods

4.4.1 TPD and STM Measurements

The two ultra-high vacuum instruments described in chapter 2 were used to perform the TPD and STM experiments. In the TPD chamber, Hydrogen 99.999% (AirGas) was deposited on to the sample by means of a 6 mm diameter collimator tube pointed directly at the sample. Hydrogen coverage calculations were based on a saturation coverage of unity when hydrogen was adsorbed on a 4 monolayer (ML) Pd film, assuming that the film terminates as Pd(111). CO and styrene coverages refer to saturation of their respective monolayer TPD peaks.¹² Carbon monoxide 99.99% (AirGas) and high purity styrene 99.9% (Aldrich) were deposited on the sample by backfilling the chamber to the required pressure. Styrene was purified on receipt by many freeze-pump-thaw cycles. Styrene yields were recorded with a heating ramp of 1 K s^{-1} by tracking the parent ion m/z 104. Ethylbenzene yields were recorded by tracking the parent ion at m/z 106 as well as the fragment at m/z 91. The presence of styrene fragments in the desorption profile of ethylbenzene can be subtracted in order to produce the desorption

profile of ethylbenzene. In the present set of TPR measurements, a very low coverage of styrene was utilized (0.06 ML), which made a negligible contribution to the ethylbenzene desorption profile; therefore, spectra subtraction was not performed. The spectrum obtained from m/z 91 is the one shown for ethylbenzene.

CO and hydrogen dosing in the LT-STM was performed through a line-of-sight doser aimed directly at the Cu(111) sample in the STM stage. The STM stage was held at either 80 K or 5 K during dosing, and could be cooled from 80 K to 5 K after dosing for imaging of hydrogen.

4.4.2 Theoretical

For the kinetic simulations, an in-house FORTRAN code implementing the graph-theoretical KMC simulation method was used.³¹ The code input consists of a lattice structure, the binding configurations of the species (along with the corresponding energies), an initial lattice configuration, the reaction mechanism and the simulation conditions. Lattice structure: the Pd/Cu(111) catalytic surface was represented as a triangular lattice with 2163 atop Cu and 237 atop Pd sites. The latter were randomly placed under the restriction that they cannot be neighbours. The three-fold Cu and Pd/Cu sites were also explicitly taken into account. Binding configurations: the simulation accounts for two binding configurations for H adatoms (on the three-fold Cu and Pd/Cu sites) and one for CO molecules (on the atop Pd sites). The binding energies were taken from previous literature and adjusted to match the experiments. Initial configuration: 1600 H adatoms were distributed among the three-fold Cu and

Pd/Cu sites according to Fermi-Dirac statistics at the initial simulation temperature. For the corked system, 237 CO molecules were placed on atop Pd sites covering all such sites. Reaction mechanism: seven reversible elementary processes were taken into account, in particular, (i) CO adsorption/desorption on atop Pd sites; H₂ dissociative adsorption/associative desorption on three-fold Cu sites (ii), on three-fold Pd/Cu sites in the absence of CO (iii) and in the presence thereof (iv), as well as H adatom diffusion between three-fold Cu sites (v), from three-fold Cu to a three-fold Pd/Cu sites (vi), and between three-fold Pd/Cu sites (vii). For each reaction, forward and backward elementary steps were considered (for instance adsorption/desorption), and all reaction energies were calculated from the binding energy data for each species to ensure thermodynamic consistency. Kinetic parameters were evaluated using literature data and adjusted to match the experiments. Hydrogen diffusion was treated as a fast quasi-equilibrated process. Simulation conditions: the initial temperature was 160 K and a temperature ramp of 1.0 K/s was used. Zero partial pressures were assumed for both H₂ and CO in the gas phase. More information on the simulation setup and the calculation of kinetic parameters is presented in section KMC Methodology Details of the Supplementary Information of reference 29.

4.5 References

- (1) Conner, W. C.; Falconer, J. L. *Chem. Rev.* **1995**, *95*, 759–788.
- (2) Graetz, J. *Chem. Soc. Rev.* **2009**, *38*, 73–82.
- (3) Jung, K.-D.; Bell, A. T. *J. Catal.* **2000**, *193*, 207–223.
- (4) Cheng, H.; Chen, L.; Cooper, A. C.; Sha, X.; Pez, G. P. *Energy Environ.*

- Sci.* **2008**, *1*, 338–354.
- (5) Wang, L.; Yang, R. T. *Catal. Rev. Sci. Eng.* **2010**, *52*, 411–461.
 - (6) Prins, R. *Chem. Rev.* **2012**, *112*, 2714–2738.
 - (7) Merte, L. R.; Peng, G.; Bechstein, R.; Rieboldt, F.; Farberow, C. A.; Grabow, L. C.; Kudernatsch, W.; Wendt, S.; Laegsgaard, E.; Mavrikakis, M.; Besenbacher, F. *Science* **2012**, *336*, 889–893.
 - (8) Groß, A. *Surf. Sci.* **2012**, *606*, 690–691.
 - (9) Wei, J.; Ji, H.; Guo, W.; Nevidomskyy, A. H.; Natelson, D. *Nat. Nanotechnol.* **2012**, No. June, 357–362.
 - (10) Eliaz, N.; Eliezer, D.; Olson, D. L. *Mater. Sci. Eng. A* **2000**, *289*, 41–53.
 - (11) Shegai, T.; Johansson, P.; Langhammer, C.; Käll, M. *Nano Lett.* **2012**, *12*, 2464–2469.
 - (12) Kyriakou, G.; Boucher, M. B.; Jewell, A. D.; Lewis, E. A.; Lawton, T. J.; Baber, A. E.; Tierney, H. L.; Flytzani-Stephanopoulos, M.; Sykes, E. C. H. *Science* **2012**, *335*, 1209–1212.
 - (13) Greeley, J.; Mavrikakis, M. *Nat. Mater.* **2004**, *3*, 810–815.
 - (14) Chopra, I. S.; Chaudhuri, S.; Veyan, J. F.; Chabal, Y. J. *Nat. Mater.* **2011**, *10*, 884–889.
 - (15) Wittstock, A.; Zielasek, V.; Biener, J.; Friend, C. M.; Bäumer, M. *Science* **2010**, *327*, 319–322.
 - (16) Li, Y.; Yang, R. T. *J. Am. Chem. Soc.* **2006**, *128*, 8136–8137.
 - (17) Hahn, C.; Shan, J.; Groot, I. M. N.; Kleyn, A. W.; Juurlink, L. B. F. *Catal. Today* **2010**, *154*, 85–91.
 - (18) Vang, R. T.; Honkala, K.; Dahl, S.; Vestergaard, E. K.; Schnadt, J.; Laegsgaard, E.; Clausen, B. S.; Nørskov, J. K.; Besenbacher, F. *Nat. Mater.* **2005**, *4*, 160–162.
 - (19) Gambardella, P.; Šljivančanin, Ž.; Hammer, B.; Blanc, M.; Kuhnke, K.; Kern, K. *Phys. Rev. Lett.* **2001**, *87*, 56103.
 - (20) Tierney, H. L.; Baber, A. E.; Kitchin, J. R.; Sykes, E. C. H. *Phys. Rev. Lett.* **2009**, *103*, 246102.
 - (21) Bellisario, D. O.; Han, J. W.; Tierney, H. L.; Baber, A. E.; Sholl, D. S.; Sykes, E. C. H. *J. Phys. Chem. C* **2009**, *113*, 12863–12869.

- (22) Tierney, H. L.; Baber, A. E.; Sykes, E. C. H. *J. Phys. Chem. C* **2009**, *113*, 7246–7250.
- (23) Aaen, A. B.; Lægsgaard, E.; Ruban, A. V.; Stensgaard, I. *Surf. Sci* **1998**, *408*, 43–56.
- (24) Tolman, R. C. *Proc. Natl. Acad. Sci. U.S.A.* **1925**, *11*, 436–439.
- (25) Hager, T.; Rauscher, H.; Behm, R. J. *Surf. Sci.* **2004**, *558*, 181–194.
- (26) Illas, F.; Lopez, N.; Ricart, J. M.; Clotet, A.; Conesa, J. C.; Fernandez-Garcia, M. *J. Phys. Chem. B* **1998**, *102*, 8017–8023.
- (27) Sakong, S.; Mosch, C.; Groß, A. *Phys. Chem. Chem. Phys.* **2007**, *9*, 2216–2225.
- (28) Lopez, N.; Nørskov, J. K. *Surf. Sci.* **2001**, *477*, 59–75.
- (29) Marcinkowski, M. D.; Jewell, A. D.; Stamatakis, M.; Boucher, M. B.; Lewis, E. A.; Murphy, C. J.; Kyriakou, G.; Sykes, E. C. H. *Nat. Mater.* **2013**, *12*, 523–528.
- (30) Johnson, A. D.; Daley, S. P.; Utz, A. L.; Ceyer, S. T. *Science* **1990**, *257*, 223–225.
- (31) Stamatakis, M.; Vlachos, D. G. *J. Chem. Phys.* **2011**, *134*, 214115.

Chapter 5: Initial Stages of Acetophenone Hydrogenation on a Pd/Cu Single Atom Alloy

5.1 Introduction

Unsaturated alcohols are important precursors for the pharmaceutical and fine chemical industries.¹⁻⁵ However, they are a challenge to produce as the selective due to the difficulty of hydrogenating C=O bonds in unsaturated carbonyls. Thermodynamically, it is easier to hydrogenated a C=C bond over a C=O bond as the enthalpy change is ~35 kJ/mol more negative for the hydrogenation of C=C bond vs a C=O bond.^{4,6,7} Kinetics also usually favor the hydrogenation of the C=C bond.⁴ These factors make it easier to produce the saturated carbonyl rather than the unsaturated alcohol. Typically in order to selectively hydrogenate a C=O bond, kinetic control must be used along with careful selection of the catalyst.^{1,2} Pd, Pt, Ni, and Ru catalysts are commonly used for C=O hydrogenation, although selectivity is often an issue when using these catalysts.^{3,8-11} Recently, modified Cu surfaces and Au have been shown to be effective at hydrogenating C=O bonds in aldehydes.^{1,2,5,7,12}

In this study, we examine the interaction of acetophenone and hydrogen on a 0.01 ML Pd/Cu(111) single atom alloy (SAA) using temperature programmed desorption (TPD) and scanning tunneling microscopy (STM). We have previously demonstrated that small amounts Pd alloy into Cu as single atom sites which congregate at step edges, forming a “brim”.¹³ Acetophenone is the simplest aromatic ketone and is used in the synthesis of a number of pharmaceuticals. Acetophenone is an interesting target for hydrogenation as it

contains a carbonyl group and a phenyl group.¹⁰ On reactive metals such as Pt or Pd this leads to issues with selectivity due to the variety of products that can be formed via full or partial hydrogenation or decomposition of the phenyl ring.¹⁰ The use of a SAA alloy could potentially allow for more selective hydrogenation of C=O bonds due to the availability of Cu binding sites and the ability of H_a to spillover between them.¹⁴⁻¹⁶ These systems have recently been shown to be effective at selective C=C and C≡C bond hydrogenations due to weak binding.¹⁵⁻¹⁸ Unfortunately, in this case we do not observe any of the desired product 1-phenylethanol nor any other hydrogenation products. However, we do observe interactions between hydrogen and acetophenone on the alloy surface that indicate the presence of partially hydrogenated species.

5.2 Results and Discussion

Figure 5.1 shows a series of TPD spectra for various coverages of acetophenone adsorbed onto a Cu(111) surface at 150 K. For coverages up to 1 ML of acetophenone the molecule desorbs intact, exhibiting a single peak with first order kinetics at 275 K. We assign this peak to desorption from the monolayer. It is common for first order peaks to broaden significantly and shift to lower temperature with increasing coverage due to repulsive lateral interactions, especially in the case of aromatic compounds, but the peak position remains between 268-275 K for the range of coverage examined.¹⁹⁻²¹ Previous studies have demonstrated that aromatic carbonyls, including 2,2,2-trifluoroacetophenone, are capable of forming a type of H-bonding interaction between a hydrogen bound to the benzene ring and the carbonyl oxygen.^{22,23}

These interactions may help to stabilize acetophenone on the surface and decrease the influence of repulsive interactions. The acetophenone monolayer eventually saturates and a new peak appears at ~200 K exhibiting zero order kinetics, which does not saturate. We assign this peak to desorption from the multilayer. The appearance of the multilayer is used to calibrate the coverage of acetophenone throughout the remainder of the experiments in this study.

It should be noted that not all acetophenone adsorbed to clean Cu(111) desorbs reversibly. Small amounts of hydrogen desorb at high temperature which is often indicative of the decomposition of adsorbed hydrocarbons (Figure 5.3).^{16,24} In addition, when imaging acetophenone on clean Cu(111) with STM, annealing to 260 K where all acetophenone should desorb does not result in a clean surface (Figure 5.5). Significant amount of species remain at the step edges and small amounts adsorbates exist on the terraces, again indicating decomposition of a fraction of the adsorbed acetophenone.

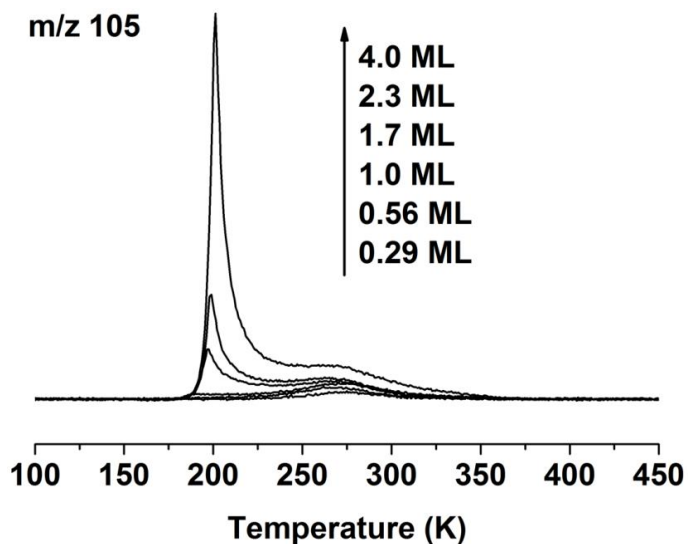


Figure 5.1 Uptake of acetophenone on clean Cu(111). M/z 105 was used to monitor desorption of acetophenone. Reported coverages are based on a peak corresponding to saturation of the monolayer.

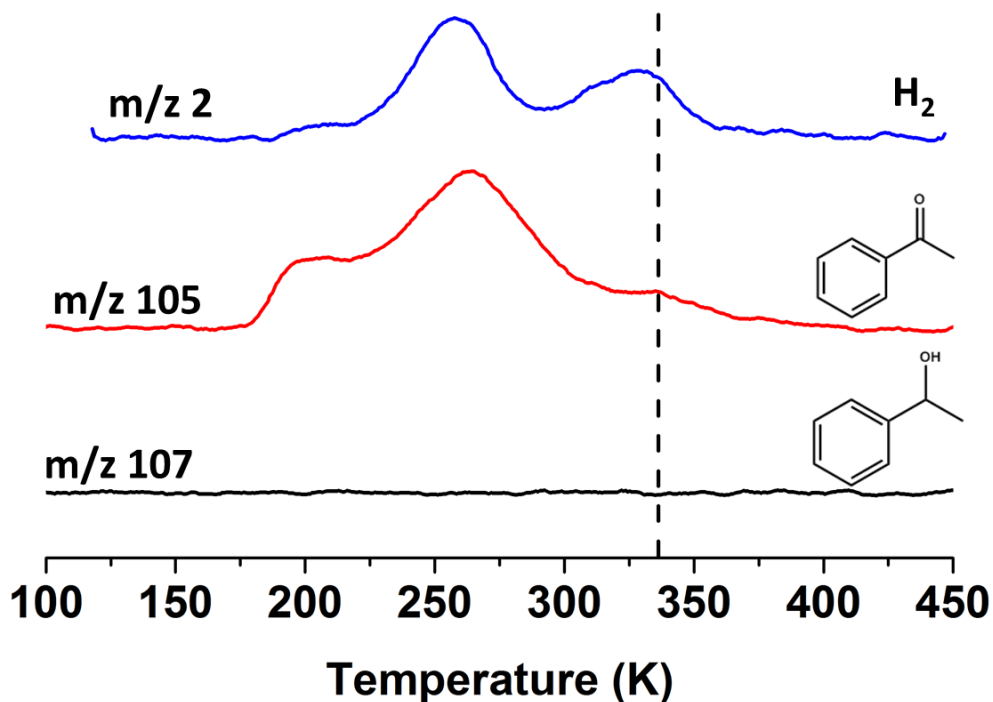


Figure 5.2 Interaction of acetophenone with H on 0.01 ML Pd/Cu(111). TPR resulting from a 0.01 ML Pd/Cu(111) surface where 1.5 ML acetophenone and 0.08 ML H are adsorbed to the surface. Spectra for m/z 2 (H_2), m/z 105 (acetophenone), and m/z 107 (1-phenylethanol) are displayed. No 1-phenylethanol is observed indicating hydrogenation does not occur. Dashed line indicates the presence of unique peaks for acetophenone and H_2 only observed when the two are co-dosed.

Figure 5.2 shows an attempt to hydrogen acetophenone on a 0.01 ML Pd/Cu(111) SAA. As discussed in Chapters 3 and 4 when 0.01 ML of Pd are substituted into the Cu lattice Pd atoms exist as single isolated atoms that are capable of dissociating H₂ and allowing H atoms to spillover to the Cu terraces.^{13,16,17,14,25} A SAA surface was prepared and cooled to 80 K. The surface was exposed to enough H₂ to give a surface coverage of 0.08 ML H, then heated to 150 K at which temperature 1.5 ML of acetophenone was adsorbed to the crystal. 1-phenylethanol, the desired alcohol product, was not observed. In addition to monitoring m/z 107 for the aromatic alcohol, masses were also monitored to track for other hydrogenation and decomposition products including, ethylbenzene, 1-cyclohexylethanol, acetylcyclohexane and ethylcyclohexane, but none of these products were observed. The enol form acetophenone, 1-phenylethenol, was also tracked, but unsurprisingly none was detected.²⁶

On the SAA surface, Acetophenone multilayers and monolayers desorb at 200 K and 268 K respectively, as was the case from the clean Cu(111) surface. However, in the presence of hydrogen on the SAA surface, a new acetophenone desorption peak appears at ~340 K. The area of this peak corresponds to a coverage of ~0.07 ML acetophenone. The appearance of this peak is accompanied by a previously unobserved hydrogen peak desorbing at ~335 K. Hydrogen normally desorbs from clean Cu(111) at ~300 K at high coverage²⁷, 210 K from the Pd/Cu SAA surface^{16,17}, and 260 K from a SAA system coked with CO or styrene.¹⁷ There is one H₂ peak at 260 K when H₂ and acetophenone are co-adsorbed indicating, unsurprisingly, that H atoms are coked by acetophenone

similar to the case of styrene.¹⁷ The peak at 260 K exhibits the expected second order kinetics for hydrogen desorption.²⁷⁻²⁹ The new peak at 335 K is consistent with a low coverage of hydrogen desorbing from a clean Cu(111) surface and corresponds to a coverage of 0.03 ML H_a.^{27,30} This hydrogen peak is too large to simply be attributed to decomposition of acetophenone on Cu as will be shown in Figure 5.3. Interestingly the peak at 335 K exhibits first order kinetics rather than the expected second order.²⁷⁻²⁹ The appearance of new peaks for both hydrogen and acetophenone at roughly the same temperature suggests a stabilizing interaction between the two species on the surface. Mullins and co-workers have observed similar effects in TPD experiments in systems where hydrogen is intermixed with a number of species including water, methanol, acetaldehyde, acetone, and propionaldehyde.^{5,7,12,31,32} In the case of water, they showed in collaboration with DFT studies by Henkelman that a water tetramer and a H atom are stabilized by 0.9 eV when forming (H₂O)₄H⁺ clusters.

To probe this stabilizing interaction between acetophenone and hydrogen we performed a series of experiments probing both the individual species and the co-adsorbed species (Figure 5.3). Acetophenone exposures correspond to ~0.5 ML, and H coverage was set to ~0.08 ML. On clean Cu(111), as previously discussed, sub-monolayer amounts of acetophenone desorb in a single peak at 270 K. Small amounts of hydrogen desorb above 350 K, indicating the decomposition of small amounts of the adsorbed molecule.^{16,24} The amount of hydrogen observed at this temperature corresponds to 0.005 ML, meaning the extent of acetophenone decomposition is very small. Acetophenone on the pure

Pd/Cu SAA behaves similarly to Cu(111) desorbing at 270 K. A slight shoulder on the high temperature side of the acetophenone peak is visible and a small hydrogen peak is seen at 330 K. H₂ is always in the chamber background, making it difficult to keep the SAA surface completely clean of H_a, and the small amount that adsorbs allows for a small amount of the stabilizing interaction between the two species. When hydrogen is adsorbed to the pure SAA surface it desorbs in a single peak exhibiting second order kinetics at ~225 K.^{16,17} Significantly, when the two species are adsorbed together a very distinct acetophenone peak appears at 340 K and a distinct hydrogen peak appears at 330 K. Both exhibit first order kinetics and are significantly higher in temperature than peaks for either of the individually dosed species. On average the ratio of the coverage of acetophenone to the coverage of H_a in these high temperature features roughly 2:1 (2.3±0.01 acetophenones per hydrogen). A likely explanation for the appearance of these new features is the existence of partially hydrogenated species on the surface.^{33,34}

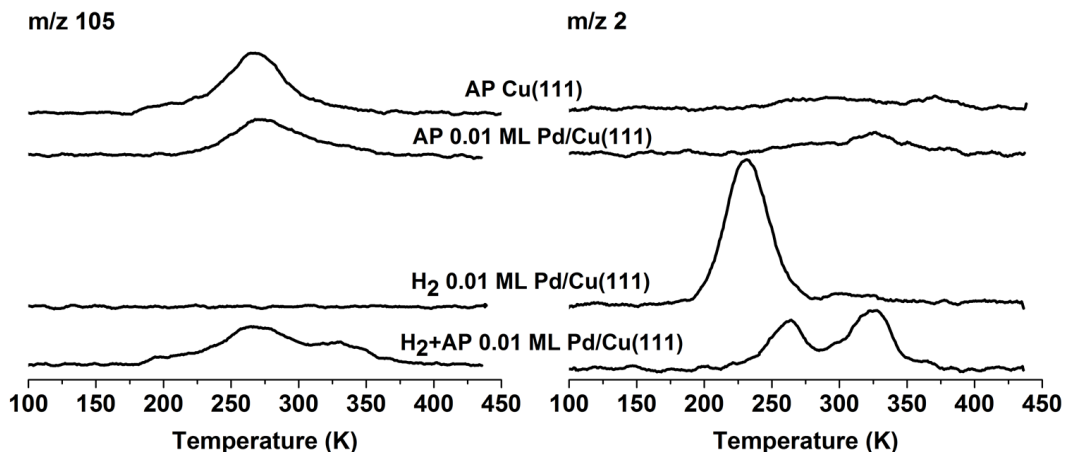


Figure 5.3 The effect of hydrogen on acetophenone. TPD spectra for m/z 105 and m/z 2 (acetophenone and H_2 respectively) for four different surfaces: acetophenone on Cu(111), acetophenone on 0.01 ML Pd/Cu(111), H_a on 0.01 ML Pd/Cu(111) and acetophenone and H_a on 0.01 ML Pd/Cu(111). The initial coverage for acetophenone is ~ 0.5 ML and the initial coverage for hydrogen is ~ 0.08 ML. Acetophenone is abbreviated as AP in the figure.

McBreen and Hammer recently published studies examining the hydrogenation of 2,2,2-trifluoroacetophenone (TFAP) on Pt(111).^{33,34} They found that the interaction of a dimer pair of a partially hydrogenated TFAP with an intact TFAP molecule stabilized the species on the surface by 0.227 eV compared to a dimer of two TFAP molecules.³⁴ This stabilized complex forms a hydrogen bond between the alcohol group of the partially hydrogenated TFAP and the carboxyl group of the intact TFAP. Our TPD results examining pure acetophenone on the SAA suggest a similar situation is occurring. This would explain the first order desorption observed for the hydrogen desorbing at 335 K, as the rate limiting step to desorption of both hydrogen and acetophenone would be the decomposition of the partially hydrogenated species. In addition the formation of such a complex would explain the 2:1 ratio of acetophenone to hydrogen desorbing at ~ 340 K. In addition, DFT studies by Mullins and

Henkelman showed that ketones could easily be partially hydrogenated on a Au(111) surface, but were more likely to decompose back to the starting ketone rather than hydrogenate fully to an alcohol.⁵ A similar situation could occur on Cu(111). Therefore, we performed low-temperature STM experiments to probe for the formation of a partially hydrogenated intermediate in our system.

At a coverage of ~0.50 ML on a surface annealed up to 120 K, acetophenone forms small clusters on the Cu terrace sites (Figure 5.4A). According to TPD results all adsorbed acetophenone should remain on the surface at this temperature. Pentamers are the primary type of cluster formed, but there are also significant amounts of trimers, tetramers, and hexamers. The clustering of acetophenone indicates an attractive interaction similar to that observed in studies of TFAP.^{22,23,33,34} Acetophenone saturates step edges on Cu(111) surfaces (Figure 5.4B) as well as the brim formed by Pd atoms near the step edges of the SAA (Figure 5.4C). Acetophenone on Pd brims is randomly packed, and does not form the distinct cluster shapes observed on the Cu(111) terraces. After an anneal to 120 K there is no visible difference in the acetophenone clusters between a surface with only adsorbed acetophenone and a surface containing both acetophenone and hydrogen, indicating the formation of a partially hydrogenated species is an activated process as H_a is very mobile at these temperatures.

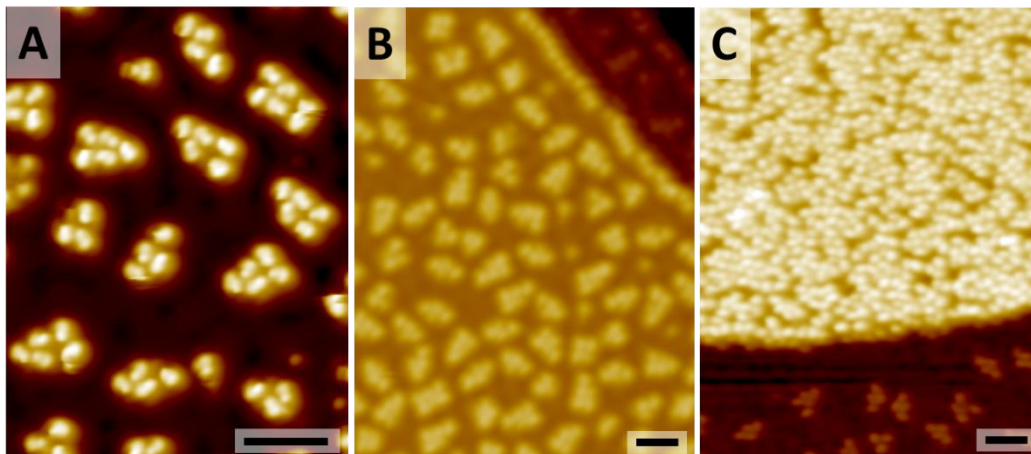


Figure 5.4 STM images of acetophenone annealed up to 120 K on Cu(111) and Pd/Cu(111) surfaces. (A) High-resolution image of acetophenone clusters on Cu(111). (B) Wide-scale image of acetophenone on terraces and steps on Cu(111). (C) Acetophenone on a H_a pre-covered 0.01 ML Pd/Cu(111) surface. The upper portion of the image contains a large Pd brim. Scale bars are all 3nm.

Annealing the surfaces seen in Figure 5.4 to 260 K and above results in significant changes to the molecular assemblies (Figure 5.5). This temperature is hot enough to remove acetophenone or H_a from either clean Cu(111) or Pd/Cu(111), but is under the temperature necessary to begin desorbing the acetophenone and H_a observed at ~ 340 K in the TPD spectra. On Cu(111) and on the SAA, annealing to 260 K results in mostly clean terraces (Figure 5.5A and B). There are small amounts of species still adsorbed to the terraces and steps of Cu(111) as well as significant amounts of adsorbates remaining on the Pd brim as seen in Figure 5.5B. These species are most likely due to the decomposition of acetophenone, which was inferred from the evolution of high temperature hydrogen in the TPD spectra shown in Figure 5.3.^{16,24} However a significant difference is observed when H_a and acetophenone are co-adsorbed.

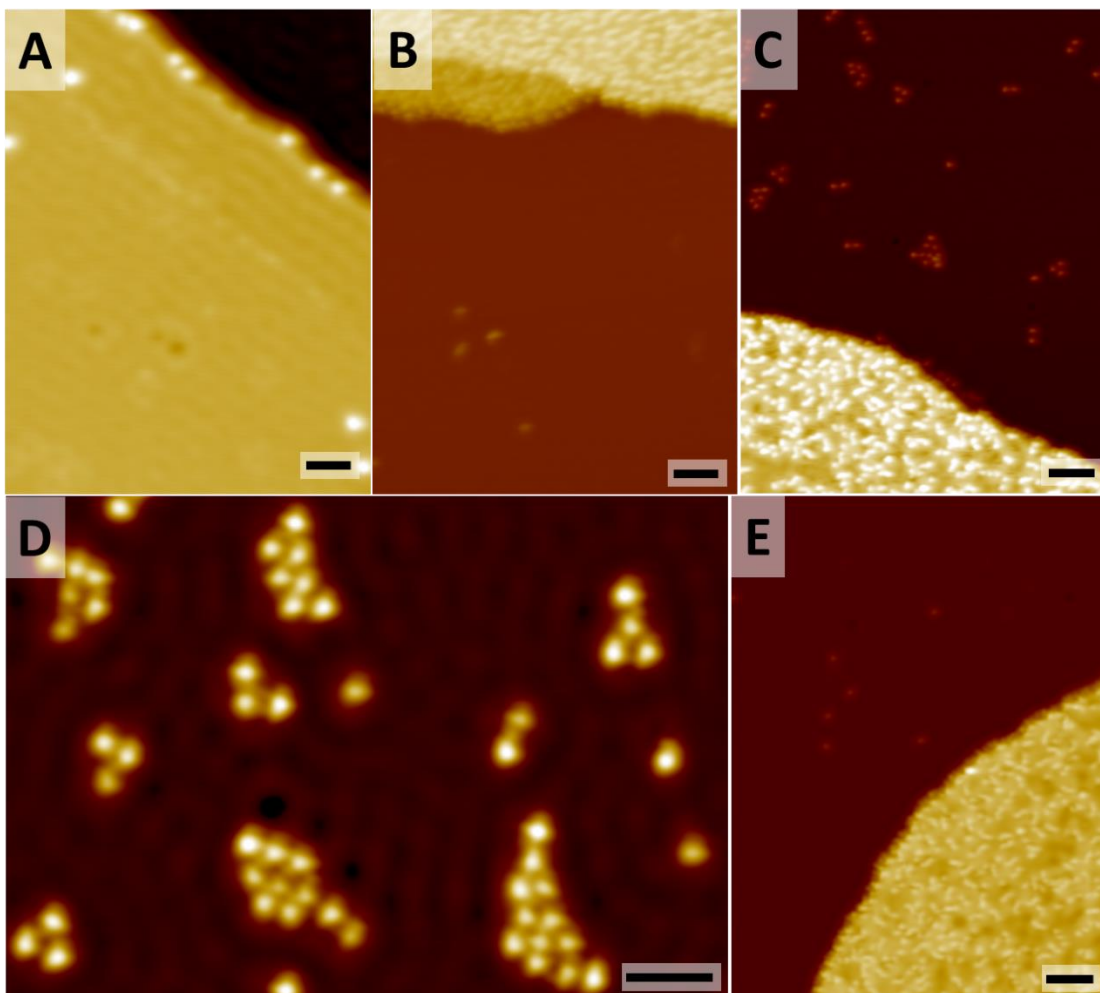


Figure 5.5 STM images probing for partially hydrogenated intermediates. (A) Acetophenone on Cu(111) annealed up to 260 K. Scale bar = 3 nm. (B) Acetophenone on 0.01 ML Pd/Cu(111) annealed up to 260 K. Scale bar = 5 nm. (C) Acetophenone and H_a on 0.01 ML Pd/Cu(111) annealed up to 260 K. Scale bar = 5 nm. (D) Same conditions as (C) showing a high-resolution image of the new intermediates observed. Scale bar = 1 nm (E) Same conditions as C but annealed up to 360 K. scale bar = 5nm.

Figure 5.5C shows a widescale image which results from annealing a surface with both H_a and acetophenone to 260 K. Compared to acetophenone on Cu(111) and the clean SAA, when on a H-pre-covered SAA surface a significant amount of adsorbates remain on the terraces after a 260 K anneal. Similar to acetophenone after a 120 K anneal, these species tend to cluster together, although the number of species in each cluster has a larger range compared to the

acetophenone clusters (Figure 5.5D). The coverage of these clusters as calculated by via STM is 0.08 ML, similar to the 0.07 ML coverage calculated for the acetophenone desorbing at 340 K in the TPD experiments. We infer from this agreement, that the desorption of acetophenone and H₂ at 340 K must be due to the decomposition of these clusters. The fact that this effect is only observed on a surface that was pre-exposed to both acetophenone and hydrogen suggests that the SAA can partially hydrogenate acetophenone. Annealing such a surface up to 360 K, above the desorption temperature of all acetophenone and H_a observed in TPD experiments, results in a relatively clean surface (Figure 5.5E). Similar to the SAA surface (Figure 5.5B), the terrace sites are now also relatively clear, although the brim still contains a significant amount of adsorbates, most likely due to the decomposition of acetophenone. This result suggests that the partial hydrogenation occurs reversibly on the Cu terrace sites which are free of Pd. The Pd brim may also perform this reaction, but there is a large amount of acetophenone decomposition on the brim areas making it difficult to detect at these sites.

5.3 Conclusions

In this study we have demonstrated that the co-adsorption of acetophenone and H_a on a SAA surface results in a stabilizing interaction due to the formation of a partially hydrogenated species. Attempts to hydrogenate acetophenone to an 1-phenylethanol were unsuccessful and none of the desired alcohol product was observed in TPR experiments. Reactive sites such as step edges and Pd atoms cause the decomposition of some of the adsorbed acetophenone. However, TPD

experiments reveal unique desorption features at 340 K when the surface is exposed to both acetophenone and H₂, which are not seen when each species is adsorbed separately. STM provides the means to visualize the intermediates whose decomposition leads to these desorption states. Based on previous results in the literature we infer that these intermediates are partially hydrogenated acetophenone species which are able to hydrogen bond with acetophenone molecules.^{5,34} As we see a 2:1 ratio of hydrogen to acetophenone in these structures based on our TPD results, the structures observed in the STM experiments could result from the interaction of a partially hydrogenated acetophenone with an intact acetophenone as suggested by McBreen.³⁴

5.4 Experimental Methods

The two ultra-high vacuum instruments described in chapter 2 were used to perform the TP and STM experiments. For TPD experiments, Hydrogen 99.999% (Airgas) was deposited on the Cu(111) sample by backfilling the chamber to a desired pressure for a certain time. Hydrogen were calculated based on a saturation coverage of unity when hydrogen was adsorbed on a 5 ML Pd film. Acetophenone >99.0% (Aldrich), purified via freeze-pump-thaw cycles, was deposited on the crystal in the same manner as hydrogen. Due to the low vapor pressure of acetophenone, the tube holding the molecule was heated using a heat gun set to 500°F for 60 s prior to each dose. The cleanliness of such a dose was confirmed via the mass spectrometer. The crystal was typically held at 150 K during acetophenone exposures. Acetophenone was monitored during TPD experiments by monitoring m/z 77, m/z 105, and m.z 120. All spectra shown in

this study are for m/z 105, the major contributor to acetophenones cracking pattern. Acetophenone coverages are calculated based on the saturation of the monolayer peak. 1-phenylethanol was tracked using m/z 79, m/z 107, and m/z 122. Other hydrogenation and decomposition products including, ethylbenzene, 1-cyclohexylethanol, acetylcyclohexane and ethylcyclohexane were tracked using m/z 91, m/z 45, m/z 55 and m/z 83 respectively. 1-phenylethenol, the enol form of acetophenone, was monitored using m/z 106.²⁶

All STM experiments were performed at 5 K. Acetophenone and hydrogen were exposed to the surface while it was held at 5 K through a collimator with a line of site to the sample in the STM stage. Acetophenone was heated prior to exposure to the sample as described in the previous paragraph. The sample was annealed up to 300 K using the wobblestick method discussed in Chapter 2. Anneals above 300 K were performed in the manipulator.

5.5 References

- (1) Chiu, M. E.; Kyriakou, G.; Williams, F. J.; Watson, D. J.; Tikhov, M. S.; Lambert, R. M. *Chem. Commun.* **2006**, 1283–1285.
- (2) Chiu, M. E.; Watson, D. J.; Kyriakou, G.; Tikhov, M. S.; Lambert, R. M. *Angew. Chem. Int. Ed.* **2006**, *45*, 7530–7534.
- (3) Hiyoshi, N.; Sato, O.; Yamaguchi, A.; Shirai, M. *Chem. Commun.* **2011**, *47*, 11546–11548.
- (4) Mohr, C.; Hofmeister, H.; Radnik, J.; Claus, P. *J. Am Chem. Soc.* **2003**, *125*, 1905–1911.
- (5) Pan, M.; Pozun, Z. D.; Brush, A. J.; Henkelman, G.; Mullins, C. B. *ChemCatChem* **2012**, *4*, 1241–1244.
- (6) Gallezot, P.; Richard, D. *Catal. Rev.-Sci. Eng.* **1998**, *40*, 81–126.
- (7) Pan, M.; Brush, A. J.; Pozun, Z. D.; Ham, H. C.; Yu, W.-Y.; Henkelman,

- G.; Hwang, G. S.; Mullins, C. B. *Chem. Soc. Rev.* **2013**, *42*, 5002–5013.
- (8) Vannice, M. A.; Sen, B. *J. Catal.* **1989**, *115*, 65–78.
- (9) Noller, H.; Lin, W. M. *J. Catal.* **1984**, *30*, 25–30.
- (10) Chen, C.-S.; Chen, H.-W.; Cheng, W.-H. *Appl. Catal. A* **2003**, *248*, 117–128.
- (11) Kluson, P.; Cervený, L. *Appl. Catal. A-General* **1995**, *128*, 13–31.
- (12) Pan, M.; Flaherty, D. W.; Mullins, C. B. *J. Phys. Chem. Lett.* **2011**, *2*, 1363–1367.
- (13) Tierney, H. L.; Baber, A. E.; Sykes, E. C. H. *J. Phys. Chem. C* **2009**, *113*, 7246–7250.
- (14) Tierney, H. L.; Baber, A. E.; Kitchin, J. R.; Sykes, E. C. H. *Phys. Rev. Lett.* **2009**, *103*, 246102.
- (15) Boucher, M. B.; Zugic, B.; Cladaras, G.; Kammert, J.; Marcinkowski, M. D.; Lawton, T. J.; Sykes, E. C. H.; Flytzani-Stephanopoulos, M. *Phys. Chem. Chem. Phys.* **2013**, *15*, 12187–12196.
- (16) Kyriakou, G.; Boucher, M. B.; Jewell, A. D.; Lewis, E. A.; Lawton, T. J.; Baber, A. E.; Tierney, H. L.; Flytzani-Stephanopoulos, M.; Sykes, E. C. H. *Science* **2012**, *335*, 1209–1212.
- (17) Marcinkowski, M. D.; Jewell, A. D.; Stamatakis, M.; Boucher, M. B.; Lewis, E. A.; Murphy, C. J.; Kyriakou, G.; Sykes, E. C. H. *Nat. Mater.* **2013**, *12*, 523–528.
- (18) Lucci, F. R.; Liu, J.; Marcinkowski, M. D.; Yang, M.; Allard, L. F.; Flytzani-Stephanopoulos, M.; Sykes, E. C. H. *Nat. Commun.* **2015**, *6*, 8550.
- (19) Xi, M.; Yang, M. X.; Jo, S. K.; Bent, B. E.; Stevens, P. *J. Chem. Phys.* **1994**, *101*, 9122.
- (20) Meyers, J. M.; Gellman, A. J. *Surf. Sci.* **1995**, *339*, 57–67.
- (21) French, C.; Harrison, I. *Surf. Sci.* **1995**, *342*, 85–100.
- (22) Stéphane Lavoie; Marc-André Laliberté; Israel Temprano, A.; McBreen, P. H. *J. Am. Chem. Soc.* **2006**, *128*, 7588–7593.
- (23) Brunelle, J.; Demers-Carpentier, V.; Lafleur-Lambert, R.; Mahieu, G.; Goubert, G.; Stéphane Lavoie; McBreen, P. H. *Top. Catal.* **2011**, *54*, 1334–1339.
- (24) Brandt, B.; Fischer, J. H.; Ludwig, W.; Libuda, J.; Zaera, F.; Schauermann,

- S.; Freund, H. J. *J. Phys. Chem. C* **2008**, *112*, 11408–11420.
- (25) Kyriakou, G.; Davidson, E. R. M.; Peng, G.; Roling, L. T.; Singh, S.; Boucher, M. B.; Marcinkowski, M. D.; Mavrikakis, M.; Michaelides, A.; Sykes, E. C. H. *ACS Nano* **2014**, *8*, 4827–4835.
- (26) Turecek, F. *Tetrahedron Lett.* **1986**, *27*, 4219–4222.
- (27) Anger, G.; Winkler, A.; Rendulic, K. D. *Surf. Sci.* **1989**, *220*, 1–17.
- (28) Gdowski, G. E.; Felter, T. E.; Stulen, R. H. *Surf. Sci.* **1987**, *181*, L147–L155.
- (29) Christmann, K.; Ertl, G.; Pignet, T. *Surf. Sci.* **1976**, *54*, 365–392.
- (30) Marcinkowski, M. D.; Murphy, C. J.; Liriano, M. L.; Wasio, N. A.; Lucci, F. R.; Sykes, E. C. H. *ACS Catal.* **2015**, *5*, 7371–7378.
- (31) Pan, M.; Pozun, Z. D.; Yu, W.-Y.; Henkelman, G.; Mullins, C. B. *J. Phys. Chem. Lett.* **2012**, *3*, 1894–1899.
- (32) Brush, A. J.; Pan, M.; Mullins, C. B. *J. Phys. Chem. C* **2012**, *116*, 20982–20989.
- (33) Demers-Carpentier, V.; Goubert, G.; Masini, F.; Dong, Y.; Rasmussen, A. M. H.; Hammer, B.; McBreen, P. H. *J. Phys. Chem. Lett.* **2012**, *3*, 92–96.
- (34) Goubert, G.; Groves, M. N.; Dong, Y.; Lemay, J.-C.; McBreen, P. H.; Hammer, B. *J. Phys. Chem. C* **2015**, *119*, 7319–7326.

Chapter 6: A Microscopic View of the Active Sites for Selective Dehydrogenation of Formic Acid on Cu(111)

This chapter was modified from an original paper published in 2015 by the same title by M. D. Marcinkowski et al. from ACS Catal., volume 5, pages 7371-7378.

6.1 Introduction

Hydrogen is prevalent in both current and future energy applications since it shows great promise as an alternative to carbon based sources. Proton exchange membrane fuel cells (PEMFCs) provide electricity by reacting hydrogen cleanly with oxygen to form H₂O. While hydrogen gas can be fed directly into PEMFCs, the storage and transportation of compressed hydrogen gas is a potential safety hazard.¹⁻⁴ In order for hydrogen to be a practical source of energy, alternative strategies for hydrogen storage are necessary. Methanol has been used as a hydrogen source in direct methanol fuel cells, but exhibits significant membrane crossover with Nafion, the typical membrane used in PEMFCs.⁵⁻⁸ As a result, interest in formic acid as a potential hydrogen storage molecule is increasing. Formic acid can be reformed to release hydrogen^{3,4,9}, or the intact molecule can be fed into a direct formic acid fuel cell (DFAFC).^{4,5,10,11} While the hydrogen content of formic acid is less than that of methanol, it is less susceptible to diffusion across the permeable Nafion membrane and thus higher concentrations of formic acid can be used in a fuel cell.^{5,6,10} Formic acid can decompose on metal surfaces either through dehydrogenation to produce CO₂ and H₂ or dehydration to produce CO and H₂O. As hydrogen is the product of interest for PEMFCs, high selectivity to dehydrogenation is preferred. In addition, since fuel cells operate at relatively

low temperatures, the CO formed via dehydration can poison the catalyst.¹⁰⁻¹⁶ Typically, DFAFCs employ Pt or Pd as the decomposition catalyst, and while these metals display high activity, they are expensive and can produce the undesired dehydration products.^{4,5,10-16}

Low Miller index Cu surfaces are known to selectively decompose formic acid through dehydrogenation,¹⁷⁻⁴¹ producing the intermediate formate, which is also involved in important reactions such as methanol synthesis on Cu.⁴²⁻⁴⁵ A formate pathway is known to promote high selectivity to the dehydrogenation.^{15,46,47} Pt and Pd surfaces also primarily decompose formic acid to formate,^{48,49} but unlike Cu, are known to produce some reactively formed CO.^{12,14,15,50-52} While the decomposition of formic acid to CO₂ and H₂ has been thoroughly examined on the Cu(110) surface¹⁷⁻³¹, the interaction of formic acid on Cu(111) has received very little attention³⁶⁻⁴¹, despite the fact that the (111) facet is dominant in many nanoparticles. There are a few studies in the literature that focus on the formate intermediate on Cu(111), although formate is often synthesized by the hydrogenation of CO₂ rather than formic acid decomposition, as this process is of interest for methanol synthesis.^{36,37,39} Intact formic acid and formate have been previously examined on Cu(111) using scanning tunneling microscopy (STM), x-ray photoelectron spectroscopy, and infrared reflection adsorption spectroscopy, but to the best of our knowledge, no formic acid temperature programmed desorption/reaction (TPD/R) work has been performed on Cu(111).^{37,38,40,41}

In this study we examine the adsorption and reaction sites of formic acid on Cu(111) over a range of temperatures. This allows us to elucidate the temperatures of elementary steps occurring during the decomposition of formic acid. Using high-resolution STM and TPD/R, each step of the reaction is observed including the intact adsorption of the formic acid, formation of the formate intermediate, and evolution of reactively formed CO₂ and H₂ at 400 K on terraces and 450 K on steps. We show that intact formic acid adsorbs on Cu(111) in the β -polymorphic configuration at 80 K, and dehydrogenates to formate by 160 K. Our TPR results demonstrate that defects in the form of step edges on the Cu surface are 100% saturated with formate while reaction to formate on the Cu(111) terraces is limited to 0.05 monolayers (ML) by competition with intact desorption of formic acid. While the steps are more reactive than the terraces, counter intuitively, CO₂ formation at steps actually occurs at a higher temperature than on terraces (450 K vs 400 K). This is because the initial dehydrogenation step to produce formate is more exothermic on step edges than terraces. Since formate is bound more strongly to step edges, the second dehydrogenation step to produce CO₂ becomes more endothermic, leading to a higher reaction barrier on step edges.⁵³ Therefore, in catalysis one would expect a tradeoff between the steps being initially more reactive to intact HCOOH, but more susceptible to being blocked and unavailable for further reaction due to the higher decomposition temperature of the formate intermediates bound there. Importantly, no restructuring of the Cu surface itself is observed.

6.2 Results and Discussion

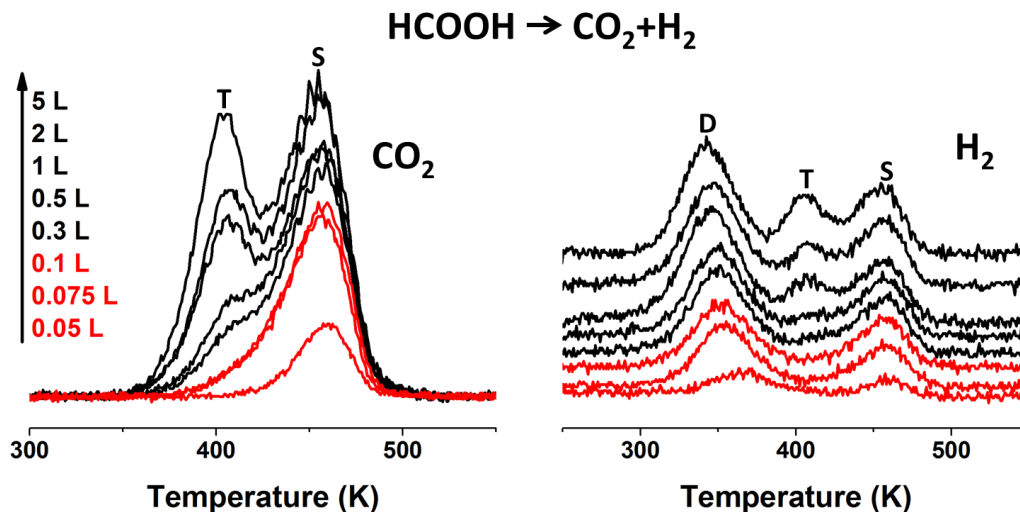


Figure 6.1 Reaction of formic acid on Cu(111). TPR spectra of CO_2 and H_2 from decomposition on Cu(111) after depositing varying amounts of formic acid. H_2 spectra are offset on the y-axis for clarity. The S and T peaks in CO_2 and H_2 spectra result from formate decomposition on steps and terraces, respectively. The D peak in the H_2 spectra originates from H_a recombination from the dehydrogenation of formic acid to formate. Spectra highlighted in red correspond to the red highlighted peaks in Figure 6.2 where no intact molecular formic acid is observed desorbing.

CO_2 and H_2 , the sole reaction products from the decomposition of formic acid adsorbed at 85 K on Cu(111) are shown in Figure 6.1. Importantly, no high temperature, reactively formed CO or H_2O are observed in our TPR spectra, indicating that only dehydrogenation occurs. CO_2 and CO can be interconverted by the water-gas shift reaction (WGSR)^{47,54,55}, but we do not observe any reaction between CO and H_2O on a Cu(111) surface allowing us to unambiguously rule out this effect. Although some signal for m/z 28 is observed, it coincides with m/z 44 and is consistent with the expected fragmentation pattern for CO_2 (Appendix Figure 6). Formic acid decomposition on Cu(111) therefore proceeds solely through the dehydrogenation pathway. This is consistent with TPD results

on the more open Cu(110) facet^{17-19,21,25} and theoretical predictions for Cu(111).^{15,53} CO₂ has two distinct desorption states exhibiting first-order order kinetics at 400 K and 450 K. This is in contrast with the single desorption state seen between 450-473 K in previous studies on clean Cu(110) single crystal surfaces.^{17-19,21,25} At low exposures below 0.1 Langmuir (1 L = 1x10⁻⁶ torr·s), only the peak at 450 K is present. This peak shifts slightly from 459 K at low coverage to 451 K at saturation, which may be indicative of repulsive interactions in the densely packed formate intermediates at step edges. At higher exposures the peak at 400 K begins to grow, but saturates at a 5 L exposure. Since CO₂ does not typically have stable binding sites on Cu single crystals, even at low temperature, these CO₂ desorption peaks are due to reaction rate limited processes.¹⁸

For H₂ desorption, three distinct peaks are observed in our TPD spectra. The lowest desorption temperature is observed at 360 K at low coverage and the symmetric peak's desorption temperature shifts to lower temperature as coverage increases, consistent with second-order order kinetics. This temperature range is consistent with H₂ desorption from Cu(111)⁵⁶ and we will show with our high-resolution STM results that the evolution of H₂ at ~360 K results from a desorption rate limited process. The two higher temperature H₂ peaks coincide with the reactively formed CO₂ at 400 K and 450 K, exhibiting first-order kinetics. This H₂ desorbs at a higher temperature than expected from Cu(111)⁵⁶ (310–370 K) and therefore desorbs in a reaction rate limited process. Up to exposures of 0.1 L only the H₂ desorption at 360 K and 450 K are observed.

Above these exposures the H₂ desorption feature at 400 K grows in the same manner as described for CO₂. We assign the desorption rate limited H₂ peak at 360 K to recombination of adsorbed H atoms resulting from the cleavage of the O-H bond in formic acid that yields surface bound formate.^{15,36-41,53} This peak is labeled D for dehydrogenation of formic acid in Figure 6.1. We assign the two reaction rate limited desorption states at 400 K and 450 K to formate decomposition on Cu(111) terraces and steps (labeled in Figure 6.1 as T and S), respectively. Experimental justification for these assignments will be presented below.

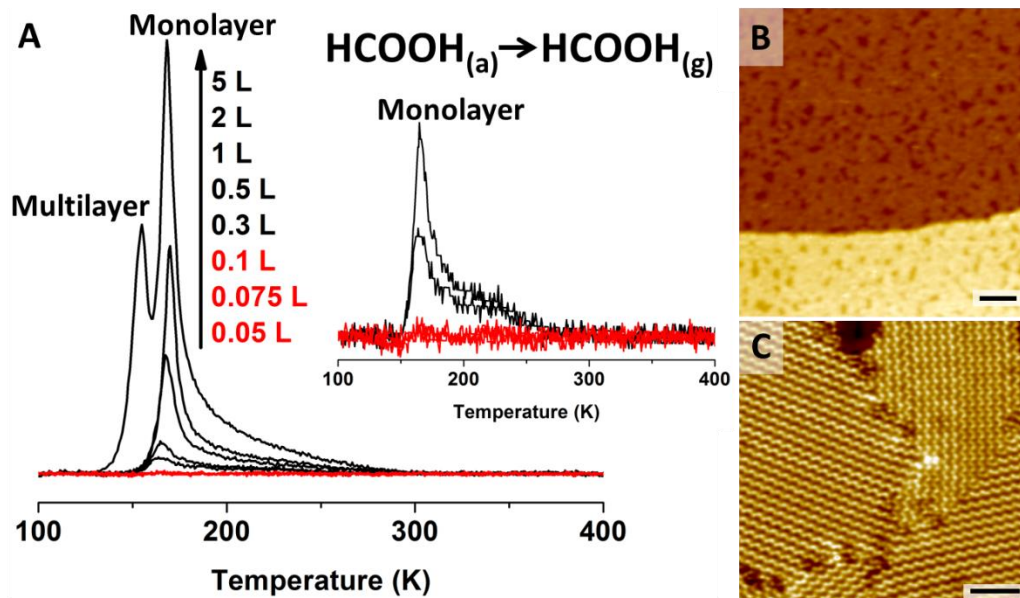


Figure 6.2 Formic acid desorption from Cu(111). (A) Molecular desorption of formic acid from a Cu(111) surface as measured by TPD after varying exposures of formic acid. Dehydrogenation products from these experiments are shown in Figure 6.1. Spectra highlighted in red show low formic acid coverage, conditions at which no intact formic acid desorbs. Inset TPD traces are a close up of the 0.05 L–0.5 L doses. (B) Wide-scale STM image showing ~ 1 ML of intact formic acid on terraces and steps annealed to 80 K. Scale bar = 10 nm. (C) STM image showing formic acid forms well-ordered domains of hydrogen bonded chains in the β conformation. The system was annealed to 120 K to equilibrate the intact formic acid molecules before STM imaging occurred. Scale bar = 3 nm.

The TPD spectra in Figure 6.1 and 6.2 originate from the same experiments and Figure 6.2A shows that intact formic acid desorbs at low temperature from Cu(111). At low exposures, no intact formic acid desorbs and only dehydrogenation products are observed, suggesting all formic acid has reacted. These low coverage spectra are highlighted in red in Figures 6.1 and 6.2. The inset of Figure 6.2A gives an expanded view of the five lowest coverages in the main figure (0.05–0.5 L). At the three lowest exposures (0.05–0.1 L) only the 360 K H_2 peak and 450 K CO_2 and H_2 peaks are present. At higher exposure, there are two desorption states for intact formic acid at 155 and 170 K both exhibiting zero

order desorption kinetics. The peak at 170 K saturates before the appearance of the 155 K peak. The 155 K state continues to grow for larger exposures and does not saturate, consistent with desorption from multilayers. The 170 K state is therefore assigned to desorption from the monolayer of formic acid. Support for these assignments include Hayden et al. who reported that formic acid multilayers desorb from Cu(110) between 147–159 K.²¹ No intact formic acid was observed desorbing from sub-monolayer coverages on Cu(110).^{17–19,21,25} A previous study using a combination of XPS, IR and STM found that on Cu(111) multilayers desorbed between 150–175 K and monolayer desorption occurred between 175–200 K.⁴¹ Interestingly, in our experiments, desorption of intact formic acid in the TPD spectra ~170 K coincides with the appearance of the dehydrogenation products at 400 K. This result will be discussed further in the context of our STM results which allow us to assign the active sites for formic acid decomposition on Cu(111).

We also examined the intact formic acid using STM (Figure 6.2B and C). Figure 6.2B shows a wide-scale STM image resulting from ~1 ML of formic acid annealed to 80 K. At this coverage all the Cu step edges are saturated and there are only a small amount of vacant areas on the terraces. Formic acid adsorbed on terraces appears as bright protrusions and forms well-ordered domains of molecular chains (Figure 6.2C). Figure 6.2C was imaged after a 120 K anneal, but the surface is essentially unchanged between 80–120 K.⁴¹ We believe that these are the first direct images of hydrogen bonded formic acid chains which have

previously been discussed in relation to IRRAS⁴¹ measurements on Cu(111) and are also consistent with the structure of 3D crystalline formic acid.⁵⁷⁻⁶³

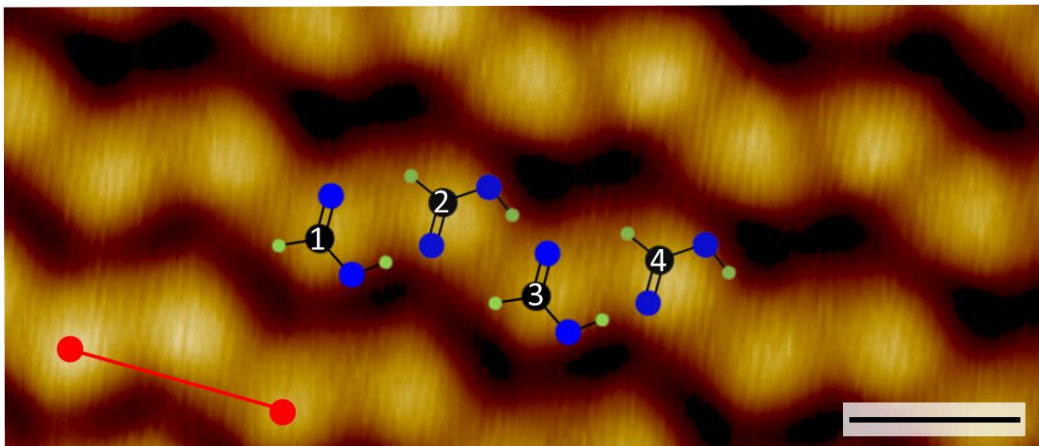


Figure 6.3 Formic acid chain structure on Cu(111). High-resolution STM image of the formic acid chains after annealing to 80 K. The repeating distance along the chain is 6.7 ± 0.2 Å as highlighted by the red line. A to-scale representation of formic acid that accounts for the expected bond lengths and angles in the β conformation is overlaid on the STM image for comparison. Scale bar = 0.5 nm.

Solid phase formic acid was previously proposed to be polymorphic^{59,60} based on far-infrared spectra which showed examples of peak splitting.⁵⁸ The β configuration of bulk formic acid has been shown to be the most stable^{62,63}, but previous results on Cu(111) suggested that the α configuration is present on the Cu(111) surface.⁴¹ These conclusions were based on earlier IR assignments of crystalline formic acid.¹⁸⁻²⁰ Our high-resolution STM results provide direct, real space images of the structure which is most consistent with the β configuration. Figure 6.3 shows a high-resolution STM image of the intact chains of hydrogen bonded formic acid. We took measurements along the chain length as shown by the red line in Figure 6.3 and found an average value of 6.7 ± 0.3 Å. This measurement is in close agreement with the distance of 6.38 Å from carbon 1 to

carbon 3 in β polymorphic formic acid as calculated by a study using an ab initio crystal orbital method.⁶² A to-scale representation based on the formic acid chain dimensions in the β configuration calculated by this study⁶² is overlaid on our STM image in Figure 6.3. The α polymorph of formic acid has an expected carbon 1 to carbon 3 distance of 4.5 Å, well below our measured result. A recent theoretical study used a computational electron-correlation method and found that the α configuration is unlikely and the peak splitting observed in the crystallographic IR study results from in-phase and out-of-phase vibrations in the β configuration.⁶³ This agrees with the explanation initially given by the original IR study of crystalline formic acid.⁵⁸

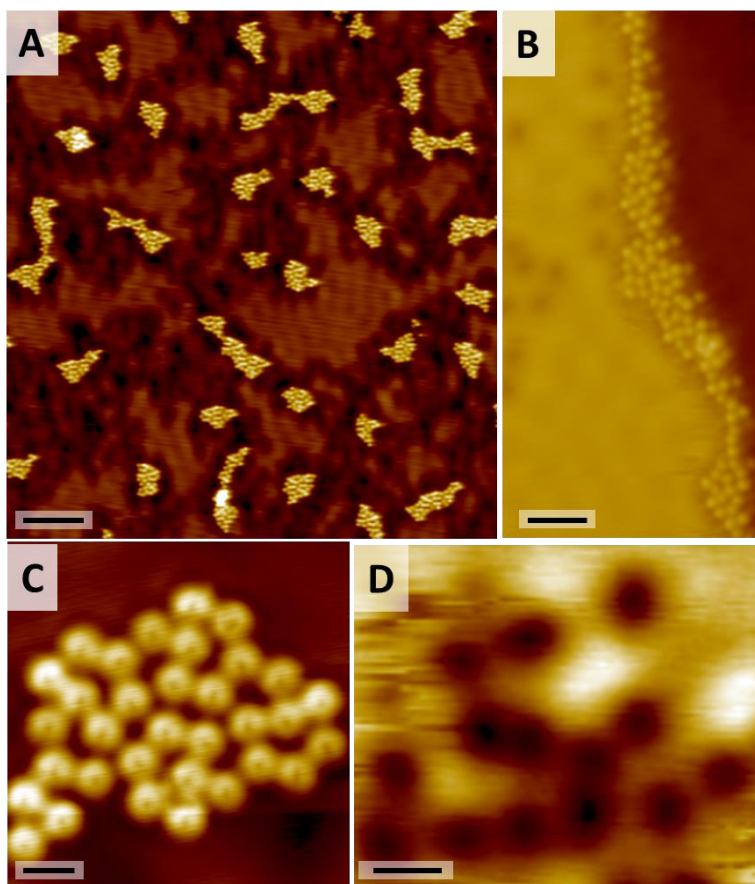


Figure 6.4 Formate and H atom intermediates on Cu(111). (A) STM image showing formate (bright protrusions) and H_a (dark depressions) on the Cu(111) terrace after annealing the sample to 160 K. Scale bar = 5 nm. (B) Formate saturates step edges. This image was obtained after a 220 K anneal. Scale bar = 2 nm. (C) High-resolution image of a formate cluster on the Cu terrace. Scale bar = 0.5 nm. (D) High-resolution image of hydrogen adatoms on the Cu terrace. Scale bar = 1 nm.

STM allows us to track the formation of intermediates on the surface that are inaccessible to TPR. We find that formic acid remains intact on the surface until 160 K, above which, significant changes are observed by STM. Figure 6.4 shows STM images that result from annealing the formic acid covered surface in Figure 6.2B between 160 and 220 K. As seen in Figure 6.4A, the formic acid chains have disappeared from the surface and have been replaced by clusters of formate (bright protrusions in Figure 6.4C) on the terraces and steps as well as

adsorbed hydrogen atoms (H_a ; dark depressions in Figure 6.4D). We assign formate as the intermediate in formic acid decomposition on our Cu(111) surface based on previous results on Cu(110)^{18–27,29–31}, Cu(100)^{32–35}, Cu(111)^{36–38,40,41} as well as recent theoretical studies which predict formate can be produced with a lower barrier than carboxyl on Cu(111).^{15,53} Formate was identified as the surface intermediate in early TPD studies on Cu(110) using HCOOD¹⁸ and DCOOH.¹⁹ More specifically on Cu(111), formate was identified by comparing the O 1s XPS spectra of intact formic multilayers of formic acid adsorbed at 130 K to a monolayer of formic acid annealed to 200 K.⁴⁰ The monolayer peak was 1.2 eV narrower than the multilayer peak consistent with the presence of two equivalent oxygen atoms, which is evidence of a formate rather than a carboxyl pathway. IRRAS further supports the formation of formate on Cu(111), as the OH and C=O peaks dominating the spectra of multilayers of formic acid disappear and are replaced with peaks representing OCO stretches upon annealing to 175 K.⁴¹ In terms of the dark depressions seen in the STM images, we have previously studied the quantum tunneling mediated diffusion of H_a with STM on Pd/Cu(111) single atom alloys and these studies guide our assignment of the depressions as H_a that result from cleavage of the O-H bond in formic acid to produce formate.^{64–67}

Comparison of Figure 6.4A with Figures 6.2B and C shows that heating the sample results in significant desorption of formic acid from the Cu(111) terraces which competes with dehydrogenation to formate. On Cu(110), dehydrogenation to formate is complete and intact formic acid is only observed at multilayer coverages, whereas we observe only ~5% conversion to formate on the Cu(111)

terraces.^{17–19,21,25} This can be explained by the Cu atoms in the Cu(110) surface being more reactive due to their under-coordination with a coordination number of 7 compared to 9 for Cu(111).⁶⁸ On average our STM results reveal that formate coverage is ~0.05 ML after annealing a monolayer of formic acid to 160 K indicating that on terraces, desorption of intact formic acid is the dominant pathway.

Comparing Figure 6.4B with Figure 6.2B shows that the Cu step edges, unlike the terraces, remained saturated with adsorbates between 85–220 K. Our TPD results showed that at low coverage (red traces in Figures 6.1 and 6.2), no intact formic acid desorbs and the dehydrogenation products desorb in a single peak at 450 K. This suggests that the CO₂ and H₂ peaks at 450 K are due to dehydrogenation occurring at the step edges. We assign the CO₂ and H₂ peaks at 400 K to dehydrogenation occurring on terraces as these peaks are only observed in TPR when the formic acid coverage is high enough to occupy all the step sites and some terrace sites (Figure 6.1) and STM confirms the presence of formate intermediates on the terraces (Figure 6.4A).

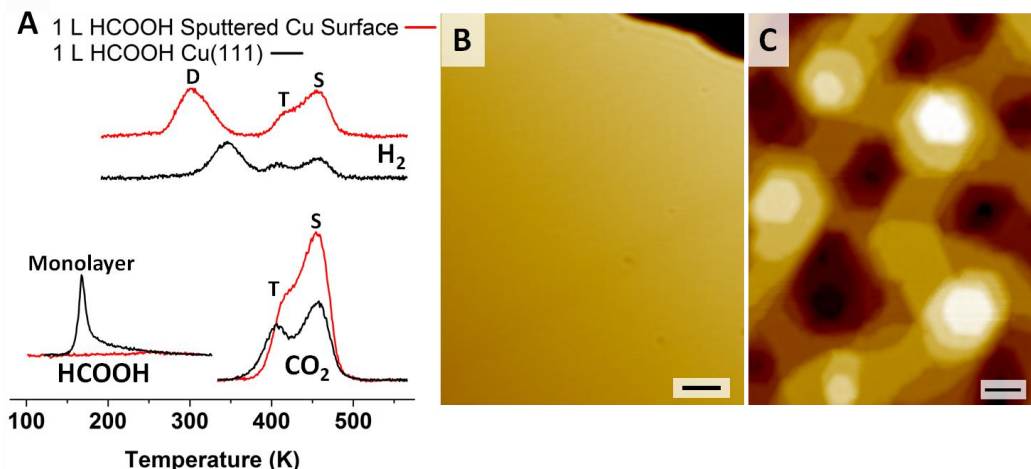


Figure 6.5 Structure sensitivity of formic acid dehydrogenation. (A) Comparison of TPR spectra of formic acid and decomposition products from a sputtered Cu surface (red) vs. a flat Cu(111) surface (black). The S and T peaks in CO₂ and H₂ spectra result from formate decomposition on steps and terraces, respectively. The D peak in the H₂ spectra originates from H_a recombination from the dehydrogenation of formic acid to formate. The intensity of the CO₂ and H₂ peaks at 450 K are greatly increased on the sputtered surface compared to the Cu(111) surface. (B) STM Image of clean Cu(111) compared to (C) sputtered Cu. Scale bars = 5 nm.

In order to confirm these proposed reaction sites, we performed an experiment where we sputtered the Cu(111) surface with Ar⁺ without a subsequent anneal. Compared to an annealed Cu(111) surface (Figure 6.5B) this treatment results in a surface with a much higher step density than Cu(111) (Figure 6.5C). Figure 6.5A shows a comparison of two TPR experiments: one resulting from 1 L of formic acid on a Cu(111) surface (black) and the other resulting from 1 L of formic acid on the sputtered Cu surface (red). It can be seen from these two TPD spectra that the intensity of the CO₂ and H₂ desorption peaks at 450 K have increased significantly for the sputtered Cu surface, confirming that they originate from formic acid decomposition at step edges. In addition, only trace amounts of intact formic acid are observed to desorb from this sputtered Cu

surface compared to the flat Cu(111) surface meaning that the highly stepped Cu surface resulting from sputtering is more reactive than flat Cu(111). One other interesting observation, is the lower temperature hydrogen peak has shifted to 300 K on the sputtered Cu surface compared to 350 K on clean Cu(111). This effect is most likely due to the increase in formate concentration on the sputtered Cu surface. Previous TPD results examining formic acid decomposition on Cu(110) also observed a 50 K shift in this hydrogen peak and proposed it was due to repulsive interactions with the surface formate.^{18,19} It stands to reason that we do not observe this effect on clean Cu(111) terraces as the formate concentration there is typically very low (0.05 ML).

Formate decomposes on Cu(111) steps at 450 K, a temperature consistent with previous TPR results on Cu(110).^{17-19,21,25} We therefore propose the active site on defective Cu(111), i.e. steps edges, is similar to that on Cu(110) terraces. Formate is known to preferentially bind to the top of rows of Cu(110) in a bidentate configuration.^{22,28,29} Atoms in Cu(111) step edges and in the top layer of Cu(110) terraces both have a coordination number of 7 and therefore, both decompose formate at a temperature of 450 K. Comparatively, atoms in Cu(111) terraces have a coordination of 9, so it is not unreasonable that we see two distinct desorption states on this surface at 400 and 450 K for terraces and steps respectively. Normally, it would be expected that the reaction would take place at lower temperature on the more under-coordinated and hence more reactive site; the step edge. However, we see the opposite trend in our TPD results shown in Figures 6.1 and 6.5. This can be explained by the fact that the decomposition of

formic acid to CO_2 and H_2 takes place in a two-step process. According to a recent theoretical investigation⁵³, on under-coordinated surfaces the first reaction step to dehydrogenate formic acid to formate is more exothermic than on close packed surfaces. However, this results in a more endothermic second reaction (formate decomposition to CO_2 and H_2) for the under-coordinated surface. This theoretical study specifically applied this principle to different metal surfaces, but stated that the principle can most likely be applied to under-coordinated sites on a surface. We show evidence that this is true when comparing two types of active sites on Cu(111), namely step edges and terraces.

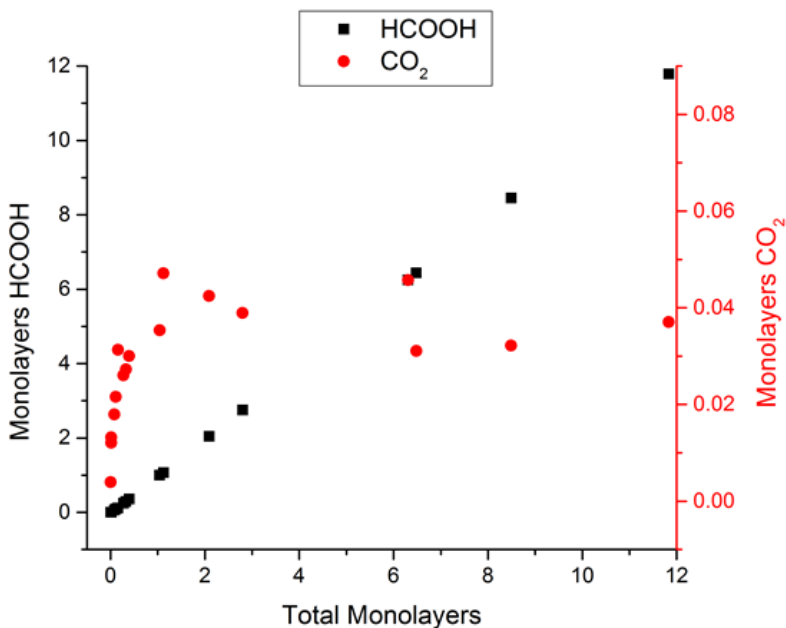


Figure 6.6 Reactivity of Formic Acid on Cu(111). Graph comparing desorption of intact formic acid (black) and reactively formed CO_2 (red) as a function of total formic acid surface coverage.

We also examined the extent of formic acid dehydrogenation over a wide range of formic acid coverages (0.1–9.0 ML). Our TPD results are summarized in Figure 6.6, which shows the partial pressure of desorbing HCOOH and CO₂ as a function of initial coverage of formic acid. CO₂ production saturates at ~1 ML, meaning that multilayers (Appendix Figure 7) are not involved in the reaction.^{17–19,21,25,41} The production of CO₂ in our system is therefore limited by the extent to which dehydrogenation can compete with desorption. The inset shows a zoom in of the lower formic acid coverages up to 1.5 ML. As discussed before, at low coverage where only surface step edges are populated, desorption of intact formic acid is not observed. As the surface coverage increases and terraces start to become populated, the reaction cannot run to completion and intact formic acid begins to desorb. We calculated our total CO₂ production from both steps and terraces at saturation based on the step edge density on our Cu(111) crystal (Appendix Figure 8). We find that the maximum CO₂ production is 0.04 ML according to our TPR results, which corresponds well with our calculated formate coverage in STM of 0.05 ML.

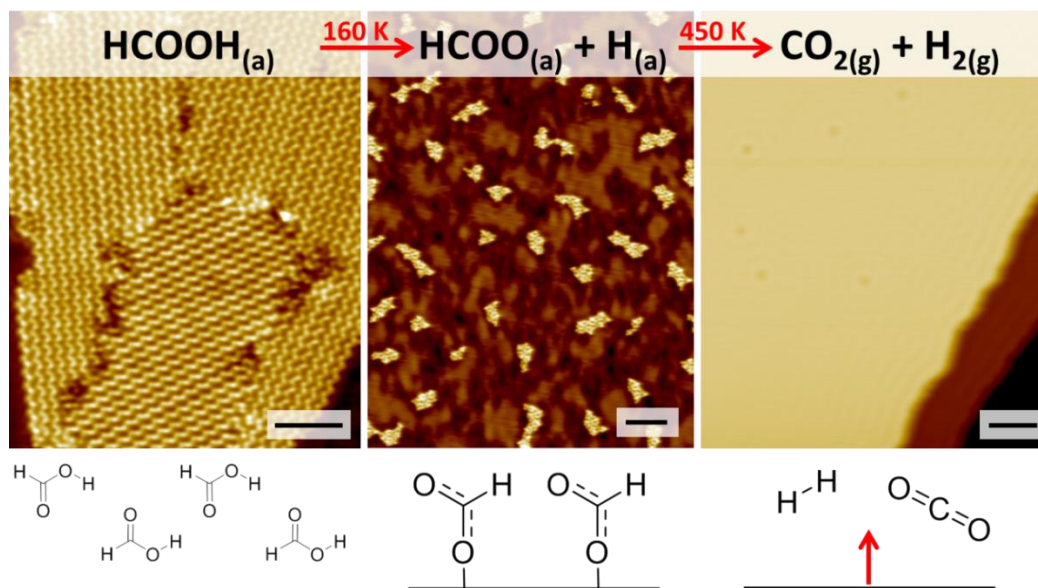


Figure 6.7 Reaction Pathway for Formic Acid Dehydrogenation on Cu(111). Summary of the key reaction steps illustrated with STM images and schematics of the corresponding species. Initially, between 80–160 K intact formic acid forms hydrogen bonded chains on the surface. Scale bar = 3 nm. At 160 K formic acid deprotonates to yield formate. Scale bar = 5 nm. Between 400–500 K formate decomposes to yield H_2 and CO_2 , which desorb instantaneously in a reaction rate limited process leaving a clean Cu surface. Scale bar = 5 nm.

Figure 6.7 summarizes the reaction steps for formic acid dehydrogenation on Cu(111) as measured with TPR and STM. Formic acid exists as intact hydrogen bonded chains in the β configuration up to 160 K (Figure 6.7 left panel), at which temperature it either desorbs intact as seen in the TPD monolayer peak in Figure 6.2 or decomposes to form formate and H_a on the surface (Figure 6.7 middle panel). The Cu steps are much more reactive than terraces and no desorption of intact HCOOH is observed from step edges. Previous work on Cu(111) has predominately observed formate adsorbing in a bidentate configuration.^{36–41} One recent study on Cu(111) reported monodentate formate at lower temperatures, which switched to bidentate formate by 300 K.⁴¹ This was predicted by theory on Cu(111)⁵⁵ and agrees with results reported on Cu(110).²⁶

We observed no discernible difference of the formate in our STM images after annealing between 160–350 K. The formate in Figure 6.7 resulted after annealing to 160 K so it is shown in the monodentate configuration in our schematic in accordance with the results on Cu(111).⁴¹ Based on the IR results from this previous study, it was proposed the monodentate formate interacts with itself through strong intermolecular interactions. This is consistent with the formate clustering we observe on Cu(111); the STM image of formate species shown in Figure 6.4C suggests that the chain like ordering of the intermediate is mediated by hydrogen bonding between monodentate species. At 360 K the hydrogen formed from cleavage of the formic acid O-H bond recombines and desorbs resulting in the TPD peak labeled D in Figure 6.1. At 400 K formate on the Cu terraces decomposes to yield CO₂ and H₂ resulting in the TPD peak labeled T in Figure 6.1. Finally, at 450 K formate on the step edges decomposes resulting in the TPD peak labeled S in Figure 6.1. This leaves a clean Cu(111) surface, as seen in the right panel in Figure 6.7. We confirmed the cleanliness of the Cu surface by running multiple TPD experiments without cleaning the crystal between runs, which showed no change in surface reactivity. Furthermore, despite the relatively strong binding of the formate intermediates we did not observe any signs of Cu surface reconstruction at any point during the reaction.

6.3 Conclusion

Using a combination of TPR and high-resolution STM we have tracked the selective dehydrogenation of formic acid on Cu(111) from reactants, to intermediates, and products. This reaction has been well studied by catalysis

groups, but there is a distinct lack of fundamental data on the reactivity of the (111) facet of Cu, which is a major termination of most nanoparticles. Formic acid remains intact below 160 K and forms a β polymorphic structure. Upon annealing above 160 K, formate and adsorbed hydrogen atoms are formed and visualized with STM. Annealing above 400 K decomposes the formate further to CO_2 and H_2 . Our results indicate that the Cu(111) surface is significantly less reactive than the well-studied Cu(110) facet.^{18,19,21,23,25,30,31} However, roughening the Cu(111) surface lead to a significant increase in reactivity. The lack of Cu surface reconstruction during the reaction indicates that the DFT results on flat Cu slabs are relevant to the reaction and our results agree well with those predictions. For example, of all the metal surfaces examined in a recent theoretical study, Cu(111) was predicted to have one of the lowest turn over frequencies to CO_2 , but was also predicted to have extremely low selectivity to CO which is important in terms of catalyst poisoning.¹⁵ Interestingly, this study predicted that Cu_3Pt alloys have the greatest potential as catalysts for formic acid decomposition in terms of both rate and selectivity to CO_2 and H_2 . Our future work is aimed at investigating the reaction of formic acid on PtCu single atom alloy surfaces.

6.4 Experimental Methods

STM experiments were performed on the instrument described in Chapter 2. The STM stage was held at 5 K during all the experiments described below. Images were taken using tunneling currents between 30-200 pA and sample biases between 20-200 mV. Formic acid with a purity of 98% was purchased from Sigma-Aldrich. Liquid formic acid was degassed through freeze-pump thaw

cycles before it was introduced into the chamber. Formic acid vapor was introduced into the STM chamber through a collimated leak valve with a direct line of sight to the Cu(111) sample. A highly defective Cu surface was prepared by sputtering with Ar⁺ for 1 min at 1 keV without an anneal step in the preparation chamber.

TPD/R experiments were performed on the apparatus described in chapter 2. Formic acid was deposited on the Cu(111) crystal by backfilling the chamber with formic acid to a desired pressure while the sample was held at 85 K. Molecular formic acid was tracked by both the major contributor to its cracking pattern m/z 29 and its parent ion m/z 46. Our results shown in this study are from the m/z 29 trace. CO₂ and H₂ desorption were detected by tracking their parent ions, m/z 44 and m/z 2 respectively. In addition, m/z 28 and m/z 18 were always monitored for detection of CO and H₂O, respectively. A highly defective Cu surface was prepared in this chamber by sputtering with Ar⁺ for 10 min at 1.50 keV.

6.5 References

- (1) Schlapbach, L.; Züttel, A. *Nature* **2001**, *414*, 353–358.
- (2) Graetz, J. *Chem. Soc. Rev.* **2009**, *38*, 73–82.
- (3) Joó, F. *ChemSusChem* **2008**, *1*, 805–808.
- (4) Johnson, T. C.; Morris, D. J.; Wills, M. *Chem. Soc. Rev.* **2010**, *39*, 81–88.
- (5) Jeong, K. J.; Miesse, C. M.; Choi, J. H.; Lee, J.; Han, J.; Yoon, S. P.; Nam, S. W.; Lim, T. H.; Lee, T. G. *J. Power Sources* **2007**, *168*, 119–125.
- (6) Verbrugge, M. W. *J. Electrochem. Soc.* **1989**, *136*, 417–423.
- (7) McGrath, K. M.; Surya Prakash, G. K.; Olah, G. A. *J. Ind. Eng. Chem.*

- 2004**, *10*, 1063–1080.
- (8) Yu, X.; Pickup, P. G. *J. Power Sources* **2008**, *182*, 124–132.
 - (9) Mellmann, D.; Barsch, E.; Bauer, M.; Grabow, K.; Boddien, A.; Kammer, A.; Sponholz, P.; Bentrup, U.; Jackstell, R.; Junge, H.; Laurenczy, G.; Ludwig, R.; Beller, M. *Chem. Eur. J.* **2014**, *20*, 13589–13602.
 - (10) Rice, C.; Ha, S.; Masel, R. I.; Waszczuk, P.; Wieckowski, A.; Barnard, T. *J. Power Sources* **2002**, *111*, 83–89.
 - (11) Rice, C.; Ha, S.; Masel, R. I.; Wieckowski, A. *J. Power Sources* **2003**, *115*, 229–235.
 - (12) Li, Q.; He, R.; Gao, J.-A.; Jensen, J. O.; Bjerrum, N. J. *J. Electrochem. Soc.* **2003**, *150*, A1599–A1605.
 - (13) Ha, S.; Larsen, R.; Masel, R. I. *J. Power Sources* **2005**, *144*, 28–34.
 - (14) Yu, X.; Pickup, P. G. *Electrochem. Commun.* **2009**, *11*, 2012–2014.
 - (15) Yoo, J. S.; Abild-Pedersen, F.; Nørskov, J. K.; Studt, F. *ACS Catal.* **2014**, *4*, 1226–1233.
 - (16) Baschuk, J. J.; Li, X. *Int. J. Energy Res.* **2001**, *25*, 695–713.
 - (17) Wachs, I. E.; Madix, R. J. *Surf. Sci.* **1979**, *84*, 375–386.
 - (18) Ying, D. H. S.; Madix, R. J. *J. Catal.* **1980**, *61*, 48–56.
 - (19) Bowker, M.; Madix, R. J. *Surf. Sci.* **1981**, *102*, 542–565.
 - (20) Hayden, B. E.; Prince, K.; Woodruff, D. P.; Bradshaw, A. M. *Vacuum* **1983**, *33*, 876–877.
 - (21) Hayden, B. E.; Prince, K.; Woodruff, D. P.; Bradshaw, A. M. *Surf. Sci.* **1983**, *133*, 589–604.
 - (22) Crapper, M. D.; Riley, C. E.; Woodruff, D. P. *Surf. Sci.* **1986**, *171*, 1–12.
 - (23) Henn, F. C.; Rodriguez, J. A.; Campbell, C. T. *Surf. Sci.* **1990**, *236*, 282–312.
 - (24) Leibsle, F. M.; Haq, S.; Frederick, B. G.; Bowker, M.; Richardson, N. V. *Surf. Sci.* **1995**, *343*, L1175–L1181.
 - (25) Bowker, M.; Rowbotham, E.; Leibsle, F. M.; Haq, S. *Surf. Sci.* **1996**, *349*, 97–110.
 - (26) Bowker, M.; Haq, S.; Holroyd, R.; Parlett, P. M.; Poulston, S.; Richardson, N. J. *Chem. Soc., Faraday Trans.* **1996**, *92*, 4683–4686.

- (27) Haq, S.; Leibsle, F. M. *Surf. Sci.* **1997**, *375*, 81–90.
- (28) Poulston, S.; Bennett, R. A.; Jones, A. H.; Bowker, M. *Phys. Rev. B* **1997**, *55*, 888–891.
- (29) Bowker, M.; Poulston, S.; Bennett, R. A.; Stone, P.; Jones, A. H.; Haq, S.; Hollins, P. *J. Mol. Catal. A Chem.* **1998**, *131*, 185–197.
- (30) Stone, P.; Poulston, S.; Bennett, R. A.; Price, N. J.; Bowker, M. *Surf. Sci.* **1998**, *418*, 71–83.
- (31) Youngs, T. G. A.; Haq, S.; Bowker, M. *Surf. Sci.* **2008**, *602*, 1775–1782.
- (32) Crapper, M. D.; Riley, C. E.; Woodruff, D. P. *Surf. Sci.* **1987**, *184*, 121–136.
- (33) Woodruff, D. P.; McConville, C. F.; Kilcoyne, A. L. D. *Surf. Sci.* **1988**, *201*, 228–244.
- (34) Krastev, E. T.; Kuhl, D. E.; Tobin, R. G. *Surf. Sci.* **1997**, *387*, L1051–L1056.
- (35) Sambì, M.; Granozzi, G.; Casarin, M.; Rizzi, G. A.; Vittadini, A.; Caputi, L. S.; Chiarello, G. **1994**, *6028*, 309–322.
- (36) Nakamura, J.; Kushida, Y.; Choi, Y.; Uchijima, T.; Fujitani, T. *J. Vac. Sci. Technol. A* **1997**, *15*, 1568–1571.
- (37) Fujitani, T.; Choi, Y.; Sano, M.; Kushida, Y.; Nakamura, J. *J. Phys. Chem B* **2000**, *104*, 1235–1240.
- (38) Sotiropoulos, A.; Milligan, P. K.; Cowie, B. C. C.; Kadodwala, M. *Surf. Sci.* **2000**, *444*, 52–60.
- (39) Nakano, H.; Nakamura, I.; Fujitani, T.; Nakamura, J. *J. Phys. Chem. B* **2001**, *105*, 1355–1365.
- (40) Wühn, M.; Weckesser, J.; Wöll, C. *Langmuir* **2001**, *17*, 7605–7612.
- (41) Baber, A. E.; Mudiyanselage, K.; Senanayake, S. D.; Beatriz-Vidal, A.; Luck, K. A.; Sykes, E. C. H.; Liu, P.; Rodriguez, J. A.; Stacchiola, D. J. *Phys. Chem* **2013**, *15*, 12291–12298.
- (42) Askgaard, T. S.; Norskov, J. K.; Ovesen, C. V.; Stoltze, P. *J. Catal.* **1995**, *156*, 229–242.
- (43) Grabow, L. C.; Mavrikakis, M. *ACS Catal.* **2011**, *1*, 365–384.
- (44) Yoshihara, J.; Campbell, C. T. *Surf. Sci.* **1998**, *407*, 256–267.
- (45) Ludviksson, A.; Zhang, R.; Campbell, C. T.; Griffiths, K. *Surf. Sci.* **1994**,

313, 64–82.

- (46) Singh, S.; Li, S.; Carrasquillo-Flores, R.; Alba-Rubio, A. C.; Dumesic, J. A. *AIChE J.* **2014**, *60*, 1303–1319.
- (47) Grabow, L. C.; Gokhale, A. A.; Evans, S. T.; Dumesic, J. A.; Mavrikakis, M. *J. Phys. Chem. C* **2008**, *112*, 4608–4617.
- (48) Avery, N. R. *Appl. Surf. Sci.* **1982**, *11–12*, 774–783.
- (49) Columbia, M. R.; Crabtree, A. M.; Thiel, P. A. *J. Am. Chem. Soc.* **1992**, *114*, 1231–1237.
- (50) Sun, S. G.; Clavilier, J.; Bewick, A. *J. Electroanal. Chem.* **1988**, *240*, 147–159.
- (51) Aslam, N. M.; Masdar, M. S.; Kamarudin, S. K.; Daud, W. R. W. *APCBEE Procedia* **2012**, *3*, 33–39.
- (52) Yu, W.-Y.; Mullen, G. M.; Flaherty, D. W.; Mullins, C. B. *J. Am. Chem. Soc.* **2014**, *136*, 11070–11078.
- (53) Herron, J. A.; Scaranto, J.; Ferrin, P.; Li, S.; Mavrikakis, M. *ACS Catal.* **2014**, *4*, 4434–4445.
- (54) Jakdetchai, O.; Nakajima, T. *J. Mol. Struct.* **2002**, *619*, 51–58.
- (55) Gokhale, A. A.; Dumesic, J. A.; Mavrikakis, M. *J. Am. Chem. Soc.* **2008**, *130*, 1402–1414.
- (56) Anger, G.; Winkler, A.; Rendulic, K. D. *Surf. Sci.* **1989**, *220*, 1–17.
- (57) Holtzberg, F.; Post, B.; Fankuchen, I. *Acta Cryst.* **1952**, *6*, 127–130.
- (58) Millikan, R. C.; Pitzer, K. S. *J. Am. Chem. Soc.* **1958**, *80*, 3515–3521.
- (59) Mikawa, Y.; Jakobsen, R. J.; Brasch, J. W. *J. Chem. Phys.* **1966**, *45*, 4750.
- (60) Mikawa, Y.; Brasch, J. W.; Jakobsen, R. J. *J. Mol. Spectrosc.* **1967**, *24*, 314–329.
- (61) Nahrngbauer, I. *Acta Cryst.* **1978**, *B34*, 315–318.
- (62) Karpfen, A. *Chem. Phys.* **1984**, *88*, 415–423.
- (63) Hirata, S. *J. Chem. Phys.* **2008**, *129*, 204104.
- (64) Tierney, H. L.; Baber, A. E.; Kitchin, J. R.; Sykes, E. C. H. *Phys. Rev. Lett.* **2009**, *103*, 246102.
- (65) Kyriakou, G.; Boucher, M. B.; Jewell, A. D.; Lewis, E. A.; Lawton, T. J.; Baber, A. E.; Tierney, H. L.; Flytzani-Stephanopoulos, M.; Sykes, E. C. H.

Science **2012**, 335, 1209–1212.

- (66) Marcinkowski, M. D.; Jewell, A. D.; Stamatakis, M.; Boucher, M. B.; Lewis, E. A.; Murphy, C. J.; Kyriakou, G.; Sykes, E. C. H. *Nat. Mater.* **2013**, 12, 523–528.
- (67) Jewell, A. D.; Peng, G.; Mattera, M. F. G.; Lewis, E. A.; Murphy, C. J.; Kyriakou, G.; Mavrikakis, M.; Sykes, E. C. H. *ACS Nano* **2012**, 6, 10115–10121.
- (68) Michel, A. C.; Lianos, L.; Rousset, J. L.; Deliche, P.; Prakash, N. S.; Massardier, J.; Jugnet, Y.; Bertolini, J. C. *Surf. Sci.* **1998**, 416, 288–294.

Chapter 7: Selective Formic Acid Dehydrogenation on Pt/Cu Single Atom Alloys

Catalysis studies were performed by Jilei Liu from Maria Flytzani-Stephanopoulos's group in The Department of Chemical and Biological Engineering at Tufts University.

7.1 Introduction

Hydrogen is considered a promising alternative energy source, however as pure hydrogen is a flammable gas at room temperature, safety issues involving its storage and transportation limit its use as a fuel.¹⁻⁴ Formic acid is a liquid at room temperature and has attracted attention as a means of hydrogen storage.⁵⁻⁷ Formic acid can be dehydrogenated to H₂ and CO₂, through either a formate or carboxyl intermediate⁸⁻¹⁰ (Figure 7.1A), and the resulting hydrogen is fed into a proton exchange membrane fuel cell (PEMFC).^{5,11,12} Alternatively, formic acid itself can be fed into a direct formic acid fuel cell (DFAFC) similar to a direct methanol fuel cell.^{6,13,14} Although methanol has both a higher volumetric capacity of hydrogen and a higher weight percent hydrogen, formic acid is far less permeable to Nafion, the membrane typically used in PEMFCs.^{13,15,16} As a result a high concentration of formic acid can be fed into a fuel cell compared to methanol. Regardless if formic acid is to be reformed, or fed directly into a DFAFC, Pd or Pt are typically used to catalytically dehydrogenate formic acid to CO₂ and H₂.^{13,14,17-19} In addition to being expensive, catalysts based on these reactive metals also perform an undesired dehydration reaction and form CO and H₂O.^{20,21} This reaction proceeds solely through the carboxyl intermediate (Figure 7.1A).⁸⁻¹⁰ CO binds very strongly to both Pd and Pt^{22,23}, and as fuel cells ideally operate at

low temperature, this makes the catalyst susceptible to poisoning and deactivation over time.^{20,21} Even very small amounts of CO in the ppm range can be detrimental, and thus selectivity to dehydrogenation over dehydration should be extremely high.^{20,24}

In order to achieve this high selectivity alternative catalysts to Pt or Pd catalysts are needed, and a variety of strategies have been utilized to overcome this obstacle. Typically these strategies have focused on utilization of less reactive noble metals such as Ag or Au alongside Pd or Pt.^{24–28} A well-known study by Tedsree et. al utilized Ag@Pd core-shell nanoparticles (NPs) to achieve high activity and selectivity to formic acid dehydrogenation at room temperature.²⁴ A similar system was tested with Au@Pd core-shell catalysts by Huang et. al, but at an elevated temperature compared to Tedsree's study.²⁵ Another strategy is the fabrication of alloys to maintain high activity, but gain high selectivity. Wang et. al synthesized NiAuPd nanocatalysts that exhibit high activity and selectivity for formic acid decomposition at room temperature.²⁶ Similarly, Zhou et. al showed that Pd-Au and Pd-Ag NPs achieved high selectivity to H₂ at 365 K.²⁷ Decreasing the size of Pd or Pt ensembles can help to increase selectivity.^{29–31} Taking this approach, a recent study by Bulushev et. al fabricated catalysts consisting of single Pt atoms supported on N-doped carbon nanofibers which exhibit extremely high selectivity and are stable up to 573 K.²⁸ This was similar to a study by Yi and co-workers who found atomically dispersed Au on CeO₂ rods and cubes to dehydrogenate formic acid with ~100% selectivity.³² Furthermore, Yi showed that these Au atoms were resistant to CO poisoning. With these results in mind, this

study focuses on the use of Pt/Cu alloys where the Pt atoms exist as single isolated species in the Cu lattice.

Single atom alloys (SAAs) typically contain small amounts of a more reactive, expensive metal substituted into the lattice of a cheaper less reactive metal.^{30,33-37} The reactive metal, typically Pt or Pd, exists as single isolated atoms in the lattice of the less reactive metal, typically Cu, Ag, or Au.³³⁻³⁶ Even with the smallest possible ensemble of Pt or Pd, these alloys are capable of performing reactions that metals such as Cu would normally be unable to, while maintaining high selectivity to the desired products. For example, SAAs of Pd/Cu and Pt/Cu perform highly selective hydrogenation reactions of styrene, acetylene, and butadiene.^{30,37} In this study, we examine the decomposition of formic acid on a SAAs of Pt in a Cu(111) surface. Cu surfaces are known to be highly selective to the dehydrogenation of formic acid.^{8,9,38-42} Pt surfaces also primarily dehydrogenate formic acid, but dehydration products can be formed which causes the selectivity of these catalysts to suffer.^{8-10,20,43,44} However, pure Cu based catalysts would be impractical due to the high barrier to dehydrogenation on Cu surfaces compared to Pt.^{8,9} In our model studies we find that SAAs of Pt/Cu drastically improve the activity of formic acid decomposition, while maintaining the high selectivity of Cu. Importantly, we also demonstrate the spillover of formate species from Pt sites to Cu. We have then extended these results to NP catalysts containing isolated Pt atoms in Cu. However, we find these NPs only exhibit a marginal increase in activity compared to pure Cu NPs. Our surface studies explain this by parsing out the mechanism revealing that single Pt atoms

are able to lower the barrier to dehydrogenation of formic acid to formate, which occurs at low temperature, but they do not catalyze the decomposition of formate to CO_2 and H_2 , which is the rate limiting step of the reaction for the NP catalysts.

7.2 Results and Discussion

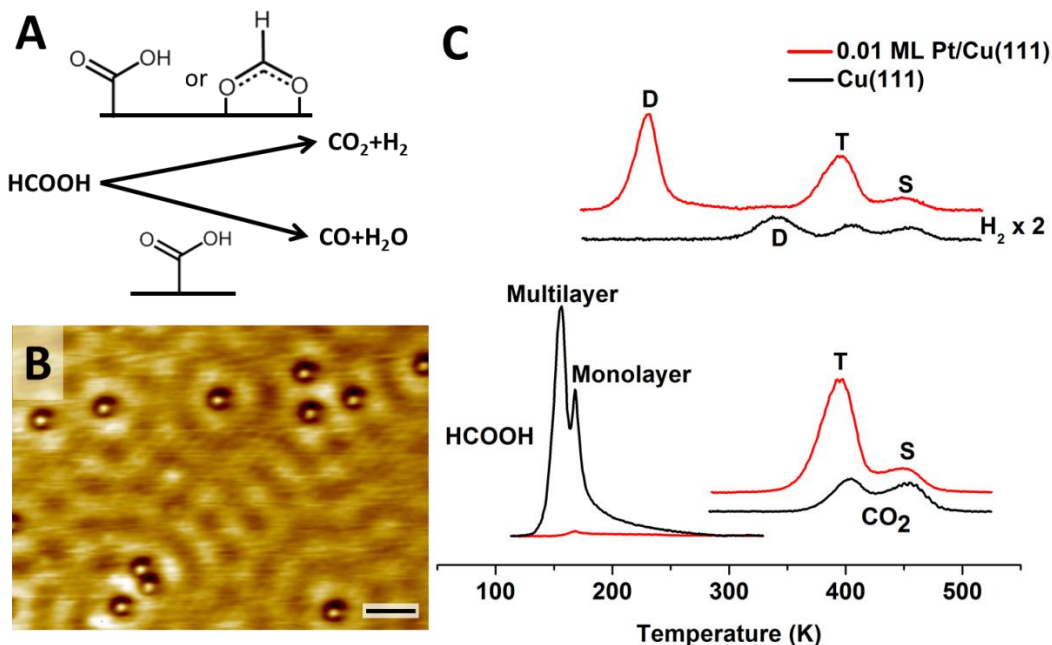


Figure 7.1 Decomposition of formic acid on metal surfaces. (A) Schematic showing the decomposition of formic acid via dehydrogenation can go through carboxyl or formate intermediates, while dehydration proceeds solely through a carboxyl intermediate. (B) High resolution STM image of a 0.01 ML Pt/Cu(111) SAA surface. Scale bar = 2 nm. (C) TPR spectra showing desorption products resulting from the reaction of multilayers of formic acid on Cu(111) (black) and from a monolayer of formic acid on 0.01 ML Pt/Cu(111) (red). The D peak results from H that is formed during the dehydrogenation of formic acid to formate. The T and S peaks result from the dehydrogenation of formate to CO_2 and H_2 on the terraces and steps respectively.

We have extensively characterized the formation of Pt/Cu SAAs formed via physical vapor deposition in previous work.^{36,45} When 0.01 ML of Pt is deposited onto a Cu(111) crystal at 380 K, a dispersed alloy is formed with

isolated Pt sites in the Cu surface. A representative STM image of Pt alloyed into a Cu(111) terrace is shown in Figure 7.1B. The Pt sites appear as individual, bright protrusions. It is easier for Pt to alloy into Cu at step edges, so the concentration of Pt near the steps is higher, but overall the alloy is highly dispersed.⁴⁶

TPR spectra of products from a 10 L dose of formic acid on Cu(111) are shown in Figure 7.1C. Our previous work, as well as other work on Cu(111), has shown that at this exposure multilayers of formic acid adsorb on the surface.^{42,47,48} At 80 K, formic acid adsorbs intact in the β polymorphic form.^{42,49,50} Formic acid multilayers desorb by 150 K and do not take part in any steps of the decomposition reaction. The acid dehydrogenates to formate on Cu(111) by 160 K. Step sites are much more reactive than terraces, and all the formic acid adsorbed at steps is decomposed to formate.⁴² Conversion of a monolayer of formic acid to formate on terraces is limited to ~ 0.05 ML, as the desorption of intact formic acid at 175 K acts as a competing pathway. H_a formed from the dehydrogenation of the acid, desorbs from Cu(111) as $H_{2(g)}$ in a desorption rate limited process at 350 K (D peak in Figure 7.1C).⁵¹ Formate decomposition exclusively yields the dehydrogenation products CO_2 and H_2 ; the dehydration products CO and H_2O are not observed. Formate decomposition occurs at 400 K on the terraces (T Peak) and 450 K on the step edges (S peak) in reaction rate limited processes.^{51,52} Normally it would be expected that the more reactive steps would have a lower barrier to reaction. However, as formic acid dehydrogenation is a two-step reaction, the initial dehydrogenation of formic acid to formate is

very facile on steps, but results in a strongly bound and not as reactive formate species on steps.⁸ Overall Cu(111) is less reactive than Cu(110) although its step edges behave similarly to the terraces of the more open surface.^{39,40,42}

The addition of 0.01 ML of Pt in the Cu(111) surface causes significant changes in the TPR spectra of the decomposition of formic acid (Figure 7.1 C). As on Cu(111) the only desorption products are formic acid, CO₂ and H₂. No reactively formed CO is observed at this low concentration of Pt. This is consistent with Bulushev's results examining formic acid decomposition on single Pt atoms supported on N-doped carbon nanofibers.²⁸ The first major change compared to Cu(111) is in the hydrogen spectra, where the D peak has shifted to 230 K on the Pt/Cu(111) surface compared to 350 K on the Cu(111).^{42,51} The desorption temperature of H₂ from Pt(111) is similar to that of Cu(111), so this temperature is lower than either clean surface.⁵³ This significant shift in H₂ desorption temperature is due to the unique energy landscape of the Pt/Cu alloy, which lowers the desorption barrier of hydrogen significantly compared to bare Cu(111) but maintains the weak binding of hydrogen adatoms. We have previously demonstrated that hydrogen desorbs from Pt/Cu(111) SAAs at 230 K and because we observe H₂ desorption from the reaction of formic acid at this temperature, this process is desorption rate limited as it is on Cu(111).^{37,45} The magnitude of this hydrogen peak also increases significantly showing increased conversion to products. The desorption of CO₂ and H₂ resulting from the decomposition of formate occurs at the same temperature on the SAA surface as it does on Cu(111) (400 K on terraces and 450 K on steps).⁴² Formate decomposes

to CO₂ by 260 K on Pt(111)⁵⁴⁻⁵⁶, which may indicate that the single Pt atoms have little impact on the chemistry of formate decomposition on Cu. However, there is a drastic increase in magnitude of the CO₂ and H₂ peaks attributed to terrace sites at 400 K. The decomposition of formate on steps at 450 K is unaffected and the magnitude of the S peak is the same for both bare Cu and the Pt/Cu SAA surface. Accompanying this increase in decomposition products, there is a significant decrease in the amount of intact formic acid desorbing at low temperature, compared to Cu(111). As previously shown on Cu(111), the production of CO₂ on the Pt/Cu alloy saturates at a monolayer of formic acid.⁴² Multilayers do not participate in the reaction, however on average, the amount of CO₂ produced on a Pt/Cu SAA surface saturated with a monolayer of formic acid is *six times* greater than on Cu(111) (Figure 7.2A). The increase in reactivity is maintained through multiple TPR experiments, so Pt sites are not poisoned by the reaction intermediates. This result also indicates that formate species can spill over from the minority 1% Pt sites where the O-H bond is broken to sites on the Cu terrace. We therefore turned to STM to visualize the formate intermediates on the surface.

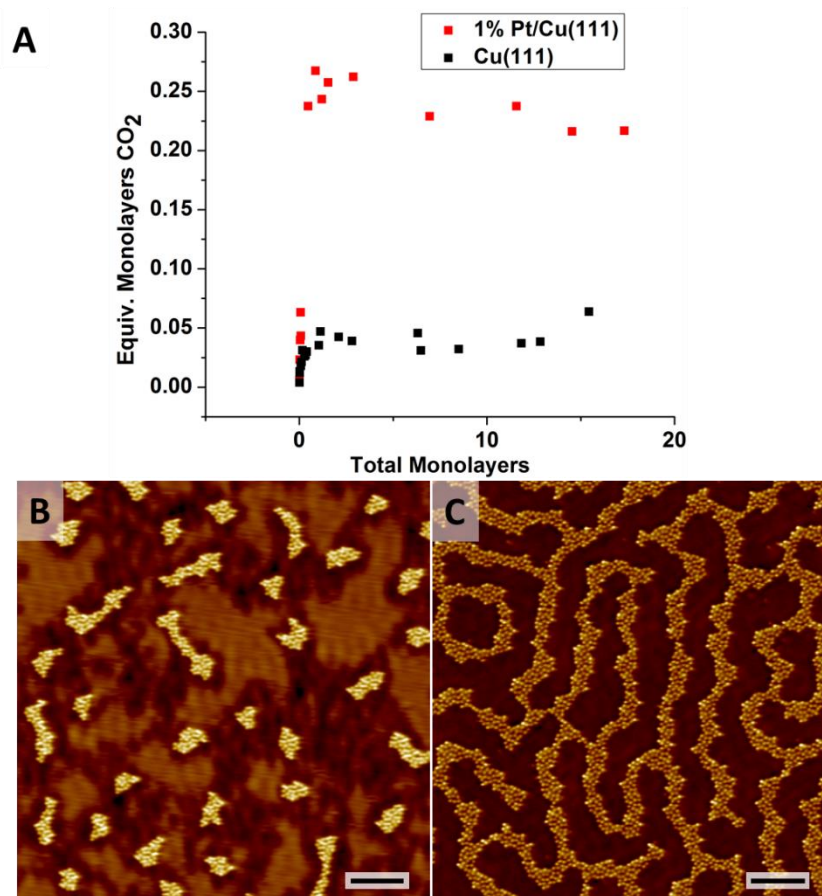


Figure 7.2 Comparison of dehydrogenation activity between Cu(111) and 0.01 ML Pt/Cu(111). (A) CO₂ resulting from a series of initial exposures of formic acid on both Cu(111) and 0.01 ML Pt/Cu(111) (Black and red symbols respectively). (B) STM image of formate and H_a intermediates on Cu(111) compared to (C) STM image of formate on 0.01 ML Pt/Cu(111). Both images result from annealing a monolayer of formic acid to 160 K on each surface followed by imaging at 5 K. The data in (A) and STM image (C) reveal that formate can spillover from Pt sites to Cu. Scale bars = 5 nm.

As discussed, on Cu(111) formic acid undergoes O-H cleavage to produce formate at 160 K.^{42,47} Decomposition through a formate intermediate is well established for all three low Miller index Cu surfaces^{38,39,47,48,57,58} as well as Pt(111).^{10,54-56,59} Desorption of the intact acid competes with this process which limits the production of formate on the terraces to 0.05 ML. Cu step edges are more reactive, and remain saturated with formate after a 160 K anneal. This is

consistent with the fact the more open Cu facets are more reactive than Cu(111).^{39,40,42} A representative STM image of a monolayer of formic acid annealed to 160 K on a Cu(111) terrace is shown in Figure 7.2B. Formate forms static clusters of various sizes and shapes randomly distributed across the surface. The clusters appear as bright protrusions. Also visible in the image are small clusters of mobile black depressions. These are H_a that result from the dehydrogenation of the acid.⁶⁰ The appearance and diffusion of H_a on Cu(111) has previously been characterized by depositing H₂ on Pd-Cu and Pt/Cu alloys, which are active for H₂ dissociation and the motion of the H_a on the surface at 5 K was shown to be predominately via quantum-tunneling mediated diffusion.^{45,60,61} On Cu(111), these H_a re-associate and desorb at 350 K resulting in the peak labeled D in Figure 7.1C.

As a direct comparison to Cu(111) in Figure 7.2B, Figure 7.2C shows a surface where a monolayer of formic acid has been annealed to 160 K on a 0.01 ML Pt/Cu(111) SAA. STM reveals that the coverage of formate is significantly increased to ~0.25 ML on the 1% Pt alloy surface. This corresponds to an average of ~14 formate molecules per Pt atom. We will show that Pt atoms are the main active site for O-H bond cleavage and that formate spillover from Pt to Cu occurs. The formate clusters have joined together to form semi-ordered, continuous chains, similar to structures observed by Baber et al. on Cu(111).⁴⁷ Significantly, STM reveals that unlike the Cu(111) case, on the Pt/Cu SAA surface H_a is absent from the surface. This is consistent with the fact that H_a is able to recombine and desorb as H₂ at a much lower temperature (230 K) as seen in Figure 7.1C.⁴⁵

However, most importantly the STM experiments reveal a similar enhancement in formate formation compared to the six fold enhancement in CO₂ production observed in the TPR experiments. This effect originates from the ability of the formate intermediate to spillover from the Pt sites where the O-H bond is cleaved on Cu(111) as both the TPD and STM data quantitatively show that there are more formate species than Pt atoms (14:1 as calculated by counting formate and Pt species in STM experiments).

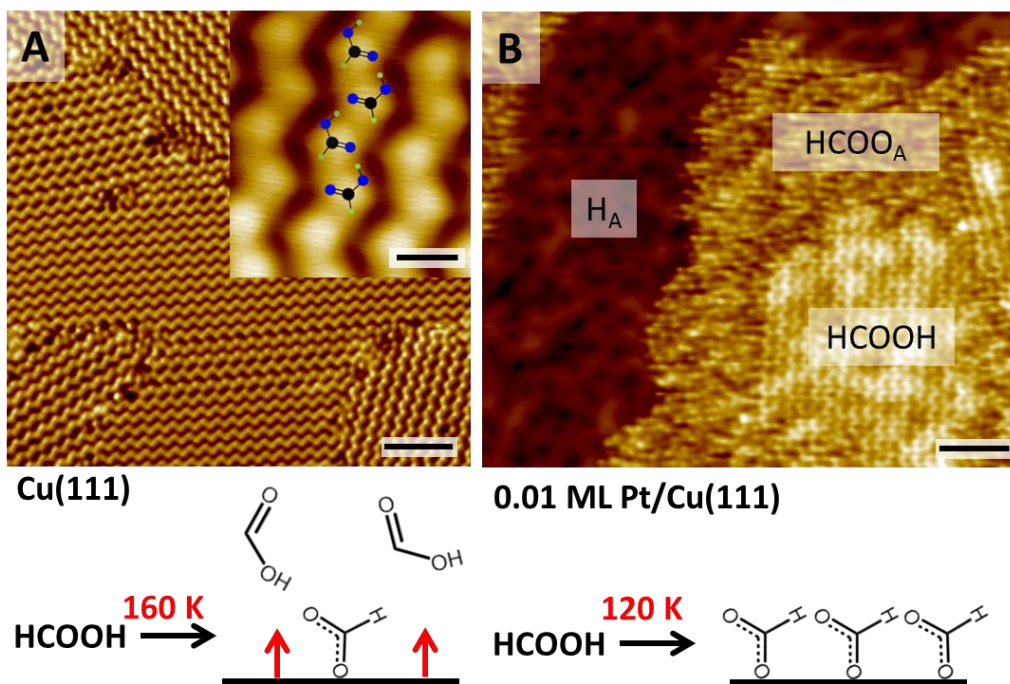


Figure 7.3 Formate formation at 120 K. (A) STM image of intact formic acid on Cu(111) after a 120 K anneal. Scale bar = 3 nm. Inset shows a high-resolution image of the formic acid hydrogen bonded chain structures which form the β conformation. Scale bar = 0.25 nm. (B) STM image of mixed domains of intact formic acid, formate, and H_a on a 0.01 ML Pt/Cu(111) surface after a 120 K anneal. Scale bar = 3 nm. Schematics illustrate the dehydrogenation of formic acid to formate on both surfaces. On Cu(111) desorption dominates over O-H bond cleavage whereas on the SAA surface formate is formed by 120 K, a temperature where intact desorption does not occur.

In order to further explain the increase in formate production on the alloy surface, we prepared monolayers of formic acid on both the Cu(111) and SAA Pt/Cu(111) surfaces and annealed to a lower temperature of 120 K (Figure 7.3). On Cu(111) this is below the temperature necessary to transform formic acid to formate.^{42,47,48} This is demonstrated in the STM image in Figure 7.3A, where only intact hydrogen bonded formic acid chains in the β polymorphic form are observed.^{42,49,50,62} The inset in the right panel shows a zoomed in chain, where a to-scale model of the β polymorph is overlaid on top of the STM image. There is no evidence for the presence of formate or H_a , whereas the Pt/Cu surface in Figure 7.3B is significantly different. The STM image shows three different species; intact formic acid (chains), formate (small clustered protrusions) and hydrogen (dark depressions). These species are isolated from each other in distinct domains. Annealing this surface a second time to 120 K decreased the amount of intact formic acid present on the surface while increasing the amount of formate and hydrogen present. This could be repeated until the surface is completely saturated with formate and hydrogen (Appendix Figure 9). This data supports our hypothesis that Pt sites are active for low temperature O-H bond cleavage and allow spillover of formate and H_a to Cu(111) sites.

The appearance of formate by 120 K indicates that the Pt/Cu alloy lowers the activation barrier necessary to dehydrogenate formic acid. This is significant because 120 K is well below the temperature intact formic acid is able to desorb from the alloy surface (170 K). On Cu(111) formate does not form until 160 K, at which point intact formic acid is also able to desorb from the surface.^{42,47} This

means on Cu(111) there are two competing processes, O-H cleavage and desorption. Desorption is dominant as evident by the low coverage of formate observed on the Cu(111) surface.^{42,47} On Pt/Cu(111) the only process at 120 K is the dehydrogenation of formic acid to formate (Schematics Figure 7.3). Interestingly, even on Pt(111) formate is not observed until 150 K.^{54,56,59} This facile activation leads to an increase in the amount of formate observed on the alloy surface after annealing it to 160 K (Figure 7.3). It should be noted that there is some desorption between the 120 K anneal and the 160 K anneal (Figure 7.3B vs Figure 7.2C). At 120 K the surface is still completely saturated, while at 160 K the surface coverage has decreased to about 0.25 ML. Some intact formic acid is observed via TPD to desorb from the Pt/Cu surface at 175 K (Figure 7.1C), which may arise from some recombination of H_a with formate on the saturated Pt/Cu surface. This reverse reaction was also observed on Pt(111) and Cu(110).^{40,56} Even with this desorption, there is still a significant increase in formate formation over that on Cu(111) which leads to the six fold increase of CO₂ production (Figure 7.2A).

The Pt/Cu SAA showed a great increase in activity compared to the bare Cu surface, while maintaining the high selectivity towards dehydrogenation that is preferred for fuel cell applications.^{20,24} A theoretical study by Yoo et. al identified an ordered Cu₃Pt alloy where the Pt atoms are isolated from each other as an ideal catalyst for formic acid dehydrogenation and our surface science results seem to corroborate this.⁹ We expanded our study to include alloys with higher Pt concentrations. We have previously characterized Pt/Cu alloys for a variety of Pt

concentrations.^{36,45,63} Pt/Cu(111) alloys remain in the single site regime up to 0.05 ML of Pt. Above 0.05 ML, Pt rich fingers begin to grow from step edges. These fingers contain linear chains of Pt atoms within them. Above 0.3 ML of Pt, islands containing areas similar to Pt(111) begin to form.

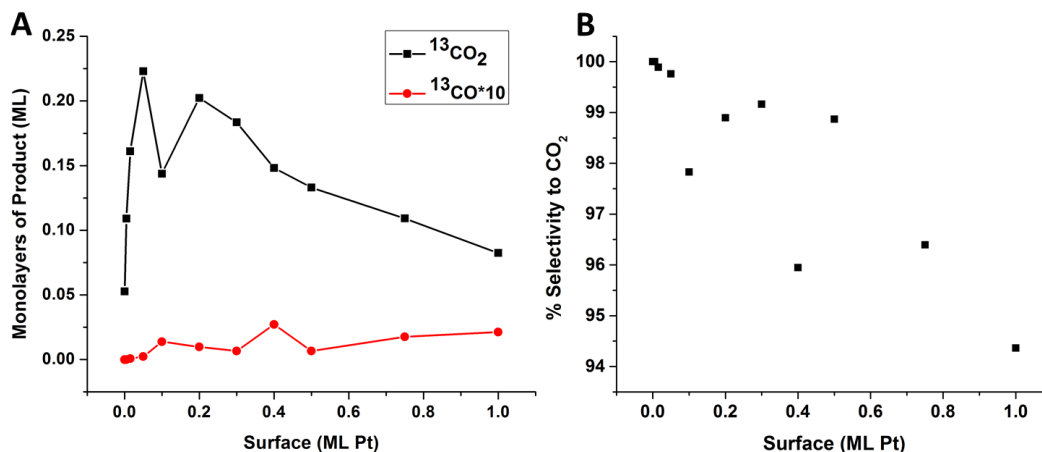


Figure 7.4 Product distribution for formic acid decomposition as a function of Pt/Cu Alloy composition. (A) Graph showing production of $^{13}\text{CO}_2$ and ^{13}CO on various Pt/Cu alloys resulting from a 1.5 L dose of formic acid on each surface. (B) Selectivity towards CO_2 on each of the Pt/Cu alloys.

The activity of formic acid decomposition on a range of Pt/Cu alloys was probed by dosing 1.5 L of H^{13}COOH onto surfaces containing between 0-1.0 ML Pt (Figure 7.4). Previous results on Pt catalysts have demonstrated that some dehydration products are formed,^{20,21} although UHV studies of formic acid on Pt(111) have not detected any reactively formed CO.⁵⁴⁻⁵⁶ Pt(110) is known to form reactively formed CO under UHV conditions.⁴³ As our extended Pt surfaces are more corrugated and defective than Pt(111), we expected some formation of CO (Appendix Figure 10). On the SAA alloy surface, CO desorbs from the Pt atoms by 350 K, but on extended Pt surfaces it is present up to 450 K.^{22,45,63}

Therefore, there is usually some CO adsorbed to the Pt from the chamber background and the use of isotopically labeled formic acid allows us to easily differentiate between ^{12}CO from the background and reactively formed ^{13}CO . On SAA surfaces up to 0.05 ML Pt, only minimal reactively formed CO is observed (Figure 7.4A). In this regime, the amount of CO_2 produced increases steadily as Pt is added to the surface. Above 0.05 ML of Pt where extended Pt surfaces begin to form, small amounts of reactively formed CO are produced and CO_2 production begins to slightly drop. CO production continues to increase above 0.3 ML Pt and CO_2 production drops even further which our STM indicate is related to the presence of larger Pt ensembles at these coverages. We also note that at ≥ 0.2 ML Pt we see a lower temperature evolution of reactively formed CO_2 (Appendix Figure 11). At these elevated Pt coverages our previous STM studies reveal that continuous 1D Pt chains are present on the surface and these must catalyze the reaction with a lower barrier albeit with $< 100\%$ selectivity.^{36,45,63} Figure 7.4B maps the selectivity to CO_2 on the different Pt/Cu alloys. In the SAA regime selectivity to CO_2 approaches 100%. However, beyond the SAA regime selectivity steadily drops. Although CO_2 is always the predominant product, with a 94% selectivity achieved even at 1 ML of Pt, even small amounts of CO can be a problem in current-generation PEM fuel cells, which operate at low temperatures.^{20,24} According to our surface science experiments, the SAA alloys are able to improve the activity of formic acid decomposition, while maintaining the high selectivity of Cu.

In order to translate our surface science results to more realistic catalytic conditions, we synthesized silica supported Pt/Cu NPs containing single atom sites through the galvanic replacement method.³⁷ Pt atoms were fully isolated in the surface of Cu NPs as indicated by various techniques.^{37,63} The catalytic activity for formic acid decomposition was studied in a flow reactor set-up to mimic the industrial process. Flow reactor reaction data for formic acid decomposition over the Pt₁Cu-SAA and Cu-NP catalysts are shown in Figure 7.5. The activity of both catalysts was essentially the same in the temperature range studied (Figure 7.5A). When we compared the activity at 100 and 120 °C, in the low conversion kinetic regime, the conversion over the Pt₁Cu-SAA catalyst (4.7% and 19.8%) was slightly higher than that of Cu-NP (3.5% and 16.5%) but not improved six fold as demonstrated in the UHV studies. For both catalysts, the selectivity to dehydrogenation products (H₂+CO₂) was 100% at all reaction temperatures studied. This is also confirmed by IR studies that no adsorbed carbonyl species were detected (Appendix Figures 12, 13, and 14). Notably, this selectivity is maintained when the formic acid was fully converted at 150 and 175 °C. These results indicate that the Pt₁Cu-SAA catalyst has the same rate limiting step for formic acid decomposition as on Cu-NP and the highly selective dehydrogenation chemistry of Cu is maintained on Pt₁Cu-SAA.

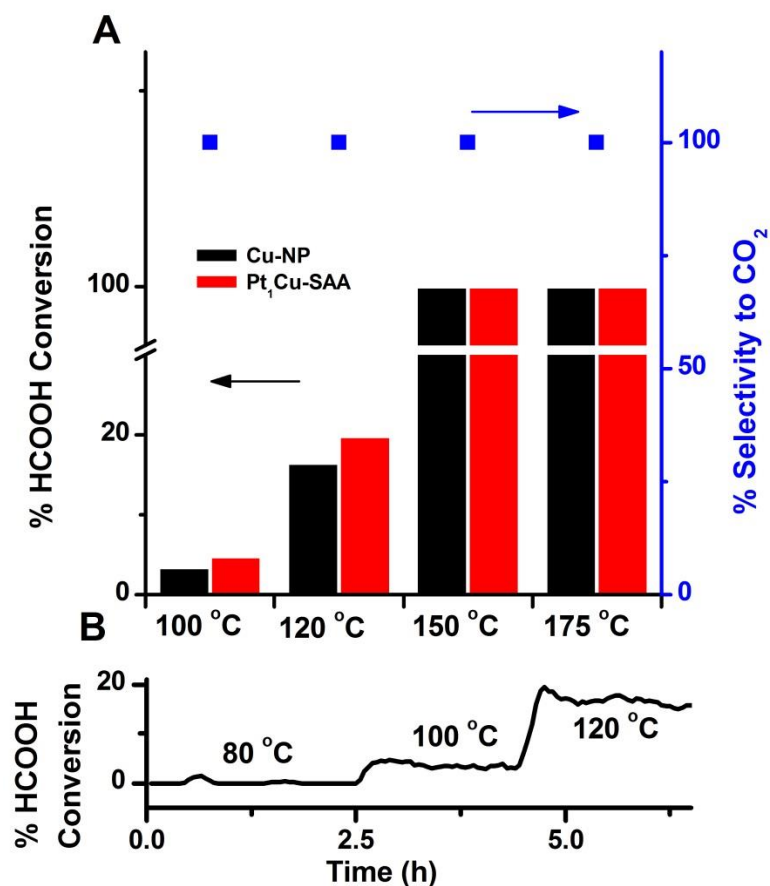


Figure 7.5 HCOOH decomposition in a flow reactor. (A) Conversion and selectivity of Pt₁Cu-SAA and Cu-NP catalysts at 100, 120, 150 and 175 °C. (B) Conversion of HCOOH on Cu-NP over the course of the experiment. Reaction condition: 500 mg catalysts, 1.5% HCOOH, balance helium, flow rate=12 ml/min.

Our results on the NPs show that there is only marginal increase in activity, or decrease in light-off temperature between Cu NPs and SAAs of Pt/Cu. The surface science results show a clear increase in activity between Cu(111) and 0.01 ML Pt/Cu(111). However, we have shown this increase arises from the lowering of the reaction barrier to dehydrogenate formic acid to formate and the ability of formate to spillover from Pt to Cu sites (Figure 7.3). The first dehydrogenation step from formic acid to formate occurs at a lower temperature

on the SAA compared to Cu(111) (120 K vs 160 K). It is predicted that the barrier to dehydrogenate formic acid to formate is lower on Pt compared to Cu.⁹ Since intact formic acid is weakly bound to metal surfaces, it is able to diffuse to a Pt atom where facile activation of the O-H bond occurs to produce formate.^{8,10} We show here that the formate can then spillover from the Pt sites to Cu, allowing the Pt sites to produce additional formate species. The combination of facile O-H activation at Pt sites, along with the ability of formate to spillover to Cu sites results in an increase in the activity of the SAA compared to Cu(111) in the UHV studies. However, this has little effect on the overall performance of the NP catalysts since facile activation of the O-H bond can occur on both Pt₁Cu-SAA and Cu NPs at the reaction temperatures studied. The dehydrogenation of formate to CO₂ and H₂ is the rate limiting step and does not occur until 400 and 450 K on the terraces and steps, respectively.^{8,10,42} These temperatures are identical on Cu(111) and 0.01 ML Pt/Cu(111), indicating that the single platinum atoms do not catalyze rate limiting reaction step. This is understood by the fact that formate binds more strongly to Cu than it does to Pt.^{8,9} This results in an increased energy cost to dehydrogenate formate on Cu compared to Pt, as the transition state to this second dehydrogenation step involves the breaking of an O-Metal bond in bidentate formate to allow the C-H bond to approach the surface.^{8,9,64,65} On the SAA it is expected that formate will bind atop to two Cu atoms as this is the most thermodynamically stable position and hence the activation barrier to form CO₂ and H₂ is the same on both surfaces. This is also supported by a study of CO oxidation on a Cu₃Pt(111) crystal where it was found that oxygen is most stable in

a threefold site surrounded by 3 Cu atoms.⁶⁶ As such the SAA surface is unable to catalyze this second dehydrogenation step any better than pure Cu. The six fold increase in CO₂ production on the SAA surface occurs solely due to the facile activation of formic acid to formate, which is very stable on the surface.^{8,10} The reaction on the NP catalysts was run between 373-468 K, well above the temperature where formate can easily form on either surface and as such the step that the SAA catalyzes in UHV does not play a large role in rate limiting the NP catalyst rate. The more important step of the reaction, the dehydrogenation of formate to CO₂ and H₂, is not affected by the Pt atoms and as such no significant increase in activity is observed between the two types of NPs.

7.3 Conclusions

We have studied formic acid dehydrogenation on Pt/Cu SAAs using both single crystal and NP studies. From the UHV studies we find formic acid is dehydrogenated to formate at 120 K on 0.01 ML Pt/Cu(111) and 160 K on Cu(111), indicating that the SAA readily activates O-H bonds compared to pure Cu and importantly the formate can spillover from Pt sites to Cu. This results in the production of six times the amount of formate on the SAA surface compared to Cu(111), since on Cu(111) the desorption of intact formic acid at 175 K acts as a competing process. Under the conditions in the surface science experiments, where a fixed amount of formic acid is initially adsorbed to the surface and then undergoes a temperature ramp, a six fold increase in the formation of CO₂ and H₂ is observed. The SAA maintains the selectivity of pure Cu to dehydrogenation. However, the NP studies reveal only small improvements in catalytic activity

from the Pt₁Cu-SAA catalyst compared to Cu-NPs, although the high selectivity of Cu-NP is maintained on the SAA. The NP experiments were run between 373-468 K which is well above the temperature at which formate is formed on either surface. Therefore, under these conditions where surface coverage is governed by equilibrium between gas phase and adsorbed species, the improvements observed in the UHV experiments are marginal. This is explained by the fact that the UHV experiments show no improvement between Cu(111) and the SAA in the second dehydrogenation step of formate to CO₂ and H₂ which occurs at ~400 K on both surfaces. Increasing the Pt concentration in the UHV studies did show an even greater increase in activity due to ensemble effects, but suffered from decreased selectivity. While we have previously shown that the advantages of SAAs observed in model studies can be transferred to NP catalysis,^{37,67} in this case little improvement is observed as the SAA does not catalyze the rate limiting step of the reaction. However, this study indicates that the Pt/Cu SAAs are capable of catalyzing O-H bond cleavage at a lower temperature than Cu(111) which could be of utility in other reactions where this step is rate limiting.

7.4 Experimental Methods

7.4.1 TPD and STM Measurements

STM experiments were performed using the instrument described in Chapter 2. All imaging was performed at 5 K. Images of the alloy surface were taken using tunneling currents between 50 pA to 200 nA with sample biases of 10-300 mV. Images of formic acid and its decomposition intermediates were

taken using tunneling currents between 30-300 pA and 20-300 mV. HCOOH was purchased from Sigma-Aldrich with a purity of 98% and was introduced into the chamber through a collimated leak valve after degassing via repeated freeze-pump-thaw cycles.

The TPD chamber described in Chapter 2 was used for the experiments in this study. To deposit formic acid on the crystal it was introduced into the chamber through a leak valve until the chamber was backfilled to the desired pressure over a certain period of time while the crystal was held at 85 K. Exposures were calculated in Langmuirs ($1 \text{ L} = 1 \times 10^{-6} \text{ torr}\cdot\text{s}$) HCOOH was tracked using m/z 29 and m/z 46. M/z 29 is displayed in all figures. CO₂ and H₂ were tracked using m/z 44 and m/z 2 respectively. CO and H₂O were always tracked using m/z 28 and m/z 18. H¹³COOH was purchased a 95 wt. % solution in H₂O with a 99% purity of ¹³C from Sigma Aldrich. H¹³COOH was monitored using m/z 46 and m/z 30. M/z 46 is displayed in all figures. In both chambers, Pt deposition was performed using Omicron Nanotechnology Focus EFM3 electron beam evaporators. The Cu surface was held at 380 K during Pt deposition. Pt coverages were calibrated using CO adsorption (Airgas 99.99%).

7.4.2 Nanoparticle synthesis and catalytic activity measurements

As previously described, Cu-NP catalysts were synthesized by immobilizing polyvinylpyrrolidone stabilized copper nanoparticles on to a silica support (fumed silica, 0.2-0.3 μm average aggregate particle size, surface area 200 m²/g) followed by calcination in air.³⁷ A Pt₁Cu-SAA catalyst was formed by

galvanic replacement with the Cu-NP sample.³⁷ The metal loading was determined by inductively coupled plasma (ICP) to be approximately 4 wt% and the Pt to Cu ratio in the Pt₁Cu-SAA is approximately 1/100. Formic acid decomposition was conducted in a packed-bed flow microreactor (L=11 inch, O.D.=1/2 inch) with 500 mg of catalyst diluted by 2.5 g of quartz particles. The samples were pre-reduced in 10% H₂ at 250 °C and then cooled to desired temperature before the reaction gas mixture (1.5% HCOOH and balance helium. Flow rate=12 ml/min) was introduced. For the isothermal HCOOH decomposition, full gas was introduced at 100 °C and temperature was increased and held at each temperature for 2 hours. The gas effluent from the reactor was analyzed by a mass-spectrometer. HCOOH, CO₂, CO, H₂ and H₂O were tracked using m/z 46, 44, 28, 2 and 18.

7.5 References

- (1) Schlapbach, L.; Züttel, A. *Nature* **2001**, *414*, 353–358.
- (2) Züttel, A.; Remhof, A.; Borgschulte, A.; Friedrichs, O. *Phil. Trans. R. Soc. A* **2010**, *368*, 3329–3342.
- (3) Graetz, J. *Chem. Soc. Rev.* **2009**, *38*, 73–82.
- (4) Barbir, F. *Energy* **2009**, *34*, 308–312.
- (5) Johnson, T. C.; Morris, D. J.; Wills, M. *Chem. Soc. Rev.* **2010**, *39*, 81–88.
- (6) Yu, X.; Pickup, P. G. *J. Power Sources* **2008**, *182*, 124–132.
- (7) Aslam, N. M.; Masdar, M. S.; Kamarudin, S. K.; Daud, W. R. W. *APCBEE Procedia* **2012**, *3*, 33–39.
- (8) Herron, J. A.; Scaranto, J.; Ferrin, P.; Li, S.; Mavrikakis, M. *ACS Catal.* **2014**, *4*, 4434–4445.
- (9) Yoo, J. S.; Abild-Pedersen, F.; Nørskov, J. K.; Studt, F. *ACS Catal.* **2014**, *4*, 1226–1233.

- (10) Scaranto, J.; Mavrikakis, M. *Surf. Sci.* **2016**, *648*, 201–211.
- (11) Joó, F. *ChemSusChem* **2008**, *1*, 805–808.
- (12) Mellmann, D.; Barsch, E.; Bauer, M.; Grabow, K.; Boddien, A.; Kammer, A.; Sponholz, P.; Bentrup, U.; Jackstell, R.; Junge, H.; Laurenczy, G.; Ludwig, R.; Beller, M. *Chem. Eur. J.* **2014**, *20*, 13589–13602.
- (13) Rice, C.; Ha, S.; Masel, R. I.; Waszczuk, P.; Wieckowski, A.; Barnard, T. *J. Power Sources* **2002**, *111*, 83–89.
- (14) Rice, C.; Ha, S.; Masel, R. I.; Wieckowski, A. *J. Power Sources* **2003**, *115*, 229–235.
- (15) Jeong, K. J.; Miesse, C. M.; Choi, J. H.; Lee, J.; Han, J.; Yoon, S. P.; Nam, S. W.; Lim, T. H.; Lee, T. G. *J. Power Sources* **2007**, *168*, 119–125.
- (16) Verbrugge, M. W. *J. Electrochem. Soc.* **1989**, *136*, 417–423.
- (17) Ha, S.; Larsen, R.; Masel, R. I. *J. Power Sources* **2005**, *144*, 28–34.
- (18) Yu, X.; Pickup, P. G. *Electrochem. Commun.* **2009**, *11*, 2012–2014.
- (19) Tang, Y.; Roberts, C. A.; Perkins, R. T.; Wachs, I. E. *Surf. Sci.* **2016**, *650*, 103–110.
- (20) Baschuk, J. J.; Li, X. *Int. J. Energy Res.* **2001**, *25*, 695–713.
- (21) Li, Q.; He, R.; Gao, J.-A.; Jensen, J. O.; Bjerrum, N. J. *J. Electrochem. Soc.* **2003**, *150*, A1599–A1605.
- (22) Ertl, G.; Neumann, M.; Streit, K. M. *Surf. Sci.* **1977**, *64*, 393–410.
- (23) Kuhn, W. K.; Szanyi, J.; Goodman, D. W. *Surf. Sci.* **1992**, *274* (3), L611–L618.
- (24) Tedsree, K.; Li, T.; Jones, S.; Chan, C. W. A.; Yu, K. M. K.; Bagot, P. A. J.; Marquis, E. A.; Smith, G. D. W.; Tsang, S. C. E. *Nat. Nanotechnol.* **2011**, *6*, 302–307.
- (25) Huang, Y.; Zhou, X.; Yin, M.; Liu, C.; Xing, W. *Chem. Mater.* **2010**, *22*, 5122–5128.
- (26) Wang, Z. L.; Ping, Y.; Yan, J. M.; Wang, H. L.; Jiang, Q. *Int. J. Hydrog. Energy* **2014**, *39*, 4850–4856.
- (27) Zhou, X.; Huang, Y.; Xing, W.; Liu, C.; Liao, J.; Lu, T. *Chem. Commun.* **2008**, No. 30, 3540–3542.
- (28) Bulushev, D. A.; Zacharska, M.; Lisitsyn, A. S.; Podyacheva, O. Y.; Hage, F. S.; Ramasse, Q. M.; Bangert, U.; Bulusheva, L. G. *ACS Catal.* **2016**, *6*,

3442–3451.

- (29) Yang, X. F.; Wang, A.; Qiao, B.; Li, J.; Liu, J.; Zhang, T. *Acc. Chem. Res.* **2013**, *46*, 1740–1748.
- (30) Kyriakou, G.; Boucher, M. B.; Jewell, A. D.; Lewis, E. A.; Lawton, T. J.; Baber, A. E.; Tierney, H. L.; Flytzani-Stephanopoulos, M.; Sykes, E. C. H. *Science* **2012**, *335*, 1209–1212.
- (31) Zhao, Z.-J.; Chiu, C.; Gong, J. *Chem. Sci.* **2015**, *6*, 4403–4425.
- (32) Yi, N.; Saltsburg, H.; Flytzani-Stephanopoulos, M. *ChemSusChem* **2013**, *6*, 816–819.
- (33) Tierney, H. L.; Baber, A. E.; Sykes, E. C. H. *J. Phys. Chem. C* **2009**, *113*, 7246–7250.
- (34) Baber, A. E.; Tierney, H. L.; Lawton, T. J.; Sykes, E. C. H. *ChemCatChem* **2011**, *3*, 607–614.
- (35) Bellisario, D. O.; Han, J. W.; Tierney, H. L.; Baber, A. E.; Sholl, D. S.; Sykes, E. C. H. *J. Phys. Chem. C* **2009**, *113*, 12863–12869.
- (36) Lucci, F. R.; Lawton, T. J.; Pronschinske, A.; Sykes, E. C. H. *J. Phys. Chem. C* **2014**, *118*, 3015–3022.
- (37) Lucci, F. R.; Liu, J.; Marcinkowski, M. D.; Yang, M.; Allard, L. F.; Flytzani-Stephanopoulos, M.; Sykes, E. C. H. *Nat. Commun.* **2015**, *6*, 8550.
- (38) Wachs, I. E.; Madix, R. J. *Surf. Sci.* **1979**, *84*, 375–386.
- (39) Ying, D. H. S.; Madix, R. J. *J. Catal.* **1980**, *61*, 48–56.
- (40) Bowker, M.; Madix, R. J. *Surf. Sci.* **1981**, *102*, 542–565.
- (41) Hayden, B. E.; Prince, K.; Woodruff, D. P.; Bradshaw, A. M. *Surf. Sci.* **1983**, *133*, 589–604.
- (42) Marcinkowski, M. D.; Murphy, C. J.; Liriano, M. L.; Wasio, N. A.; Lucci, F. R.; Sykes, E. C. H. *ACS Catal.* **2015**, *5*, 7371–7378.
- (43) Thomas, F. S.; Masel, R. I. *Surf. Sci.* **2004**, *573*, 169–175.
- (44) Motoo, S.; Furuya, N. *J. Electroanal. Chem.* **1985**, *184*, 303–316.
- (45) Lucci, F. R.; Marcinkowski, M. D.; Lawton, T. J.; Sykes, E. C. H. *J. Phys. Chem. C* **2015**, *119*, 24351–24357.
- (46) Dastoor, P. C.; O'Connor, D. J.; MacLaren, D. A.; Allison, W.; Noakes, T. C. Q.; Bailey, P. *Surf. Sci.* **2005**, *588*, 101–107.

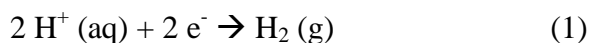
- (47) Baber, A. E.; Mudiyanse, K.; Senanayake, S. D.; Beatriz-Vidal, A.; Luck, K. A.; Sykes, E. C. H.; Liu, P.; Rodriguez, J. A.; Stacchiola, D. J. *Phys. Chem* **2013**, *15*, 12291–12298.
- (48) Wühn, M.; Weckesser, J.; Wöll, C. *Langmuir* **2001**, *17*, 7605–7612.
- (49) Millikan, R. C.; Pitzer, K. S. *J. Am. Chem. Soc.* **1958**, *80*, 3515–3521.
- (50) Hirata, S. *J. Chem. Phys.* **2008**, *129*, 204104.
- (51) Anger, G.; Winkler, A.; Rendulic, K. D. *Surf. Sci.* **1989**, *220*, 1–17.
- (52) Burghaus, U. *Prog. Surf. Sci.* **2014**, *89* (2), 161–217.
- (53) Christmann, K.; Ertl, G.; Pignet, T. *Surf. Sci.* **1976**, *54*, 365–392.
- (54) Avery, N. R. *Appl. Surf. Sci.* **1982**, *11–12*, 774–783.
- (55) Columbia, M. R.; Thiel, P. A. *Surf. Sci.* **1990**, *235*, 53–59.
- (56) Columbia, M. R.; Crabtree, A. M.; Thiel, P. A. *J. Am. Chem. Soc.* **1992**, *114*, 1231–1237.
- (57) Crapper, M. D.; Riley, C. E.; Woodruff, D. P. *Surf. Sci.* **1987**, *184*, 121–136.
- (58) Woodruff, D. P.; McConville, C. F.; Kilcoyne, A. L. D. *Surf. Sci.* **1988**, *201*, 228–244.
- (59) Avery, N. R. *Appl. Surf. Sci.* **1982**, *13*, 171–179.
- (60) Jewell, A. D.; Peng, G.; Mattera, M. F. G.; Lewis, E. A.; Murphy, C. J.; Kyriakou, G.; Mavrikakis, M.; Sykes, E. C. H. *ACS Nano* **2012**, *6*, 10115–10121.
- (61) Tierney, H. L.; Baber, A. E.; Kitchin, J. R.; Sykes, E. C. H. *Phys. Rev. Lett.* **2009**, *103*, 246102.
- (62) Karpfen, A. *Chem. Phys.* **1984**, *88*, 415–423.
- (63) Liu, J.; Lucci, F. R.; Yang, M.; Lee, S.; Marcinkowski, M. D.; Therrien, A. J.; Williams, C. T.; Sykes, E. C. H.; Flytzani-Stephanopoulos, M. *J. Am. Chem. Soc.* **2016**, *138*, 6396–6399.
- (64) Gokhale, A. A.; Dumesic, J. A.; Mavrikakis, M. *J. Am. Chem. Soc.* **2008**, *130*, 1402–1414.
- (65) Grabow, L. C.; Gokhale, A. A.; Evans, S. T.; Dumesic, J. A.; Mavrikakis, M. *J. Phys. Chem. C* **2008**, *112*, 4608–4617.
- (66) Zhang, C. J.; Baxter, R. J.; Hu, P.; Alavi, A.; Lee, M. H. *J. Chem. Phys.* **2001**, *115*, 5272–5277.

- (67) Boucher, M. B.; Zugic, B.; Cladaras, G.; Kammert, J.; Marcinkowski, M. D.; Lawton, T. J.; Sykes, E. C. H.; Flytzani-Stephanopoulos, M. *Phys. Chem. Chem. Phys.* **2013**, *15*, 12187–12196.

Chapter 8: Evidence of Isotopic Scrambling between H₂O and D₂ on Pd/Cu Alloys

8.1 Introduction

The presence and importance of water is ubiquitous throughout scientific research in many fields. The interaction of water with surfaces has been extensively studied due to the relevance of water as an adsorbate to both heterogeneous catalysis and electrochemistry.¹⁻³ Surface science has proven capable of modeling phenomenon that occur in electrochemistry including the formation of the electric-double layer on electrodes.^{4,5} With this success in mind, surface science can be applied to other principles in electrochemistry including the standard hydrogen electrode (SHE), the reference for electrochemical redox potentials. The SHE is derived from the following half-cell reaction.



This expression involves aqueous protons, electrons generated from a metal surface, and gaseous hydrogen.⁶ Examining the interaction of hydrogen and water on metal single crystals can help develop an understanding of this fundamental process.⁶⁻⁹

In this study we examine the interaction of H₂O and D_a on Pd/Cu alloy surfaces using temperature programmed desorption (TPD). We have previously shown that these Pd/Cu alloys allow for the dissociation and spillover of hydrogen and deuterium.¹⁰⁻¹² We find that as the concentration of Pd increases isotopic exchange begins to take place between adsorbed H₂O and D_a leading to the

desorption of HDO and HD species. The literature shows this reaction also occurs on Pt and Au surfaces due to the formation of $(\text{H}_2\text{O})_n\text{H}^+$ clusters.^{6,7,9} However, Cu surfaces are typically unable to activate this process.^{7,8} The difference between these surfaces was proposed to be due to differences in work functions of the metals, as Cu has a relatively low work function compared to Pt, Pd, or Au.^{7,13} Since our Pd/Cu alloys enable isotopic exchange, this infers that the addition of Pd to Cu begins to shift the work function of the surface closer to that of Pd. This study also probes the formation and breaking of O-H bonds in water clusters on Pd/Cu alloy surfaces.

8.2 Results and Discussion

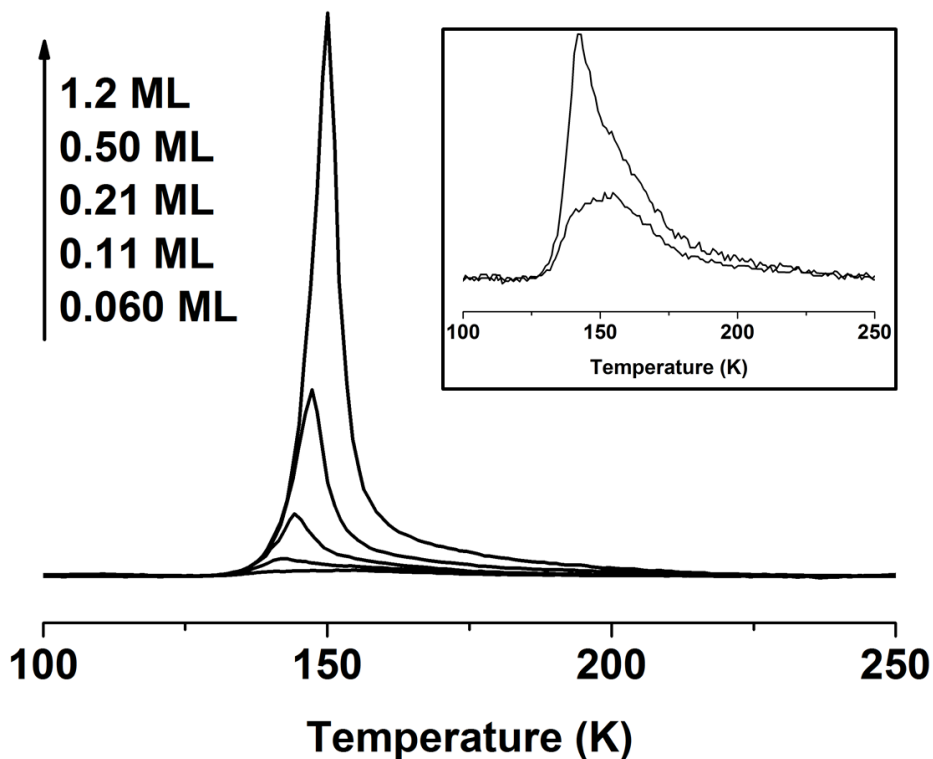


Figure 8.1 TPD spectra of the uptake of H_2O on Cu(111) at 85 K. Inset shows a zoomed in view of the two lowest coverage spectra in the main figure (0.060 ML and 0.11 ML).

The adsorption of water on the Cu(111) surface has been well studied and our findings agree well with previously published results.¹⁴⁻¹⁶ At the intermediate to high coverage in this study water desorbs in a single peak exhibiting zero order kinetics which shifts from 142 K up to 150 K as coverage increases (Figure 8.1). This is consistent with a metastable phase of water which interacts relatively strongly with the surface which was discussed by Hinch and Dubois.¹⁴ Even in this regime, the intermolecular interactions between water molecules is stronger than the interaction of water with Cu.¹⁵ Increasing the coverage of water eventually results in the growth of a polycrystalline ice like structure that desorbs above 160 K, but in our experiments we never examine a water coverage high enough to obtain this phase.^{14,15} At very low coverage, water desorbs from the surface in a single peak at 152 K that exhibits first order like kinetics (Figure 8.1 Inset). This is due to water preferentially binding to step edges of the Cu crystal due to the absence of neighboring water molecules with which it can interact.^{1,3,14,15} In the experiment where the initial water coverage is 0.11 ML the transition between the two phases is observed (Figure 8.1 Inset). In the TPD spectra for 0.11 ML water primarily desorbs in a sharp peak at 142 K, but a clear shoulder is also evident in the TPD spectra, indicating the presence of some water strongly bound to defects.

We next examined the interaction of water with deuterium on Cu(111). As Cu surfaces are typically inactive for deuterium activation¹⁷, we prepared Pd/Cu alloys at 380 K with Pd loadings of 0.01, 0.05, 0.10 and 0.20 ML. Pd is known to alloy into the Cu lattice at step edges forming a “brim” of Pd around the step

edges.^{11,18,19} Up to 0.05 ML, Pd exists as isolated atoms substituted in the Cu lattice and therefore makes a SAA.^{11,18,20} At a coverage of 0.10 ML Pd, isolated atoms are still the primary species although small amounts of dimers and trimers are also present. By 0.20 ML Pd, larger Pd clusters form in fingers protruding from the brim.¹⁹ We have demonstrated that these alloys are effective at dissociating hydrogen and deuterium and allowing them to spillover to the Cu terraces.¹⁰⁻¹²

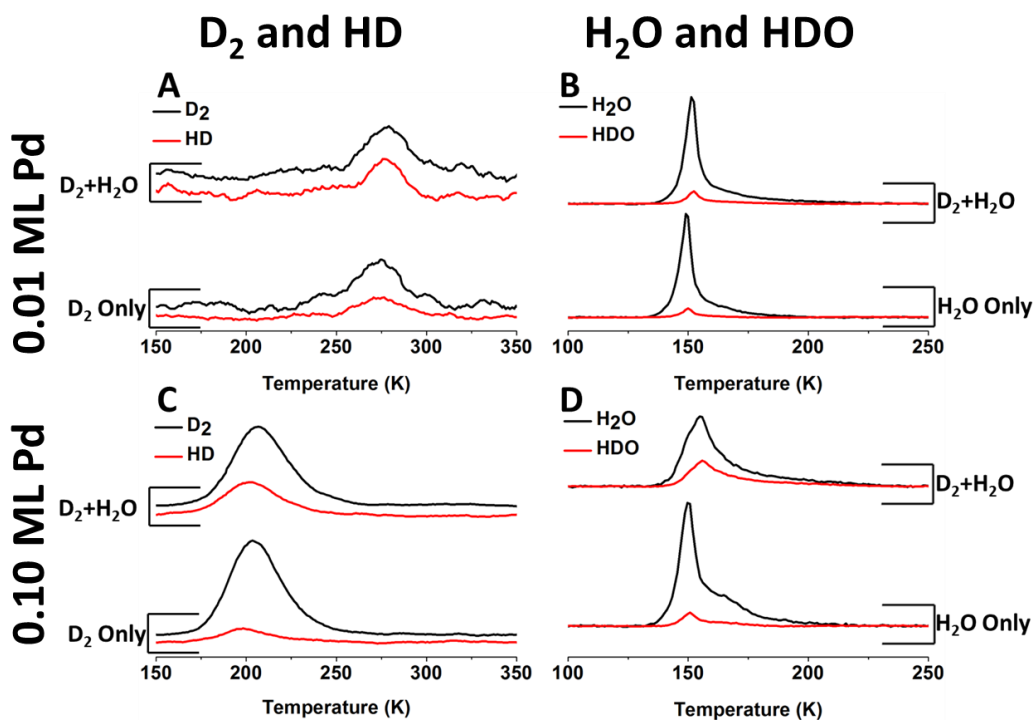


Figure 8.2 Evidence of isotopic scrambling between D and H₂O on Pd/Cu alloys. TPD spectra on a 0.01 ML Pd/Cu alloy are displayed in (A) and (B). TPD spectra on a 0.10 ML Pd/Cu alloy are displayed in (C) and (D). (A,C) Desorption of D₂ and HD on surfaces exposed to D₂ (bottom) and H₂O with D₂ (top). (B,D) Desorption of H₂O and HDO on surfaces exposed to H₂O (bottom) and H₂O with D₂ (top). In all cases the surface is exposed to H₂O at 85 K and D₂ at 150 K. Deuterium exposures were 100 Langmuirs (1 L = 1 × 10⁻⁶ torr s) while water exposures were 2 L.

Figure 8.2 shows a set of experiments performed on 0.01 and 0.10 ML Pd/Cu(111) surfaces. The alloy surfaces were exposed solely to D₂, solely to H₂O, or to both species at the same time. On the 0.01 ML surface, there is little difference between TPD spectra where both H₂O and D₂ are adsorbed and spectra where the species are individually adsorbed (Figure 8.2A). When only D₂ is exposed to the surface, D₂ desorbs from the 0.01 ML surface at ~280 K (Figure 8.2A bottom). While this is significantly higher than the temperature of hydrogen desorption from the same alloy surface (210 K),^{11,20} the D_a coverage in this experiment corresponds to a coverage of < 0.005 ML, and second order kinetics shifts this peak to higher temperature.^{21,22} It is difficult to obtain high coverages of deuterium with such a low Pd loading.^{12,20} In addition, the kinetic isotope effect causes D₂ to desorb from a surface at higher temperature than H₂ due to stronger binding of D_a vs H_a.²³ If isotopic scrambling does occur between H₂O and D_a, it is expected that the amount of HD and HDO desorbing from the surface should increase when the two species are co-adsorbed compared to when they are adsorbed individually. In addition the amount of D₂ and H₂O should decrease. On the 0.01 ML Pd/Cu alloy there is no increase in the amount of HD desorbing from the surface when H₂O and D_a are co-adsorbed (Figure 8.2A top) compared to when only D_a is adsorbed. In addition there is only a very minor increase in the amount of HDO formed when the two species are co-adsorbed compared to when only H₂O is adsorbed (Figure 8.2B). This implies that isotopic scrambling does not occur when the Pd coverage is very low. Previous work has showed that

isotopic scrambling does not occur on Cu(110) surfaces so it is unsurprising that a slightly modified Cu(111) surface will also not perform this chemistry.^{7,8}

Increasing the Pd concentration to 0.10 ML causes significant changes compared to the 0.01 ML surface. Deuterium desorbs from such a surface at 200 K (Figure 8.2C bottom). This shift to lower temperature is expected as hydrogen adsorbed onto a 0.10 ML surface desorbs at 175 K due to strain in the surface induced by the larger Pd atoms trying to fit into the Cu lattice.¹¹ On both alloy surfaces the TPD spectra of water displays a small additional desorption feature at 170 K, which we attribute to water binding slightly stronger to Pd sites on the surface.²⁴ This effect is more noticeable on the 0.10 ML Pd/Cu alloy. Significantly, when H₂O and D_a are co-adsorbed on the 0.10 ML alloy surface there is an increase in HD desorbing as well as a decrease in the amount of D₂ compared to when only D_a is adsorbed (Figure 8.2C). This is accompanied by an increase in HDO and a decrease in H₂O when the two species are co-adsorbed compared to when only H₂O is adsorbed (Figure 8.2D). These changes imply that isotopic change is occurring between the two species. Similar results were observed on Pt and Au surfaces.^{6-9,25,26} In addition to isotopic exchange, Pan et al. observed significant stabilizing effects between hydrogen and water on Au(111),⁹ while Shan et al. showed that water was destabilized in the presence of hydrogen on Ni(111).²⁷ We observed little change in the temperature of desorption for either species when they are co-adsorbed compared to when they are individually adsorbed, which is similar to results on Pt and Cu surfaces.^{7,8,26}

The mechanism for isotopic exchange between water and hydrogen species on metal surfaces is most easily explained by the formation of $(\text{H}_2\text{O})_n\text{H}^+$ clusters on the surface.^{9,26,28} Initial studies examining co-adsorbed hydrogen and water on Pt hypothesized that H_3O^+ was formed based on HREELS results.^{7,25} However, H_3O^+ is unstable on metal surfaces.^{9,26} HREELS studies by Chen et al. and DFT studies by Pan et al. show that it is more likely that formation of $(\text{H}_2\text{O})_n\text{H}^+$ structures as these clusters are more thermodynamically stable than H_2O and H_a separately adsorbed on the surface.^{9,26} In our case, when D_a and H_2O are adsorbed on the surface, some D is incorporated into $(\text{H}_2\text{O})_n\text{D}^+$ clusters, forming a new O-D bond. During the TPD ramp, the clusters break apart as species desorb, breaking either O-H or O-D bonds. In some cases D remains incorporated in a water molecule and a H_a is formed. This leaves a HDO molecule and an H_a that can recombine with a D_a to desorb as HD. It is interesting that alloying small amounts of Pd onto the surface allows for such an interaction as no isotopic exchange was observed on Cu(110) surfaces.^{7,8} To further probe this interaction we examine a wider range of Pd concentrations.

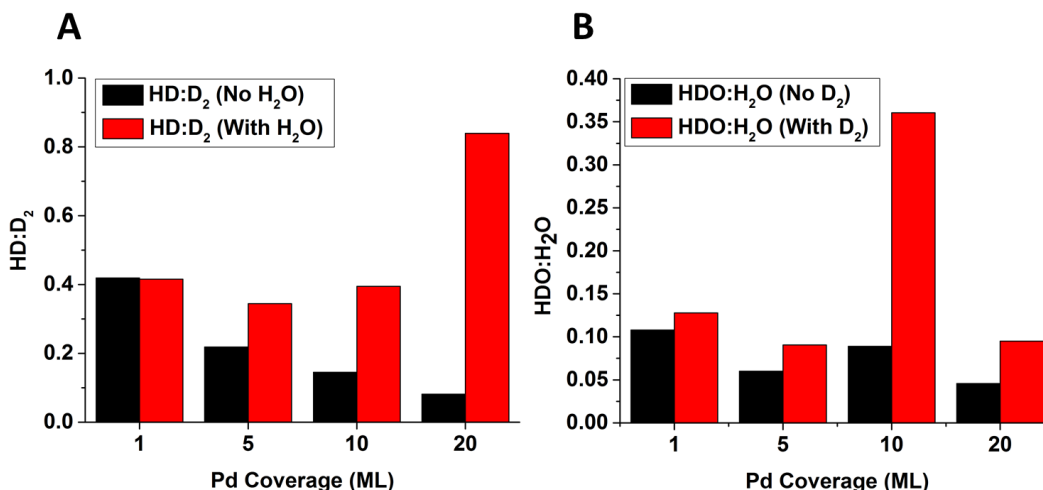


Figure 8.3 Isotopic exchange on a range of Pd concentrations. (A) Ratio of HD:D₂ after exposing the crystal to D₂ (black bars) and to D₂ and H₂O (red) bars for four different Pd concentrations. (B) Ratio of HDO:H₂O after exposing the crystal to H₂O (black bars) and to D₂ and H₂O (red bars).

Figure 8.3 shows the ratios of HD:D₂ (a) and the ratios of HDO:H₂O (b) for four different alloy surfaces for experiments where only H₂O or D_a was adsorbed (black bars) and experiments where both H₂O and D_a were adsorbed (red bars). An increase in the ratio of either HD:D₂ or HDO:H₂O when the species are co-adsorbed shows that isotopic exchange is occurring. As previously discussed, no isotopic exchange is observed on a 0.01 ML Pd/Cu(111) surface. The ratio of HD:D₂ is nearly identical in both experiments and the ratio of HDO:H₂O is only slightly larger when H₂O and D₂ are co-adsorbed. Isotopic exchange is observed on a 0.05 ML Pd/Cu(111) surface as both ratios increase in the presence of both species. The extent of isotopic exchange increases when the Pd concentration is raised to 0.10 ML. However, for a 0.20 ML Pd/Cu(111) surface, while isotopic exchange does seem to occur the results are not as clear cut. The ratio of HD:D₂ drastically increases, but only a modest increase is seen in

the ratio of HDO:H₂O. It is possible on this surface that a large amount of H₂ was adsorbed from the chamber background. H₂ activation becomes more facile with increasing Pd concentration and H₂ is the major component present in the background of the ultra-high vacuum experiment used to perform TPD experiments.²⁰ Significant amounts of H₂ were observed to desorb in the co-adsorption experiment on the 0.20 ML surface. If the amount of H_a on the surface is increased this H_a will also interact with H₂O and limit the amount of D_a that does. In addition the excess H_a can combine with D_a to form excess HD, while the amount of HDO formed remains low.

In general, the trend seems to be that occurrence of isotopic change increases with increasing Pd concentration. It is expected that the process of incorporating H_a into a water cluster is an activated process, and it may be that increasing the amount of Pd in the Cu lowers the barrier to this process.⁹ However, this process occurs readily on Au(111) so it is surprising that even bare Cu cannot perform this chemistry.⁷⁻⁹ Lackey et al. found that isotopic exchange between H₂O and D₂ does not occur on Cu(110) but does on Pt(111). They attributed this finding to the higher work function of Pt which helps stabilize electron transfer to the surface from adsorbates, allowing for formation of a positively charged water clusters.⁷ With this theory in mind, the activity of Cu vs Au can be explained. Au(111)'s work function is 5.31 eV, Pt(111)'s is 5.7 eV and Pd(111)'s is 5.6 eV.¹³ These surfaces are all able to perform isotopic exchange through (H₂O)_nH⁺. Cu(111) has a significantly lower work function than any of these surfaces (4.94 eV) and thus is unable to stabilize the (H₂O)_nH⁺ clusters.¹³

However, the addition of at least 0.05 ML Pd affects the Cu(111) surface enough to allow for isotopic exchange, possibly due to a change in the work function of the alloy surface.

8.3 Conclusion

We have demonstrated that Pd/Cu(111) alloys are capable of performing isotopic exchange between H₂O and D₂. Very low loadings of Pd (0.01 ML) are inactive for this reaction, but increasing the concentration of Pd to 0.05 ML above causes the surface to be active. In general isotopic exchange increases with increasing Pd coverage. Isotopic exchange is most likely caused by the incorporation of D_a into (H₂O)_nD⁺ clusters which break up as species begin to desorb. While Cu surfaces are typically unable to perform this chemistry, we hypothesize the addition of relatively small amounts of Pd influences the work function of the alloy surface making it a better electron acceptor. Despite the formation of (H₂O)_nD⁺ the desorption temperature of D₂ and H₂O is unaffected, which is consistent with results on Cu and Pt surfaces where both species are adsorbed⁶⁻⁸, but inconsistent with chemistry observed on a Au(111) surface.⁹ Water adsorbs slightly more strongly to Pd sites in the alloy surface. Our experiments probe a reaction relevant to electrochemistry and demonstrate the ability of the Pd/Cu alloy system to activate O-H bonds.

8.4 Experimental Methods

The ultra-high vacuum chamber described in Chapter 2 was used to perform the TPD experiments in this chapter. Deuterium (99.999% Airgas) was

exposed to the surface via a collimated high-precisions leak valve that could be pointed directly at the sample surface. The sample was always held at 150 K during deuterium adsorption. Deuterium coverages were calculated based on a saturation of unity when hydrogen was adsorbed on a 5.0 ML Pd film. M/z 4, m/z 3, and m/z 2 were tracked for D₂, HD and H₂ respectively. In most experiments desorption of H₂ was not observed. Deionized H₂O was obtained from a Nanopure water system and was exposed to the sample via backfilling the chamber with water vapor through a high-precision leak valve. Water coverages were calculated by correcting areas under the TPD peaks for the cross section and cracking patterns of water and directly comparing this corrected area to the corrected area of a monolayer of methanol.¹⁶ M/z 18, m/z 19, and m/z 20 were tracked for H₂O, HDO and D₂O. Only minimal amounts of D₂O were detected (2 orders of magnitude below the H₂O signal). Pd was deposited at 380 K using a Focus EFM3 electron beam evaporator and Pd coverages were calibrated via CO (99.99% Airgas) titration.

8.5 References

- (1) Henderson, M. A.; London, A.; York, N.; Paris, O.; Tokyo, S. *Surf. Sci. Rep.* **2002**, *46*, 1–308.
- (2) Thiel, P. A.; Madey, T. E. *Surf. Sci. Rep.* **1987**, *7*, 211–385.
- (3) Hodgson, A.; Haq, S. *Surf. Sci. Rep.* **2009**, *64*, 381–451.
- (4) Sass, J. K.; Bange, K.; Döhl, R.; Piltz, E.; Unwin, R. *Ber. Bunsenges. Phys. Chem.* **1984**, *359*, 354–359.
- (5) Sass, J. K. *Vacuum* **1983**, *33*, 741–751.
- (6) Kizhakevariam, N.; Stuve, E. M. *Surf. Sci.* **1992**, *275*, 223–236.

- (7) Lackey, D.; Schott, J.; Sass, J. K.; Woo, S. I. *Chem. Phys. Lett.* **1991**, *184*, 277–281.
- (8) Schott, J.; Lackey, D.; Sass, J. K. *Surf. Sci.* **1990**, *238*, L478–L480.
- (9) Pan, M.; Pozun, Z. D.; Yu, W.-Y.; Henkelman, G.; Mullins, C. B. *J. Phys. Chem. Lett.* **2012**, *3*, 1894–1899.
- (10) Tierney, H. L.; Baber, A. E.; Kitchin, J. R.; Sykes, E. C. H. *Phys. Rev. Lett.* **2009**, *103*, 246102.
- (11) Kyriakou, G.; Boucher, M. B.; Jewell, A. D.; Lewis, E. A.; Lawton, T. J.; Baber, A. E.; Tierney, H. L.; Flytzani-Stephanopoulos, M.; Sykes, E. C. H. *Science (80-.)*. **2012**, *335*, 1209–1212.
- (12) Kyriakou, G.; Davidson, E. R. M.; Peng, G.; Roling, L. T.; Singh, S.; Boucher, M. B.; Marcinkowski, M. D.; Mavrikakis, M.; Michaelides, A.; Sykes, E. C. H. *ACS Nano* **2014**, *8*, 4827–4835.
- (13) Skriver, H. L.; Rosengaard, N. M. *Phys. Rev.* **1992**, *46*, 7157–7168.
- (14) Hinch, B. J.; Dubois, L. H. *J. Chem. Phys.* **1992**, *96*, 3262–3268.
- (15) Hinch, B. J.; Dubois, L. H. *Chem. Phys. Lett.* **1991**, *181*, 10–15.
- (16) Boucher, M. B.; Marcinkowski, M. D.; Liriano, M. L.; Murphy, C. J.; Lewis, E. A.; Jewell, A. D.; Mattera, M. F. G.; Kyriakou, G.; Flytzani-stephanopoulos, M.; Sykes, E. C. H. *ACS Nano* **2013**, *7*, 6181–6187.
- (17) Anger, G.; Winkler, A.; Rendulic, K. D. *Surf. Sci.* **1989**, *220*, 1–17.
- (18) Tierney, H. L.; Baber, A. E.; Sykes, E. C. H. *J. Phys. Chem. C* **2009**, *113*, 7246–7250.
- (19) Aaen, A. B.; Lægsgaard, E.; Ruban, A. V.; Stensgaard, I. *Surf. Sci* **1998**, *408*, 43–56.
- (20) Boucher, M. B.; Zugic, B.; Cladaras, G.; Kammert, J.; Marcinkowski, M. D.; Lawton, T. J.; Sykes, E. C. H.; Flytzani-Stephanopoulos, M. *Phys. Chem. Chem. Phys.* **2013**, *15*, 12187–12196.
- (21) Ranke, W. In *Lecture at the Fritz Haber Institut of the MPG*; Berlin, 2003.
- (22) Kolasinski, K. W. *Surface Science*, 3rd ed.; Wiley, 2012.
- (23) Yates, J. T.; Peden, C. H. F.; Houston, J. E.; Goodman, D. W. *Surf. Sci.* **1985**, *160*, 37–45.
- (24) Clay, C.; Cummings, L.; Hodgson, A. *Surf. Sci.* **2007**, *601*, 562–568.
- (25) Wagner, F. T.; Moylan, T. E. *Surf. Sci.* **1988**, *206*, 187–202.

- (26) Chen, N.; Blowers, P.; Masel, R. I. *Surf. Sci.* **1999**, *419*, 150–157.
- (27) Shan, J.; Aarts, J. F. M.; Kleyn, A. W.; Juurlink, L. B. F. *Phys. Chem. Chem. Phys.* **2008**, *10*, 2227–2232.
- (28) Hammer, N. I.; Diken, E. G.; Johnson, M. a; Walters, R. S.; Jaeger, T. D.; Duncan, M. a; Christie, R. a; Jordan, K. D. *Science* **2004**, *304*, 1137–1140.

Chapter 9: A Route to More Efficient C-H Activation with Pt/Cu Single Atom Alloys

9.1 Introduction

C-H activation in alkanes has become a topic of increased interest in recent years.¹⁻⁴ Due to the increased production of shale gas from hydraulic fracturing, the supply of light alkanes such as ethane and propane has increased significantly.^{5,6} However, there are few methods available to utilize these chemicals due to their relative inertness.^{4,7} It has become a goal of chemists to find catalysts capable of facilely activating these typically unreactive bonds in order to open new routes to synthesize a variety of fine chemicals. For example, dehydrogenation of alkanes produces alkenes, which are pre-cursors to industrially relevant polymers.^{3,5} Ni based catalysts are often used for C-H activation, due to the fact that Ni is relatively inexpensive, but suffer from coking as Ni breaks C-C bonds in alkanes and can completely dehydrogenate alkanes to carbon.⁸⁻¹⁰ Pt, which is also frequently used as a C-H activation catalyst, suffers from coking like Ni.¹¹⁻¹³ Cu based catalysts are typically not considered viable due to the high barrier to C-H activation on Cu surfaces, but do avoid the problem of coking.¹⁴

In this work, we examine C-H activation in methyl groups on a 0.01 ML Pt/Cu(111) SAA (Figure 9.1A). At this low concentration, Pt exists as isolated atoms substituted into the Cu(111) lattice. We have previously characterized such Pt/Cu surfaces and refer to them as *single atom alloys* (SAAs).¹⁵⁻¹⁷ These SAAs are capable of selective hydrogenation and dehydrogenation chemistry.^{15,16} We

show that the SAA activates C-H bonds in CH₃ at 350 K, a temperature intermediate to that of Cu(111) and Pt(111) (450 and 270 K respectively) while avoiding the problem of coking. In order to study C-H activation in a well-defined system, we use ultra-high vacuum (UHV) conditions which allow the use temperature programmed reaction (TPR) and high-resolution scanning tunneling microscopy (STM) and we make use of methyl iodide as a model system. CH₃I has been well studied on a number of metal surfaces in UHV, including Pt and Cu, and is known to dissociate to form CH₃ and I.¹⁸⁻³¹ Methyl iodide serves as a stand in for methane, which does not adsorb intact to metals nor easily activate under conditions used in our experiments.³² It allows us to examine the intermediates of methane dehydrogenation under UHV conditions where we can observe reaction kinetics with TPD and image intermediates and active sites using STM. The effect of co-adsorbed iodine is minimal, except as a site blocker (Appendix Figures 15 and 16).^{31,33}

9.2 Results and Discussion

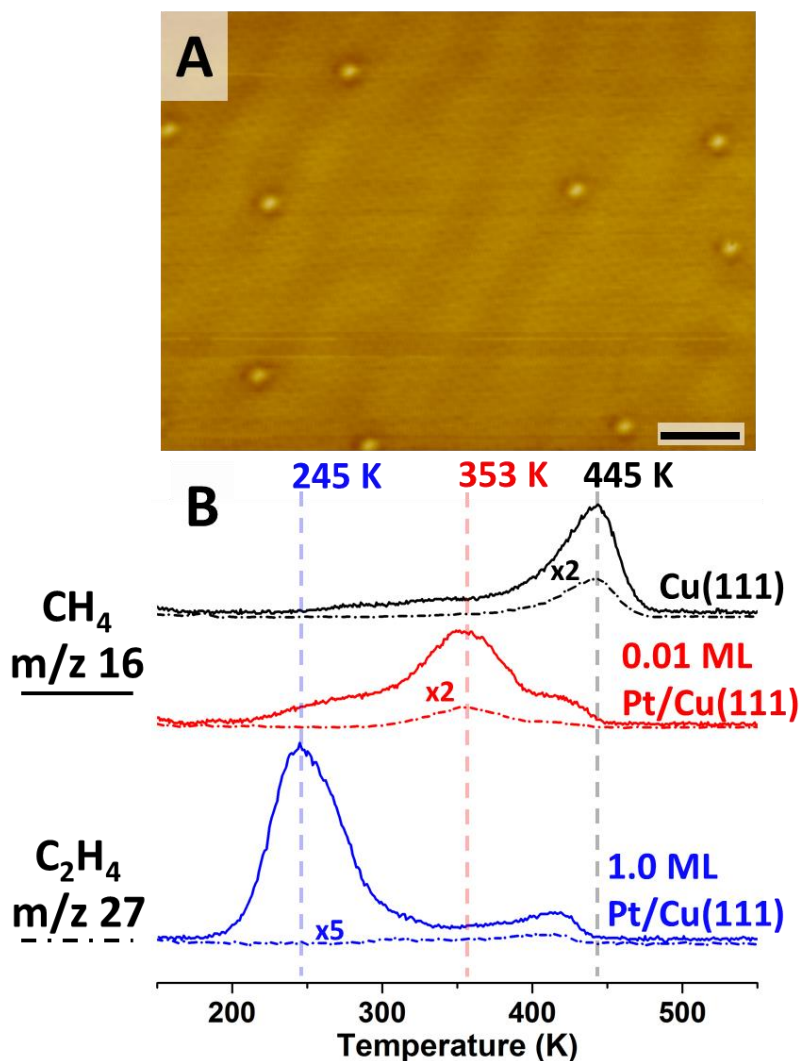


Figure 9.1 Decomposition of methyl iodide on various metal surfaces. (a) STM image of a 0.01 ML Pt/Cu(111) SAA. (b) TPR spectra for methane and ethene for Cu(111), 0.01 ML Pt/Cu(111) and 1.0 ML Pt/Cu(111) resulting from deposition of 4.5 L of methyl iodide on each surface.

TPR spectra resulting from the reaction of 4.5 Langmuirs ($1 \text{ L} = 1 \times 10^{-6}$ Torr s) of methyl iodide on several surfaces are presented in Figure 9.1B. No intact CH_3I desorbs from any of the surfaces studied after this exposure. The major desorption product observed for all surfaces examined is methane. In addition, ethene, ethane, and propene are produced. For clarity, only traces for

methane (solid lines) and ethene (dashed lines) are displayed in Figure 9.1. Appendix Figure 17 contains examples of traces for all desorption products. In general when ethene is formed, ethane and propene are as well. All products are reaction rate limited as these small hydrocarbons normally desorb from Cu(111) at very low temperatures.^{25,34,35} The black spectra correspond to methyl iodide's reaction on Cu(111) and agrees well with previously published results on this surface.²⁴⁻²⁶ Methane and the larger hydrocarbons desorb at ~450 K, the temperature at which the C-H bond in CH₃ dissociates. It has been previously demonstrated that the rate limiting step to the production of desorption products is the activation of this C-H bond to produce methylene and H_a.^{18,20} Methane is formed by the hydrogenation of remaining methyl groups, while the larger hydrocarbons form through the coupling of methylene and methyl. The ability to perform these coupling reactions allows the Cu surface to avoid coking. The red spectra corresponds to a 0.01 ML Pt/Cu(111) SAA alloy. On the SAA surface methane and carbon coupling products desorb at ~350 K, 100 K cooler than on the pure Cu(111) surface. The SAA has significantly lowered the barrier to C-H activation in CH₃, while still avoiding coking through C-C coupling. To further clarify that this reaction is indeed rate limited by C-H activation, we performed experiments where we directly hydrogenated methyl groups on the surface. When hydrogen is available, methane can be formed as low as 200 K via direct hydrogenation of methyl similar to results on Ni and Pt surfaces.^{27,28,36} The results of these experiments are discussed in Appendix Figure 18. A small amount of products still desorb for the SAA surface at ~425 K, a similar temperature as on

Cu(111). The Pt evaporation source used in these experiments covers only 61% of the Cu(111) crystal when depositing resulting in some areas that still behave as Cu(111). The blue spectra correspond to methyl iodide's reaction on a surface where 1 ML of Pt has been deposited on Cu(111). A representative STM image of such a surface is shown in Appendix Figure 10 (Under Appendix for Chapter 7). The majority of methane desorbs at ~250 K, a temperature close to that of methyl decomposition on a pure Pt(111) crystal.^{22,28,29} Despite activating C-H bonds at a low temperature, Pt(111) is unable to perform C-C coupling and methylene groups remain unreacted on the surface until high temperature, where they decompose further to yield surface bound carbon and gas phase H₂.^{21,22,28,29} We obtain similar results on our 1 ML Pt/Cu(111) surface, no coupling products are observed at 250 K, showing that this alloy's chemistry is more similar to that of Pt(111) than Cu(111). Hydrogen from methylene decomposition desorbs at high temperature similar to Pt(111) (Appendix Figure 19).^{22,28,29} No hydrogen desorbs from Cu(111) or the SAA surfaces. We examined alloy surfaces intermediate to 0.01 ML and 1 ML and find in general as the amount of Pt increases the temperature of C-H activation drops, but so does the production of coupling products. These results are shown in Appendix Figure 20. Our TPR results demonstrate that the Pt/Cu single atom alloy is able to activate C-H bonds at relatively low temperature like Pt(111), but avoid coking through carbon coupling like Cu(111).

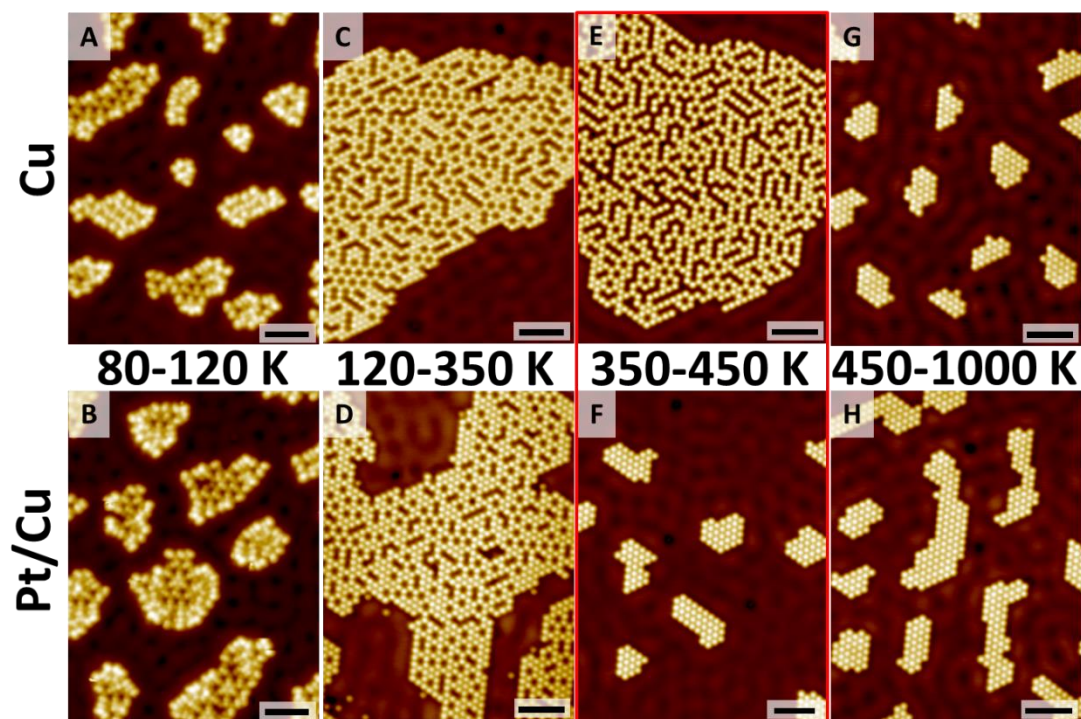


Figure 9.2 STM images revealing the various stages of the reaction of methyl iodide on Cu(111) and 0.01 ML Pt/Cu(111) (top and bottom rows respectively) after annealing to various temperatures. Scale bars = 3 nm. In images C-H iodine appears as brighter protrusions, while methyl groups appear as darker protrusions.

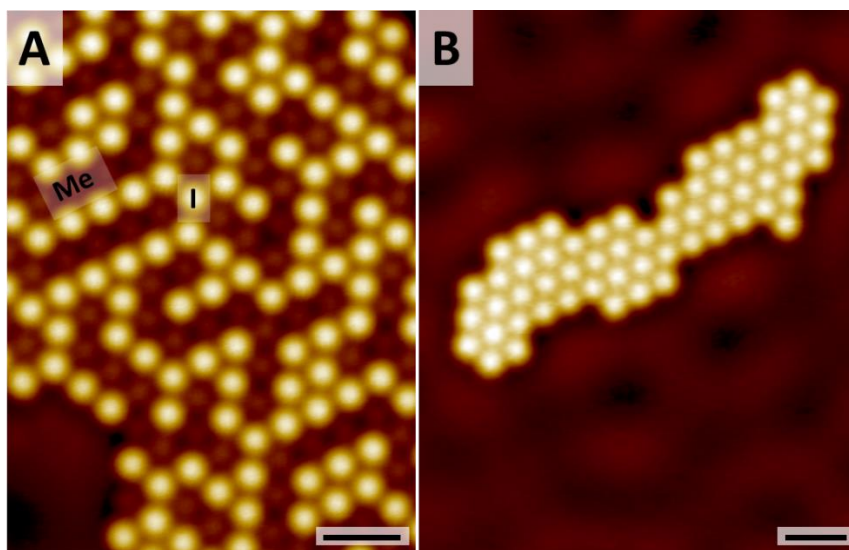


Figure 9.3 (A) High resolution STM images of mixed phase methyl and iodine after a 120 K anneal on Cu(111) and (B) iodine on Cu(111) after a 450 K anneal. Scale bars = 1 nm.

We performed STM experiments in order to quantify surface intermediates not visible in TPR experiments. Figure 9.2 shows a series of STM images taken at 5K, but annealed to different temperatures for both Cu(111) and a SAA of Pt/Cu(111). Between 80-120 K on both surfaces we observe unordered, clustered protrusions (Figure 9.2A and B). These images are of intact methyl iodide, as this is below the temperature that the C-I bond dissociates on Cu(111). Annealing either surface to 120 K results in new ordered structures on the surface (Figure 9.2C and D). On both surfaces there are intermixed bright and dark features ordered into large well-defined 2D clusters running in the $\sqrt{3}$ direction. A high-resolution STM image clearly displaying this structure is shown in Figure 9.3A. The clusters exhibit similar behavior to pure methyl groups formed via pyrolysis of azomethane on Cu(111).³⁷ We will show the bright features are iodine atoms while the dark features are methyl groups. For the Pt/Cu surface in Figure 9.2D, there are individual iodine atoms that are not connected to the larger, ordered structure. These mark positions where iodine is absorbed to single platinum atomic sites. Annealing to a higher temperature between 350-450 K results in the first major difference between the Cu(111) and 0.01 ML Pt/Cu(111) surfaces. On Cu(111) both bright and dark features remain on the surface, while on Pt/Cu the dark features have been removed leaving only bright ones, which form a $\sqrt{3} \times \sqrt{3} R30^\circ$ structure. A high-resolution STM image of such a surface is shown in Figure 9.3B. From the TPR results it is known that on 0.01 ML Pt/Cu(111) C-H activation of CH₃ occurs at 350 K. As discussed, we therefore assign dark dots as CH₃ and the bright ones as iodine atoms. Previously published

results show that both these species adsorb in fcc hollow sites and pack in a $\sqrt{3} \times \sqrt{3} R30^\circ$ structure, in good agreement with our results.^{33,37-42} On Cu(111) the barrier for C-H activation is higher and so methyl groups are still observed in Figure 9.2E where the surface was annealed to 350 K, while for Pt/Cu(111) in Figure 9.2F the C-H bond has been activated leaving only adsorbed iodine atoms. The images of iodine in Figure 9.2F-H agree with previously published STM studies of halides on Cu(111).^{41,42} Importantly no other species besides iodine are observed on the Pt/Cu surface, indicating it does not suffer from carbon coking like pure Pt(111). Annealing the surface even further to 450-1000K (9.2Figure 2G) allows the C-H bond to activate on Cu(111) leaving only iodine on the surface. On the Pt/Cu surface no change is observed when annealing to 450 K (Figure 9.2H) Iodine is very stable on Cu(111) and remains on the surface above 800 K.⁴² Annealing above 1000 K for both surfaces results in a clean Cu(111) surface (Appendix Figure 21), again showing that no carbon moieties are left on the surface as a result of the reaction of methyl iodide.

9.3 Conclusion

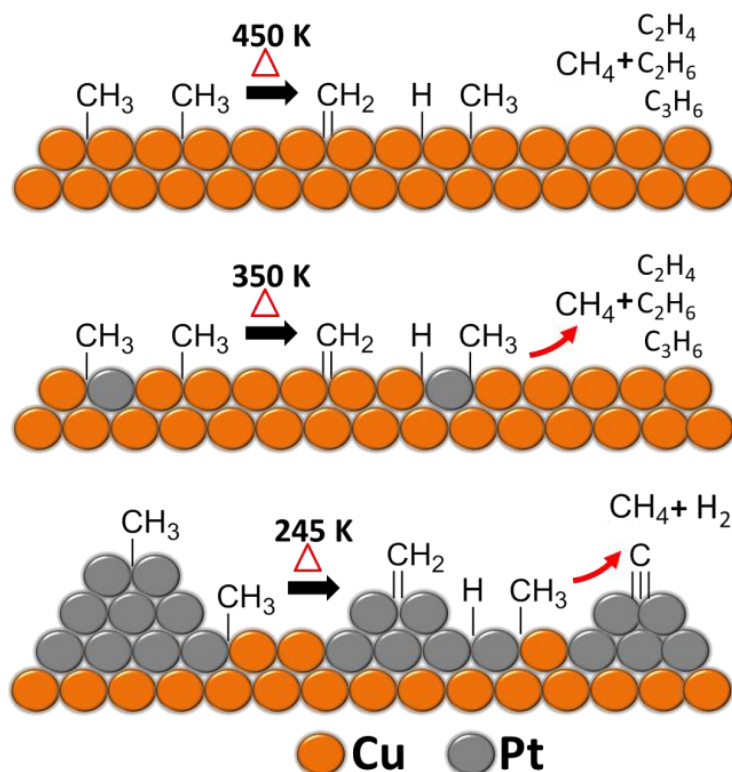


Figure 9.4 Schematics for the reaction of methyl groups with Cu(111), 0.01 ML Pt/Cu(111), and 1 ML Pt/Cu(111).

Figure 9.4 summarizes the key results of our work. On Cu(111) C-H activation does not occur until 450 K, but carbon coupling products are produced along with methane, which avoids coking.²⁴⁻²⁶ On Pt/Cu SAAs the barrier to C-H activation is lowered allowing the reaction to occur by 350 K, 100 K cooler than Cu(111), while still producing coupling products. On the 1 ML Pt/Cu(111) surface the chemistry is similar to that of Pt(111).^{21,22,28,29} Only methane and hydrogen desorb from the Pt(111) regions, indicating that similarly to Pt(111) some carbon containing species must remain on the surface. In conclusion, Pt/Cu SAAs provide a unique energy landscape where the activation barrier for C-H

activation is lowered compared to Cu(111), while still providing the ability to produce C-C products and avoid coking unlike Pt(111). We hypothesize that our results would carry over to other systems such as Ni/Cu or Pd/Cu. These results indicate that SAAs are promising candidates for C-H activation catalysts.

9.4 Experimental Methods

The two UHV chambers described in Chapter 2 were used to perform the TPD and STM experiments in this chapter. Methyl iodine was purchased from Sigma Aldrich with a purity of 99.5%. Liquid methyl iodide was degassed through freeze-pump thaw cycles before being introduced into the chambers. Hydrogen 99.999% and deuterium 99.999% were purchased from AirGas. For TPD experiments, m/z 142 was monitored to detect intact methyl iodide. M/z 41, 30, and 27 were monitored for coupling products propene, ethane, and ethene respectively. M/z 16 and 15 were monitored for methane. M/z 28 was monitored for various hydrocarbon fragments and for CO. M/z 18 and 2 were always monitored for water and hydrogen. STM images of methyl iodine were obtained at 5 K. Molecules were dosed on the Cu(111) crystals by backfilling the chamber to a desired pressure for a certain time using high precision leak valves. Pt deposition in all chambers was accomplished using flux-monitored Omicron Nanotechnology Focus EFM 3 electron beam evaporators. Pt coverages were calibrated using CO adsorption which was purchased from AirGas with a purity of 99.99%.

9.5 References

- (1) Labinger, J. A.; Bercaw, J. E. *Nature* **2002**, *417*, 507–514.
- (2) Wencel-Delord, J.; Glorius, F. *Nat. Chem.* **2013**, *5*, 369–375.
- (3) Zhao, Z.-J.; Chiu, C.; Gong, J. *Chem. Sci.* **2015**, *6*, 4403–4425.
- (4) Shilov, A. E.; Shul'pin, G. B. *Chem. Rev.* **1997**, *97*, 2879–2932.
- (5) Sattler, J. J. H. B.; Ruiz-Martinez, J.; Santillan-Jimenez, E.; Weckhuysen, B. M. *Chem. Rev.* **2014**, *114*, 10613–10653.
- (6) Bruijninx, P. C. A.; Weckhuysen, B. M. *Angew. Chem. Int. Ed.* **2013**, *52*, 11980–11987.
- (7) Mansuy, D. *Coord. Chem. Rev.* **1993**, *125*, 129–142.
- (8) Swaan, H. M.; Kroll, V. C. H.; Martin, G. A.; Mirodatos, C. *Catal. Today* **1994**, *21*, 571–578.
- (9) Ruckenstein, E.; Hu, Y. H. *Appl. Catal. A* **1995**, *133*, 149–161.
- (10) Rostrup-Nielsen, J. R.; Alstrup, I. *Catal. Today* **1999**, *53* (3), 311–316.
- (11) Jiang, F.; Zeng, L.; Li, S.; Liu, G.; Wang, S.; Gong, J. *ACS Catal.* **2015**, *5*, 438–447.
- (12) Larsson, M.; Hulten, M.; Blekkan, E. A.; Andersson, B. *J. Catal.* **1996**, *164*, 44–53.
- (13) Iglesias-Juez, A.; Beale, A. M.; Maaijen, K.; Weng, T. C.; Glatzel, P.; Weckhuysen, B. M. *J. Catal.* **2010**, *276*, 268–279.
- (14) Yang, F.; Koeller, J.; Ackermann, L. *Angew. Chem. Int. Ed.* **2016**, *55*, 4759–4762.
- (15) Lucci, F. R.; Marcinkowski, M. D.; Lawton, T. J.; Sykes, E. C. H. *J. Phys. Chem. C* **2015**, *119*, 24351–24357.
- (16) Lucci, F. R.; Liu, J.; Marcinkowski, M. D.; Yang, M.; Allard, L. F.; Flytzani-Stephanopoulos, M.; Sykes, E. C. H. *Nat. Commun.* **2015**, *6*, 8550.
- (17) Lucci, F. R.; Lawton, T. J.; Pronschinske, A.; Sykes, E. C. H. *J. Phys. Chem. C* **2014**, *118*, 3015–3022.
- (18) Azizian, S.; Gobal, F. *Langmuir* **2000**, *16*, 8095–8099.
- (19) Bushell, J.; Carley, A. F.; Coughlin, M.; Davies, P. R.; Edwards, D.; Morgan, D. J.; Parsons, M. *J. Phys. Chem. B* **2005**, *109*, 9556–9566.

- (20) Chiang, C.-M.; Wentzlaff, T. H.; Bent, B. E. *J. Phys. Chem.* **1992**, *96*, 1836–1848.
- (21) French, C.; Harrison, I. *Surf. Sci.* **1995**, *342*, 85–100.
- (22) Henderson, M. A.; Mitchell, G. E.; White, J. M. *Surf. Sci.* **1987**, *184*, L325–L331.
- (23) Jenks, C. J.; Bent, B.; Zaera, F. *J. Phys. Chem B* **2000**, *104*, 3008–3016.
- (24) Jenks, C. J.; Bent, B. E.; Zaera, F. *J. Phys. Chem. B* **2000**, No. 100, 3017–3027.
- (25) Lin, J.-L.; Bent, B. E. *J. Vac. Sci. Technol. A* **1992**, *10*, 2202–2209.
- (26) Lin, J.-L.; Bent, B. E. *J. Phys. Chem.* **1993**, *97*, 9713–9718.
- (27) Tjandra, S.; Zaera, F. *J. Catal.* **1994**, *147*, 598–600.
- (28) Zaera, F. *Surf. Sci.* **1992**, *262*, 335–350.
- (29) Zaera, F.; Hoffmann, H. *J. Phys. Chem. C* **1991**, *95* (13), 6297.
- (30) Zhou, X.-L.; White, J. M. *Surf. Sci.* **1991**, *241*, 270–278.
- (31) Chao-Ming, C.; Bent, B. E. *Surf. Sci.* **1992**, *279*, 79–88.
- (32) Liao, M.-S.; Au, C.-T.; Ng, C.-F. *Chem. Phys. Lett.* **1997**, *272*, 445–452.
- (33) Pascal, M.; Lamont, C. L. A.; Kittel, M.; Hoefl, J. T.; Constant, L.; Polcik, M.; Bradshaw, A. M.; Toomes, R. L.; Woodruff, D. P. *Surf. Sci.* **2002**, *512*, 173–184.
- (34) Canning, N. D. S.; Baker, M. D.; Chesters, M. A. *Surf. Sci.* **1981**, *111*, 441–451.
- (35) Meyers, J. M.; Gellman, A. J. *Surf. Sci.* **1995**, *339*, 57–67.
- (36) Johnson, A. D.; Daley, S. P.; Utz, A. L.; Ceyer, S. T. *Science* **1992**, *257*, 223–225.
- (37) Chan, Y. L.; Pai, W. W.; Chuang, T. J. *J. Phys. Chem. B* **2004**, *108*, 815–818.
- (38) Michaelides, A.; Hu, P. *J. Chem. Phys.* **2001**, *114*, 2523–2526.
- (39) Citrin, P. H.; Eisenberger, P.; Hewitt, R. C. *Phys. Rev. Lett.* **1980**, *45*, 1948–1951.
- (40) Wertheim, G. K. *Surf. Sci.* **1982**, *121*, 411–420.
- (41) Inukai, J.; Osawa, Y.; Itaya, K. *J. Phys. Chem. B* **1998**, *102*, 10034–10040.

- (42) Andryushechkin, B. V.; Eltsov, K. N.; Shevlyuga, V. M. *Surf. Sci.* **2001**, 472, 80–88.

Chapter 10: Future Directions and Conclusions

The density functional theory and Kinetic Monte Carlo simulations presented in this chapter were performed by Matthew Darby from the laboratory of Michail Stamatakis in the Department of Chemical Engineering at University College London. Catalysis studies were performed by Jilei Liu from the laboratory of Maria Flytzani-Stephanopolous in the Department of Chemical and Biological Engineering at Tufts University.

The viability of single atom alloys (SAAs) as catalysts for a variety of chemical reactions including H₂ activation, hydrogenations of C=C and C=O bonds, dehydrogenations, and C-H activation were demonstrated in the previous seven chapters. In general, the use of SAAs allowed for the model catalysts to achieve improved activity over Cu catalysts, while also maintaining high selectivity. In this chapter we discuss some ongoing projects related to this work and draw final conclusions on SAAs. 10.1 examines alternative molecular corks, continuing the work in Chapter 4. 10.2 discusses the possibility of hydrogenating an aldehyde using SAAs and is a continuation of the work in Chapter 5 on acetophenone hydrogenation. In 10.3, results from ongoing theory and catalysis studies on the C-H activation project discussed in Chapter 9 are shown.

10.1 Alternative Molecular Corks

In order to bring the cork system closer to practicality, it is necessary to find a cork molecule that can hold hydrogen on the surface above room temperature. CO provided an excellent, simple system to study, but is only

practical for controlling hydrogen uptake and release at cryogenic temperatures.¹ In order to achieve this a molecule must bind strongly to single Pd atoms, but still be able to desorb reversibly. With this in mind, we performed some preliminary work on thioethers which are known to bind very strongly to metal surfaces through their S atom.²⁻⁴ Figure 10.1 shows a series of temperature programmed desorption (TPD) spectra examining the applicability of dibutyl sulfide (DBS, structure shown at the bottom of Figure 10.1) as a cork molecule on a 0.01 ML Pd/Cu(111) SAA. In each experiment in Figure 10.1A, the surface was saturated with hydrogen, and then exposed to various amounts of DBS. DBS coverage is based on the saturation of the monolayer desorption peak. DBS desorbs from a single state at 390 K from the SAA surface. When a small amount of DBS is adsorbed to the surface (0.02 ML), H₂ desorbs at 246 K, only a ~36 K shift from H₂ desorbing from a clean Pd/Cu SAA surface (210 K), and 14 K cooler than when CO is used as a molecular cork (260 K). However, when the DBS coverage is increased to 0.09 ML H₂ desorbs at 268 K. Increasing the coverage of DBS even further to 0.27 ML increases the H₂ desorption temperature to 295 K, room temperature. The H₂ peak at 400 K increases with increasing DBS coverage indicating some of the molecules may be decomposing on the SAA surface.

This gradual increase in hydrogen desorption temperature with increasing DBS coverage is in stark contrast to the CO molecular cork system described in Chapter 4. Provided the Pd sites in the surface were saturated with CO, hydrogen desorbed at 260 K and this temperature did not change with increasing CO coverage. If the Pd sites were not completely blocked by CO, H₂ desorbed at 210

K. There are several possible explanations for this behavior. First, we should consider the relative binding energy of DBS to Cu vs Pd. CO binds much stronger to Pd(470 K)⁵ than it does to Cu (175 K)⁶⁻⁸, making Pd atoms the clear preferential binding site for CO in the SAA system. However, sulfur containing compounds such as DBS bind very strongly even to Au(111) where they desorb at temperature >400 K.² Sulfur atoms are predicted to bind very strongly to both Cu and Pd surfaces, with binding energies >4.4 eV.^{9,10} The TPD spectra of DBS on Cu(111) vs the SAA is very similar. Unlike the case of CO no additional peaks are seen with the addition of Pd atoms, implying that DBS binds to both Cu and Pd sites with a similar binding strength. There is a 5 K shift in the desorption temperature of DBS from 385 K on Cu(111) to 390 K upon the addition of Pd, showing that there is a very slight preference for adsorption on the Pd sites (Figure 10.1B). The similarity of binding strengths between the two sites may allow for DBS to easily diffuse between Pd and Cu sites, leaving the Pd sites free for hydrogen recombination. Using larger concentrations of DBS may keep the Pd atoms covered with DBS even when diffusion begins to occur. In comparison CO has a very strong preference to remain on the Pd sites and is unlikely to diffuse to Cu. Another possible explanation for this behavior is due to its strong binding DBS may modify the electronic structure of the surface and change the barrier to hydrogen desorption.¹¹ This would also make sense, as unlike in the case of CO, H₂ leaves the surfaces well before DBS desorbs. Recent work in our group by Felicia Lucci and Matthew Darby from UCLA on a Pt/Cu SAA cork system

indicates the cork effect is a mixture of electronic and geometric effects, and thus the reason for the behavior of DBS could be a mixture of the two hypotheses.

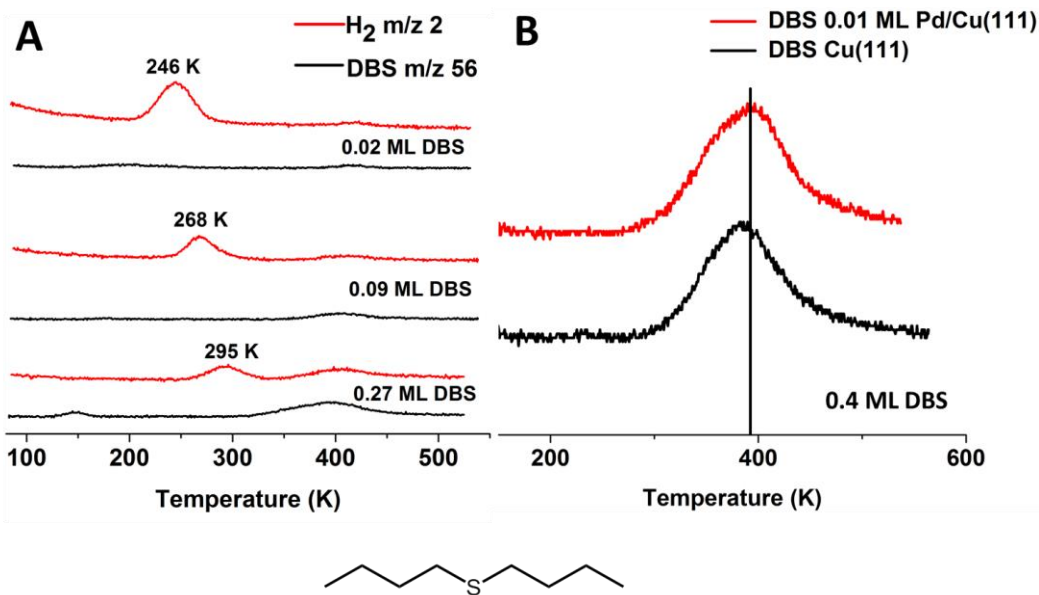


Figure 10.1 DBS as a molecular cork. (A) TPD spectra showing the effect of DBS (black traces) coverage on H₂ (red traces) desorption temperature on a 0.01 ML Pd/Cu(111) SAA. DBS is tracked with m/z 56 and H₂ is tracked with m/z 2. The DBS coverage is reported above each DBS spectra. (B) Desorption of DBS from a Pd/Cu SAA surface (red) and a Cu(111) surface. Initial coverage corresponds to 0.4 ML DBS on each surface. The black line reveals the slight shift to higher temperature upon addition of Pd to the surface. The structure of DBS is shown at the bottom of the figure.

While DBS does push the desorption temperature of H₂ close to room temperature, large coverages are required to cork the Pd sites and surface decomposition limits the repeated use of the system for hydrogen storage. DBS does reveal that in order for a cork to be successful there must be a large preference for the cork adsorbate to bind to the Pd sites over Cu. Additional thought is needed if the cork idea is to be successfully applied to hydrogen storage systems. We also mentioned in Chapter 4 that the cork effect may boost the yield of ethylbenzene in the hydrogenation of styrene, due to hydrogen remaining on

the surface until a higher temperature. However, as styrene acts as a cork it is impossible to test the system in the absence of the cork effect to compare. To see if the cork is a viable strategy for improving activity in heterogeneous catalysis we need to find a reactant that does not cork the system. In addition the reaction must be reaction rate limited rather than desorption rate limited and occur between 210-260 K.

10.2 Hydrogenation of Benzaldehyde

It was shown in Chapter 5 that acetophenone could be partially hydrogenated to form an acetophenone-H⁺ species on the Pd/Cu SAA surface. We are interested in expanding this work and finding a situation where SAAs can completely hydrogenate a C=O bond. Previous work by Pan et al. demonstrated that the hydrogenation of an aldehyde tends to be more facile than that of a ketone due to the relative instability of aldehydes in the gas phase.¹²⁻¹⁴ Based on these findings, we attempted to hydrogenate benzaldehyde, the simplest aromatic aldehyde, on a Pt/Cu SAA. Unfortunately, we were no more successful in this system than in the case with acetophenone. Low coverages of benzaldehyde desorb from the Pt/Cu SAA at 240 K. Similar to the case of acetophenone, when benzaldehyde and H_a are co-adsorbed on the SAA a new desorption feature appears at 324 K, but no benzyl alcohol, the desired hydrogenation product, is observed (Figure 10.2A). In addition hydrogen desorbs at 317 K, a much higher temperature than when it normally desorbs from the SAA surface.^{15,16} As with acetophenone, this speaks to the formation of a partially hydrogenated benzaldehyde species that eventually decomposes back to hydrogen and

benzaldehyde, rather than being fully hydrogenated to benzyl alcohol. Increasing the Pt concentration to 0.20 ML did not improve the situation, and in fact leads to an undesired decomposition reaction (Figure 10.2B). As with the 0.01 ML surface, new features for hydrogen and benzaldehyde are present at 320 and 340 K respectively. However, large amounts of m/z 78 are also observed at 351 K, consistent with the desorption of benzene formed via the decomposition of benzaldehyde. M/z 79 is also observed, but as it follows the m/z 78 trace exactly is most likely due to the natural occurrence of m/z 79 in the fragmentation pattern of benzene. The formation of larger Pt ensembles therefore does not promote the desired reaction and causes undesired decomposition of the reactant. Based on these results, and those presented in Chapter 5 it seems it may be difficult for an SAA to fully hydrogenate a C=O bond under UHV conditions.

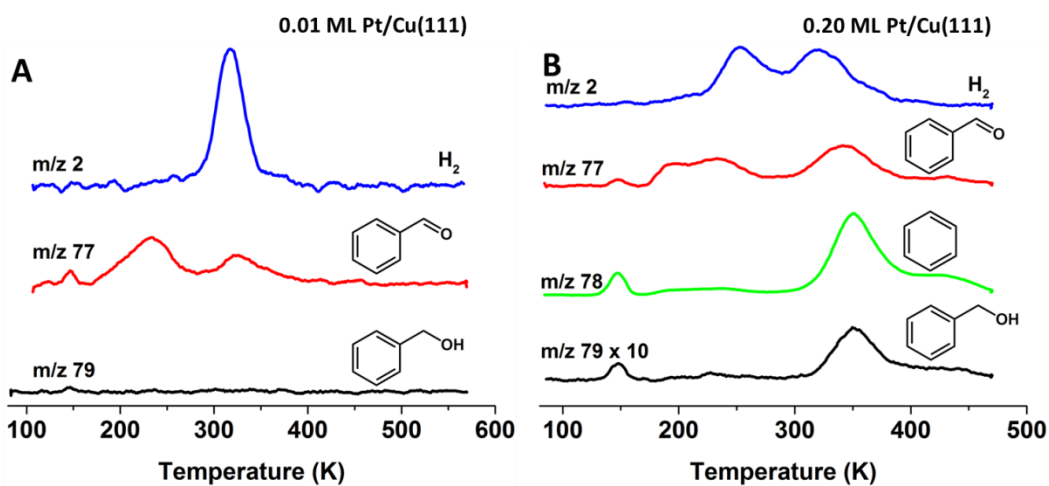


Figure 10.2 Co-adsorption of hydrogen and benzaldehyde on Pt/Cu alloys. (A) TPD spectra for H₂ (blue), benzaldehyde (red) and benzyl alcohol (black) after exposing a 0.01 ML Pt/Cu(111) SAA surface to hydrogen and benzaldehyde. (B) TPD spectra for the same molecules shown in (A) along with the desorption of benzene (green) on a 0.20 ML Pt/Cu(111) surface. The signal for m/z 79 is multiplied by ten in (B).

10.3 C-H Activation Expanded: Density Functional Theory, Kinetic Monte Carlo and Catalysis Studies

The model studies using methyl groups in Chapter 9 found that the use of Pt/Cu SAAs significantly lowered the activation barrier to C-H activation, forming the product methane 100 K cooler than on Cu(111) while maintaining the excellent selectivity of Cu. These studies are ongoing and we are currently collaborating with the group of Michail Stamatakis to examine methane and methyl dehydrogenation using density functional theory (DFT) and Kinetic Monte Carlo simulations (KMC). Figure 10.3 shows a set of KMC simulations modeling the activation of methyl to form methane for the (111) surfaces of Cu, 0.01 ML Pt/Cu, and Pt. This figure is analogous to the experiment performed in Figure 9.1B. In the simulations methane desorbs at 455 K on Cu(111), 373 K on Pt/Cu(111) and 288 K on Pt(111). These desorption temperatures agree very well with our experimental results where methane desorbs from Cu(111) at 445 K,^{17,18} from Pt/Cu(111) at 353 K, and from a 1.0 ML Pt/Cu(111) surface at 245 K. The biggest discrepancy in these finds is the comparison of the two Pt surfaces, but as shown in Appendix Figure 10, our 1.0 ML Pt surface does not result in a pristine Pt(111) overlayer. The results of the KMC experiments agree very well with experiments from the literature examining methyl decomposition on Pt(111) where methane desorbs at 285 K.^{19,20} The KMC results backup the experimental findings; the Pt/Cu alloy lowers the barrier to C-H activation significantly compared to Cu(111) but Pt surfaces have an even lower activation barrier.

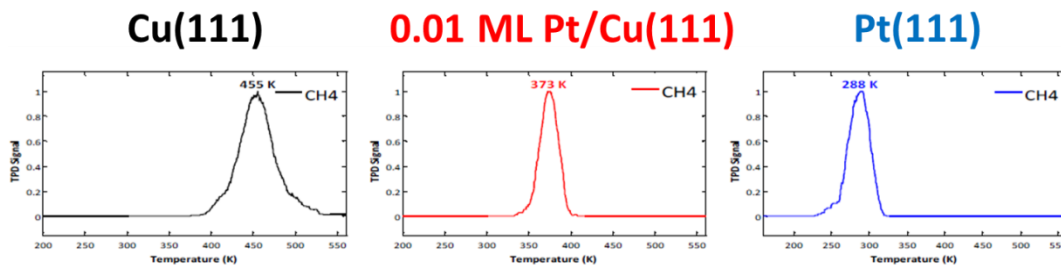


Figure 10.3 KMC simulations of methyl decomposition on Cu(111) (black), 0.01 ML Pt/Cu(111) (red), and Pt(111) (blue). A heating rate of 1K/s was used in the simulations.

While Pt alloys activate C-H bonds at lower temperature, as discussed in Chapter 9 the advantage of the SAAs for C-H activation is they avoid poisoning, and our density functional theory studies modeling methane decomposition on the three surfaces of interest also confirm this results (Figure 10.4). They also predict that the SAA surface can lower the barrier to methane activation, which we were unable to probe in our UHV studies. Figure 10.4 shows a potential energy diagram for the decomposition of methane to surface bound atomic carbon. Perhaps the most striking result in this figure is that the barrier to activate the C-H bond in methane on the SAA is predicted to be much closer to that of pure Pt than Cu. The barrier to activating methyl groups is also lower than Cu as predicted by experiments, but not as low as the barrier to activate methyls on Pt. The next step in the reaction, going from $\text{CH}_2 \rightarrow \text{CH}$ is of interest for whether the surface will coke or not. The landscape for Cu(111) and the SAA are very similar in this case, with a relatively high barrier and the reaction is endothermic. On Pt the barrier is lower and the reaction is exothermic, implying that it is easier to poison the Pt surface. In general all the adsorbates examined in the study are bound more

strongly to Pt and easier to form, making it more susceptible to poisoning than Cu or the SAA surface.

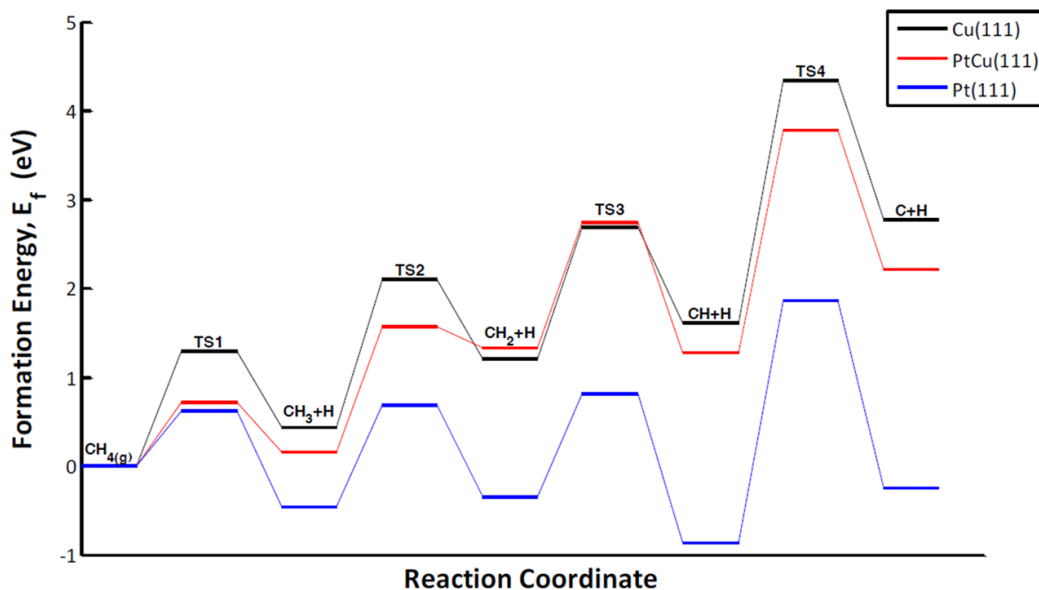


Figure 10.4 Potential energy diagram for the successive C-H scissions of C_xH_y species from methane to atomic C on Cu(111) (black), Pt/Cu(111) SAA (red) and Pt(111) (blue). The energies plotted are formation energies with respect to gas phase CH_4 and H_2 whose energies are zeroed.

Encouraged by the results of surface science experiments and theoretical calculations, we have begun to test the ability of SAAs to activate C-H bonds under practical conditions. We studied the $H \rightarrow D$ exchange reaction for butane on Cu, Pt and Pt_1Cu -SAA nanoparticles (NPs) (Figure 10.5). Figure 10.5A compares the effectiveness for all three types of nanoparticles at producing butane- D_1 . The experiments shown in the figure are the second cycle of running the reaction up to $400^\circ C$. The Cu NPs are unable to perform this reaction up to $400^\circ C$. Pt NPs activate the reaction by $100^\circ C$, but as shown in Figure 10.5B experience significant deactivation across multiple cycles, indicating the possibility of coke formation. The Pt_1Cu -SAA nanoparticles are able to activate the reaction by $250^\circ C$

and have been stable for a reaction cycle lasting up to 12 hours. These results mirror our findings in Chapter 9, and show that the SAA provides a lower barrier to activation than Cu catalysts, while avoiding the coking associated with Pt. This highlights surface science as a predictive tool for developing efficient catalysts.

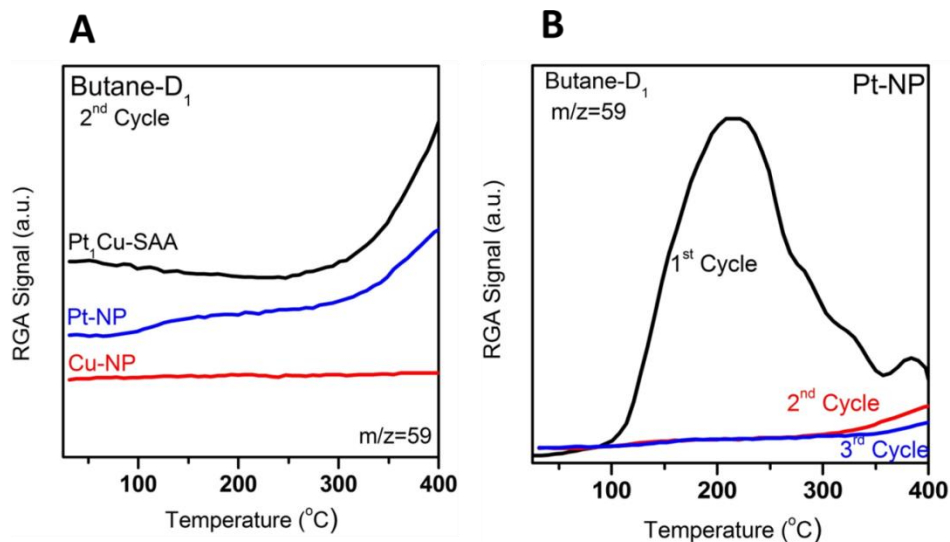


Figure 10.5 The H→D exchange reaction for butane on Cu, Pt and Pt₁Cu NPs. M/z 59 is monitored for the production of butane-D₁. 100 mg of catalyst were used for each experiment. The catalyst were exposed to a gas flow consisting of 5% butane and 2% D₂ in Ar using a flow rate of 50 mL/min. Catalysts were heated at 5°C/min. (A) Activity of the three catalysts for butane-D₁ formation during the second reaction cycle of each catalyst. (B) The first three reaction cycles for the Pt-NPs.

10.4 Conclusion

Cu based SAAs display great catalytic promise for a wide variety of chemical reactions. In this thesis we have tested the applicability of Pd/Cu and Pt/Cu SAAs as model catalysts for, H₂ activation, hydrogenations of C=C and C=O bonds, and dehydrogenations of both O-H and C-H bonds. Using a combination of scanning tunneling microscopy (STM) and TPD we are able to obtain a molecular scale view of the surface bound reactants and intermediates,

and obtain information about the binding strength of adsorbates and reaction barriers. SAAs typically offer more facile activation of reactants compared to bare Cu, while using only small, economically friendly amounts of Pd and Pt. This was demonstrated in the case of H₂ activation, O-H activation in both formic acid and H₂O, and C-H activation in methyl groups. In addition to improving the activity of the Cu surface, SAAs frequently yield improved selectivity and resistance to deactivation compared to Pt or Pd based catalysts by using the smallest ensemble possible of these reactive metals. SAAs were shown to improve selectivity in the hydrogenation of styrene, the decomposition of formic acid, and activation of methyl groups. In many of the systems studied, spillover of activated reactants from the dopant metal to the inert host plays a key role in promoting activity and selectivity. Cu based SAAs make efficient use of these rare and expensive dopant atoms to turn the relatively inert Cu surface into an efficient catalyst. While this thesis has focused specifically on two SAA systems using Cu as a host metal, the SAA principle can be applied to a wide range of catalytic alloy systems.^{21–23} Given the extensive number of possible metal combinations, SAAs could allow chemists and engineers to tailor ideal catalysts for many chemical reactions.

10.5 References

- (1) Marcinkowski, M. D.; Jewell, A. D.; Stamatakis, M.; Boucher, M. B.; Lewis, E. A.; Murphy, C. J.; Kyriakou, G.; Sykes, E. C. H. *Nat. Mater.* **2013**, *12*, 523–528.
- (2) Lavrich, D. J.; Wetterer, S. M.; Bernasek, S. L.; Scoles, G. *J. Phys. Chem. B* **1998**, *102*, 3456–3465.
- (3) Rodriguez, J. A.; Hrbek, J. *Acc. Chem. Res.* **1999**, *32*, 719–728.
- (4) Oudar, J. *Catal. Rev. Sci. Eng.* **1980**, *22*, 171–195.
- (5) Kuhn, W. K.; Szanyi, J.; Goodman, D. W. *Surf. Sci.* **1992**, *274*, L611–

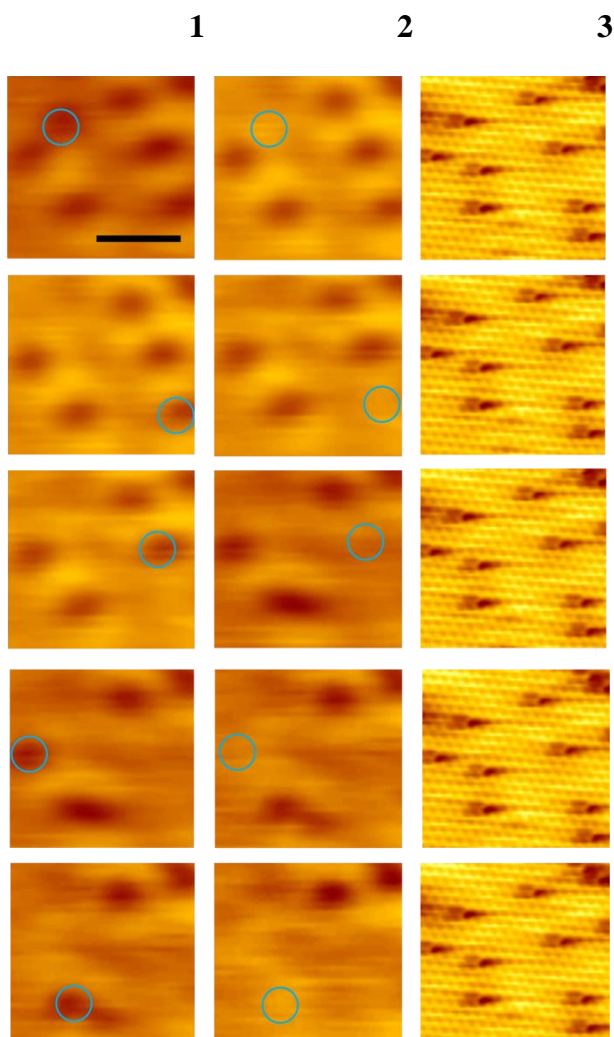
L618.

- (6) Kneitz, S.; Gemeinhardt, J.; Steinrück, H. *Surf. Sci.* **1999**, *440*, 307–320.
- (7) Kirstein, W.; Krueger, B.; Thieme, F. *Surf. Sci.* **1986**, *176*, 505–529.
- (8) Bonicke, I.; Kirstein, W.; Spinzig, S.; Thieme, F. *Surf. Sci.* **1994**, *313*, 231–238.
- (9) Alfonso, D. R. *Surf. Sci.* **2005**, *596*, 229–241.
- (10) May, M.; Gonzalez, S.; Illas, F. *Surf. Sci.* **2008**, *602*, 906–913.
- (11) Kiskinova, M.; Szabó, A.; Yates, J. T. *J. Chem. Phys.* **1988**, *89*, 7599–7608.
- (12) Pan, M.; Pozun, Z. D.; Brush, A. J.; Henkelman, G.; Mullins, C. B. *ChemCatChem* **2012**, *4*, 1241–1244.
- (13) Pan, M.; Brush, A. J.; Pozun, Z. D.; Ham, H. C.; Yu, W.-Y.; Henkelman, G.; Hwang, G. S.; Mullins, C. B. *Chem. Soc. Rev.* **2013**, *42*, 5002–5013.
- (14) Pan, M.; Flaherty, D. W.; Mullins, C. B. *J. Phys. Chem. Lett.* **2011**, *2*, 1363–1367.
- (15) Lucci, F. R.; Marcinkowski, M. D.; Lawton, T. J.; Sykes, E. C. H. *J. Phys. Chem. C* **2015**, *119*, 24351–24357.
- (16) Lucci, F. R.; Liu, J.; Marcinkowski, M. D.; Yang, M.; Allard, L. F.; Flytzani-Stephanopoulos, M.; Sykes, E. C. H. *Nat. Commun.* **2015**, *6*, 8550.
- (17) Lin, J.-L.; Bent, B. E. *J. Vac. Sci. Technol. A* **1992**, *10*, 2202–2209.
- (18) Lin, J.-L.; Bent, B. E. *J. Vac. Sci. Technol. A* **1992**, *10*, 2202–2209.
- (19) Zaera, F.; Hoffmann, H. *J. Phys. Chem. C* **1991**, *95*, 6297.
- (20) Henderson, M. A.; Mitchell, G. E.; White, J. M. *Surf. Sci.* **1987**, *184*, L325–L331.
- (21) Wang, Z.-T.; Darby, M. T.; Therrien, A. J.; El-Soda, M.; Michaelides, A.; Stamatakis, M.; Sykes, E. C. H. *J. Phys. Chem. C* **2016**, *120* (25), 13574–13580.
- (22) Lucci, F. R.; Darby, M. T.; Mattera, M. F. G.; Ivimey, C. J.; Therrien, A. J.; Michaelides, A.; Stamatakis, M.; Sykes, E. C. H. *J. Phys. Chem. Lett.* **2016**, *7*, 480–485.
- (23) Bellisario, D. O.; Han, J. W.; Tierney, H. L.; Baber, A. E.; Sholl, D. S.; Sykes, E. C. H. *J. Phys. Chem. C* **2009**, *113*, 12863–12869.

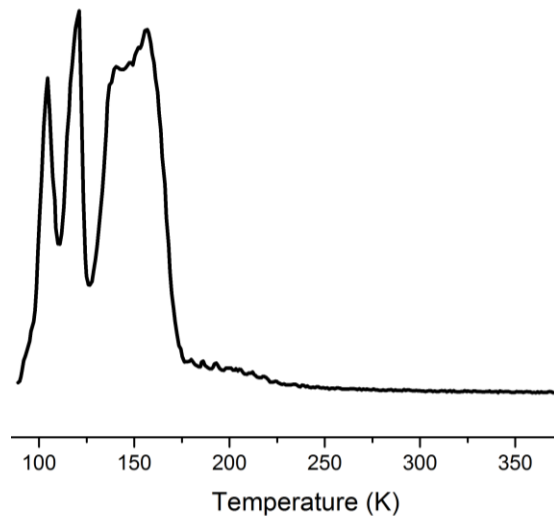
Appendix

Appendix to Chapter 4

To support our finding that CO preferentially occupies atomic Pd sites in the Cu/Pd surface alloy, we performed molecular manipulation experiments in which, using the STM tip, CO molecules were desorbed one-by-one¹ revealing the nature of the surface sites beneath with atomic resolution. Appendix Figure 1 below shows an example in which individual CO molecules were removed one at a time from their preferred adsorption sites with a 4.8 V pulse before the same area was imaged with atomic resolution. These experiments reveal a perfect correlation between the CO adsorption site and the individual Pd atoms in the surface beneath and show that one CO molecule is adsorbed above each Pd atom in the surface.

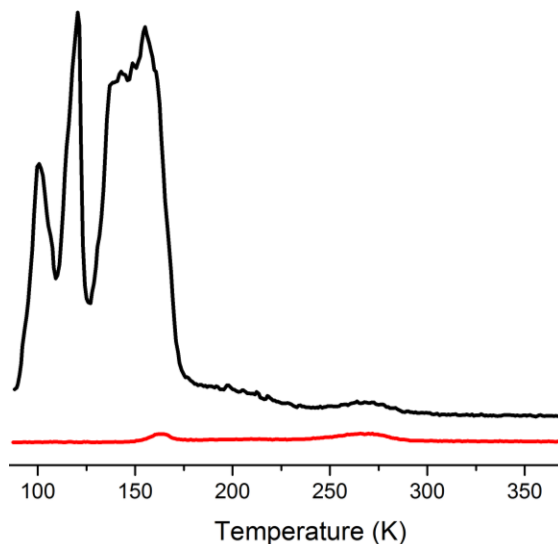


Appendix Figure 1 High resolution STM imaging and manipulation of individual CO molecules (appearing as diffuse depressions) adsorbed at their preferred sites on the Pd/Cu alloy surface. The blue circles in column 1 highlight each point at which a 4.8 V pulse was used to remove a single CO molecule. Column 2 shows the same regions after each molecule was removed, and the atomic resolution images in column 3 were acquired after removal of all the CO molecules from the area and reveal an exact correlation between preferred adsorption site of each CO molecule and the Pd atoms (appearing as localized depressions) in the surface beneath. Scale bar = 2 nm.



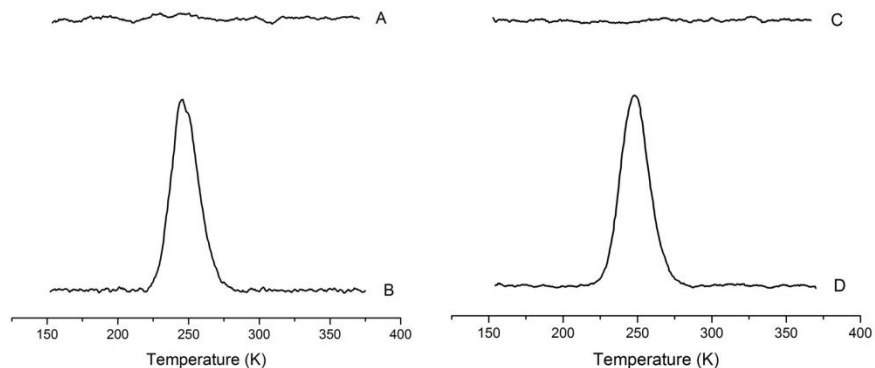
Appendix Figure 2 CO TPD from clean Cu(111) after a saturation exposure of 10 L.

CO adsorbs on Cu(111) without decomposition and saturates at an exposure of ≥ 8 L in our system in agreement with earlier reports.² The resulting TPD spectrum (Appendix Figure 2) shows three distinct desorption peaks, which have previously been investigated in detail.²⁻⁴ The low temperature peak (~ 110 K) is assigned to desorption from a densely packed (7×7) unit cell, the mid temperature peak (~ 130 K) to desorption of the intermediate (4×4) unit cell, and the largest peak, centered around 170 K to desorption from the $(\sqrt{3} \times \sqrt{3})$ unit cell. Saturation of CO on Cu(111) at low temperatures yields a (7×7) unit cell that corresponds to 0.52 ML, i.e. 0.52 CO molecules per surface Cu atom.



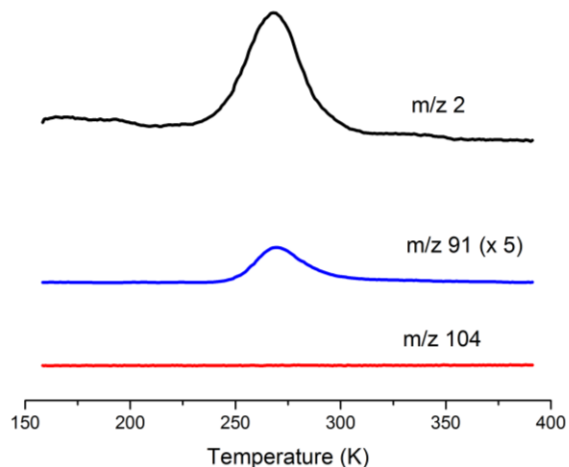
Appendix Figure 3 CO TPD spectra from 0.01 ML of Pd in Cu(111) after a saturation CO exposure of 10 L (black) and 0.1 L (red).

Desorption of CO from a 0.01 ML Pd/Cu(111) SAA results in a TPD spectrum with very similar features to that of pure Cu(111) except for a small high temperature desorption peak of CO at 270 K which is correlated with CO binding at individual Pd atom sites as shown in the STM image in Figure 4.1C-E in Chapter 4. The TPD spectra in Appendix Figure 3 show desorption of 10 L (black) and 0.1 L (red) CO from 0.01 ML Pd in Cu(111). The 10 L CO dose saturates the monolayer and looks almost identical to Appendix Figure 2 except for the higher temperature peak associated with CO bound to Pd sites which indicates that in a 0.01 ML Pd/Cu(111) SAA the vast majority of the surface sites are Cu(111). The 0.1 L CO dose is enough to saturate the Pd sites and populate a small fraction of the available Cu surface as evidenced by the small peak at 160 K in the red trace.



Appendix Figure 4 TPD spectra for uncorked (A) and corked (B) hydrogen after a 190 K anneal for 10 min. TPD spectra for uncorked (C) and corked (D) hydrogen after a 210 K anneal for 10 min.

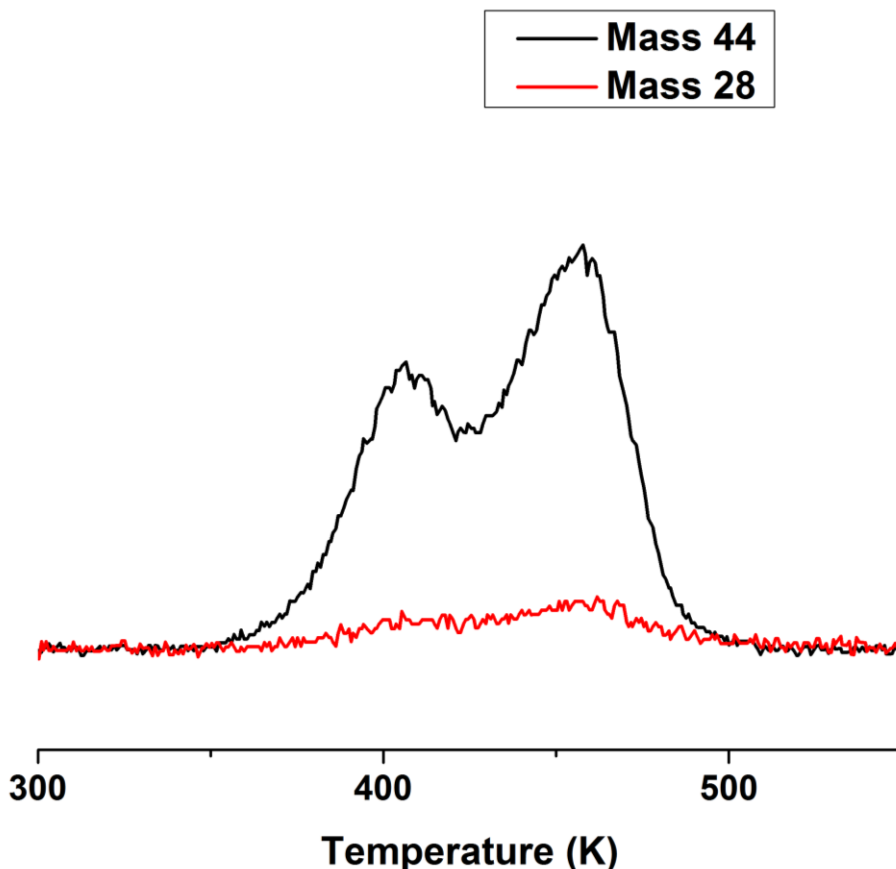
In order to investigate if the cork effect could be used to store hydrogen on the Cu(111) surface above its normal desorption temperature, we performed isothermal annealing experiments both with and without the CO cork. Hydrogen and CO were deposited at 85 K, the system was then ramped to the desired temperature, held for 10 min and cooled to 150 K before the TPD spectra were acquired. This data, shown below in Appendix Figure 4, reveals that when the system is uncorked, a 10 min anneal in a temperature window between 190 - 210 K leads to desorption of surface bound H. However, annealing the corked system under identical conditions results in retention of the surface-bound hydrogen. This provides direct evidence for storage of weakly bound H atoms that have spilled over onto Cu from Pd sites. Common hydrogen storage materials utilize small Pt/Pd particles to promote uptake by activating molecular H₂ and facilitating spillover of hydrogen atoms onto a support. Given that CO desorbs from low index Pd surfaces ~500 K we suggest that the molecular cork effect could be used to store hydrogen over a much wider range of temperatures in practical systems.



Appendix Figure 5 TPR spectrum showing complete hydrogenation of styrene on a 0.01 ML of Pd in Cu(111) surface after a exposure to 200 L H₂ and 0.01 ML Styrene. M/z 2 corresponds to hydrogen, m/z 91 corresponds to ethylbenzene, and m/z 104 corresponds to styrene.

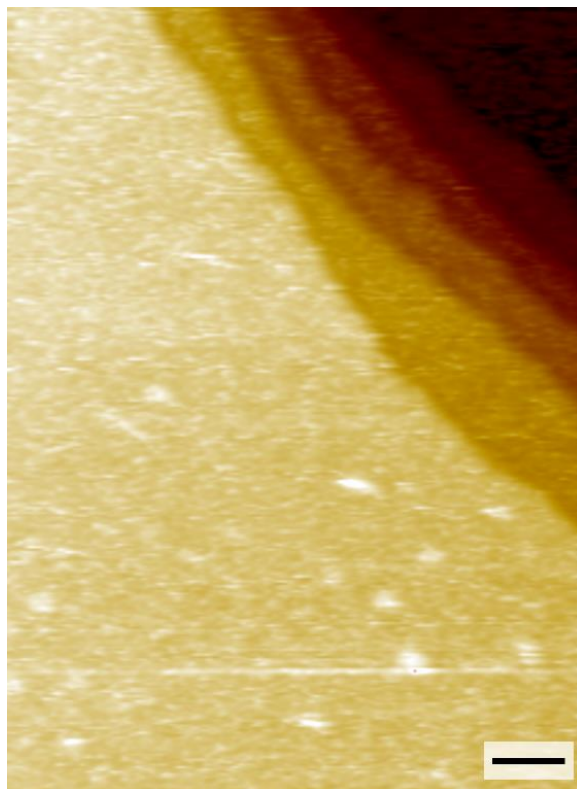
The presence of styrene on Cu(111) causes the surface hydrogen to be coked even at a coverage of 0.01 ML of styrene as evidenced by the hydrogen peak being shifted 55 K higher in temperature in the TPR spectrum in Appendix Figure 5. This TPR of styrene shows that effectively all styrene has converted to ethylbenzene at this low styrene coverage.

Appendix to Chapter 6



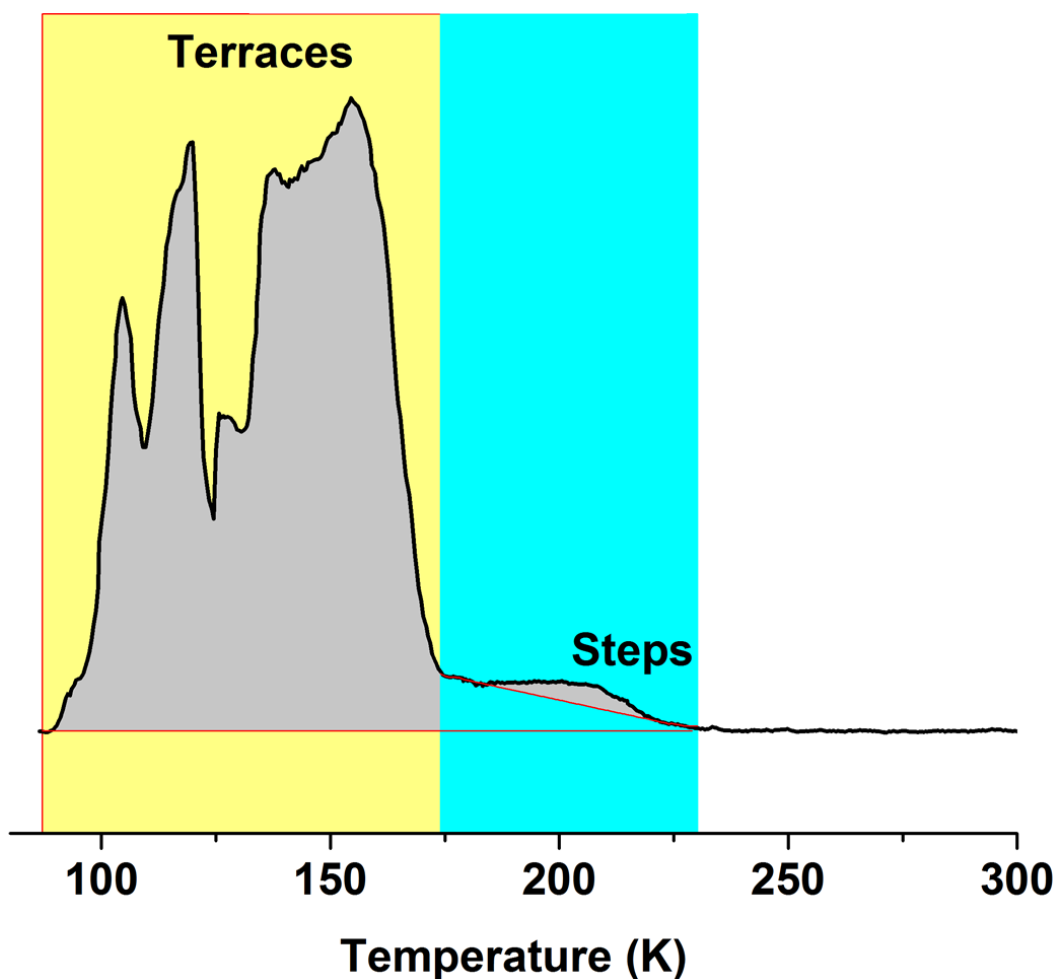
Appendix Figure 6 TPD traces for m/z 44 and m/z 28 resulting from the decomposition of 1 L of formic acid exposed to Cu(111) at 85 K.

The cracking pattern for CO_2 has a contribution from m/z 28, which is also the parent ion for CO. The measured signal for m/z 28 that is 9% of the signal for m/z 44, the parent ion and major contributor to the cracking pattern for CO_2 (Appendix Figure 6). This ratio is in good agreement with expected 10% contribution based on NIST's mass spectrometry database.⁵ This result demonstrates that there is no reactively formed CO produced during the decomposition of formic acid on Cu(111), which means the reaction proceeds solely through dehydrogenation.



Appendix Figure 7 STM image of multilayers of formic acid on Cu(111). Imaged at 5 K. Scale bar = 5 nm.

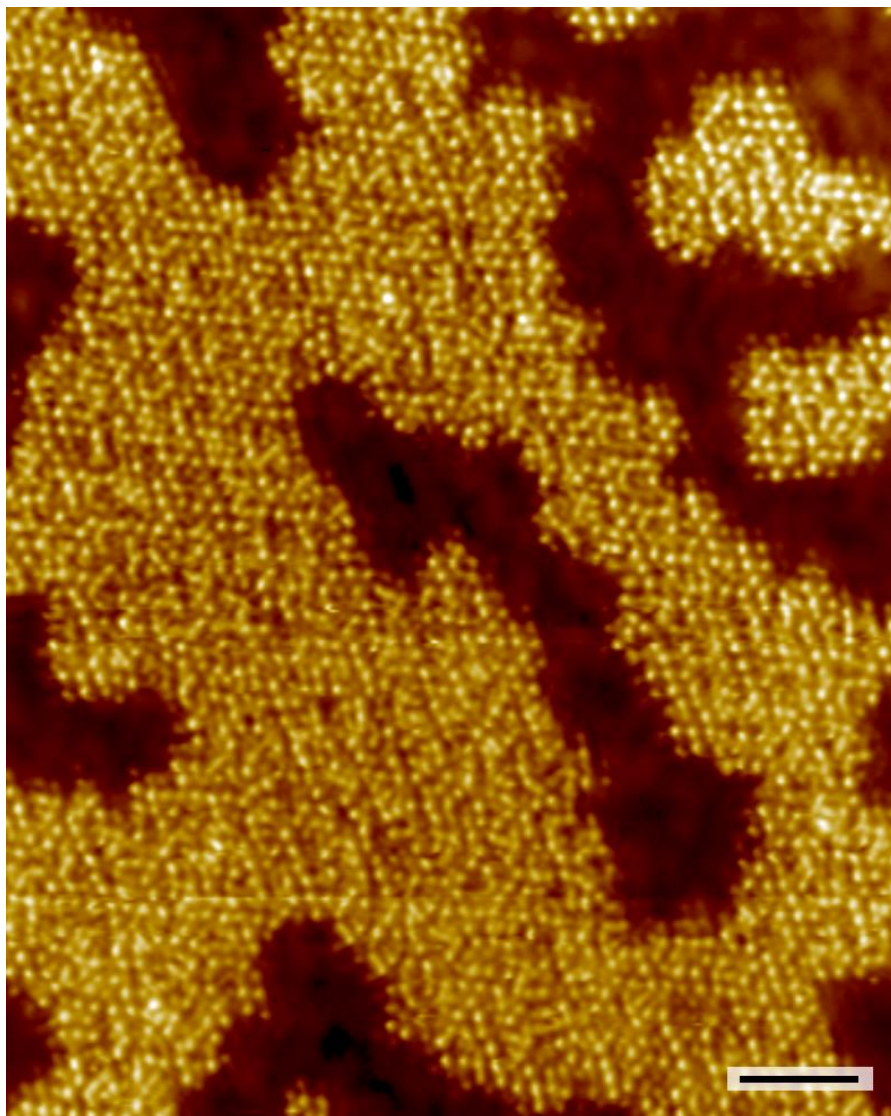
Formic acid does not form an ordered multilayer on Cu(111). Multilayers appear to be mobile even at 5 K due to the influence of the STM tip (Appendix Figure 7). This demonstrates that formic acid molecules in the multilayer have minimal interaction with the surface, which is expected as they do not react and simply desorb as intact formic acid at 150 K. Annealing this surface to 160 K yields the same formate coverage as one monolayer of formic acid.



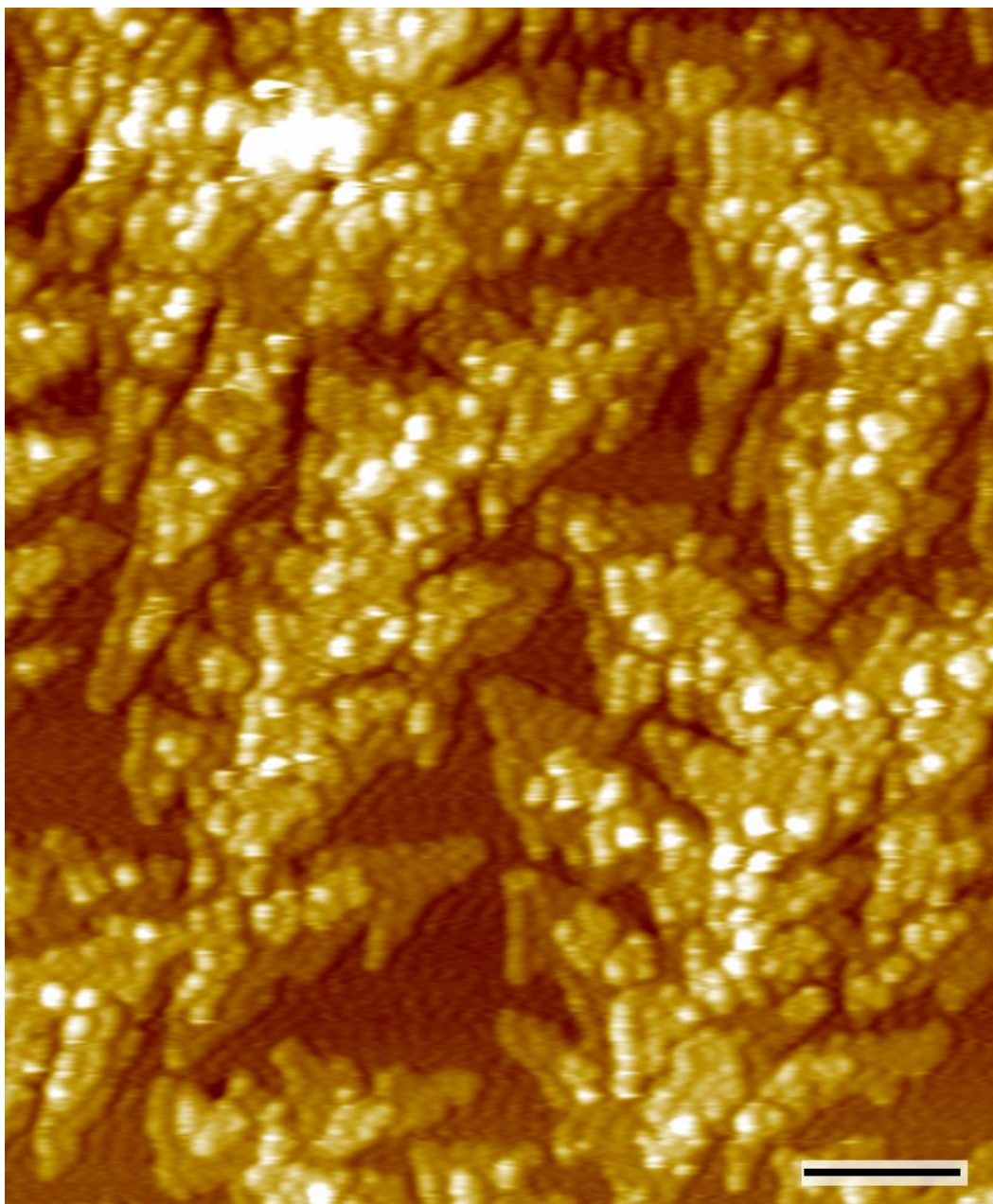
Appendix Figure 8 CO TPD demonstrating how the crystal's step density can be calculated by integrating the different CO peaks.

The desorption of CO from Cu(111) has been well studied and each desorption peak is easily identifiable and its packing structure on Cu terraces was discussed in Appendix Figures 2 and 3. The highest temperature peak at 220 K is consistent with CO desorbing from Cu(111) steps.⁶ We are able to determine the step density of our Cu(111) crystal by taking the ratio of the area of the step peak to the total area under the TPD curve. Using the step density (1.54%) we are able to calculate the amount of CO₂ produced from formic acid dehydrogenation on the terraces compared to the steps.

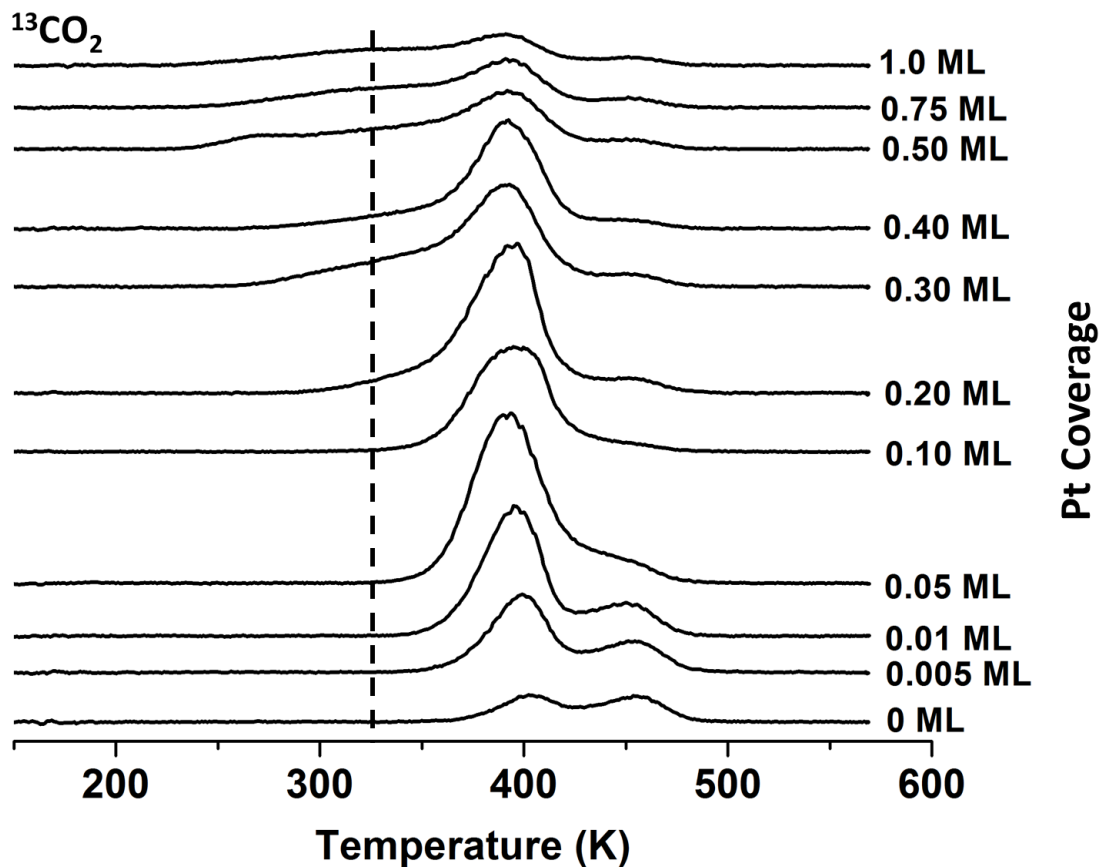
Appendix to Chapter 7



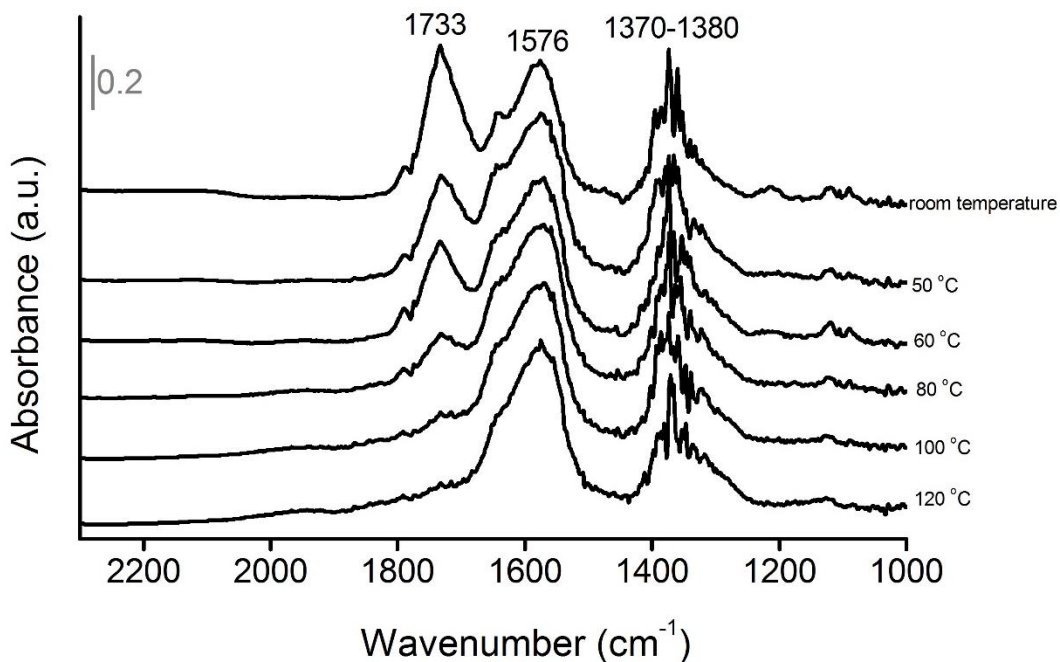
Appendix Figure 9 Formate on 0.01 ML Pt/Cu(111). This surface resulted from annealing a monolayer of formic acid to 120 K twice in succession. Scale bar = 3 nm. Unlike the surface in Figure 7.3B where some intact formic acid is present, this image shows that all formic acid is converted to formate upon successive anneals.



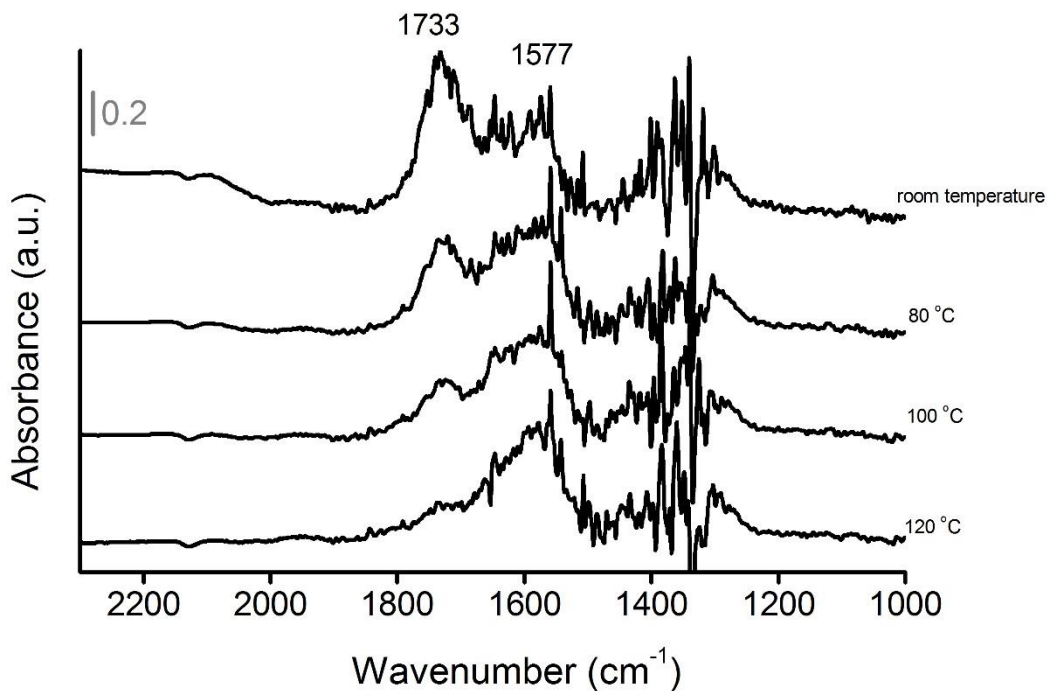
Appendix Figure 10 STM image of 1.0 ML of Pt deposited on a Cu(111) surface at 380 K. Scale bar = 25 nm. Large Pt islands form on the surface, creating a very corrugated landscape. Some areas in the islands behave similarly to Pt(111). However, there are some areas of the surface not covered by islands where Pt still exists as single isolated species substituted into the still exposed Cu(111) lattice.⁷



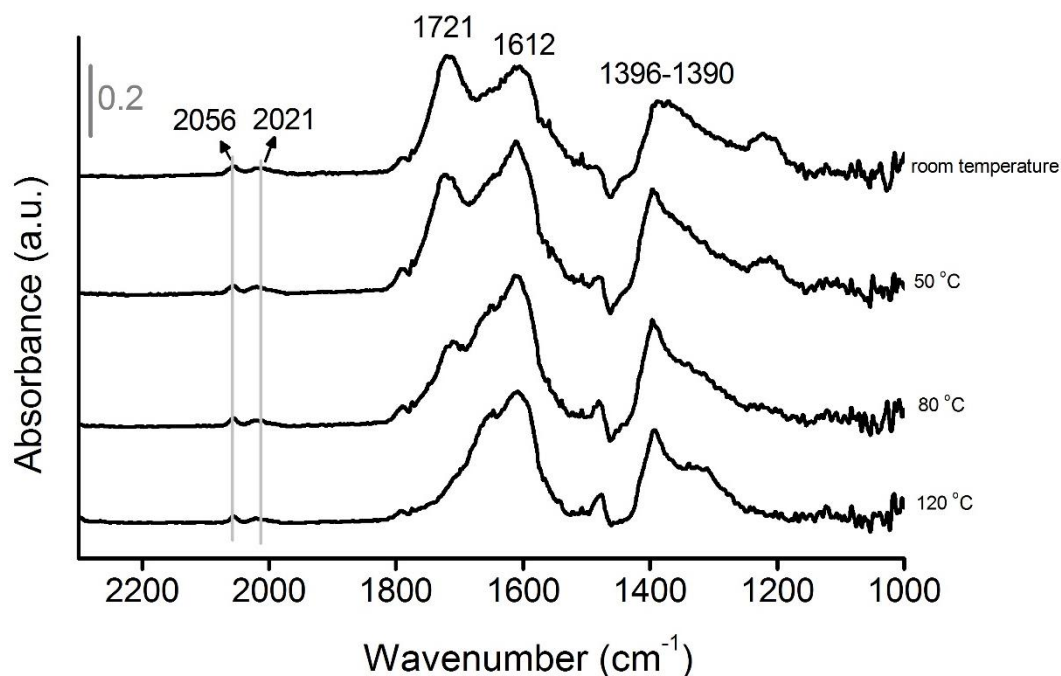
Appendix Figure 11 TPR spectra for $^{13}\text{CO}_2$ resulting from depositing 1.5 L of H^{13}COOH onto surfaces with varied Pt coverage. Dashed line marks a low temperature desorption peak which results from formate decomposition on extended Pt surfaces. This peak is not observed on the Cu(111) or SAA surface, only when chains and areas similar to Pt(111) have begun to form.



Appendix Figure 12 Diffuse Reflectance Infrared Fourier Transform Spectroscopy (DRIFTS) spectra collected at different temperatures exposing the Pt₁Cu-SAA catalyst to 5 μ L formic acid carried by a 10 ml/min He flow.



Appendix Figure 13 DRIFTS spectra collected at different temperatures after exposing the Cu-NP catalyst to 5 μ L formic acid carried by a 10 ml/min He flow.



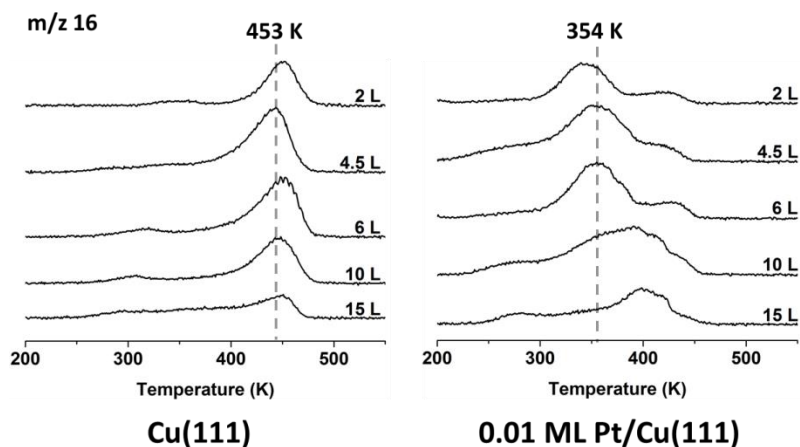
Appendix Figure 14 DRIFTS spectra collected at different temperatures after exposing the PtCu-bimetallic catalyst to 5 μL formic acid carried by a 10 ml/min He flow.

In order to detect the reactants, intermediates and products of the formic acid decomposition reaction, Diffuse Reflectance Infrared Fourier Transform Spectroscopy (DRIFTS) was performed on Pt₁-Cu SAA, Cu-NP and PtCu-bimetallic samples after passing formic acid vapor through the sample (Appendix Figures 12, 13, and 14). Absorption bands between 1733 and 1720 cm⁻¹ are assigned to formic acid and the bands at 1576 and 1370 cm⁻¹ are assigned to asymmetrical and symmetrical vibrations of formate.⁸⁻¹⁰ As the temperature was increased, the intensity of the formic acid band decreased while the formate bands were not significantly changed, which indicates the stronger binding of formate to the metal surface. Bands at 2056 and 2021 cm⁻¹ corresponding to adsorbed carbonyl were only observed on PtCu-bimetallic, which is in agreement with the

results of our TPD study finding CO formation with increasing Pt loading on the surface of the Pt-Cu(111) alloy.

PtCu-bimetallic was prepared as described in Liu et al.⁷ and contains 2.2 at% Pt, 5.6 at% Cu on γ -Al₂O₃ (ultra-pure grade 99.99%, surface area 70-100 m² g⁻¹, Inframat Advanced Materials; heat treated in air at 400 °C). DRIFTS was performed on a Thermo Nicolet iS50 FT-IR equipped with a Harrick DRIFTS cell. All of the samples were pre-reduced *in situ* in 20% H₂ at 200 °C. After purging with Helium for 10 minutes, background spectra were collected at room temperature. Then 5 μ L of formic acid was injected to the gas cell under He gas flow. IR spectra were collected at different temperatures after each temperature was stabilized for 10 minutes.

Appendix to Chapter 9

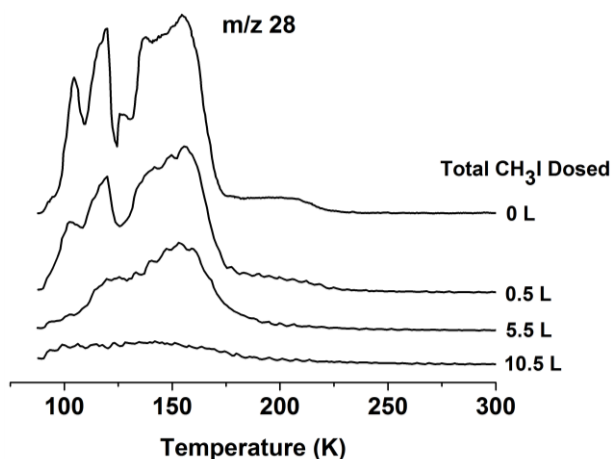


Appendix Figure 15 Methane desorption from various Langmuir (1 L = 1×10^{-6} torr s) exposures of methyl iodide on Cu(111) and 0.01 ML Pt/Cu(111). Each experiment was performed on a clean surface.

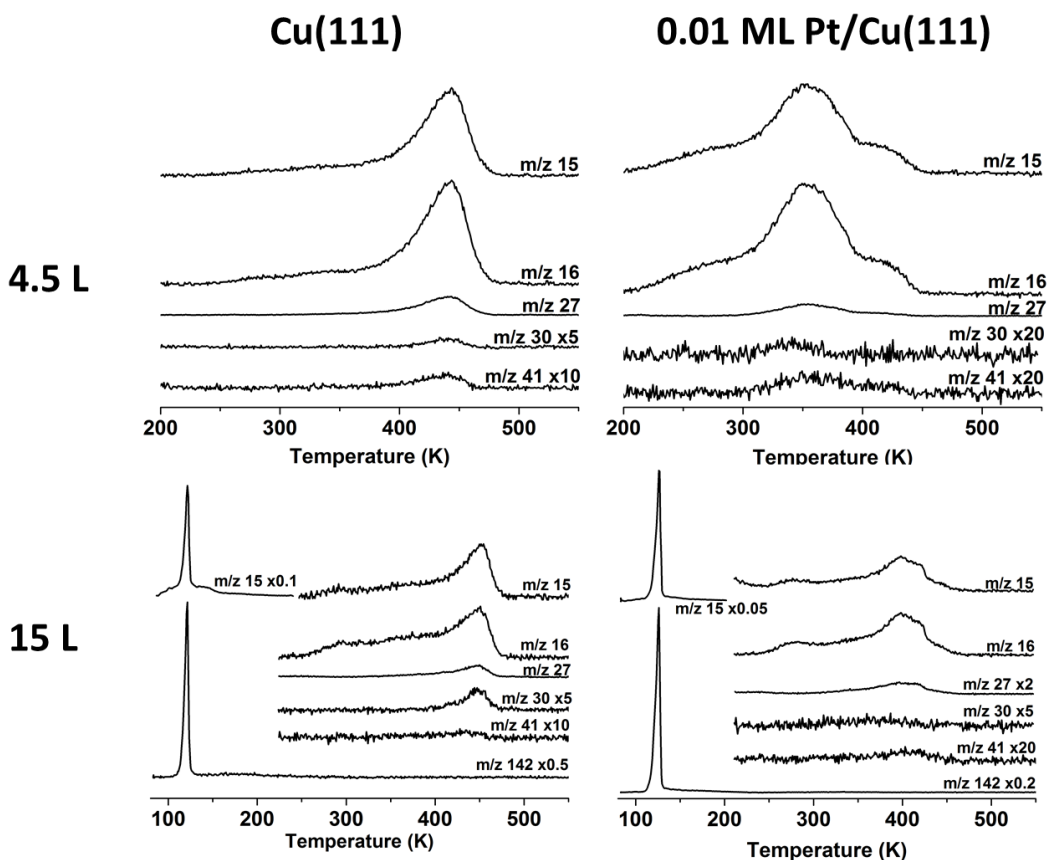
Iodine is known to strongly adsorb to metal surfaces and act as a site blocker.^{11,12} As shown in Appendix Figure 15, on Cu(111) as additional methyl iodide is deposited on the surface the temperature at which methane desorbs does not change, but the area of the methane peak begins to drop after a 4.5 L dose. This is due to iodine blocking Cu sites from accommodating methyl groups, causing methyl iodide to desorb intact or methyl rejection as will be shown in Appendix Figure 17. On the 0.01 ML Pt/Cu(111) surface there is also an eventual decrease in the area of desorbing methane, but in addition the temperature shifts from 350 K to around 400 K after the exposure of methyl iodide increases past 6 L. This is because iodine atoms are blocking the single Pt sites and preventing their low temperature activation of C-H bonds.

To further demonstrate the site blocking properties of iodine we performed experiments with CO on pure Cu(111) (Appendix Figure 16). The behavior of CO

on Cu(111) is well documented. CO forms three distinct packing phases on Cu(111), a densely packed (7x7) unit cell, an intermediate (4x4) unit cell, and a least densely packed ($\sqrt{3} \times \sqrt{3}$) unit cell.²⁻⁴ These three phases desorb at 110 K, 130 K, and 170 K respectively. In addition CO bound to Cu(111) steps desorbs at 220 K.⁶ In these experiments various amounts of methyl iodide were exposed to the surface followed by a heating ramp to remove all species with the exception of iodine. After each methyl iodide exposure a saturation dose of CO was exposed to the crystal. When no methyl iodide is exposed to the surface the familiar desorption trace of CO from Cu(111) is seen. However, as more iodine is added to the surface the signal from each CO adsorption site gradually decreases until after a 10.5 L exposure of methyl iodide very little CO is able to adsorb to the surface. However, the temperature CO desorbs from the surface is unaffected by the iodine, indicating that it acts solely as a site blocker.



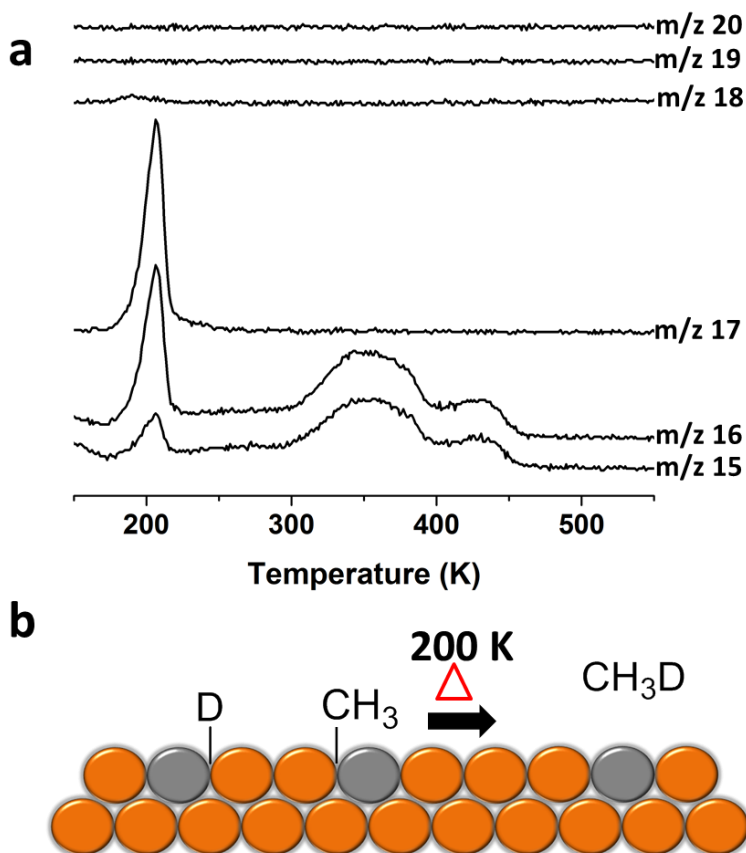
Appendix Figure 16 Desorption of CO from surfaces previously exposed to various amounts of methyl iodide. The surface was thermally annealed to remove everything besides iodine prior to exposure to CO in each case.



Appendix Figure 17 TPR traces for all desorption products observed following 4.5 and 15 L exposures of methyl iodide on both Cu(111) and 0.01 ML Pt./Cu(111).

As mentioned in Chapter 9 at relatively low coverage (4.5 L exposure) the main desorption product detected after exposing the surface to methyl iodide is methane which exhibits large signals for both m/z 15 and 16. The second most abundant desorption product at these exposures is ethene which is tracked via m/z 27. In addition to ethene, trace amounts of ethane and propene desorb from the surface which are tracked via m/z 30 and m/z 41 respectively. The ratio of methane to carbon coupling products is larger on the 0.01 ML Pt/Cu(111) surface, although the overall carbon count desorbing from each surface is the same. The increase in methane production on the alloy surface is most likely due to low

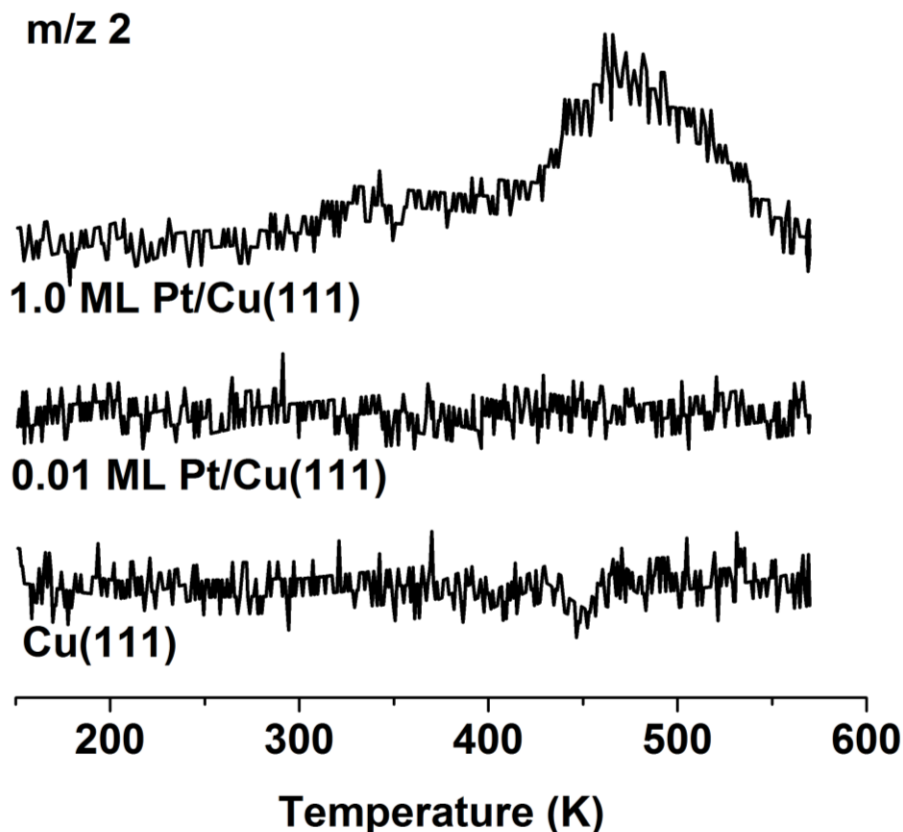
temperature hydrogenation of methyl groups from H atoms adsorbed from the chamber background. This can be seen by the low temperature shoulder apparent for the two methane masses (15 and 16) where no coupling products are observed. At larger exposures of methyl iodide, intact methyl iodide desorbs at low temperature on both surfaces. In addition, as previously reported by Bent and co-workers methyl rejection is also observed as there is a large desorption feature from m/z 15 at low temperature.¹³ Bent also reported a high temperature methyl rejection pathway occurring at 450 K at high coverage, but we do not see evidence of this in our work. In spectra presented in Chapter 9 all exposures were low enough to avoid desorption of intact methyl iodide and methyl rejection.



Appendix Figure 18 Methyl iodide and deuterium on Pt/Cu SAAs. (a) TPR spectra of possible methane products resulting from the reaction of methyl iodide on a D-pre-covered 0.01 ML Pt/Cu(111) surface. (b) Schematic showing the interaction of H atoms with methyl groups on Pt/Cu.

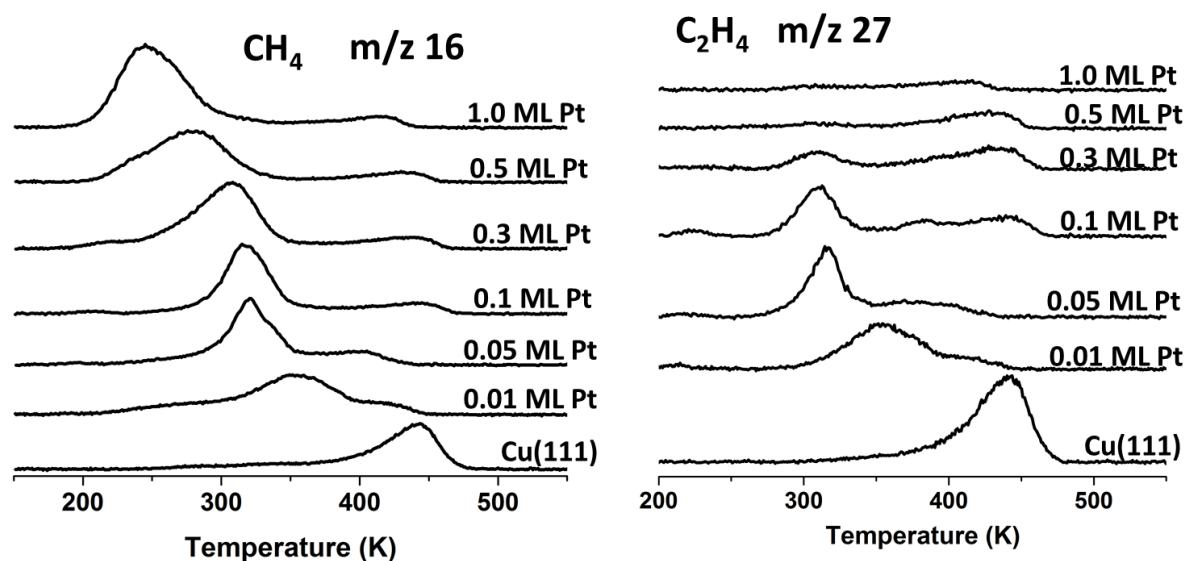
We have previously demonstrated that Pt/Cu(111) SAAs are capable of dissociating H₂.^{14,15} To examine the direct hydrogenation of methyl groups to methane we performed an experiment where methyl iodide was exposed to a 0.01 ML Pt/Cu SAA that had been pre-covered with hydrogen. On this hydrogen pre-covered surface, methane desorbs at 200 K, well below the temperatures methane desorbs from either clean surface. In addition at 200 K, no carbon coupling products are observed. On this surface, C-H activation is not the rate limiting step. Rather it is the hydrogenation of methyl that limits the production of methane. It is known that pre-covering Pt(111) with hydrogen allows for hydrogenation of

methyls.¹⁶ To confirm this was the case on our SAA surface, we performed a similar experiment using a deuterium pre-covered surface (Appendix Figure 18). M/z 15-20 were tracked to track for CH₄, CH₃D, CH₂D₂, CHD₃, and CD₄. We observe predominately m/z 17 with a large contribution from m/z 16 and a small amount of m/z 15. In other words if we assign the parent ion as M, we observe M, M-1, and M-2. M/z 16 (M-1) is ~70% of the signal from m/z 17 while m/z 15 (M-2) is ~20% of the signal from m/z 17. Normally the primary contributor to CH₄'s cracking pattern is the parent ion m/z 16. According to NIST's cracking pattern for methane m/z 15 (M-1) and m/z 14 (M-2) both contribute with relative intensities 89% and 20% of m/z 16 respectively.⁵ Therefore our observed cracking pattern is in good agreement with the sole desorption product at 200 K being CH₃D. This indicates that the methane results from hydrogenation of the methyl groups, and no C-H activation occurs at this temperature. The production of methane at low temperature is limited by the saturation of hydrogen on the 0.01 ML Pt/Cu(111) surface, which is 0.1 ML. As our coverage of methyl groups present on the surface is greater than this we still observe some CH₄ desorbing at 350 K resulting from C-H activation in methyl groups.



Appendix Figure 19. Hydrogen desorption after adsorption of 4.5 L CH_3I on Cu(111), 0.01 ML Pt/Cu(111) and 1.0 ML Pt/Cu(111).

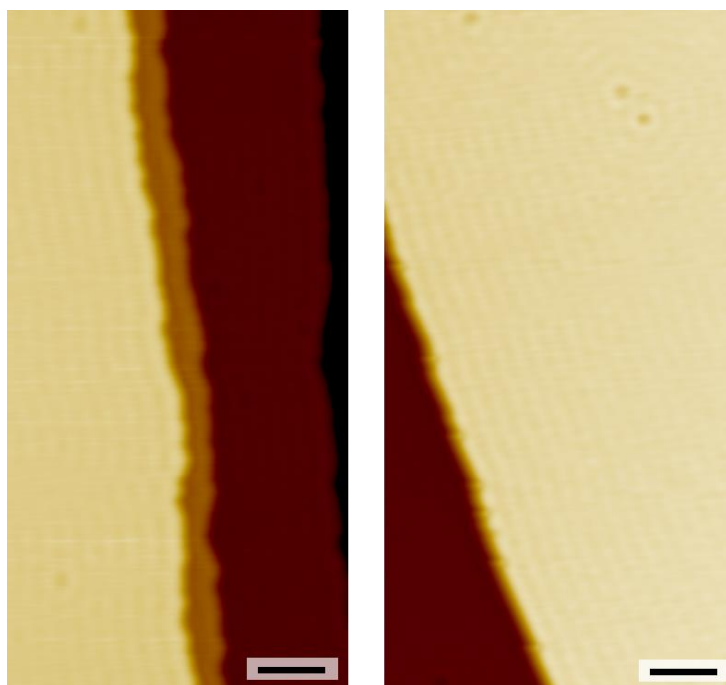
High temperature desorption of hydrogen is a good indication that hydrocarbons are decomposing on a surface, leaving carbon fragments which cause coking. Bent's work showed only iodine remained on a Cu(111) surface after TPRs of methyl iodide, indicating no coking occurs on this surface.^{13,17,18} Our results confirm this, as there is no desorption of hydrogen from Cu(111) as shown in Appendix Figure 19. The same is true for the SAA 0.01 ML Pt/Cu(111) surface. However, on the 1.0 ML Pt/Cu(111) surface significant hydrogen desorption is observed at ~500 K. On pure Pt(111), hydrogen also desorbs at this temperature and this was attributed to the decomposition of methylene groups resulting C-H activation in methyl groups.^{16,19}



Appendix Figure 20. TPR spectra of methane and ethene produced via reaction of 4.5 L of methyl iodide on various Pt/Cu(111) alloy surfaces.

To further analyze the effect of Pt on C-H activation, we performed TPR experiments with alloys containing various concentrations of Pt, up to 1 ML of Pt. We have previously characterized these alloys using STM.^{7,20} Based on our STM results, it is known that up to 0.05 ML of Pt, SAAs are formed. Above 0.05 ML Pt rich fingers containing linear chains of Pt grow from the step edges. The higher the coverage the more prominent these features become. Above 0.5 ML Pt, areas at the edges of the fingers become Pt(111) like. Appendix Figure 20 shows methane and ethene TPR spectra for Cu(111) and six different Pt/Cu alloys. In general the methane desorbs at lower temperature with increasing Pt coverage. The temperature change is most drastic between Cu(111) and 0.01 ML Pt/Cu(111) where the C-H activation temperature changes from 450 K to 350 K as previously discussed. Beyond this point the decrease in temperature is nearly linear. At 0.05 ML, where Pt chains begin to form, the temperature drops further to 323 K. By

0.5 ML, where some Pt(111) sites are present, the C-H bond activates at 280 K. Finally by 1 ML of Pt the C-H bond activates at 250 K as previously discussed. The production of coupling products also decreases with increasing Pt coverage. There is initially slight decrease in ethene production, which is accompanied by an increase in methane production between Cu(111) and 0.01 ML Pt/Cu(111). However, both ethene and methane production remain roughly constant up to 0.1 ML Pt, where the surface still mostly consist of single Pt sites, with some Pt chains. Beyond this point ethene production decreases while methane production increases. These trends demonstrate that as more Pt is added the surface chemistry of the alloy becomes more and more similar to Pt(111). The lack of coupling products at high Pt coverages imply that some carbon species remain on the surface, similar to Pt(111). High temperature hydrogen as shown in Appendix Figure 19 is first seen when the surface coverage of Pt reaches 0.30 ML, the coverage where regions of Pt(111) are expected to start forming.



Cu(111) 0.01 ML Pt/Cu

Appendix Figure 21. STM images of Cu(111) and 0.01 ML Pt/Cu(111) annealed to 1000. Both surfaces had previously been populated with methyl iodide.

Annealing both Cu(111) and 0.01 ML Pt/Cu(111) to 1000 K removes all iodine from the surfaces (Appendix Figure 21). After a 1000 K anneal, Pt has diffused into the bulk so the SAA surface appears identical to bare Cu(111). Most importantly, on both surfaces there is no evidence of carbon species once the iodine is removed. Previous research demonstrated that no carbon remains on Cu(111) after the reaction of methyl iodide, but this experiment shows the same result for the SAA surface.^{13,17,18}

References

- (1) Bartels, L.; Meyer, G.; Rieder, K.-H.; Velic, D.; Knoesel, E.; Hotzel, A.; Wolf, M.; Ertl, G. *Phys. Rev. Lett.* **1998**, *80*, 2004–2007.
- (2) Raval, R.; Parker, S.; Pemble, M.; Hollins, P. *Surf. Sci.* **1988**, *203*, 353–377.
- (3) Kirstein, W.; Krueger, B.; Thieme, F. *Surf. Sci.* **1986**, *176*, 505–529.
- (4) Kneitz, S.; Gemeinhardt, J.; Steinrück, H. *Surf. Sci.* **1999**, *440*, 307–320.
- (5) NIST Chemistry Webbook. <http://webbook.nist.gov/chemistry/> (accessed May 19, 2016).
- (6) Bonicke, I.; Kirstein, W.; Spinzig, S.; Thieme, F. *Surf. Sci.* **1994**, *313*, 231–238.
- (7) Liu, J.; Lucci, F. R.; Yang, M.; Lee, S.; Marcinkowski, M. D.; Therrien, A. J.; Williams, C. T.; Sykes, E. C. H.; Flytzani-Stephanopoulos, M. *J. Am. Chem. Soc.* **2016**, *138*, 6396–6399.
- (8) Binet, C.; Daturi, M.; Lavalley, J.-C. *Catal. Today* **1999**, *50*, 207–225.
- (9) Li, C. *J. Catal.* **1990**, *125*, 445–455.
- (10) Jiang, K.; Xu, K.; Zou, S.; Cai, W.-B. *J. Am. Chem. Soc.* **2014**, *136*, 4861–4864.
- (11) Chao-Ming, C.; Bent, B. E. *Surf. Sci.* **1992**, *279*, 79–88.
- (12) Pascal, M.; Lamont, C. L. A.; Kittel, M.; Hoefl, J. T.; Constant, L.; Polcik, M.; Bradshaw, A. M.; Toomes, R. L.; Woodruff, D. P. *Surf. Sci.* **2002**, *512*, 173–184.
- (13) Lin, J.-L.; Bent, B. E. *J. Phys. Chem.* **1993**, *97*, 9713–9718.
- (14) Lucci, F. R.; Marcinkowski, M. D.; Lawton, T. J.; Sykes, E. C. H. *J. Phys. Chem. C* **2015**, *119*, 24351–24357.
- (15) Lucci, F. R.; Liu, J.; Marcinkowski, M. D.; Yang, M.; Allard, L. F.; Flytzani-Stephanopoulos, M.; Sykes, E. C. H. *Nat. Commun.* **2015**, *6*, 8550.
- (16) Zaera, F. *Surf. Sci.* **1992**, *262*, 335–350.
- (17) Lin, J.-L.; Bent, B. E. *J. Vac. Sci. Technol. A* **1992**, *10*, 2202–2209.
- (18) Jenks, C. J.; Bent, B. E.; Zaera, F. *J. Phys. Chem. B* **2000**, No. 100, 3017–

3027.

- (19) Henderson, M. A.; Mitchell, G. E.; White, J. M. *Surf. Sci.* **1987**, *184*, L325–L331.
- (20) Lucci, F. R.; Lawton, T. J.; Pronschinske, A.; Sykes, E. C. H. *J. Phys. Chem C.* **2014**, *118*, 3015–3022.